Numerical methods for radiative transfer in circumstellar environnements

Jérémy Perdigon

UNIVERSITÉ CÔTE D'AZUR

ÉCOLE DOCTORALE
SCIENCES FONDAMENTALES ET APPLIQUÉES

THÈSE DE DOCTORAT

Méthodes numériques pour le transfert de rayonnement dans les milieux circumstellaires

Jérémy Perdigon

Laboratoire Lagrange

Présentée en vue de l'obtention du grade de docteur en Sciences de la Planète et de l'Univers de l'Université Côte d'Azur
Dirigée par : Marianne Faurobert
Co-encadrée par : Gilles Niccolini
Soutenue le : 25 Novembre 2022

Devant le jury, composé de :

Marianne Faurobert (Directrice), Professeur des Universités, Université Côte d'Azur
Niccolini Gilles (Co-Directeur), Maître de Conférences, Université Côte d'Azur
Alex C. Carciofi (Rapporteur), Professeur, Universidade de São Paulo (Brésil)
Frédéric Paletou (Rapporteur), Astronome, Observatoire Midi-Pyrénées
Armando Domiciano de Souza (Examinateur), Astronome Adjoint, Observatoire de la Côte d'Azur
Anne Dutrey (Examinatrice), Directrice de Recherche, Université de Bordeaux
José F. Gomez (Examinateur), Chargé de Recherche, Instituto Astrofísica Andalucía (Espagne)
Holger Homann (Examinateur), Maître de Conférences, Université Côte d'Azur

Observatoire de la CÔTE d'AZUR

LAGRANGE

Abstract

The study of the radiative transfer problem is crucial for the characterisation of circumstellar environments. Radiative processes play a major role in the determination of physical observables of these astrophysical objects, such as the temperature, abundances, velocity fields, etc. The description of the frequency dependent and multi-dimensional radiation field is both a theoretical and numerical challenge, especially in the presence of scattering. The development of approximate descriptions and/or numerical methods is necessary in order to efficiently and accurately describe the radiation. This thesis investigate one approximate and one numerical method for solving the radiative transfer equation, coupled with the radiative equilibrium equation, in axis-symmetric circumstellar envelope of dust.

We first considered one of these approximate descriptions, the Flux-Limited Diffusion (FLD) which recasts the radiative transfer equation into a non-linear diffusion equation, asymptotically exact in both optically-thin and thick regimes. One important aspect for the accuracy of the method lies in the derivation of appropriate boundary conditions. We derived non-linear mixed boundary conditions aimed to be accurate enough in all optical regimes. We implemented the FLD approximation together with our derived boundary conditions and tested their accuracy by comparing our results (temperature profiles and spectral energy distributions) with benchmarks from literature, for spherically-symmetric and for axis-symmetric configurations. Our results showed a very good agreement for the spherically symmetric case, enabling astrophysical applications for objects compatible with this symmetry. For the axis-symmetric case, the agreement is not as good and is the result of the limitations of FLD approximation itself. In all cases, we show that the boundary conditions we derived correctly describe the mean specific radiation field at all the boundaries of circumstellar envelope.

Second, we investigated the Discontinuous Galerkin finite element method (DG-FEM) applied to the radiative transfer equation in spherical coordinates. The method make use of elements and flux integrals along their boundaries, insuring local conservation. However, as opposed to the classical finite-element methods, the reconstructed solution is discontinuous across the element edges. A useful feature of the method is the possibility for the user to control the order of the method, allowing to resolve strong spatial and angular gradients with a limited number of points. We implemented the method in a code that compute the specific intensity, the temperature structure and the emissivity, allowing to compute images and SED's from ray tracing techniques. We tested its accuracy by comparing our results with the previously mentioned benchmarks. Our results shows a very good agreement, for all the tested cases, and show that the method can be used for further astrophysical applications.

Key words: Radiative transfer - Numerical methods - Circumstellar matter

Résumé

L'étude du problème de transfert de rayonnement est cruciale dans la caractérisation des environnements circumstellaires. Les processus radiatifs jouent un rôle majeur dans la détermination des observables physiques de ces objets astrophysiques, tels que la température, les abondances, les champs de vitesse, etc. La description du champ de rayonnement multidimensionnel et dépendant de la fréquence, est un défi à la fois théorique et numérique, en particulier en présence de la diffusion. L'élaboration de descriptions approximatives et/ou de méthodes numériques est nécessaire afin de décrire efficacement et avec précision le rayonnement. Cette thèse étudie une méthode approximative et une méthode numérique afin de résoudre l'équation de transfert radiatif, couplée à l'équation de l'équilibre radiatif, dans une enveloppe circumstellaire de poussière à symétrie axiale.

Nous avons d'abord considéré l'une de ces descriptions approximatives, l'approximation "Flux Limited Diffusion" (FLD) qui refond l'équation de transfert radiatif en une équation de diffusion non-linéaire, asymptotiquement exacte dans les régimes optiquement minces et épais. Un aspect important concernant la précision de la méthode réside dans la détermination de conditions aux limites appropriées. Nous avons dérivé des conditions aux limites mixtes non-linéaires visant à être suffisamment précises dans tous les régimes optiques. Nous avons implémenté dans un code l'approximation FLD avec nos conditions aux limites et testé leur précision en comparant nos résultats (profils de température et distributions spectrale d'énergie) avec des cas tests de la littérature, pour les enveloppes à symétrie sphérique et axiale. Nos résultats ont montré un très bon accord avec les tests en sphérique, permettant des applications astrophysiques pour des objets compatibles avec cette symétrie. Concernant les enveloppes axis-symétriques, l'accord n'est pas aussi bon et vient des limitations de l'approximation FLD en elle-même. Dans tous les cas, nous montrons que les conditions aux limites que nous avons dérivé décrivent correctement le comportement de la radiation sur les surfaces de l'enveloppe.

Dans un deuxième temps, nous avons étudié la méthode DG-FEM ("Discontinuous Galerkin finite element method"), que nous avons appliqué à l'équation de transfert radiatif en coordonnées sphériques. La méthode utilise les éléments finis et des intégrales de flux le long de leurs interfaces, assurant la conservation locale. Cependant, contrairement aux méthodes classiques par éléments finis, la solution reconstruite est discontinue sur le bord des éléments. Une caractéristique utile de la méthode est la possibilité pour l'utilisateur de contrôler l'ordre de la méthode, permettant de résoudre de forts gradients spatiaux et angulaires avec un nombre limité de points. Nous avons implémenté la méthode dans un code qui calcule l'intensité spécifique, la structure en température et l'émissivité, permettant de calculer des images et des SED à partir de techniques de lancer de rayons ("ray tracing"). Nous avons testé sa précision en comparant nos résultats avec les cas tests mentionnés précédemment. Nos résultats montrent un très bon accord, pour tous les cas testés, et confirment que la méthode peut être utilisée pour des applications astrophysiques ultérieures.

Mots clés : Transfert de rayonnement - Méthodes numériques - Matière circumstellaire

Contents

List of Figures

List of Tables

Chapter 1

Introduction

This chapter is an introduction to the work of this thesis and is mainly dedicated to the description of light and its interaction with matter. Our current understanding of light is that of a propagation of energy through an electromagnetic wave. The description of this phenomenon must be addressed by the Maxwell equations. However, for light propagating inside a macroscopic medium, it is usually too complicated to be done this way. At the macroscopic scale, where the characteristic length of the medium is much larger than the electromagnetic wavelength, we can use the approximation of geometric optics, in which light can be considered as propagating along rays.

In Sect. 1.1, we present an overview of the theory, required for the understanding of the work of this thesis. We also review the main numerical techniques used to solve the radiative transfer problem. For a more detailed and exhaustive presentation of the radiative transfer theory, we recommend the books of Pomraning (1973); Hubeny and Mihalas (2014); Oxenius (1986). In Sect. 1.2, we give a brief presentation of one of the typical circumstellar object where radiative transfer is used for its study. We also discuss the radiative transfer problem specific to circumstellar envelopes. Finally, in Sect. 1.3 we present the work of this thesis.

1.1 The radiative transfer theory

Radiative transfer is a theory which essentially treats light as a distribution of classical point particles travelling along these rays. Disregarding polarisation, the complete state of this system of particles is characterised by a distribution (scalar) that we commonly call the radiation field.

1.1.1 The radiation field

The radiation field is assumed to be described by a distribution of mass-less particles, called photons. Each photon carries an energy, proportional to its frequency ν, via the Planck-Einstein relation $E = h\,\nu$ with h the Planck constant. At a given time, the complete description of the radiation field would require to know the position and the velocity of all particles, which is impossible given the numbers of photons at stake.

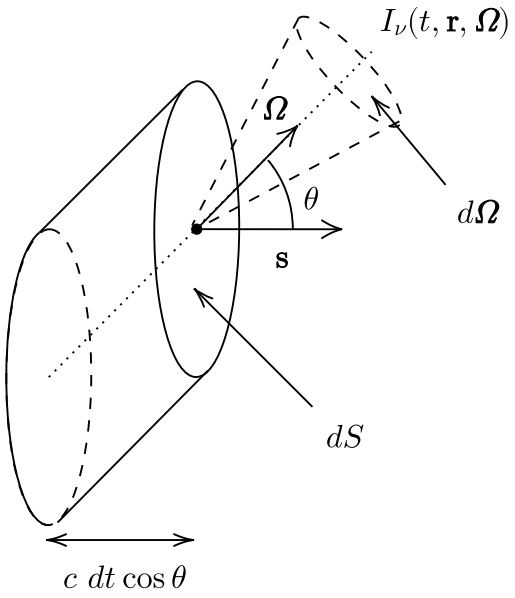

Figure 1.1 – Illustration showing the volume of the cylinder enclosing the photons flowing through an oriented surface $\mathrm{d}\boldsymbol{S}$, in the direction $\boldsymbol{\Omega}$.

Instead, we rather adopt a macroscopic approach and we commonly define the distribution function $f_{\boldsymbol{p}}(t, \boldsymbol{r}, \boldsymbol{p})$ such as, at time t, the number of photons $dN(t)$ in a volume element $\mathrm{d}^3\boldsymbol{r}$ centred around the position $\boldsymbol{r}$, having a momentum inside $\mathrm{d}^3\boldsymbol{p}$ around $\boldsymbol{p}$ is

$$\mathrm{d}N(t) = f_{\boldsymbol{p}}\,(t, \boldsymbol{r}, \boldsymbol{p})\ \ \mathrm{d}^3\boldsymbol{r}\,\mathrm{d}^3\boldsymbol{p}, \tag{1.1}$$

with $\mathrm{d}^3\boldsymbol{r}\,\mathrm{d}^3\boldsymbol{p}$, the six-dimensional volume element in the phase space. Instead of using momentum, it is of common usage to rather use the angle and frequency coordinates. Since $\mathrm{d}^3\boldsymbol{p} = p^2\ \mathrm{d}p\,\mathrm{d}\boldsymbol{\Omega}$, and $\boldsymbol{p} = (h\,\nu/c)\,\boldsymbol{\Omega}$, with c the speed of light, $\mathrm{d}\boldsymbol{\Omega}$ the solid angle element on the unit sphere and $\boldsymbol{\Omega}$ the unit vector pointing in the direction of propagation, we can rewrite $\mathrm{d}N(t)$ as

$$\mathrm{d}N(t) = \frac{h^3\,\nu^2}{c^3} f_{\boldsymbol{p}}\,(t, \boldsymbol{r}, \boldsymbol{p})\ \ \mathrm{d}^3\boldsymbol{r}\,\mathrm{d}\nu\,\mathrm{d}\boldsymbol{\Omega} = f_{\nu,\boldsymbol{\Omega}}\,(t, \boldsymbol{r}, \nu, \boldsymbol{\Omega})\ \ \mathrm{d}^3\boldsymbol{r}\,\mathrm{d}\nu\,\mathrm{d}\boldsymbol{\Omega}, \tag{1.2}$$

with $f_{\nu,\boldsymbol{\Omega}}\,(t, \boldsymbol{r}, \nu, \boldsymbol{\Omega})\ \ \mathrm{d}\boldsymbol{r}\,\mathrm{d}\nu\,\mathrm{d}\boldsymbol{\Omega}$, the number of photons, at time t, in a volume element $\mathrm{d}^3\boldsymbol{r}$ centred around $\boldsymbol{r}$, in the frequency bin $d\nu$ centred around ν and in the solid angle $\mathrm{d}\boldsymbol{\Omega}$ around the direction $\boldsymbol{\Omega}$.

With this distribution, we can compute the energy $\mathrm{d}E$ flowing in a time $\mathrm{d}t$ though any arbitrary oriented surface $\mathrm{d}\boldsymbol{S} = \mathrm{d}S\ \boldsymbol{s}$ (with $\boldsymbol{s}$, a unit vector normal to the surface), in the frequency bin $\mathrm{d}\nu$, in a solid angle $\mathrm{d}\boldsymbol{\Omega}$ around $\boldsymbol{\Omega}$. Fig. 1.1, displays the volume $\mathrm{d}V = c\,\mathrm{d}t\mathrm{d}\boldsymbol{S}.\boldsymbol{\Omega} = c\,\mathrm{d}t\ \cos\theta\,\mathrm{d}S$ enclosing the photons that are crossing the surface $\mathrm{d}S$, in the time interval $\mathrm{d}t$, in a frequency bin $\mathrm{d}\nu$ and in a solid angle $\mathrm{d}\boldsymbol{\Omega}$ around the direction $\boldsymbol{\Omega}$. Multiplying this volume by the energy density of photons $h\,\nu\,f_{\nu,\boldsymbol{\Omega}}\,(t, \boldsymbol{r}, \nu, \boldsymbol{\Omega})$ yields the energy

$$\mathrm{d}E = c\,h\,\nu\,f_{\nu,\boldsymbol{\Omega}}\,(t, \boldsymbol{r}, \nu, \boldsymbol{\Omega})\ \cos\theta\ \mathrm{d}S\,\mathrm{d}t\,\mathrm{d}\nu\,\mathrm{d}\boldsymbol{\Omega}. \tag{1.3}$$

The quantity of primary importance in the radiative transfer theory is the specific intensity $I(t, \boldsymbol{r}, \nu, \boldsymbol{\Omega})$, defined as

$$I(t, \boldsymbol{r}, \nu, \boldsymbol{\Omega}) = c\, h\, \nu\, f_{\nu,\boldsymbol{\Omega}}\,(t, \boldsymbol{r}, \nu, \boldsymbol{\Omega})\,. \tag{1.4}$$

It is a non-negative distribution, expressed in $\mathrm{J.m^{-2}.Hz^{-1}.s^{-1}.sr^{-1}}$ in SI units. In the following, we denote the frequency dependence with the subscript ν and may drop the variable dependencies when needed, for clarity.

There are three important physical quantities related to radiation. They correspond to the first three angular moments of the specific intensity. The zeroth moment of I_ν is the mean specific intensity $J_\nu\,(t, \boldsymbol{r})$, defined as

$$J_\nu\,(t, \boldsymbol{r}) = \frac{1}{4\pi} \int_{4\pi} I_\nu\,(t, \boldsymbol{r}, \boldsymbol{\Omega})\ \mathrm{d}\boldsymbol{\Omega}, \tag{1.5}$$

where the integration is performed across all directions. A related quantity is the monochromatic energy density $E_\nu\,(t, \boldsymbol{r})$ (in $\mathrm{J.m^{-3}.Hz^{-1}}$) defined as,

$$E_\nu\,(t, \boldsymbol{r}) = \int_{4\pi} h\, \nu\, f_{\nu,\boldsymbol{\Omega}}\ \mathrm{d}\boldsymbol{\Omega} = \frac{1}{c} \int_{4\pi} I_\nu\ \mathrm{d}\boldsymbol{\Omega} = \frac{4\pi}{c} J_\nu. \tag{1.6}$$

An important and interesting situation is when the photon gas is in equilibrium with matter at temperature T. In such cases, the specific intensity I_ν is equal to the Planck function $B_\nu(T)$

$$I_\nu\,(t, \boldsymbol{r}, \boldsymbol{\Omega}) = B_\nu(T(t, \boldsymbol{r})) = 2\frac{h\,\nu^3}{c^2} \frac{1}{\exp\left\{\frac{h\,\nu}{k_\mathrm{B}\,T}\right\} - 1}, \tag{1.7}$$

with k_B, the Boltzmann constant. In this case, it can be shown that the total energy density $E(t, \boldsymbol{r})$ is directly proportional to the fourth power of the temperature (see e.g Pomraning, 1973, I-2)

$$E(t, \boldsymbol{r}) = \int_0^\infty E_\nu\ \mathrm{d}\nu = \frac{4\sigma}{c} T^4 \quad \text{or} \quad J(t, \boldsymbol{r}) = \int_0^\infty J_\nu\ \mathrm{d}\nu = \frac{\sigma}{\pi} T^4, \tag{1.8}$$

with σ the Stefan-Boltzmann constant.

Let us consider now, the flux of photons F_N crossing at time t, an arbitrary oriented surface $\mathrm{d}\boldsymbol{S}$, in the frequency interval $\mathrm{d}\nu$,

$$F_N = \int_{4\pi} c\, \boldsymbol{\Omega}.\boldsymbol{s}\ \mathrm{d}S\ f_{\nu,\boldsymbol{\Omega}}\,(t, \boldsymbol{r}, \nu, \boldsymbol{\Omega})\ \mathrm{d}\boldsymbol{\Omega}. \tag{1.9}$$

$c\,\boldsymbol{\Omega}.\boldsymbol{s}$ is the component of the velocity normal to the surface (see Fig. 1.1). Multiplication of Eq. (1.9) by the energy of the photon $h\,\nu$ yields the flux of energy F_E flowing across

$\mathrm{d}S$. Consequently, we define the radiative flux $\boldsymbol{F}_\nu(t,\boldsymbol{r})$ such as $F_E = \boldsymbol{F}_\nu(t,\boldsymbol{r}).\mathrm{d}\boldsymbol{S}$, so we write

$$\boldsymbol{F}_\nu\,(t,\boldsymbol{r}) = \int_{4\pi} \boldsymbol{\Omega}\, I_\nu \,\mathrm{d}\boldsymbol{\Omega}. \tag{1.10}$$

$\boldsymbol{F}_\nu\,(t,\boldsymbol{r})$ is expressed in $\mathrm{J.m^{-2}.s^{-1}.Hz^{-1}}$. Similarly to Eq. (1.5), the Eddington flux $\boldsymbol{H}_\nu(t,\boldsymbol{r})$ can be defined as

$$\boldsymbol{H}_\nu(t,\boldsymbol{r}) = \frac{1}{4\pi}\int_{4\pi} \boldsymbol{\Omega}\, I_\nu \,\mathrm{d}\boldsymbol{\Omega} = \frac{\boldsymbol{F}_\nu}{4\pi}, \tag{1.11}$$

and is the first angular moment of the specific intensity. It satisfies the following flux-limiting property

$$\begin{gathered} |\boldsymbol{H}_\nu| = \frac{1}{4\pi}\left|\int_{4\pi} \boldsymbol{\Omega}\, I_\nu \,\mathrm{d}\boldsymbol{\Omega}\right| \leq \frac{1}{4\pi}\int_{4\pi} |\boldsymbol{\Omega}|\; I_\nu \,\mathrm{d}\boldsymbol{\Omega}, \\ |\boldsymbol{H}_\nu| \leq J_\nu \quad \text{or} \quad |\boldsymbol{F}_\nu| \leq c\, E_\nu. \end{gathered} \tag{1.12}$$

We see that the norm of the radiative flux can never exceed the product of the speed of light with the energy density, as expected.

The third quantity of interest is the pressure tensor. Pressure is defined as the rate of momentum flowing across a surface. For example the rate of photons flowing in the direction $\boldsymbol{\Omega}$ across a surface element $\boldsymbol{s}_i$ normal to the i-direction is $c\,\boldsymbol{\Omega}.\boldsymbol{s}_i\, f_{\nu,\boldsymbol{\Omega}}$ and the j-component of the momentum is $(h\,\nu/c)\,\boldsymbol{\Omega}.\boldsymbol{s}_j$. Multiplying these two quantities and integrating over all directions yields the pressure $\bar{\boldsymbol{P}}^{ij}_\nu\,(t,\boldsymbol{r})$, or the rate of the j-component of the momentum flow per unit area normal to $\boldsymbol{s}_i$,

$$\bar{\boldsymbol{P}}^{i,j}_\nu\,(t,\boldsymbol{r}) = \int_{4\pi} h\,\nu\,\boldsymbol{\Omega}.\boldsymbol{s}_i\,\boldsymbol{\Omega}.\boldsymbol{s}_j\, f_{\nu,\boldsymbol{\Omega}} \,\mathrm{d}\boldsymbol{\Omega} = \frac{1}{c}\int_{4\pi} \Omega_i\,\Omega_j\, I_\nu \,\mathrm{d}\boldsymbol{\Omega}. \tag{1.13}$$

In Eq. (1.13), we denote the components of $\boldsymbol{\Omega}$ along the i,j-directions Ω_i and Ω_j, respectively. If we generalise Eq. (1.13), we can define the pressure tensor $\bar{\boldsymbol{P}}_\nu\,(t,\boldsymbol{r})$ as

$$\bar{\boldsymbol{P}}_\nu\,(t,\boldsymbol{r}) = \frac{1}{c}\int_{4\pi} \boldsymbol{\Omega}\otimes\boldsymbol{\Omega}\, I_\nu \,\mathrm{d}\boldsymbol{\Omega}, \tag{1.14}$$

with $\boldsymbol{\Omega}\otimes\boldsymbol{\Omega}$ the tensorial product of $\boldsymbol{\Omega}$ with itself. $\bar{\boldsymbol{P}}_\nu(t,\boldsymbol{r})$ is a symmetric second-order tensor (matrix) and is expressed in $\mathrm{Pa.Hz^{-1}}$. Analogous to Eqs. (1.5) and (1.11), we define the Eddington pressure tensor $\bar{\boldsymbol{K}}_\nu(t,\boldsymbol{r})$ which is the second angular moment of I_ν,

$$\bar{\boldsymbol{K}}_\nu(t,\boldsymbol{r}) = \frac{1}{4\pi}\int_{4\pi} \boldsymbol{\Omega}\otimes\boldsymbol{\Omega}\, I_\nu \,\mathrm{d}\boldsymbol{\Omega} = \frac{c}{4\pi}\bar{\boldsymbol{P}}_\nu. \tag{1.15}$$

We see that the trace of the Eddington pressure tensor $\bar{\boldsymbol{K}}_\nu$ is equal to the mean specific intensity J_ν,

$$\begin{gathered} tr(\bar{\boldsymbol{K}}_\nu) = \frac{1}{4\pi}\int_{4\pi} |\boldsymbol{\Omega}|^2\, I_\nu \,\mathrm{d}\boldsymbol{\Omega}, \\ Tr(\bar{\boldsymbol{K}}_\nu) = J_\nu \quad \text{or} \quad Tr(\bar{\boldsymbol{P}}_\nu) = c\, E_\nu. \end{gathered} \tag{1.16}$$

1.1.2 The interaction of the radiation field with matter

We saw in the last section that the radiation field is essentially described by a distribution function of photons along a given beam of radiation of direction $\mathbf{\Omega}$. We now want to describe quantitatively how photons are removed or added from this beam. The interactions of photons with matter involves physical processes at microscopic scales, however the radiative transfer theory is a macroscopic description of light and all of these processes can be described by macroscopic coefficients. These coefficients determine how many photons are removed or added from a given beam of photons interacting with matter.

Absorption

Let us consider a photon travelling in an arbitrary direction $\mathbf{\Omega}$ inside matter. We say that an absorption event occurs when the photon is absorbed by matter and disappears from the beam. The absorption coefficient $\kappa_\nu^{\rm abs}(t, \boldsymbol{r})$ is defined such as the probability that the photon is absorbed, in a travelling distance $\mathrm{d}s$, is

$$\text{probability for the photon to be absorbed} = \kappa_\nu^{\rm abs}(t, \boldsymbol{r})\ \mathrm{d}s. \tag{1.17}$$

$\kappa_\nu^{\rm abs}$ has the dimension of m^{-1}. Since it is related to the properties of the material itself, it is a function of space, time and frequency. We note that the absorption coefficient is independent of the direction of propagation $\mathbf{\Omega}$, as matter does not have a preferential direction (in the rest frame of the material).

Scattering

In the same way as for absorption, we can define the scattering coefficient $\kappa_\nu^{\rm sca}(t, \boldsymbol{r})$ such as

$$\text{probability for photon to be scattered} = \kappa_\nu^{\rm sca}(t, \boldsymbol{r})\ \mathrm{d}s. \tag{1.18}$$

However, contrary to absorption, in a scattering event the photon does not disappear but is rather added to a different beam $\mathbf{\Omega'}$ with a different frequency ν'. To describe this, we can introduce the differential scattering coefficient $\kappa_\nu^{\rm sca}(\nu \to \nu', \mathbf{\Omega} \to \mathbf{\Omega'})$ such as the probability for a photon to be scattered, in a travelling distance $\mathrm{d}s$, from (ν, Ω) to (ν', Ω') in a frequency bin $\mathrm{d}\nu'$ and in a solid angle $\mathrm{d}\mathbf{\Omega'}$ is

$$\begin{aligned}\text{probability for the photon } (\nu, \Omega) \text{ to be scattered into } (\nu', \Omega') \\ = \kappa_\nu^{\rm sca}(\nu \to \nu', \mathbf{\Omega} \to \mathbf{\Omega'})\ \mathrm{d}\nu'\, \mathrm{d}\mathbf{\Omega'}\, \mathrm{d}s.\end{aligned} \tag{1.19}$$

Hence, the probability for a photon to be scattered in any frequency and direction, corresponding to Eq. (1.18), is the sum of all the contributions resulting from the differential scattering,

$$\kappa_\nu^{\rm sca}(t, \boldsymbol{r}) = \int_0^\infty \int_{4\pi} \kappa_\nu^{\rm sca}(\nu \to \nu', \mathbf{\Omega} \to \mathbf{\Omega'})\ \mathrm{d}\nu'\, \mathrm{d}\mathbf{\Omega'}. \tag{1.20}$$

In the following, we will consider the particular situation where the differential scattering only depends on the angle between the initial beam $\mathbf{\Omega'}$ and the scattered direction $\mathbf{\Omega'}$ (e.g the case of spherical dust grains), so we can rewrite it as $\kappa_\nu^{\rm sca}(\nu \to \nu', \mathbf{\Omega}.\mathbf{\Omega'})$ with $\mathbf{\Omega}.\mathbf{\Omega'}$,

the cosine of this angle. If there is no frequency change during the event, the scattering is said to be coherent. If the scattering is independent of the scattered angle $\mathbf{\Omega}.\mathbf{\Omega}'$, it is said to be isotropic. Let's finally mention that it is useful in practice to define the differential scattering coefficient as proportional to the scattering coefficient κ_ν^{sca},

$$\kappa_\nu^{\text{sca}}(\nu \to \nu', \mathbf{\Omega}.\mathbf{\Omega}') = \kappa_\nu^{\text{sca}}(t, \boldsymbol{r})\, P\left(\nu \to \nu', \mathbf{\Omega}.\mathbf{\Omega}'\right). \tag{1.21}$$

$P\left(\nu \to \nu', \mathbf{\Omega}.\mathbf{\Omega}'\right)$ is called the phase function and represents the conditional density of probability that a photon is scattered from $(\nu, \mathbf{\Omega})$ to $(\nu', \mathbf{\Omega}')$, knowing that a scattering event occurred. From Eq. (1.20), the phase function is normalised as

$$\int_0^\infty \int_{4\pi} P(\nu \to \nu', \mathbf{\Omega}.\mathbf{\Omega}')\, \mathrm{d}\nu'\, \mathrm{d}\mathbf{\Omega}' = 1 \tag{1.22}$$

For coherent scattering the phase function can be expressed $P(\nu \to \nu', \mathbf{\Omega}.\mathbf{\Omega}') = P(\mathbf{\Omega}.\mathbf{\Omega}')\, \delta(\nu, \nu')$. Additionally, if the scattering is also isotropic, we have $P(\nu \to \nu', \mathbf{\Omega} \to \mathbf{\Omega}') = \frac{1}{4\pi}\delta(\nu, \nu')$.

Emission

We can quantitatively describe the emission of matter with the help of a source term $Q_\nu(t, \boldsymbol{r})$. As for absorption, because it depends on general properties of the material itself, it is a general function of space, time and frequency but not angle. It is defined such as the energy density created by matter, in a $\mathrm{d}t$ time, in a solid angle $\mathrm{d}\mathbf{\Omega}$ and a frequency bin $\mathrm{d}\nu$ is

$$\text{energy density emitted} = Q_\nu(t, \boldsymbol{r})\, \mathrm{d}\mathbf{\Omega}\, \mathrm{d}\nu\, \mathrm{d}t. \tag{1.23}$$

1.1.3 The radiative transfer equation

Derivation

The radiative transfer equation is merely an equation for the conservation of photons $f_{\nu,\mathbf{\Omega}}$ (equivalent I_ν) along a given ray $\mathbf{\Omega}$. This conservation law can be derived by computing the energy balance, in a time $\mathrm{d}t$, in a frequency interval $\mathrm{d}\nu$ and a solid angle $\mathrm{d}\mathbf{\Omega}$ around $\mathbf{\Omega}$, flowing inside a volume element $\mathrm{d}\mathcal{V}$ containing matter (see Fig. 1.2). Let this volume element be of length $\mathrm{d}s = |d\boldsymbol{r}|$ and cross-section $\mathrm{d}S$ normal to $\mathbf{\Omega}$. Using Eq. (1.3), the energy entering the volume $\mathrm{d}\mathcal{V}$ is,

$$\text{energy entering } \mathrm{d}\mathcal{V} = I_\nu(t, \boldsymbol{r}, \mathbf{\Omega})\, \mathrm{d}S\, \mathrm{d}\mathbf{\Omega}\, \mathrm{d}\nu\, \mathrm{d}t, \tag{1.24}$$

while the energy that emerges from the volume at a later time $t + \mathrm{d}t$ is

$$\text{energy emerging from } \mathrm{d}\mathcal{V} = I_\nu(t + \mathrm{d}t, \boldsymbol{r} + \mathrm{d}\boldsymbol{r}, \mathbf{\Omega})\, \mathrm{d}S\, \mathrm{d}\mathbf{\Omega}\, \mathrm{d}\nu\, \mathrm{d}t. \tag{1.25}$$

From our discussions in Sect. 1.1.2, the energy that is lost along the beam due to the material inside $\mathrm{d}\mathcal{V}$ comes from absorption and scattering processes,

$$\begin{aligned} &\text{energy lost from interactions with } \mathrm{d}\mathcal{V} \\ &= (\text{energy entering } \mathrm{d}\mathcal{V}) \times \left(\kappa_\nu^{\text{abs}} + \kappa_\nu^{\text{sca}}\right) \mathrm{d}s \\ &= \kappa_\nu^{\text{ext}}(t, \boldsymbol{r})\, I_\nu(t, \boldsymbol{r}, \mathbf{\Omega})\, \mathrm{d}s\, \mathrm{d}S\, \mathrm{d}\mathbf{\Omega}\, \mathrm{d}\nu\, \mathrm{d}t. \end{aligned} \tag{1.26}$$

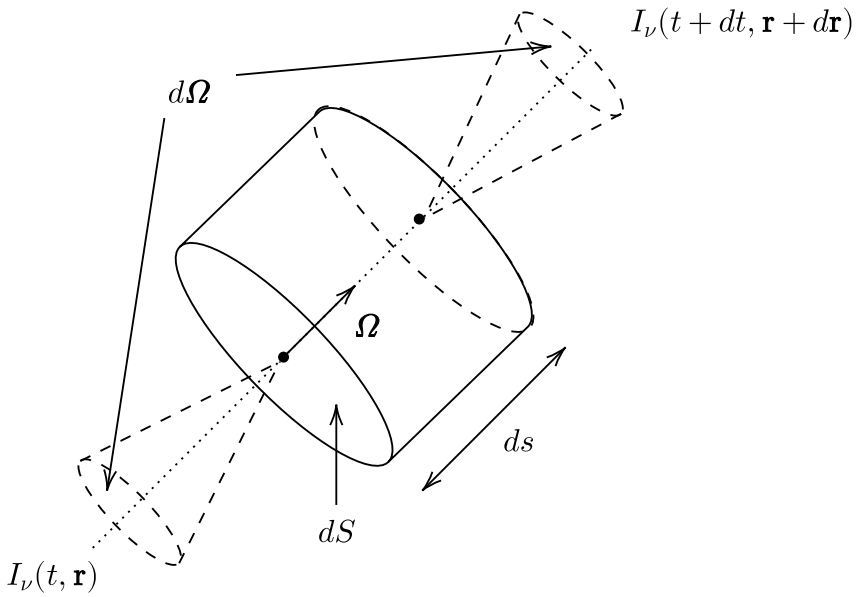

Figure 1.2 – Radiation flowing in a direction $\boldsymbol{\Omega}$, in a solid angle $\mathrm{d}\boldsymbol{\Omega}$, across a volume element $\mathrm{d}\mathcal{V}$ filled with matter.

In Eq. (1.26), we introduced the extinction coefficient $\kappa_\nu^{\mathrm{ext}}(t, \boldsymbol{r}) = \kappa_\nu^{\mathrm{abs}} + \kappa_\nu^{\mathrm{sca}}$, such that $\kappa_\nu^{\mathrm{ext}}\ \mathrm{d}s$ represents the probability for the photon to be removed from the beam in a travelling distance $\mathrm{d}s$, either from absorption or scattering. Finally, the energy created or injected inside the beam by the material inside $\mathrm{d}\mathcal{V}$, also comes from two contributions; the emission and the scattering from all the other beams of radiation,

$$\begin{aligned} &\text{energy injected from interactions with } \mathrm{d}\mathcal{V} \\ &= \left(Q_\nu(t, \boldsymbol{r}) + \kappa_\nu^{\mathrm{sca}}(t, \boldsymbol{r}) \int_0^\infty \int_{4\pi} P(\nu' \to \nu, \boldsymbol{\Omega}'.\boldsymbol{\Omega})\, I_{\nu'}(t, \boldsymbol{r}, \boldsymbol{\Omega}')\ \mathrm{d}\nu'\, \mathrm{d}\boldsymbol{\Omega}' \right) \\ &\qquad\qquad \mathrm{d}s\, \mathrm{d}S\, \mathrm{d}\boldsymbol{\Omega}\, \mathrm{d}\nu\, \mathrm{d}t. \end{aligned} \tag{1.27}$$

Now, using conservation of energy, we can relate the emerging and entering energy into $\mathrm{d}\mathcal{V}$ according to the following balance

$$\begin{aligned} &\text{energy emerging from } \mathrm{d}\mathcal{V} - \text{energy entering } \mathrm{d}\mathcal{V} \\ &= \text{energy injected from interactions with } \mathrm{d}\mathcal{V} \\ &\quad - \text{energy lost from interactions with } \mathrm{d}\mathcal{V} \end{aligned} \tag{1.28}$$

or equivalently,

$$I_\nu(t + \mathrm{d}t, \boldsymbol{r} + \mathrm{d}\boldsymbol{r}, \boldsymbol{\Omega}) - I_\nu(t, \boldsymbol{r}, \boldsymbol{\Omega}) = \left(\eta_\nu(t, \boldsymbol{r}, \boldsymbol{\Omega}) - \kappa_\nu^{\mathrm{ext}}\, I_\nu(t, \boldsymbol{r}, \boldsymbol{\Omega})\right)\ \mathrm{d}s. \tag{1.29}$$

We defined the emissivity η_ν as the sum of the emission and the scattering terms. If we neglect the second order terms in $\mathrm{d}s$, the emerging specific intensity can be rewritten,

using $\mathrm{d}t = \mathrm{d}s/c$,

$$I_\nu(t + \mathrm{d}t, \boldsymbol{r} + \mathrm{d}\boldsymbol{r}, \boldsymbol{\Omega}) \approx I_\nu(t, \boldsymbol{r}, \boldsymbol{\Omega}) + \left(\frac{1}{c}\partial_t I_\nu(t, \boldsymbol{r}, \boldsymbol{\Omega}) + \partial_s I_\nu(t, \boldsymbol{r}, \boldsymbol{\Omega})\right) \mathrm{d}s, \tag{1.30}$$

where ∂_s denotes the spatial derivative along s, the path ray coordinate in the direction $\boldsymbol{\Omega}$. We obtain the following partial integro-differential equation for the specific intensity I_ν

$$\frac{1}{c}\partial_t I_\nu + \partial_s I_\nu + \kappa_\nu^{\mathrm{ext}} I_\nu = \eta_\nu, \tag{1.31}$$

with,

$$\eta_\nu(t, \boldsymbol{r}, \boldsymbol{\Omega}) = Q_\nu(t, \boldsymbol{r}) + \kappa_\nu^{\mathrm{sca}}(t, \boldsymbol{r}) \int_0^\infty \int_{4\pi} P(\nu' \to \nu, \boldsymbol{\Omega}'.\boldsymbol{\Omega})\, I_{\nu'}(t, \boldsymbol{r}, \boldsymbol{\Omega}')\, \mathrm{d}\nu'\, \mathrm{d}\boldsymbol{\Omega}. \tag{1.32}$$

The derivative along the ray can be rewritten with the operator $\boldsymbol{\Omega}.\boldsymbol{\nabla}$, independent of the coordinate system

$$\frac{1}{c}\partial_t I_\nu + \boldsymbol{\Omega}.\boldsymbol{\nabla} I_\nu + \kappa_\nu^{\mathrm{ext}} I_\nu = \eta_\nu. \tag{1.33}$$

We derived the radiative transfer equation for one given ray $(\nu, \boldsymbol{\Omega})$ and we may be tempted to think that solving independently Eq. (1.33) for all rays would lead to the solution of the complete radiation field. Unfortunately this is not true, because of the scattering term in η_ν. As it can been seen from Eq. (1.32), one given ray $(\nu, \boldsymbol{\Omega})$ is coupled to all the other rays $(\nu', \boldsymbol{\Omega}')$ in general which shows that all rays must eventually be solved together. Physically it means that inside a medium, the radiation field at one point is dependent of the state of the radiation field at all the other points. The non-local property of the radiation is a serious problem in solving Eq. (1.33) and very few analytic solutions exist, especially in the multi-dimensional case (see e.g Frisch, 2022, for an extensive review of exact methods).

Boundary conditions

The radiative transfer equation Eq. (1.31) or Eq. (1.33) is a first-order differential equation for both time and space. Consequently, it must be supplemented with an initial and a boundary condition. For the initial condition, it is straightforward because we simply have to specify the radiation field at the origin of the time coordinate t_0

$$I_\nu(t_0, \boldsymbol{r}, \boldsymbol{\Omega}) = \xi_\nu(\boldsymbol{r}, \boldsymbol{\Omega}), \tag{1.34}$$

with $\xi_\nu(\boldsymbol{r}, \boldsymbol{\Omega})$, a given function specifying the initial state of the radiation field. For the spatial boundary condition, we must specify, at each surface point $\boldsymbol{r}_s$ and along each incident ray ($\boldsymbol{\Omega}.\boldsymbol{s} \leq 0$ with $\boldsymbol{s}$ an outward normal vector), the incident specific intensity entering the computational domain

$$I_\nu(t, \boldsymbol{r}_s, \boldsymbol{\Omega}) = \Gamma_\nu(t, \boldsymbol{r}_s, \boldsymbol{\Omega}), \quad \boldsymbol{\Omega}.\boldsymbol{s} < 0 \tag{1.35}$$

with $\Gamma_\nu(t, \boldsymbol{r}_s, \boldsymbol{\Omega})$, a given function specifying the incident intensity upon the domain.

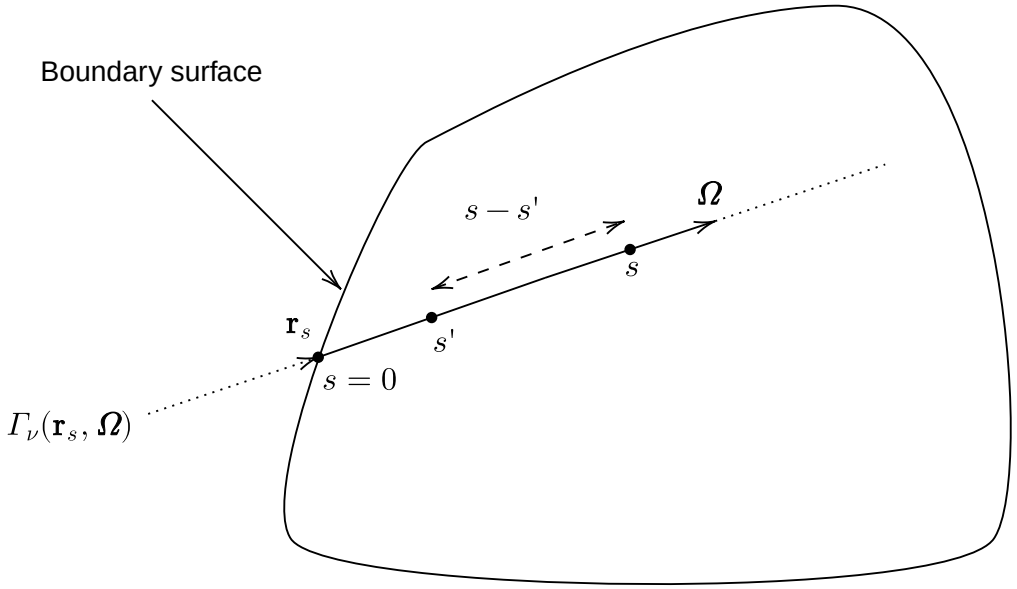

Figure 1.3 – Geometry of a ray entering a volume of material at the boundary point $\boldsymbol{r}_s$.

Integral form

The integro-differential radiative transfer Eq. (1.33) can be rewritten under the form of an integral. This integral form gives a graphical physical understanding of the radiative transfer equation and is the starting step for some numerical methods. Assume for a moment that the emissivity η_ν is known (or that it does not depend on I_ν itself), then the equation becomes a simple linear advection equation that can be solved with the method of characteristics (see *e.g* Olver, 2016). If we further consider the time-independent case, it becomes a simple first-order linear differential equation that can be easily solved,

$$\partial_s I_\nu + \kappa_\nu^{\text{ext}} I_\nu = \eta_\nu. \tag{1.36}$$

The general solution of Eq. (1.36) is

$$I_\nu(s) = a_\nu \exp\{-\tau_\nu(s)\} + \int_0^s \eta_\nu(s') \exp\{-(\tau_\nu(s) - \tau_\nu(s'))\}\, \mathrm{d}s', \tag{1.37}$$

with a_ν a constant given by the boundary conditions. $\tau_\nu(s) = \int_0^s \kappa_\nu^{\text{ext}}(s")\, \mathrm{d}s"$ is called the optical depth and is the integrated extinction coefficient along the ray. For a given ray entering the medium, we can arbitrarily choose to put the origin of the s coordinate at the intersection of the ray with the boundary surface $\boldsymbol{r}_s$ of the domain (see Fig. 1.3).

Then, the boundary condition gives $I_\nu(0) = \Gamma_\nu(\boldsymbol{r}_s, \boldsymbol{\Omega}) = a_\nu$ and Eq. (1.37) is rewritten

$$I_\nu(s) = \Gamma_\nu(\boldsymbol{r}_s, \boldsymbol{\Omega}) \exp\{-\tau_\nu(s)\} + \int_0^s \eta_\nu(s') \exp\{-\tau_\nu(s', s)\}\, \mathrm{d}s', \quad \text{with} \quad \tau_\nu(s', s) = \int_{s'}^s \kappa_\nu^{\mathrm{ext}}(s")\, \mathrm{d}s". \tag{1.38}$$

$\tau_\nu(s', s)$ is the optical depth integrated between the point s' and s. Eq. (1.38) is called the formal solution of the radiative transfer Eq. (1.33). It can be numerically or exactly integrated, as long as the source function is already known or does not depend on I_ν (see *e.g* Chevallier and Rutily, 2005, for an analytic case). Under this form, we can see that the specific intensity at a distance s from the boundary point $\boldsymbol{r}_s$, in the direction $\boldsymbol{\Omega}$, is made of two contributions. The first term represents the specific intensity entering the domain, attenuated by the exponential of the optical depth. The second term is the contribution from the envelope itself. It is made of the sum (integral) of the emission of all the points s' on the ray between 0 and s, attenuated by the material between s' and s.

When the media is dense/opaque and/or the distance s becomes large, the optical depth $\tau_\nu(s)$ becomes important and consequently $\exp\{-\tau_\nu(s)\} \to 0$. Hence the boundary term becomes negligible. Additionally, as the medium gets more and more dense or opaque, the terms that contribute the most in the emission are situated closer and closer from the point s. In the limit $\tau_\nu(s', s) \gg 1$, called the optically-thick regime, the radiative transfer equation becomes local and has a diffusion behaviour. In the limit $\tau_\nu(s', s) \ll 1$, called the optically-thin regime, the emission term becomes negligible and the radiation field is essentially specified by the transmitted incident radiation $\Gamma_\nu(\boldsymbol{r}_s, \boldsymbol{\Omega})$. In this limit, the radiative equation becomes a purely transport problem.

1.1.4 Approximate description of the radiative transfer problem: the moment closure problem

The specific intensity $I_\nu(t, \boldsymbol{r}, \boldsymbol{\Omega})$ is a distribution of seven variables (one for time, three for space, two for directions and one for frequency). The discretisation of this seven-dimensional space, required to solve numerically the radiative transfer equation, makes the number of computed and stored values required to be huge. As an example, let us consider the time-independent, frequency-dependent, three-dimensional specific intensity and assume we want to use 100 points per variable, which is a reasonable number. The specific intensity will be described by $(100)^6 = 10^{12}$ variables ($\sim$ 7.5 Tb on the computer RAM in double precision). To make things worse, the radiation fields exhibits most of the time strong spatial and angular gradients, and the number of points must be increased accordingly to better sample these variations.

Solving the radiative transfer equation is both a theoretical and numerical challenge, especially in the frequency-dependent and multi-dimensional case (see *e.g* Rutily and Chevallier, 2006). One approach to tackle this problem involves approximate methods. In the following, we present the angular moments of the radiative transfer equation,

associated with the physical quantities presented in Sect. 1.1.1. We show how they can be useful in obtaining an approximate description for the radiative transfer problem.

The zero-order moment equation can be found by integration of Eq. (1.33) over all directions and division by 4π,

$$\frac{1}{c}\partial_t J_\nu + \boldsymbol{\nabla}.\boldsymbol{H}_\nu + \kappa_\nu^{\text{ext}}\, J_\nu = \frac{1}{4\pi}\int_{4\pi} \eta_\nu \, \mathrm{d}\boldsymbol{\Omega}. \tag{1.39}$$

We note that the integration over all frequencies of Eq. (1.39) yields the equation

$$\frac{1}{c}\partial_t J + \boldsymbol{\nabla}.\boldsymbol{H} = \int_0^\infty \left(\frac{1}{4\pi}\int_{4\pi} \eta_\nu \, \mathrm{d}\boldsymbol{\Omega} - \kappa_\nu^{\text{ext}}\, J_\nu \right) \mathrm{d}\nu, \tag{1.40}$$

which is an equation for the conservation of the radiative energy flowing across any arbitrary volume. In a stationary regime, the matter reaches an equilibrium state and the left-hand side of Eq. (1.40) is zero. The radiation field satisfies the radiative equilibrium equation

$$\int_0^\infty \left(\frac{1}{4\pi}\int_{4\pi} \eta_\nu \, \mathrm{d}\boldsymbol{\Omega} - \kappa_\nu^{\text{ext}}\, J_\nu \right) \mathrm{d}\nu = 0. \tag{1.41}$$

This equation couples the emissivity η_ν with the mean radiation field J_ν. Eventually it must be solved simultaneously with the radiative transfer Eq. (1.33).

In the same way, if we multiply Eq. (1.33) by $\boldsymbol{\Omega}$ and perform integration, we obtain the first-order moment equation for the radiation field

$$\frac{1}{c}\partial_t \boldsymbol{H}_\nu + \boldsymbol{\nabla}.\bar{\boldsymbol{K}}_\nu + \kappa_\nu^{\text{ext}} \boldsymbol{H}_\nu = \frac{1}{4\pi}\int_{4\pi} \boldsymbol{\Omega}\, \eta_\nu \, \mathrm{d}\boldsymbol{\Omega}. \tag{1.42}$$

Similarly to Eq. (1.40), it is an equation for the conservation of radiative momentum flowing across an arbitrary volume.

Equations for higher moments can be found similarly, by successive integration. As we can see, we have an infinite set of equations coupling the successive moments of the radiation field. Each equation for the n^{th} moment of the intensity involves the divergence of the $(n+1)^{\text{th}}$ moment. The truncation of this infinite set of equations is known as the moment closure problem.

One common approach is to close the system with the help of the Eddington tensor $\bar{\boldsymbol{T}}_\nu$ (Eddington, 1920), defined as $\bar{\boldsymbol{K}}_\nu = \bar{\boldsymbol{T}}_\nu\, J_\nu$ and known when solving the moment equations. $\bar{\boldsymbol{T}}_\nu$ can be either estimated by calculations or approximated by an analytical formula, based on the geometry of the problem. The Eddington tensor $\bar{\boldsymbol{T}}_\nu$ is known in the two limiting cases; if the radiation field is perfectly isotropic, we have $\bar{\boldsymbol{T}}_\nu = \mathbb{I}/3$, with $\mathbb{I}$ the identity matrix and $\boldsymbol{H}_\nu = \boldsymbol{0}$. On the other hand, if the radiation field is sharped-peak in a given direction (e.g in the z direction), then $\boldsymbol{H}_\nu = J_\nu\, \hat{z}$ and the only non-zero component of the Eddington tensor is $\bar{\boldsymbol{T}}_\nu^{zz} = 1$.

As an example, we consider the classical Eddington approximation (Eddington, 1920) which corresponds to the closure relation $\bar{\boldsymbol{T}}_\nu = \mathbb{I}/3$. A Fick-law for the radiative flux can be obtained, $\boldsymbol{H}_\nu = -\boldsymbol{\nabla} J_\nu/(3\,\kappa_\nu^{\rm ext})$, if we neglect $\partial_t \boldsymbol{H}_\nu$ term in Eq. (1.42) to obtain a diffusion behaviour and assume an isotropic emissivity η_ν. The radiative transfer problem is then described by a linear diffusion equation for J_ν

$$\frac{1}{c}\partial_t J_\nu - \boldsymbol{\nabla}.\left(\frac{1}{3\,\kappa_\nu^{\rm ext}}\,\boldsymbol{\nabla}\,J_\nu\right) = \eta_\nu - \kappa_\nu^{\rm ext}\,J_\nu. \tag{1.43}$$

The numerical advantage in solving Eq. (1.43) instead of Eq. (1.33) is clear, because J_ν does not have the angular dependence of the specific intensity, hence the dimension of the problem is reduced. Let us notice that, in using Eq. (1.43) to compute J_ν, we also introduce an error, which becomes greater as $\bar{\boldsymbol{K}}_\nu$ deviates from $\mathbb{I}\,J_\nu/3$ (or I_ν deviates from being isotropic). Let us also mention that the Eddington approximation does not always satisfy the flux-limiting condition Eq. (1.12) and can then lead to non-physical solutions.

1.1.5 Numerical methods for solving the radiative transfer problem

We saw in Sect. 1.1.3 that the non-local property of the radiation field results in a limited number of analytic solutions. We then have to turn to numerical solutions of the radiation transfer equation. Numerous numerical methods have been developed in order to solve the radiative transfer equation. The main difficulty in solving the radiative equation arises from the presence of scattering. To have some insights on the numerical difficulties in solving the problem, let us assume an emissivity function of the form given by the previous section,

$$\eta_\nu = \kappa_\nu^{\rm abs}\,B_\nu(T) + \kappa_\nu^{\rm sca}\,J_\nu. \tag{1.44}$$

The operation of computing the specific intensity I_ν can be rewritten with the operator formalism (Rybicki and Hummer, 1992),

$$I_\nu = \Psi_{\nu,\boldsymbol{\Omega}}[\eta_\nu] \tag{1.45}$$

We note that in practice, the $\Psi_{\nu,\boldsymbol{\Omega}}$ operator does not have to be explicitly given. This operator symbolises the use of a given numerical method to obtain the specific intensity from the known emissivity (*i.e* performing a formal solution). Integration over all directions yields the mean specific intensity J_ν, that can also be described with an operator,

$$J_\nu = \int_{4\pi} \Psi_{\nu,\boldsymbol{\Omega}}[\eta_\nu]\;{\rm d}\boldsymbol{\Omega} = \Psi_\nu[\eta_\nu]. \tag{1.46}$$

Then, using Eq. (1.44), the emissivity satisfies

$$(1 - \kappa_\nu^{\rm sca}\,\Psi_\nu)\,[\eta_\nu] = \kappa_\nu^{\rm abs}\,B_\nu(T). \tag{1.47}$$

$(1 - \kappa_\nu^{\rm sca}\,\Psi_\nu)$ is the operator coupling the emissivity η_ν at all points in space. Solving the linear system Eq. (1.47) is equivalent to solve the radiative transfer equation Eq. (1.33), for all rays at the same time.

One first approach to solve Eq. (1.47) is to directly invert the operator $(1 - \kappa_\nu^{\rm sca}\,\Psi_\nu)$. In most cases, especially in multi-dimensional problems, this is numerically prohibitive since the matrix associated with the operator can be huge. Another approach is to rather use an iterative method. The simplest iterative scheme that we can think of is, denoting by the superscript n the iteration index,

$$\eta_\nu^{n+1} = \kappa_\nu^{\rm abs}\,B_\nu(T) + \kappa_\nu^{\rm sca}\,\Psi_\nu[\eta_\nu^n]. \tag{1.48}$$

This iterative method is commonly called the Λ-iteration in the literature (in reference to the Λ operator that rather acts on the source function $S_\nu = \eta_\nu/\kappa_\nu^{\rm ext}$) . While being easy to implement, it was shown to present pathological convergence behaviour in optically-thick regions. Cannon (1973) was the first to notice that the convergence could be improved if we were to invert only a part of the full operator $(1 - \kappa_\nu^{\rm sca}\,\Psi_\nu)$. If we decompose the Ψ_ν operator as $\Psi_\nu = \Psi_\nu^\star + (\Psi_\nu - \Psi_\nu^\star)$, with $\Psi_\nu^\star$ the part that can be inverted, then inserting this in the previous iterative scheme yields,

$$(1 - \kappa_\nu^{\rm sca}\,\Psi_\nu^\star)\,[\eta_\nu^{n+1}] = \kappa_\nu^{\rm abs}\,B_\nu(T) + (\Psi_\nu - \Psi_\nu^\star)\,[\eta_\nu^n]. \tag{1.49}$$

This scheme is called the accelerated Λ-iteration (ALI). In order for ALI to be efficient, $\Psi_\nu^\star$ should be easy to invert and store in the computer memory. We will not go into further details on how to derive $\Psi_\nu^\star$ (or $\Lambda_\nu^\star$) and refer to Hubeny and Mihalas (2014) for an extended discussion of the different techniques in order to obtain it. The determination of the approximate operator depends on the type of numerical method used, the dimensionality and the geometry of the problem. In its simplest form, $\Psi_\nu^\star$ (or $\Lambda_\nu^\star$) can be taken to be the exact or the approximate diagonal of the full operator Ψ_ν (or Λ_ν) (Olson et al., 1986; Olson and Kunasz, 1987). In this case, the terms $\Psi_\nu^\star[\eta_\nu]$ in Eq. (1.49) reduce to a simple scalar multiplication.

In the following, we present a non-exhaustive overview of the most common numerical methods that have been used to solve the formal solution Eq. (1.45), in the context of circumstellar envelopes. We restrict our presentation to the time-independent problem. A more detailed presentation of the different methods with some existing codes is available in Steinacker et al. (2013).

Finite difference

One simple and direct approach is to discretise the radiative transfer Eq. (1.33) and approximate the partial derivatives with a finite-difference operator.

The major flaw of using finite difference in radiative transfer is that, since the radiation field exhibit strong spatial and angular gradients, it introduces oscillations and negative values for I_ν that can propagate across the whole domain, for second-order or higher approximations. In the context of circumstellar envelopes, the radiation field is discontinuous in directions because the angular distribution of the incident radiation, in the boundary conditions, is discontinuous (see *e.g* Eq. 1.70).

This angular instability can be fixed with the use of a fixed Cartesian coordinate system from which the angular coordinates are defined. Then, the directional derivative operator

$\boldsymbol{\Omega}.\boldsymbol{\nabla}$ in Eq. (1.33) only contains spatial derivatives and the radiative transfer equation is rewritten

$$\sin\theta\cos\varphi\,\partial_x I_\nu + \sin\theta\sin\varphi\,\partial_y I_\nu + \cos\theta\,\partial_z\ I_\nu + \kappa_\nu^{\text{ext}}\, I_\nu = \eta_\nu, \tag{1.50}$$

where, (θ, φ) are the usual spherical angular coordinates with respect to the Cartesian coordinate system $(\hat{x}, \hat{y}, \hat{z})$. The major disadvantage of using a fixed coordinate system for the angular coordinates, is that the direction of the sources is changing with the position (contrary to the spherical coordinate system, for instance, where the star always points around $\hat{r}$), so it makes any angular grid refinement procedure to resolve these sources, hard to implement.

As a representative example of this method, we mention the work of Steinacker et al. (2003). The authors solve the Cartesian radiative transfer Eq. (1.50), on a direction grid (θ, φ) that is equally spaced on the unit sphere and with second-order finite-difference operators for the spatial derivatives. Since the grid size is essential for the efficiency of the method, the authors use an adaptive optimised multi-wavelength spatial grid (Steinacker et al., 2002).

Long/Short characteristics

This class of methods is based on the integral form of the radiative transfer equation Eq. (1.38). As for finite-difference, the spatial domain is discretised into a computational grid where we want to evaluate the specific intensity, at each grid point and for a set of directions. Following Eq. (1.38), the intensity at the point P, in the direction $\boldsymbol{\Omega}$ (see Fig. 1.4) is written

$$I_\nu(\boldsymbol{r}_P, \boldsymbol{\Omega}) = I_\nu(\boldsymbol{r}_U, \boldsymbol{\Omega})\, \exp\left\{-\tau_\nu(\boldsymbol{r}_U, \boldsymbol{r}_P)\right\} + \int_{\boldsymbol{r}_U}^{\boldsymbol{r}_P} \eta_\nu(s')\, \exp\left\{-\tau_\nu(s', \boldsymbol{r}_P)\right\}\, \mathrm{d}s'. \tag{1.51}$$

The point U lies on the boundary of the domain, and the value of the specific intensity at this point is given by the boundary condition $I_\nu(\boldsymbol{r}_U, \boldsymbol{\Omega}) = \Gamma_\nu(\boldsymbol{r}_U, \boldsymbol{\Omega})$. The ray from U to P is intersecting several cells of the grid (grey cells in Fig. 1.4) and the specific intensity can be computed recursively, starting from the boundary U,

$$I_\nu(s_{k+1}) = I_\nu(s_k)\, \exp\left\{-\tau_\nu(s_k, s_{k+1})\right\} + \int_{s_k}^{s_{k+1}} \eta_\nu(s')\, \exp\left\{-\tau_\nu(s', s_{k+1})\right\}\, \mathrm{d}s'. \tag{1.52}$$

The s_k denote the first intersection with the cell edge encountered by the ray (black squares on Fig. 1.4, with $I_\nu(\boldsymbol{r}_U, \boldsymbol{\Omega}) = I(s_0)$). In practice, we evaluate all the quantities at the grid points and the functions η_ν and κ_ν^{ext} inside the cell k can be reconstructed from the grid adjacent points. The way of computing the intensity at the point P, from the integration from the boundary U is called the long characteristic (LC) method. While being quite accurate, it is numerically expensive because some computations are redundant, for example, for rays crossing two adjacent grid-points.

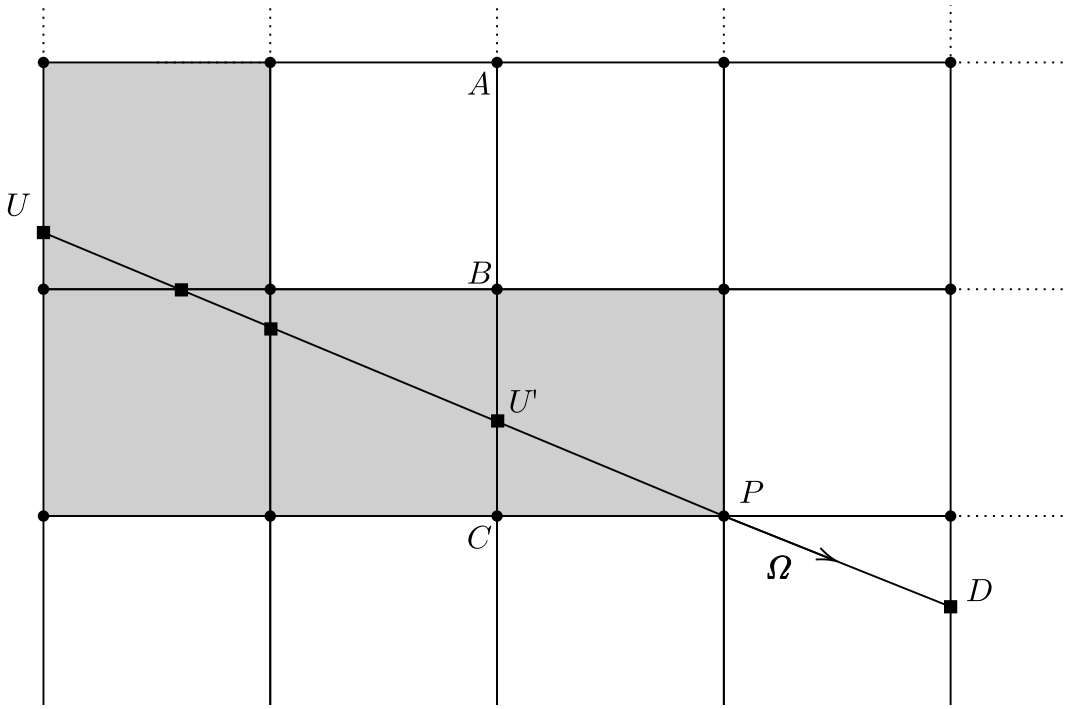

Figure 1.4 – Illustration showing the basic concept of long/short characteristics, in two-dimensional Cartesian coordinates. The intensity at point P is computed by integration of the transfer equation along the entire ray from the upstream boundary U (long characteristic, see Eq. 1.51). The short characteristic is the line connecting point U' to P. The value of the intensity at U' is determined by second-order interpolation between the points A, B and C.

In order to prevent for this redundancy, Kunasz and Auer (1988) proposed to rather perform the integration only on a small portion of the ray, from U' to P (called the short characteristic in contrast to the long one where the integral is performed from U),

$$I_\nu(\boldsymbol{r}_P, \boldsymbol{\Omega}) = I_\nu(\boldsymbol{r}_{U'}, \boldsymbol{\Omega}) \exp\{-\tau_\nu(\boldsymbol{r}_{U'}, \boldsymbol{r}_P)\} + \int_{\boldsymbol{r}_{U'}}^{\boldsymbol{r}_P} \eta_\nu(s') \exp\{-\tau_\nu(s', \boldsymbol{r}_P)\} \, \mathrm{d}s'. \quad (1.53)$$

The upstream intensity can be found by interpolation, *e.g* in Fig. 1.4 with the second-order interpolation,

$$I_\nu(\boldsymbol{r}_{U'}, \boldsymbol{\Omega}) = a \, I_\nu(\boldsymbol{r}_A, \boldsymbol{\Omega}) + b \, I_\nu(\boldsymbol{r}_B, \boldsymbol{\Omega}) + c \, I_\nu(\boldsymbol{r}_C, \boldsymbol{\Omega}), \quad (1.54)$$

with a, b, c, the usual Lagrange weights. An essential ingredient for the short characteristics method to work is that the ray calculations should be performed in the right order so that the upstream intensities $I_\nu(\boldsymbol{r}_A, \boldsymbol{\Omega})$, $I_\nu(\boldsymbol{r}_B, \boldsymbol{\Omega})$, $I_\nu(\boldsymbol{r}_C, \boldsymbol{\Omega})$ are known before the integral is performed. In order to do so, the grid must be swept from the two upstream boundaries (top,left in Fig. 1.4) towards the two downstream boundaries (bottom, right in Fig. 1.4). The integral from U' to P can be computed with a second-order accuracy by interpolating the emissivity η_ν between the points D, P and U'.

The short characteristics method is computationally less expensive than the long characteristics one, however it is also less accurate because of the interpolation errors introduced when computing the upstream intensity $I_\nu(\boldsymbol{r}_{U'}, \boldsymbol{\Omega})$ in Eq. (1.54). Another flaw of the short characteristics method is that the source function and/or opacities in Eq. (1.53) can present pathological values (*e.g* negative) because of the interpolation method used. A further method is needed to identify and correct for these values (see *e.g* Auer and Paletou, 1994).

Finally, we mention that the long or short characteristics method is not restricted to any particular geometry. The spatial and angular grids can be refined, for example according to the density gradient for the spatial grid and in the direction of the sources for the angular ones.

For an application of this method to the two–dimensional radiative transfer, in the context of axis-symmetric circumstellar envelopes, we refer to Dullemond and Turolla (2000).

Monte Carlo methods

Monte Carlo techniques are among the most popular methods for dealing with the radiation field, in the context of circumstellar envelopes. They are based on the probabilistic description of the interactions between light and matter. Their popularity arises from the fact that they are easier to implement than the other methods, are intrinsically three-dimensional and can simply be adapted to any geometry.

In Monte-Carlo methods, the total luminosity of the external sources (central star in our case) is divided into N packets of photons for which we follow their journey across the circumstellar medium (see Fig. 1.5). A Monte-Carlo cycle is mainly divided into three steps:

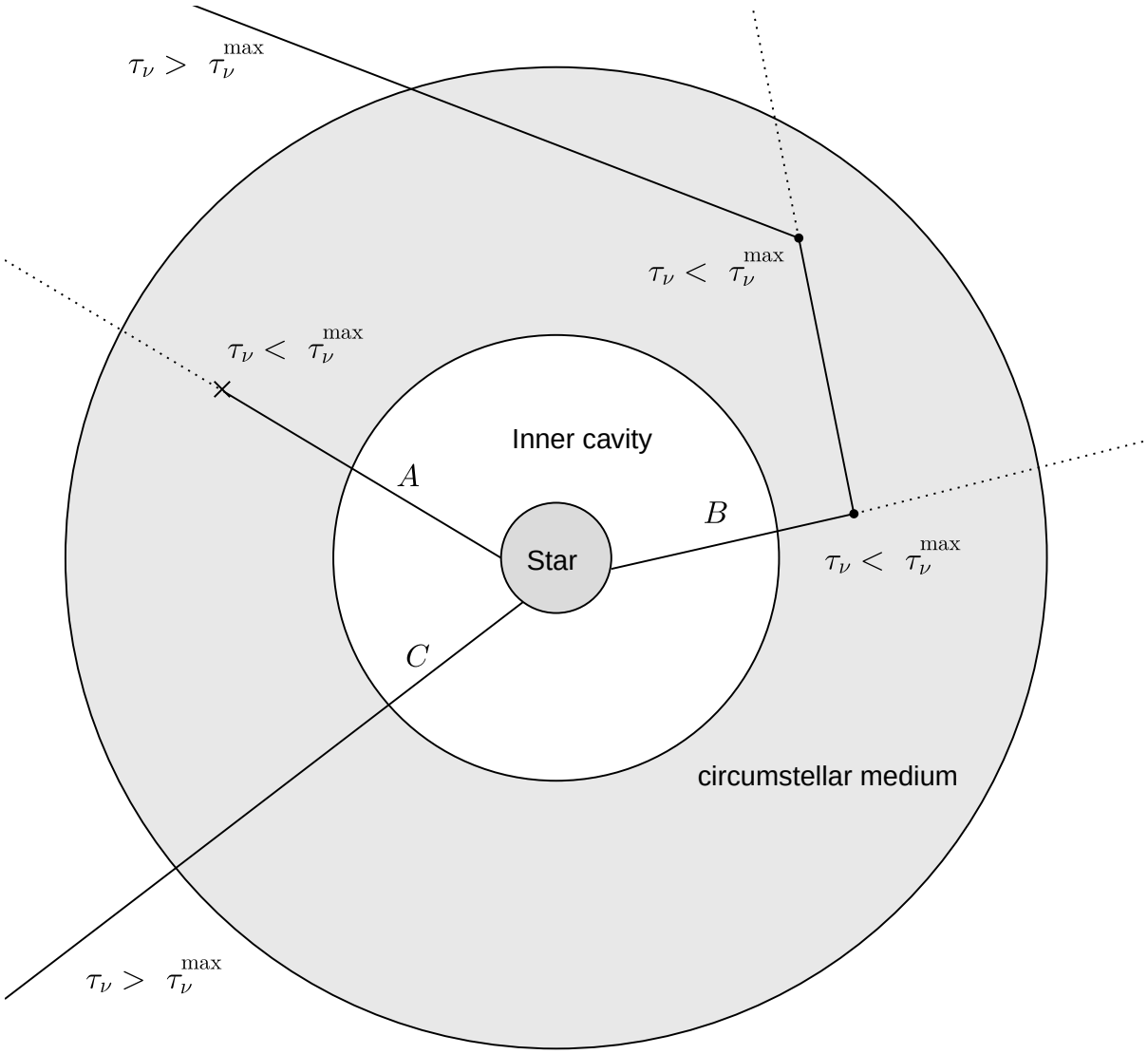

Figure 1.5 – Example of propagation of the photons packets through the circumstellar medium, generated by a central star (see Sect. 1.1.5). Path A: the packet interact with the circumstellar matter ($\tau_\nu < \tau_\nu^{\max}$) and gets absorbed. Path B: the packets interacts and gets diffused two times before escaping the medium. Path C: the packet does not interact ($\tau_\nu > \tau_\nu^{\max}$) and escapes the circumstellar medium.

Generation of the packets of photons from the external sources

As an example of external source, let us take the example of a spherical star that radiates as a black body. The monochromatic luminosity of the star is $L_\nu^\star = 4\pi\, R_\star^2\, B_\nu(T_\star)$, and each packet of photons has an energy rate given by $L_\nu^\star/N$. The location on the stellar surface where the packet is emitted and its direction $\mathbf{\Omega}$ is determined by drawing random numbers. For a spherically-symmetric star, there is not prefered location, hence the probability that a packet is emitted in the interval $[\Theta, \Theta + \mathrm{d}\Theta[$ and $[\Phi, \Phi + \mathrm{d}\Phi[$ (see Fig. 1.7 for the definition of the coordinates) is

$$f_{\Theta,\Phi}\ \mathrm{d}\Theta\,\mathrm{d}\Phi = \frac{1}{4\pi}\sin\Theta\ \mathrm{d}\Theta\,\mathrm{d}\Phi, \tag{1.55}$$

with $f_{\Theta,\Phi}$, the associated probability density function (PDF). The previous equation consists in assuming that this probability is equal to the surface element $dA = R_\star^2\,\sin\Theta\,\mathrm{d}\Theta\,\mathrm{d}\Phi$, divided by the surface of the sphere $4\pi\,R_\star^2$. Since Θ and Φ are independent coordinates, we can rewrite their associated PDF as

$$\begin{aligned} f_\Theta &= \frac{1}{2}\ \sin\Theta\ \mathrm{d}\Theta, \\ f_\Phi &= \frac{1}{2\pi}\ \mathrm{d}\Phi. \end{aligned} \tag{1.56}$$

In practice, we use an uniform random variable X with the associated values x uniformly distributed on the interval $[0, 1[$. The PDF of X is, by definition $f_X(x) = 1$. To link this variable to the position on the sphere, we impose that the probability that the variable X has a value in the range $[x, x + \mathrm{d}x[$ is the same as the probability for the photon packet to be emitted in the interval $[\Theta, \Theta + \mathrm{d}\Theta[$ and $[\Phi, \Phi + \mathrm{d}\Phi[$. If we use a random variable X_1 for the Θ coordinate, we have *e.g*,

$$\begin{aligned} f_{X_1}(x_1)\ \mathrm{d}x_1 = \mathrm{d}x_1 &= f_\Theta\ \mathrm{d}\Theta, \\ x_1 &= \int_0^\Theta f_{\Theta'}\ \mathrm{d}\Theta'. \end{aligned} \tag{1.57}$$

Which gives, $\cos\Theta = 1 - 2\,x_1$. Similarly, the angle Φ can be determined with the help of another uniform random variable X_2 and yields $\Phi = 2\pi\,x_2$.

The same procedure can be done in order to compute the direction in which the photon package is launched into the circumstellar medium.

Travelling distance before interaction

Once the packet is created and launched, the next step consists of randomly determining whether it will interact with the circumstellar material, and if so, where this interaction will take place. Looking at the integral form Eq. (1.38), we can see that, along a given ray, a given packet of photons at a given optical depth τ_ν is, without emission, diminished by the factor $\exp(-\tau_\nu)$ when travelling $\mathrm{d}\tau_\nu$ along the ray. Hence the probability of interaction can be assumed to be

$$f_{\tau_\nu}\ \mathrm{d}\tau_\nu = \exp(-\tau_\nu)\ \mathrm{d}\tau_\nu. \tag{1.58}$$

Again, using a random variable X_3, we find the correspondence between the travelled optical depth along the ray and the random number x_3,

$$x_3 = \int_0^{\tau_\nu} \exp\left(-\tau'_\nu\right) \, \mathrm{d}\tau'_\nu = 1 - \exp\left(-\tau_\nu\right), \tag{1.59}$$

or equivalently, $\tau_\nu = -\ln\left(1 - x_3\right)$ or simply $\tau_\nu = -\ln\left(x_4\right)$ by noticing that X_4, such as $x_4 = 1 - x_3$ is also a uniform random variable, in the interval $[0, 1[$. Once τ_ν has randomly been drawn, the associated travelling distance s can be computed, by using the definition of the optical depth,

$$\tau_\nu = \int_0^{s} \kappa_\nu^{\mathrm{ext}}(s') \, \mathrm{d}s'. \tag{1.60}$$

In practice $\kappa_\nu^{\mathrm{ext}}$ is defined on a grid and the previous integral can be computed numerically, by computing the optical depth on each portion of the ray crossing the grid. Note that if the optical depth τ_ν is superior to $\tau_\nu^{\max}$ the optical depth, along the ray to the boundary surface, the photon does not interact and escapes the medium (see *e.g* path C in Fig. 1.5).

Type of interaction

Once the path length s has been determined, we now need to know what type of interaction will occur, *i.e* a scattering or an absorption event. The probability of a scattering event is simply given by the albedo $\epsilon_\nu = \kappa_\nu^{\mathrm{sca}}/\kappa_\nu^{\mathrm{ext}}$. Again, using a uniform random variable X, we can determine the type of interaction: if $x \leq \epsilon_\nu$, we have a scattering event, otherwise the photon packet gets absorbed ($x > \epsilon_\nu$).

In the case of an absorption event, the photon package is destroyed; this is the end of the photon life cycle.The absorbed photon packet luminosity is stored in the interaction cell and is used at a later stage to evaluate the mean specific intensity J_ν.

If the interaction is a scattering event, the next step is to determine the new direction of propagation and the new frequency of the photon packet. In the general case of anisotropic and non-coherent scattering, the PDF expressing the probability that a photon with a direction $\mathbf{\Omega}'$ and a frequency ν' will be scattered in the direction $\mathbf{\Omega}$ with the frequency ν is directly given by the phase function $P(\nu' \to \nu, \mathbf{\Omega}'.\mathbf{\Omega})$ defined in Eq. (1.21),

$$f_{\nu,\mathbf{\Omega}} \, \mathrm{d}\mathbf{\Omega} \, \mathrm{d}\nu = P(\nu' \to \nu, \mathbf{\Omega}'.\mathbf{\Omega}) \, \mathrm{d}\mathbf{\Omega} \, \mathrm{d}\nu. \tag{1.61}$$

Once the new direction and frequency has been determined, the photon packet continues its journey through the medium until it gets either absorbed or escapes the envelope. For the escaping packets, they can be placed into frequency and direction-of-observation bins that can further provide the emergent spectral energy distribution.

After all the packets from the external source have been absorbed or have left the domain, the luminosity stored in each cell can be used to compute the mean specific intensity J_ν, the temperature T and the emission term Q_ν. Then each cell can re-emit the packets, starting another Monte-Carlo cycle, to compute the new emission term in each cell.

The procedure is then repeated until a set convergence level is reached. We mention that Bjorkman and Wood (2001) developed an efficient algorithm in order to avoid this iteration scheme and where each absorbed photon packet contributes to the increase of the temperature inside the cell and is directly re-emitted in the medium with another frequency.

We note that this method treats the scattering explicitly, hence no further Λ-iteration is needed, highlighting its numerical efficiency. One major flaw of Monte-Carlo techniques is the noise associated to all the physical observables derived from the photon packets. This random noise can make the Monte Carlo algorithm slow, because of the necessity an important number of packets required to decrease the noise in places where it is important, like optically-thick regions.

1.2 Circumstellar envelopes

Circumstellar envelopes regroup a large variety of astrophysical objects that are linked to different stages of stellar evolution. They range from early-stages, where they are left-overs of the collapse of large molecular clouds into a proto-star, to late-stages where for example, strong stellar winds strip away the outer layers of AGB stars, forming dense circumstellar envelopes. In this section, we focus exclusively on the presentation of protoplanetary discs, as they are relevant for the numerical tests we perform in this thesis.

1.2.1 Protoplanetary discs

Protoplanetary discs are the remnants of the star-formation process. Stars form through the gravitational collapse of cold interstellar clouds. At early-stages, only a fraction of this cloud can assemble into a compact object such as a star. The outer regions, with higher angular momentum, are collapsing onto a disc rather than the protostar itself (Terebey et al., 1984). The presence of such disks has been observed around young low/intermediate-mass premain-sequence stars (T Tauri stars, brown dwarfs and Herbig Ae/Be stars). It should be noted that all low/intermediate-mass pre-main-sequence stars have discs. The presence of circumstellar material has direct consequences on the light we receive from them. For instance, a reliable indicator of the presence of dust is a infrared flux in the spectrum, in excess of what can possibly be explained by an usual stellar photosphere. Based on this feature Lada (1987) introduced a classification of discs based on the importance of this infrared excess. Later, by studying the fraction of stars with NIR excess flux in young clusters of ages from 0.5 to 5 million years, Haisch et al. (2001) established that the disc fraction decreases with age and that these objects have a lifetime of a few million years.

A picture of a typical protoplanetary disc is shown in Fig. 1.6. The disc is made of a gas and a dust component. Note that in this thesis, we only focus on the modelling of radiation inside the dust part. The inner radius is typically just a few stellar radii ($0.02 - 0.03$ AU), where the stellar magnetic field lines channel gas at near free-fall velocities that then shocks at the stellar surface (Hartmann review). Further away ($0.1 - 1$ AU), the temperature becomes cold enough so that gas molecules can condensate into dust

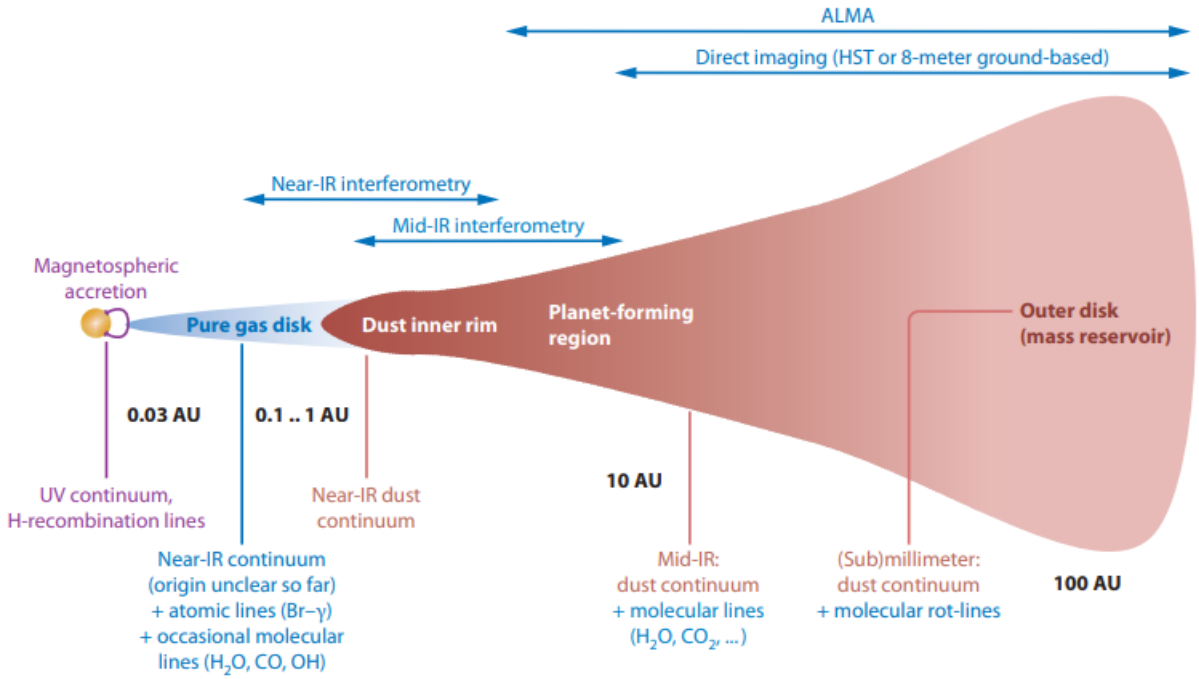

Figure 1.6 – Schematic representation of a protoplanetary disc (credit: Dullemond and Monnier, 2010).

grains. The outer radius of the dust disc can range between a few tens of astronomical units up to 1 000 AU or more. Additionally, the temperature across the whole disc varies from more than 10^4 K in the inner regions down to $10 - 30$ K in the outer regions.

This large range in temperatures and spatial scale means that different observational techniques probe different regions inside the disc. Telescopes/instruments operating in the far-infrared and millimetre regimes [1] predominantly observe the outer ($\geq$ 10 AU) structures, where the temperature of the circumstellar dust is cold enough to emit in this wavelength range. The recent advent of near and mid-infrared interferometry (Gravity Collaboration et al., 2017; Lopez et al., 2022) now allows to probe the dust and gas inner regions, and to constrain the geometry and location of the dust inner rim (Dullemond and Monnier, 2010). Finally optical and UV observations typically probe the regions very close to the stellar surface, although optical interferometry (Eisenhauer, 2019) is needed to observe them.

1.2.2 Optical properties of circumstellar dust

In Sect. 1.1.1, we defined the absorption and scattering coefficients but did not give detail on how to compute them. At the microscopic scale, absorption and scattering are the result of the interaction of a photon with a particle, like an electron (free or bounded inside an atom). The associated coefficients are then evaluated by taking into account

1. see *e.g* https://www.eso.org/sci/facilities/alma.html

the bound-bound (line), bound-free (photoionisation) and free-free transitions (see *e.g* Hubeny and Mihalas, 2014, for a detailed description).

In contrast, circumstellar dust is made of a collection of millions of atoms. At the macroscopic scale, the interaction between this aggregate of particles and light can be described with the help of the Maxwell's electromagnetic theory.

In general, the absorption and scattering coefficients can be defined as

$$\kappa_\nu^{\rm abs} = C_\nu^{\rm abs}\, n, \quad \kappa_\nu^{\rm sca} = C_\nu^{\rm sca}\, n, \tag{1.62}$$

where $C_\nu^{\rm abs}, C_\nu^{\rm sca}$ are the optical cross-section coefficients (in $\rm m^2$) associated with the absorption and scattering processes and n is the number density, *i.e* the number of dust particles per unit of volume. The theory of absorption and scattering of light by small particle (but big compared with the atomic size) is described in great details in Bohren and Huffman (1998). To summarise, the optical cross-section coefficients are estimated by illuminating a particle with an incident wave (a plane wave usually) and computing energy absorption and scattering rate due to the particle. These rates depend on the complex refractive index of the considered particle. In the astrophysical context, we note that the theory was used, *e.g* by Draine and Lee (1984), to compute the optical cross-sections for graphite and silicate grains, with the help of available laboratory and astronomical data for the refractive indexes of such materials.

Inside circumstellar environments, the chemical composition of dust is in reality made of several dust species with several grain radii. Usually, the number density of the dust mixture can be assumed to be (see *e.g* Woitke et al., 2009),

$$n = \int_{a_{\rm min}}^{a_{\rm max}} f(a)\ {\rm d}a, \tag{1.63}$$

where a is the grain radius and $f(a)$ is a prescribed dust size distribution function (in $\rm cm^{-4}$). The dust opacities are then, *e.g* for absorption,

$$\kappa_\nu^{\rm abs} = \int_{a_{\rm min}}^{a_{\rm max}} C_\nu^{\rm abs}(a)\, f(a)\ {\rm d}a. \tag{1.64}$$

1.2.3 The radiative transfer equation in axis-symmetric envelopes

In this thesis we focus on spherically-symmetric and axis-symmetric envelopes, the first geometry being a particular case of the second one. We saw in Sect. 1.1.2 that the radiation field depends on the state of the matter that interacts with it. The general problem is thus described by the equations of hydrodynamics coupled with the radiative transfer equation. In this thesis, we assume the circumstellar material to be in a stationary state and that its density profile is known, then we only have to deal with the radiative problem.

We want to describe the time-independent radiation field inside a static axis-symmetric circumstellar envelope. The situation is illustrated in Fig. 1.7. A central spherical star

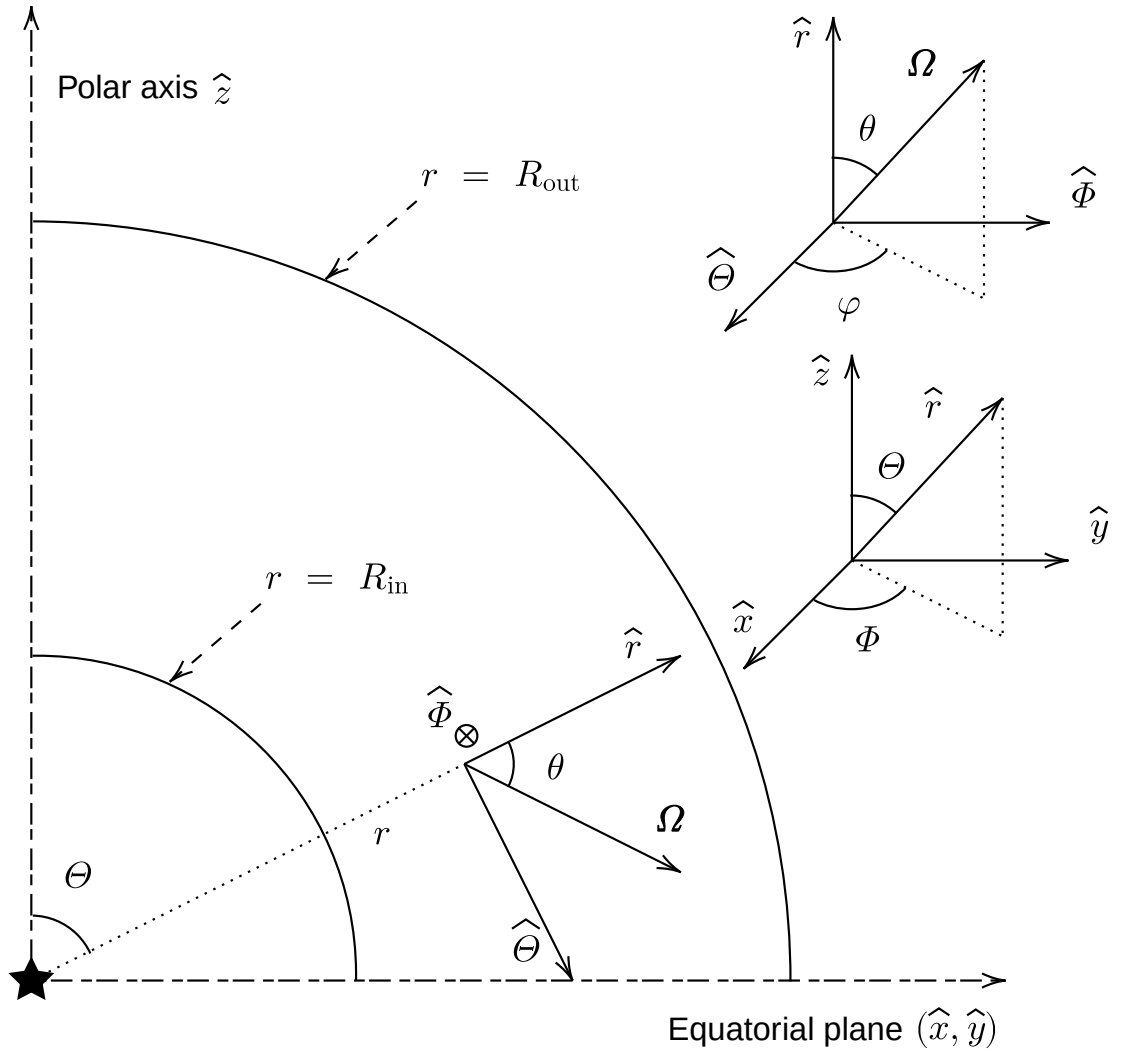

Figure 1.7 – Illustration picturing the coordinate system. The radiation field in the envelope, at a given position $\boldsymbol{r}$, in a given direction $\boldsymbol{\Omega}$ is described by two spatial (r, Θ) and two angular $(\mu = \cos\theta, \varphi)$ coordinates.

of radius $R_\star$ lies inside an inner cavity, free of matter, of radius $R_{\rm in}$. The envelope itself spans from the radius $R_{\rm in}$ up to an outer radius $R_{\rm out}$. We assume that no matter is present outside this shell. We consider the material to be exclusively made of dust. In addition to the axial symmetry around the pole ($\Theta = 0$), we also assume a planar symmetry with respect to the equatorial plane, at $\Theta = \pi/2$. We choose to describe the problem with the spherical coordinate system, both for the spatial and angular variables. Consequently, given the symmetries, the domain of definition is $D \subset \mathbb{R}^4$ with $D \ni \boldsymbol{x} = (r, \Theta, \mu = \cos\theta, \varphi) \in [R_{\rm in}, R_{\rm out}] \times]0, \pi/2] \times [-1, 1] \times [0, \pi]$. The associated radiation field is described by the time-independent version of the radiation transfer equation Eq. (1.31),

$$\mu\,\partial_r I_\nu + \frac{\sqrt{1-\mu^2}\cos\varphi}{r}\partial_\Theta I_\nu + \frac{1-\mu^2}{r}\partial_\mu I_\nu - \frac{\cot\Theta\sqrt{1-\mu^2}\sin\varphi}{r}\partial_\varphi I_\nu + \kappa_\nu^{\rm ext}\, I_\nu = \eta_\nu. \tag{1.65}$$

In our study, we consider thermal emission and coherent/isotropic scattering, hence the emissivity is $\eta_\nu = \kappa_\nu^{\rm abs}\, B_\nu\,(T) + \kappa_\nu^{\rm sca}\, J_\nu$. We assume that the radiative equilibrium is fulfilled (see Eq. 1.41)

$$\int_0^\infty \kappa_\nu^{\rm abs}\, J_\nu \,\mathrm{d}\nu = \int_0^\infty \kappa_\nu^{\rm abs}\, B_\nu(T)\,\mathrm{d}\nu. \tag{1.66}$$

Decoupling the stellar and the envelope radiation field

In the astrophysical context, the circumstellar matter is illuminated by a central star and it is customary to decompose the radiation field into two contributions (see e.g Steinacker et al., 2003), $I_\nu = I_\nu^\star + I_\nu^{\rm env}$, with $I_\nu^\star$ the direct stellar radiation field attenuated by the circumstellar extinction and $I_\nu^{\rm env}$, the radiation from the envelope (thermal emission + scattering). The radiation field then verifies the system of equations

$$\begin{cases} \boldsymbol{\Omega}.\boldsymbol{\nabla}\, I_\nu^\star + \kappa_\nu^{\rm ext}\, I_\nu^\star = 0, \\ \boldsymbol{\Omega}.\boldsymbol{\nabla}\, I_\nu^{\rm env} + \kappa_\nu^{\rm ext}\, I_\nu^{\rm env} = \kappa_\nu^{\rm abs}\, B_\nu + \kappa_\nu^{\rm sca}\, J_\nu, \end{cases} \tag{1.67}$$

with $J_\nu = J_\nu^\star + J_\nu^{\rm env}$. In Steinacker et al. (2003), the thermal emission term is put into the right-hand side of the first Eq. (1.67), but having it in the second equation is advantageous if the optical coefficients are independent of temperature. In such cases, the equations decouple and $I_\nu^\star$ can be solved and computed once and for all. The stellar radiation field can be expressed, by integration of the first equation in Eq. (1.67) along the rays that intersect the star

$$I_\nu^\star = \begin{cases} B_\nu\,(T_\star)\,\exp\left\{-\int_0^{s(R_{\rm in})} \kappa_\nu^{\rm ext}(s')\,\mathrm{d}s'\right\} & \mu^\star \le \mu \le 1, \\ 0 & \text{otherwise.} \end{cases} \tag{1.68}$$

$B_\nu\,(T_\star)$ is the stellar radiation field at the surface of the star (we assume that the star radiates as a black-body with a constant temperature $T_\star$), $\mu^\star = (1 - (R_\star/r)^2)^{1/2}$ is the cosine of the angle under which the star is seen at radius r and $s(R_{\rm in})$ is the distance between a given point $\boldsymbol{r}$ in the envelope and the intersection of inner radius with the ray.

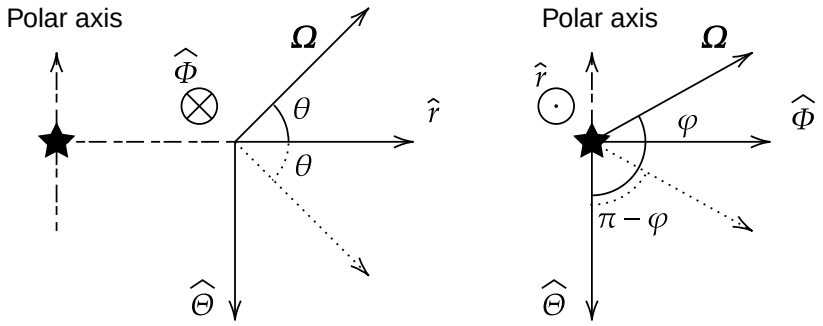

Figure 1.8 – Representation of the direction vector $\boldsymbol{\Omega}$ at the equator. The dot-arrows represent the symmetric of $\boldsymbol{\Omega}$ with respect to the equatorial plane $(\hat{r}, \hat{\Phi})$. The left and right two-dimensional views allow to see the corresponding direction angles.

The argument in the exponential is the negative of the optical depth integrated along the ray. In the point source approximation, the stellar mean intensity can be expressed analytically as,

$$J_\nu^\star \approx \frac{(1-\mu^\star)}{2} B_\nu(T_\star) \exp\left\{ -\int_{R_{\rm in}}^{r} \kappa_\nu^{\rm ext}(r', \Theta)\, {\rm d}r' \right\}. \tag{1.69}$$

In general, the integral in Eq. (1.69) can be carried out numerically, providing the stellar source term $J_\nu^\star$ for the second equation in Eq. (1.67).

Boundary conditions

To complete the description of the problem, we need to specify the boundary conditions for $I_\nu^{\rm env}$. At the inner radius $r = R_{\rm in}$ (and $\boldsymbol{s} = -\hat{r}$), the incident radiation comes directly from the opposite point of the cavity,

$$I_\nu^{\rm env}(R_{\rm in}, \Theta, \mu, \varphi) = \begin{cases} I_\nu^{\rm env}(R_{\rm in}, \Theta', \mu', \varphi') & 0 < \mu \leq \mu^\star, \\ 0 & \mu^\star \leq \mu \leq 1, \end{cases} \tag{1.70}$$

with $(R_{\rm in}, \Theta', \mu', \varphi')$ the local coordinates of the opposite point (see Fig. A.1). We give a derivation of their expressions in appendix A.

On the outer edge $r = R_{\rm out}$ (and $\boldsymbol{s} = \hat{r}$), we assume that there is no incident radiation upon the surface,

$$I_\nu^{\rm env}(R_{\rm out}, \Theta, \mu, \varphi) = 0 \quad -1 \leq \mu \leq 0. \tag{1.71}$$

At the equator $\Theta = \pi/2$ (and $\boldsymbol{s} = \hat{\Theta}$), the planar symmetry requires the radiation field to verify, as pictured by Fig. 1.8,

$$I_\nu^{\rm env}(r, \pi/2, \mu, \varphi) = I_\nu^{\rm env}(r, \pi/2, \mu, \pi - \varphi) \quad \forall\, \varphi > \pi/2. \tag{1.72}$$

1.3 Plan of the thesis

Throughout this chapter, we presented a general overview of the radiative transfer problem and saw basically two approaches in solving it, approximate and numerical methods.

In Chapter 2, we investigate the Flux-Limited Diffusion (FLD) theory. The FLD is an approximate description of the radiation transfer problem. It is an equation for the zero-order moment equation Eq. (1.39), with a closure relation for the radiative flux $\boldsymbol{H}_\nu$ similar to the Eddington diffusion equation Eq. (1.43). However, contrary to the Eddington approximation, the FLD theory is flux-limited, meaning it always satisfy Eq. (1.12). Furthermore it is asymptotically exact in the optically-thin and thick regimes. The FLD approximation has already been applied in codes, used for astrophysical applications (see Table 2.1), but with inconsistent boundary conditions. One aim of this thesis is to investigate if the inclusion of physically more consistent boundary conditions can improve the accuracy of the approximation. We start by deriving general non-linear mixed boundary conditions aimed to work in all optical regimes. We then implement these boundary conditions and the FLD approximation in a code and perform some numerical tests.

The second part of this thesis focuses on a numerical method for solving partial differential equations that did not receive a lot of attention in the context of the astrophysical radiative transfer. The Discontinuous Galerkin finite element method (DG-FEM) is derived from the finite-element method with the specificity that the solution is discontinuous at the elements edges. While some applications exist in one dimensional cases, in the context of neutron transport or stellar atmospheres, to our knowledge it has not been extended to multidimensional circumstellar envelopes. In Chapter 3, we use the DG-FEM to solve the time-independent, frequency-dependent radiative transfer equation Eq. (1.65). We implement the method in a code and we compare our results with previous benchmark from the literature.

Finally, in Chapter 4, we conclude and present some future work.

Chapter 2

The Flux-limited diffusion approximation in circumstellar envelopes

In the last chapter, we saw that we could obtain an approximate description of the radiative transfer problem by closing the system of moment equations for the radiative transfer equation. In this chapter, we consider one of these approximate descriptions, the Flux-Limited Diffusion (FLD hereafter), derived by Levermore and Pomraning (1981). As for the Eddington approximation, the FLD theory recasts the radiative transfer equation into a presumably simpler diffusion equation. However, contrary to the Eddington approximation, it is asymptotically exact in both optically-thin and thick regimes, and the radiative transfer problem is described by a non-linear diffusion equation for the mean specific intensity J_ν.

One important aspect for the accuracy of the method lies in the implementation of appropriate boundary conditions. In contrast to the usual boundary conditions for the radiative transfer (see Eq. 1.35), the boundary conditions for the FLD approximation, or any other diffusion-like description, can only be satisfied in an integral sense (over the directions) with a prescribed arbitrary weight. The choice of this weight corresponds to different physical hypotheses, *e.g* imposing the incident flux or the incident intensity in several arbitrary directions. Mathematically, the type of boundary condition also have some implications on the accuracy of the solution. A non-exhaustive list of implemented boundary conditions, for the FLD approximation in an astrophysical context, is shown in Table 2.1.

In most applications, Dirichlet boundary conditions are applied with a prescribed value for the temperature at the boundaries of the medium. In the problems we consider in this thesis, the temperature at the boundaries is not known a priori and must be derived as part of the solution of the radiative transfer equation Eq. (1.65) coupled with the radiative equilibrium equation Eq. (1.66). The same type of problem occurs with the use of a Neumann boundary condition because the gradient of J_ν is proportional to the radiative flux that also needs to be computed from the solution itself. In general we need frequency-dependent non-linear mixed boundary conditions that can properly describe

Study	Boundary condition	Scattering (Yes/No)	Hybrid (Yes/No)	$\Delta T/T$ (%)
Sonnhalter et al. (1995)	$J_\nu(R_{\rm out}) = B_\nu(T_{\rm out})$	Yes (isotropic)	No	/
Yorke and Sonnhalter (2002)	$J_\nu(R_{\rm out}) = B_\nu(T_{\rm out})$	Yes (isotropic)	No	/
Kuiper et al. (2010)	$\boldsymbol{\nabla} J_\nu\|_{r=R_{\rm in}} = 0$ $J_\nu(R_{\rm out}) = B_\nu(T_{\rm out})$	No	Yes	11.1
Mignon-Risse et al. (2020)	$J_\nu = B_\nu(T_{\rm out})$	No	Yes	25

Table 2.1 – Non-exhaustive list of boundary conditions that can be found in literature for the FLD approximation in circumstellar envelopes. The column "hybrid" informs if the FLD approximation is applied to the full radiation field or only to a part of it (*e.g* see Eq. 1.67). The last column corresponds to the max relative difference in temperature between the FLD and the benchmarks from literature (Pascucci et al., 2004).

radiation, from the optically-thin up to the optically-thick regime.

The purpose of this chapter is to investigate if the FLD approximation, supplemented with general frequency-dependent boundary conditions, can accurately describe the radiation field and the temperature in spherical and axis-symmetric circumstellar environments. The chapter is organised as follows: in Sect. 2.1, we recall the bases of the FLD theory. In Sect. 2.2, we derive general boundary conditions for the FLD approximation. In Sect. 2.3 we focus on the special case of spherically-symmetric circumstellar envelopes (numerical implementation + tests) and extend the study to axis-symmetric configurations in Sect. 2.4.

2.1 The Flux-limited diffusion theory

To introduce our notations and the relevant quantities of the theory, we present and detail the original work from Levermore and Pomraning (1981). First, we derive the closure relation that leads to the FLD equation. Second, we address the problem of the associated boundary conditions.

2.1.1 Derivation of the Flux-limited diffusion equation

We start from the radiative transfer equation Eq. (1.33), with matter at local thermal equilibrium and with isotropic and coherent scattering,

$$\frac{1}{c}\partial_t I_\nu + \boldsymbol{\Omega}.\boldsymbol{\nabla} I_\nu + \kappa_\nu^{\rm ext} I_\nu = \kappa_\nu^{\rm abs} B_\nu + \kappa_\nu^{\rm sca} J_\nu. \tag{2.1}$$

The zero-order moment equation is obtained by integrating Eq. (2.1) over all directions and divide by 4π,

$$\frac{1}{c}\partial_t J_\nu + \boldsymbol{\nabla}.\boldsymbol{H}_\nu = \kappa_\nu^{\rm abs}\left(B_\nu - J_\nu\right). \tag{2.2}$$

Levermore and Pomraning (1981) assumed the following form for the specific intensity,

$$I_\nu\left(t,\boldsymbol{r},\boldsymbol{\Omega}\right) = J_\nu\left(t,\boldsymbol{r}\right)\,\psi_\nu\left(t,\boldsymbol{r},\boldsymbol{\Omega}\right). \tag{2.3}$$

$\psi_\nu\,(t, \boldsymbol{r}, \boldsymbol{\Omega})$ is called the normalised intensity. This function is known in the two following limiting cases; in the optically-thin regime, the specific intensity I_ν is sharped-peaked in a given direction $\boldsymbol{\Omega}_0$ and $\psi_\nu = 4\pi\, J_\nu\, \delta(\boldsymbol{\Omega}.\boldsymbol{\Omega}_0)$ with $\delta(\boldsymbol{\Omega}.\boldsymbol{\Omega}_0)$ the angular Dirac delta distribution in the direction $\boldsymbol{\Omega}_0$. In the optically-thick regime, the radiation field is almost isotropic (Eddington, 1920) and $\psi_\nu = 1 - \boldsymbol{\Omega}.\boldsymbol{\nabla}\, J_\nu/(\kappa_\nu^{\rm ext}\, J_\nu)$. From the definition of J_ν (see Eq. 1.5) we have the normalisation condition

$$\frac{1}{4\pi}\int_{4\pi} \psi_\nu\,(t, \boldsymbol{r}, \boldsymbol{\Omega})\ \mathrm{d}\boldsymbol{\Omega} = 1. \tag{2.4}$$

Subsequently, from the definition of the Eddington flux (see Eq. 1.11) , we have $\boldsymbol{H}_\nu(t, \boldsymbol{r}) = J_\nu(t, \boldsymbol{r})\, \boldsymbol{h}_\nu(t, \boldsymbol{r})$ with $\boldsymbol{h}_\nu$ the normalised flux, defined as,

$$\boldsymbol{h}_\nu\,(t, \boldsymbol{r}) = \frac{1}{4\pi}\int_{4\pi} \boldsymbol{\Omega}\, \psi_\nu\,(t, r, \boldsymbol{\Omega})\ \mathrm{d}\boldsymbol{\Omega}. \tag{2.5}$$

Now, if we insert Eq. (2.3) into the radiative transfer equation Eq. (2.1), we obtain

$$J_\nu\left(\frac{1}{c}\partial_t\psi_\nu + \boldsymbol{\Omega}.\boldsymbol{\nabla}\,\psi_\nu\right) + \psi_\nu\left(\frac{1}{c}\partial_t J_\nu + \boldsymbol{\Omega}.\boldsymbol{\nabla}\,J_\nu + \kappa_\nu^{\rm ext}\,J_\nu\right) = \kappa_\nu^{\rm abs}\,B_\nu + \kappa_\nu^{\rm sca}\,J_\nu. \tag{2.6}$$

Eq. (2.6) is exact and is just a way to rewrite the radiative transfer equation, with the given form for the specific intensity Eq. (2.3). The FLD approximation consists in assuming that the normalised intensity ψ_ν is conserved along a given direction $\boldsymbol{\Omega}$, meaning that we have

$$\frac{1}{c}\partial_t\psi_\nu + \boldsymbol{\Omega}.\boldsymbol{\nabla}\,\psi_\nu = 0. \tag{2.7}$$

This assumption is asymptotically true, in both optically-thin and thick regimes. Integration over all directions of Eq. (2.7) together with the normalisation condition Eq. (2.4) yields,

$$\boldsymbol{\nabla}.\boldsymbol{h}_\nu = 0. \tag{2.8}$$

We can then rewrite Eq. (2.6), using the FLD approximation Eq. (2.7) and substituting the term $\partial_t J_\nu/c$ by its expression in Eq. (2.2),

$$\psi_\nu\left(\kappa_\nu^{\rm abs}\,(B_\nu - J_\nu) - J_\nu\,\boldsymbol{\nabla}.\boldsymbol{h}_\nu - \boldsymbol{h}_\nu.\boldsymbol{\nabla}\,J_\nu + \boldsymbol{\Omega}.\boldsymbol{\nabla}\,J_\nu\right) = \kappa_\nu^{\rm abs}\,B_\nu + \kappa_\nu^{\rm sca}\,J_\nu. \tag{2.9}$$

Finally we obtain the following expression for the normalised intensity ψ_ν, directly from Eq. (2.9),

$$\psi_\nu = \frac{\kappa_\nu^{\rm abs} B_\nu + \kappa_\nu^{\rm sca} J_\nu}{\kappa_\nu^{\rm abs}\,(B_\nu - J_\nu) + (\boldsymbol{\Omega} - \boldsymbol{h}_\nu)\,.\,\boldsymbol{\nabla}\,J_\nu}. \tag{2.10}$$

Introducing the effective albedo ω_ν and the dimensionless vector $\boldsymbol{R}_\nu$ defined by

$$\omega_\nu = \frac{\kappa_\nu^{\rm abs}\,B_\nu + \kappa_\nu^{\rm sca}\,J_\nu}{\kappa_\nu^{\rm ext}\,J_\nu}, \quad \boldsymbol{R}_\nu = -\frac{\boldsymbol{\nabla}\,J_\nu}{\omega_\nu\,\kappa_\nu^{\rm ext}\,J_\nu}, \tag{2.11}$$

we can rewrite the normalised intensity ψ_ν as,

$$\psi_\nu = \frac{1}{1 + (\boldsymbol{h}_\nu - \boldsymbol{\Omega})\,.\boldsymbol{R}_\nu}. \tag{2.12}$$

and the normalised flux,

$$\boldsymbol{h}_\nu\left(t,\boldsymbol{r}\right)=\frac{1}{4\pi}\int\limits_{4\pi}\frac{\boldsymbol{\Omega}\ \mathrm{d}\boldsymbol{\Omega}}{1+\left(\boldsymbol{h}_\nu-\boldsymbol{\Omega}\right).\boldsymbol{R}_\nu}. \tag{2.13}$$

$R_\nu=|\boldsymbol{R}_\nu|$ is a very important quantity in the FLD theory. It corresponds to the ratio of the (effective) mean free path over the characteristic length of variation of J_ν. Consequently, the limits $R_\nu\gg 1$ and $R_\nu\ll 1$ correspond to the optical-thin and thick regimes, respectively.

For now, Eq. (2.12) can be seen as an equation relating ψ_ν and the first moment $\boldsymbol{h}_\nu$. To obtain a closed form for the function ψ_ν, we need to find an expression for $\boldsymbol{h}_\nu$. From Eq. (2.13), we can see that $\boldsymbol{h}_\nu$ is proportional to $\boldsymbol{R}_\nu$. This can be seen by performing the angular integration, choosing the z-axis aligned along $\boldsymbol{R}_\nu$,

$$\boldsymbol{h}_\nu=\frac{1}{4\pi}\int\limits_0^{2\pi}\mathrm{d}\varphi\int\limits_{-1}^{1}\frac{\sqrt{1-\mu^2}\,\cos\varphi\ \hat{x}+\sqrt{1-\mu^2}\,\sin\varphi\ \hat{y}+\mu\ \hat{z}}{1+\boldsymbol{h}_\nu.\boldsymbol{R}_\nu-\mu\,R_\nu}\,\mathrm{d}\mu. \tag{2.14}$$

Since $\boldsymbol{h}_\nu$, $\boldsymbol{R}_\nu$ and consequently $\boldsymbol{h}_\nu.\boldsymbol{R}_\nu$ are independent of $\boldsymbol{\Omega}$, the only non-zero component is along $\hat{z}$ or equivalently along $\boldsymbol{R}_\nu$. Thus we have

$$\boldsymbol{h}_\nu=\lambda_\nu\,\boldsymbol{R}_\nu, \tag{2.15}$$

with λ_ν a coefficient of proportionality. Finally, we obtain an expression for λ_ν with the help of the normalisation condition Eq. (2.4),

$$\frac{1}{4\pi}\int\limits_{4\pi}\frac{1}{1+\lambda_\nu\,R_\nu^2-\boldsymbol{\Omega}.\boldsymbol{R}_\nu}\,\mathrm{d}\boldsymbol{\Omega}=1. \tag{2.16}$$

To perform the integration, we again align the z-axis with $\boldsymbol{R}_\nu$,

$$\begin{aligned}\frac{1}{4\pi}\int\limits_0^{2\pi}\mathrm{d}\varphi\int\limits_{-1}^{1}\frac{1}{1+\lambda_\nu\,R_\nu^2-\mu.R_\nu}\,\mathrm{d}\mu&=1,\\ \frac{1}{2R_\nu}\ln\left(\frac{1+\lambda_\nu\,R_\nu^2+R_\nu}{1+\lambda_\nu\,R_\nu^2-R_\nu}\right)&=1,\\ \frac{1}{R_\nu}\tanh^{-1}\left(\frac{R_\nu}{1+\lambda_\nu\,R_\nu^2}\right)&=1,\end{aligned} \tag{2.17}$$

which leads to the following expression for λ_ν,

$$\lambda_\nu=\frac{1}{R_\nu}\left(\coth R_\nu-\frac{1}{R_\nu}\right) \tag{2.18}$$

λ_ν is called the flux-limiting parameter. In the optically-thick case ($R_\nu\ll 1$), $\lambda_\nu\to 1/3$, while in the optically-thin case ($R_\nu\gg 1$), $\lambda_\nu\to 1/R_\nu$. A representation of the flux

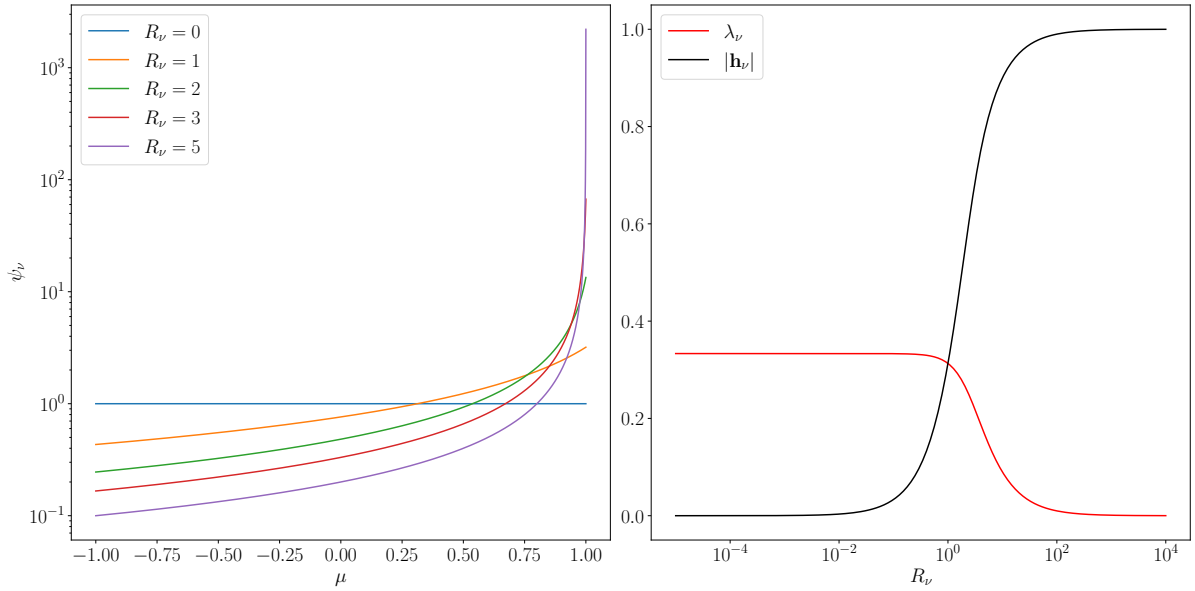

Figure 2.1 – Left: Representation of ψ_ν Eq. (2.19) versus $\mu = \boldsymbol{\Omega}.\boldsymbol{R}_\nu/R_\nu$, the cosine of the angle between $\boldsymbol{\Omega}$ and $\boldsymbol{R}_\nu$, for different optical regimes (denoted by the value of R_ν). Right: λ_ν Eq. (2.18) and $|\boldsymbol{h}_\nu| = \lambda_\nu R_\nu$ versus R_ν, illustrating the flux-limited property Eq. (1.12) of the FLD flux Eq. (2.20).

limiting parameter λ_ν is shown in Fig. 2.1-right. The ψ_ν function Eq. (2.12) can then be rewritten as,

$$\psi_\nu = \frac{1}{R_\nu \coth R_\nu - \boldsymbol{\Omega}.\boldsymbol{R}_\nu}. \tag{2.19}$$

The function ψ_ν versus $\mu = \boldsymbol{\Omega}.\boldsymbol{R}_\nu/R_\nu$ is shown in Fig. 2.1-left for several values of R_ν. For optically-thick regimes ($R_\nu \to 0$), $\psi_\nu \to 1 - \mu\, R_\nu$ while for the optically-thin cases, $\psi_\nu \to \delta(\mu - 1)$, as expected.

We obtain the following closure relation, associated with the FLD approximation, relating the first moment of the radiation field $\boldsymbol{H}_\nu$ and its lower moment (J_ν and its gradient via R_ν)

$$\boldsymbol{H}_\nu(t, \boldsymbol{r}) = \boldsymbol{h}_\nu(t, \boldsymbol{r})\, J_\nu(t, \boldsymbol{r}) = \lambda_\nu\, \boldsymbol{R}_\nu\, J_\nu = -D_\nu\, \boldsymbol{\nabla}\, J_\nu, \tag{2.20}$$

with the non-linear diffusion coefficient $D_\nu = \lambda_\nu/(\omega_\nu \kappa_\nu^{\rm ext})$. As shown by Fig. 2.1-right, a very desirable property of Eq. (2.20) is that the product $\lambda_\nu\, R_\nu = |\boldsymbol{h}_\nu|$ cannot exceed unity. In the optically-thin regime ($R_\nu \gg 1$), $\lambda_\nu \to 1/R_\nu$ and consequently $|\boldsymbol{h}_\nu| \to 1$. In the optically-thick regime ($R_\nu \ll 1$), $\lambda_\nu \to 1/3$ and $|\boldsymbol{h}_\nu| \to R_\nu/3$. Hence the flux limiting condition Eq. (1.12) is always satisfied. We note that ψ_ν is symmetric around $\boldsymbol{H}_\nu$ and thus that the angular distribution of specific intensity I_ν, in the FLD approximation, only depends on the angle with respect to the gradient of mean specific intensity J_ν.

The Eddington tensor, in the FLD approximation is, as defined in Sect. 1.1.4,

$$\bar{\boldsymbol{T}}_\nu(t, \boldsymbol{r}) = \frac{1}{4\pi} \int_{4\pi} \boldsymbol{\Omega} \otimes \boldsymbol{\Omega}\, \psi_\nu(t, \boldsymbol{r})\, {\rm d}\boldsymbol{\Omega}. \tag{2.21}$$

Eq. (2.21) satisfies the condition Eq. (1.16) because of the normalisation condition of the function ψ_ν Eq. (2.4). If we choose again to align the z-axis with the vector $\boldsymbol{R}_\nu$, $\bar{\boldsymbol{T}}_\nu$ is a diagonal matrix, with the diagonal components being,

$$\begin{aligned} \bar{\boldsymbol{T}}_\nu^{x,x} = \bar{\boldsymbol{T}}_\nu^{y,y} &= \frac{1}{4}\int_{-1}^{1} \frac{(1-\mu^2)\ \mathrm{d}\mu}{R_\nu\ \coth R_\nu - \mu\, R_\nu} = \frac{1}{2}\left(1 - \frac{\lambda_\nu\, R_\nu}{\tanh R_\nu}\right), \\ \bar{\boldsymbol{T}}_\nu^{z,z} &= \frac{1}{2}\int_{-1}^{1} \frac{\mu^2\ \mathrm{d}\mu}{R_\nu\ \coth R_\nu - \mu\, R_\nu} = \frac{\lambda_\nu\, R_\nu}{\tanh R_\nu}. \end{aligned} \tag{2.22}$$

In the optically-thin limit ($R_\nu \gg 1$), $\bar{\boldsymbol{T}}_\nu^{x,x}, \bar{\boldsymbol{T}}_\nu^{y,y} \to 0$ and $\bar{\boldsymbol{T}}_\nu^{z,z} \to 1$ while the optically-thick case ($R_\nu \ll 1$), $\bar{\boldsymbol{T}}_\nu^{x,x}, \bar{\boldsymbol{T}}_\nu^{y,y}, \bar{\boldsymbol{T}}_\nu^{y,y} \to 1/3$. The Eddington tensor, in the FLD approximation, is thus asymptotically exact in the two limiting cases.

Using the closure relation Eq. (2.20) in Eq. (2.2), we obtain the following FLD non-linear diffusion equation for J_ν,

$$\frac{1}{c}\partial_t J_\nu - \boldsymbol{\nabla}.\left(D_\nu\ \boldsymbol{\nabla}\, J_\nu\right) = \kappa_\nu^{\mathrm{abs}}\left(B_\nu - J_\nu\right). \tag{2.23}$$

In the optically-thin case ($D_\nu \to 1/(\omega_\nu\, \kappa_\nu^{\mathrm{ext}}\, R_\nu)$, $\kappa_\nu^{\mathrm{abs}}, \kappa_\nu^{\mathrm{sca}} \to 0$), the FLD equation reduces to a non-linear advection equation,

$$\frac{1}{c}\partial_t J_\nu - \boldsymbol{\nabla}.\left(\boldsymbol{v}_\nu\, J_\nu\right) = 0, \tag{2.24}$$

with the advection velocity $\boldsymbol{v}_\nu = \boldsymbol{\nabla}\, J_\nu / |\,\boldsymbol{\nabla}\, J_\nu|$ i.e, the unit vector in the direction of $\boldsymbol{\nabla}\, J_\nu$. In the optically-thick regime, the FLD equation reduces to a linear diffusion equation,

$$\frac{1}{c}\partial_t J_\nu - \boldsymbol{\nabla}.\left(\frac{1}{3\,\omega_\nu\,\kappa_\nu^{\mathrm{ext}}}\ \boldsymbol{\nabla}\, J_\nu\right) = \kappa_\nu^{\mathrm{abs}}\left(B_\nu - J_\nu\right). \tag{2.25}$$

2.1.2 Boundary conditions

To complete the FLD description, the non-linear diffusion equation Eq. (2.23) must be supplemented with boundary conditions. As explained in Sect. 1.1.3, the boundary conditions for the radiative transfer equation are imposed by specifying the incoming specific intensity Γ_ν at the boundaries of the domain. In the FLD theory, because of the particular form of specific intensity Eq. (2.3), we cannot impose an arbitrary distribution Γ_ν. Consequently, the actual boundary conditions for the radiative transfer equation Eq. (1.35) are in general incompatible with the FLD approximation. We can only hope to impose, at the boundary $\boldsymbol{r}_s$, an integrated quantity (on the solid angle), of the form,

$$\int_{\boldsymbol{s}.\boldsymbol{\Omega}\leq 0} W\left(\boldsymbol{\Omega}\right)\, I_\nu\left(t, \boldsymbol{r}_s, \boldsymbol{\Omega}\right)\ \mathrm{d}\boldsymbol{\Omega} = \int_{\boldsymbol{s}.\boldsymbol{\Omega}\leq 0} W\left(\boldsymbol{\Omega}\right)\, \Gamma_\nu\left(t, \boldsymbol{r}_s, \boldsymbol{\Omega}\right)\ \mathrm{d}\boldsymbol{\Omega}. \tag{2.26}$$

with $W(\boldsymbol{\Omega})$ a weight function and $\boldsymbol{s}$, the unit vector normal to the surface, pointing outside of the domain. In practice, two weights are commonly used. The Marshak

boundary condition is obtained by setting $W(\boldsymbol{\Omega}) = \boldsymbol{s}.\boldsymbol{\Omega}$ and amounts to specify the incident radiative flux flowing inside the domain. The Mark boundary condition consists in setting $W(\boldsymbol{\Omega}) = \delta(\boldsymbol{\Omega} - \boldsymbol{\Omega}_0)$ which amounts to prescribe the specific intensity in a particular direction $\boldsymbol{\Omega}_0$. In general, Eq. (2.26) can be written in the form of a non-linear boundary condition, dropping the $\boldsymbol{r}_s$ and t variables for simplicity,

$$\alpha_\nu \, J_\nu - \beta_\nu \, \boldsymbol{s}.\boldsymbol{H}_\nu = \frac{1}{4\pi} \int\limits_{\boldsymbol{s}.\boldsymbol{\Omega} \leq 0} W\left(\boldsymbol{\Omega}\right) \, \Gamma\left(\boldsymbol{\Omega}\right) \, \mathrm{d}\boldsymbol{\Omega}, \tag{2.27}$$

with α_ν and β_ν, non-linear coefficients depending on R_ν. Their expressions depend on the choice of $W(\boldsymbol{\Omega})$.

Several expressions for theses coefficients have been proposed in the literature. Pomraning (1988) derived their expression from the decomposition of the radiative transfer problem into an interior problem, solved in the FLD approximation, and an additional boundary layer term that essentially reduces to a one-dimensional semi-infinite problem (classical half-space albedo problem). The matching of the interior and the boundary layer solution yields a boundary condition for the FLD equation. These coefficients depend on integrals of the Chandrasekhar-H function and on the values of R_ν at the boundary. While being rather complex to implement in an astrophysical application, this derivation is expected to fail in cases where a boundary layer cannot be defined, like in optically-thin cases. Sanchez and Pomraning (1991) derived expressions for α_ν and β_ν coefficients for the special case of Marshark weight $W(\boldsymbol{\Omega}) = \boldsymbol{s}.\boldsymbol{\Omega}$, but with the assumption that the gradient of J_ν (or the vector $\boldsymbol{R}_\nu$) at the boundary is aligned with $\boldsymbol{s}$, which is only exact in plane-parallel or spherical media. Additionally, we expect the Marshak boundary condition to perform poorly, in the case of a vacuum boundary with no incoming radiation, as we will explain in Sect. 2.2.2. For astrophysical applications, we need boundary conditions that are accurate enough in all circumstances.

2.2 Derivation of boundary conditions for the Flux-limited diffusion approximation

In this section, we derive non-linear mixed [1] boundary conditions, compatible with all optical-regimes and relatively easy to implement in a code, for astrophysical applications. We first generalise the work of Sanchez and Pomraning (1991), by computing the non-linear coefficients of the Marshark-type boundary condition ($W(\boldsymbol{\Omega}) = \boldsymbol{s}.\boldsymbol{\Omega}$) with no particular assumption on the symmetry of the vector $\boldsymbol{R}_\nu$. Second we use two different approaches to derive a vacuum boundary condition.

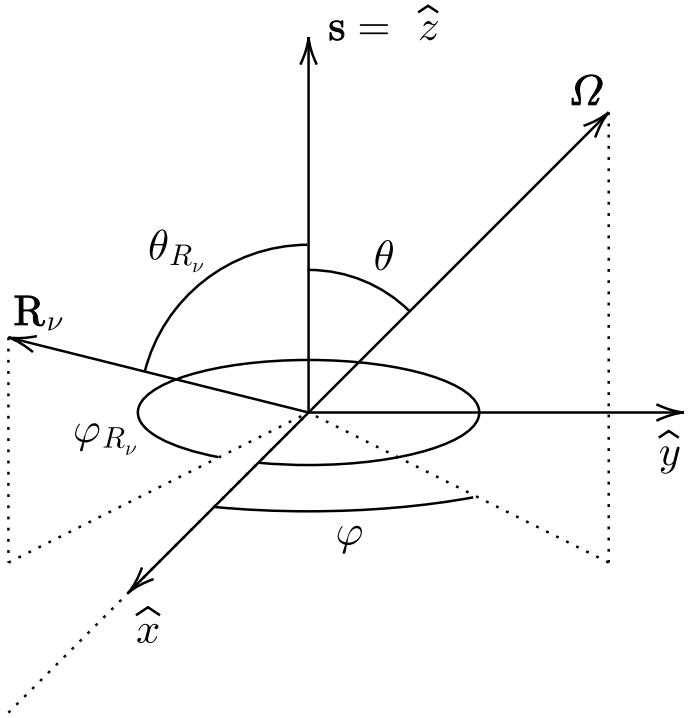

Figure 2.2 – The vector $\boldsymbol{R}_\nu$ and $\boldsymbol{\Omega}$ at a point on the boundary.

2.2.1 Marshark-type boundary condition

We want to write Eq. (2.26) at the boundary of the domain $\boldsymbol{r}_s$ with the Marshak weight (dropping the t and $\boldsymbol{r}_s$ variables for simplicity),

$$J_\nu \int\limits_{\boldsymbol{s}.\boldsymbol{\Omega}\leq 0} \boldsymbol{s}.\boldsymbol{\Omega}\, \psi_\nu\left(\boldsymbol{\Omega}\right)\, \mathrm{d}\boldsymbol{\Omega} = \int\limits_{\boldsymbol{s}.\boldsymbol{\Omega}\leq 0} \boldsymbol{s}.\boldsymbol{\Omega}\, \Gamma\left(\boldsymbol{\Omega}\right)\, \mathrm{d}\boldsymbol{\Omega}. \tag{2.28}$$

We used the form Eq. (2.3) for the specific intensity I_ν and the normalised intensity ψ_ν is given by Eq. (2.19). To put the boundary condition in the desired form Eq. (2.27), we need to compute the left-hand side of Eq. (2.28). The vector $\boldsymbol{R}_\nu$ makes an angle θ_{R_ν} ($\mu_{R_\nu} = \cos\theta_{R_\nu}$) with $\boldsymbol{s}$ and φ_{R_ν} with an arbitrary oriented axe $\hat{x}$ (see Fig. 2.2). To perform the integration, we align the z axis with $\boldsymbol{s}$. The left-hand side of Eq. (2.28) is

$$\frac{J_\nu}{R_\nu} \int_0^{2\pi} \mathrm{d}\varphi \int_{-1}^{0} \frac{\mu\, \mathrm{d}\mu}{\coth R_\nu - \left[\mu\,\mu_{R_\nu} + \left(1-\mu_{R_\nu}^2\right)^{\frac{1}{2}} \left(1-\mu^2\right)^{\frac{1}{2}} \left(\cos\varphi_{R_\nu}\, \cos\varphi + \sin\varphi_{R_\nu}\, \sin\varphi\right)\right]}. \tag{2.29}$$

or, in the factorised form,

$$\frac{J_\nu}{R_\nu} \int_{-1}^{0} \frac{\mu\, \mathrm{d}\mu}{\coth R_\nu - \mu\,\mu_{R_\nu}} \int_0^{2\pi} \frac{\mathrm{d}\varphi}{1 - \frac{\left(1-\mu_{R_\nu}^2\right)^{\frac{1}{2}} \left(1-\mu^2\right)^{\frac{1}{2}} \left(\cos\varphi_{R_\nu}\, \cos\varphi + \sin\varphi_{R_\nu}\, \sin\varphi\right)}{\coth R_\nu - \mu\,\mu_{R_\nu}}}. \tag{2.30}$$

The integral on φ is analytic [2] and Eq. (2.30) is simplified as

$$\begin{aligned} &\frac{2\pi J_\nu}{R_\nu} \int_{-1}^{0} \frac{\mu\, \mathrm{d}\mu}{\left[\left(\coth R_\nu - \mu\,\mu_{R_\nu}\right)^2 - \left(1-\mu_{R_\nu}^2\right)\left(1-\mu^2\right)\right]^{1/2}}, \\ &= \frac{2\pi J_\nu}{R_\nu \tanh R_\nu} \int_{-\tanh R_\nu}^{0} \frac{x\, \mathrm{d}x}{\left[x^2 - 2\,\mu_{R_\nu}\, x + 1 - \tanh^2 R_\nu \left(1-\mu_{R_\nu}^2\right)\right]^{1/2}}, \end{aligned} \tag{2.31}$$

with the variable change $x = \mu \tanh R_\nu$. Again, the integral on x can be performed exactly [3] and yields,

$$\begin{aligned} = -\frac{2\pi\, J_\nu}{R_\nu\, \tanh R_\nu} \Bigg[&\mu_{R_\nu}\left(R_\nu - \tanh R_\nu\right) + 1 - \sqrt{1 - \left(1-\mu_{R_\nu}^2\right)\tanh^2 R_\nu} \\ &+ \mu_{R_\nu} \ln\left(\frac{1-\mu_{R_\nu}}{\cosh R_\nu \left(\sqrt{1 - \left(1-\mu_{R_\nu}^2\right)\tanh^2 R_\nu} - \mu_{R_\nu}\right)} \right) \Bigg]. \end{aligned} \tag{2.32}$$

1. that depend on J_ν and its gradient.
2. $\int\limits_0^{2\pi} \frac{\mathrm{d}\varphi}{1-(a\cos\varphi + b\sin\varphi)} = \frac{2\pi}{(1-a^2+b^2)^{1/2}} \qquad \forall\, a, b \,|\, a^2+b^2 < 1.$
3. $\int \frac{x\, \mathrm{d}x}{\left(x^2+ax+b\right)^{\frac{1}{2}}} = \left(x^2+ax+b\right)^{\frac{1}{2}} - \frac{a}{2}\ln\left(\left|a+2x+2\left(x^2+ax+b\right)^{\frac{1}{2}}\right|\right)$

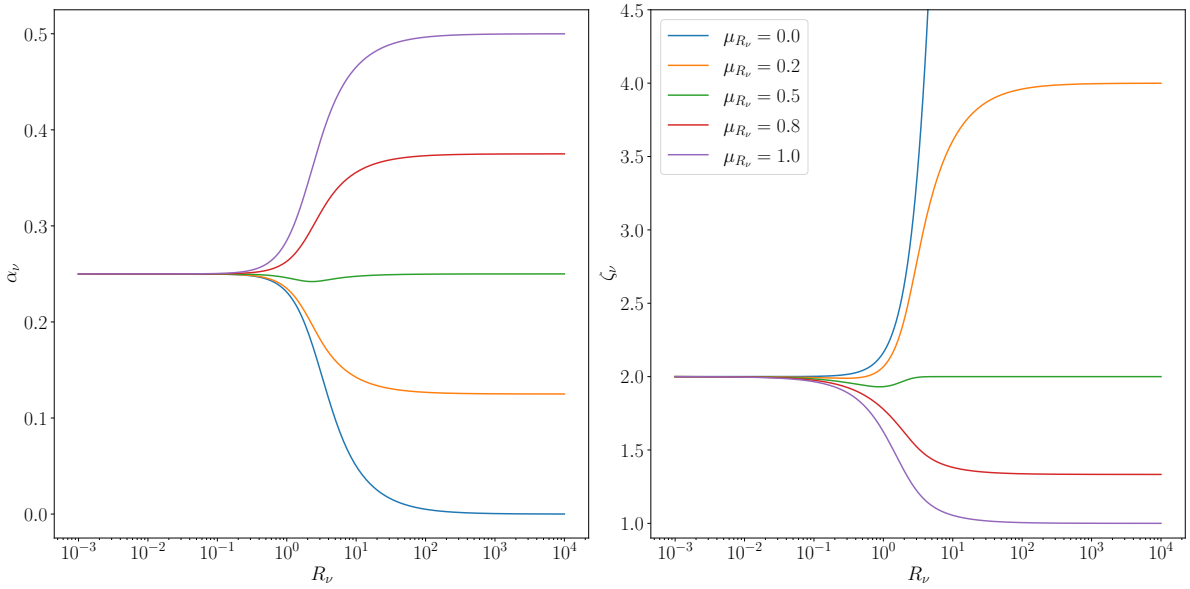

Figure 2.3 – The function α_ν Eq. (2.33) and ζ_ν Eq. (2.40) (left and right, respectively) versus R_ν, for several values of $\mu_{R_\nu} = \boldsymbol{s}.\boldsymbol{R}_\nu/R_\nu$. In the optically-thick regime ($R_\nu \ll 1$), $\alpha_\nu \to 1/4$ and $\zeta_\nu \to 2$, while in the optically-thin case ($R_\nu \gg 1$), $\alpha_\nu \to |\mu_{R_\nu}|/2$ and $\zeta_\nu \to 1/\mu_{R_\nu}$. Note that for $\mu_{R_\nu} = 0$, the function ζ_ν diverges.

To obtain a non-linear mixed boundary condition in the form of Eq. (2.27), we note that $\boldsymbol{s}.\boldsymbol{H}_\nu = \boldsymbol{s}.R_\nu\,\lambda_\nu\,J_\nu = \mu_{R_\nu}\,R_\nu\,\lambda_\nu\,J_\nu$ with λ_ν given by Eq. (2.18). We finally rewrite Eq. (2.28)

$$\alpha_\nu J_\nu - \frac{1}{2}\boldsymbol{s}.\boldsymbol{H}_\nu = H_\nu^{\rm inc}$$

$$\text{with} \quad H_\nu^{\rm inc} = \frac{1}{4\pi}\int\limits_{\boldsymbol{s}.\boldsymbol{\Omega}\leq 0} |\boldsymbol{s}.\boldsymbol{\Omega}|\;\Gamma\left(\boldsymbol{\Omega}\right)\;\mathrm{d}\boldsymbol{\Omega}$$

$$\text{and} \quad \alpha_\nu = \frac{1-\sqrt{1-\left(1-\mu_{R_\nu}^2\right)\tanh^2 R_\nu}+\mu_{R_\nu}\ln\left(\dfrac{1-\mu_{R_\nu}}{\cosh R_\nu\left(\sqrt{1-\left(1-\mu_{R_\nu}^2\right)\tanh^2 R_\nu}-\mu_{R_\nu}\right)}\right)}{2\,R_\nu\,\tanh R_\nu}. \tag{2.33}$$

The coefficient α_ν is an even function of μ_{R_ν}. In the optically-thick regime ($R_\nu \ll 1$), $\alpha_\nu \to 1/4$ and it corresponds to the classical Marshak boundary condition for the Eddington approximation (see Pomraning, 1973, III-2). In the optically-thin regime ($R_\nu \gg 1$), $\alpha_\nu \to |\mu_{R_\nu}|/2$. A representation of α_ν is given in Fig. 2.3-left, for several values of μ_{R_ν}. For practical numerical purposes, Eq. (2.33) can be rewritten in the form of a non-linear mixed boundary condition, using Eq. (2.20),

$$\alpha_\nu\,J_\nu + \frac{1}{2}\,D_\nu\,\boldsymbol{s}.\boldsymbol{\nabla}\,J_\nu = H_\nu^{\rm inc}. \tag{2.34}$$

2.2.2 Vacuum boundary

The vacuum boundary condition corresponds to the case where there is no incident radiation upon the surface ($H_\nu^{\rm inc} = 0$). If we rewrite the Marshak boundary condition we previously derived in Eq. (2.33), using $\boldsymbol{H}_\nu = \boldsymbol{h}_\nu J_\nu$, we obtain

$$\alpha_\nu - \frac{1}{2}\,\boldsymbol{s}.\boldsymbol{h}_\nu = 0 \quad \forall\, J_\nu \neq 0. \tag{2.35}$$

On a vacuum boundary $\boldsymbol{h}_\nu$ is pointing outside the domain, consequently $\boldsymbol{s}.\boldsymbol{h}_\nu = \mu_{R_\nu}|\boldsymbol{h}_\nu|$ with $\mu_{R_\nu} > 0$. The solution of Eq. (2.35) is only achieved in the asymptotic optically-thin limit $R_\nu \to \infty$ ($\alpha_\nu \to \mu_{R_\nu}/2$, $|\boldsymbol{h}_\nu| \to 1$) and corresponds to a sharp-peaked distribution for the specific intensity ($I_\nu \propto \delta(\boldsymbol{\Omega}.\boldsymbol{R}_\nu)$). We see here a flaw of the Marshak boundary condition that gives a non-physical behaviour, since the intensity is not necessarily peaked when $H_\nu^{\rm inc} \to 0$ (*e.g* the intensity at a vacuum boundary of an optically-thick envelope is almost isotropic on the emergent half-sphere).

Another approach is then required to describe the behaviour of the radiation at a vacuum boundary. Inspired by Pomraning (1986), we seek a boundary condition in the form of a closure relation between the mean specific intensity J_ν and the radiative flux $\boldsymbol{H}_\nu$, at the surface boundary

$$J_\nu - \zeta_\nu\, \boldsymbol{s}.\boldsymbol{H}_\nu = 0, \tag{2.36}$$

with ζ_ν, a coefficient to be determined. At a vacuum boundary and without incoming radiation, ζ_ν has to be understood as the ratio of the energy density over the emerging flux,

$$\zeta_\nu = \frac{\int\limits_{4\pi} I_\nu \,\mathrm{d}\boldsymbol{\Omega}}{\int\limits_{4\pi} \boldsymbol{s}.\boldsymbol{\Omega}\, I_\nu \,\mathrm{d}\boldsymbol{\Omega}}. \tag{2.37}$$

This ratio depends on the anisotropy of the emergent radiation field. In the optically-thin limit, the radiation field is sharp-peaked along the direction of $\boldsymbol{R}_\nu$ ($I_\nu \propto \delta(\boldsymbol{\Omega}.\boldsymbol{R}_\nu)$), hence $\zeta_\nu \to 1/\mu_{R_\nu}$. In the diffusion regime, the emergent field is isotropic and $\zeta_\nu \to 2$. In the original study of Levermore and Pomraning (1981), ζ_ν was chosen to be equal to 2, which means that it correctly describes the optically-thick cases where $R_\nu \ll 1$.

In a general case where radiation at different frequencies have different optical behaviours, we need ζ_ν to be a function of R_ν. In the framework of the FLD approximation, $I_\nu = J_\nu\, \psi_\nu$ and we can use this specific angular dependence of I_ν to compute an estimate of ζ_ν,

$$\zeta_\nu = \frac{\int\limits_{\boldsymbol{s}.\boldsymbol{\Omega}\geq 0} \psi_\nu \,\mathrm{d}\boldsymbol{\Omega}}{\int\limits_{\boldsymbol{s}.\boldsymbol{\Omega}\geq 0} \boldsymbol{s}.\boldsymbol{\Omega}\, \psi_\nu \,\mathrm{d}\boldsymbol{\Omega}}. \tag{2.38}$$

We perform the integration with the same convention as in Sect. 2.2.1. The integration on φ is the same and ζ_ν is rewritten

$$\zeta_\nu = \tanh R_\nu \frac{\int\limits_0^{\tanh R_\nu} \frac{\mathrm{d}x}{\left[x^2 - 2\,\mu_{R_\nu}\, x + 1 - \tanh^2 R_\nu \left(1-\mu_{R_\nu}^2\right)\right]^{1/2}}}{\int\limits_0^{\tanh R_\nu} \frac{x\;\mathrm{d}x}{\left[x^2 - 2\,\mu_{R_\nu}\, x + 1 - \tanh^2 R_\nu \left(1-\mu_{R_\nu}^2\right)\right]^{1/2}}}. \tag{2.39}$$

The integral in the numerator is also exact [4] and the integral in the denominator is the same as the one used in Sect. 2.2.1. The coefficient ζ_ν is then, in the FLD formalism,

$$\zeta_\nu = \frac{A_\nu \tanh R_\nu}{1 - \sqrt{1 - \left(1 - \mu_{R_\nu}^2\right) \tanh^2 R_\nu} + \mu_{R_\nu} \left(A_\nu - \tanh R_\nu\right)}$$
$$\text{with} \quad A_\nu = R_\nu + \ln \left(\frac{1 - \mu_{R_\nu}}{\cosh R_\nu \left(\sqrt{1 - \left(1 - \mu_{R_\nu}^2\right) \tanh^2 R_\nu} - \mu_{R_\nu} \right)} \right). \tag{2.40}$$

In the two limits $R_\nu \gg 1$ and $R_\nu \ll 1$, we recover $\zeta_\nu \to 1/\mu_{R_\nu}$ and $\zeta_\nu \to 2$, respectively. A representation of ζ_ν is given in Fig. 2.3-right, for several values of μ_{R_ν}.

In practice, numerical tests revealed that this boundary condition can exhibit oscillations in the solution, for some frequencies. This phenomenon is not fully understood at present the time. We found that this effect can be avoided if we rather use a value of R_ν on the boundary, extrapolated from the values in the interior, which we call R_ν^{e}. For consistency, this same extrapolated value must be used when computing the diffusion coefficient D_ν on the boundary. The vacuum boundary condition Eq. (2.36) can then be rewritten in the following mixed form

$$J_\nu + \zeta_\nu(R_\nu^{\mathrm{e}})\, D_\nu(R_\nu^{\mathrm{e}})\, \boldsymbol{s}.\boldsymbol{\nabla}\, J_\nu = 0, \tag{2.41}$$

where we have used $\boldsymbol{H}_\nu \approx -D_\nu(R_\nu^{\mathrm{e}})\ \boldsymbol{\nabla}\, J_\nu$.

Another approach: the use of a ghost cell

As we will see in the numerical tests, we often make use of ghosts cells when discretising the FLD equation, in order to ease the implementation of the boundary conditions. The physical values within these cells, outside of the physical domain, are constrained to impose the boundary conditions at the edge of the domain. If we can provide by some means an estimate for the value of J_ν at this ghost cell, then the value of J_ν will automatically be constrained on the boundary, by the numerical scheme. Let us consider a point outside of the domain, at the position $\boldsymbol{r}_s + \mathrm{d}r\, \boldsymbol{s}$ where we want to estimate J_ν. In practice, for a spherical convex boundary of radius R_{out} (see Fig. 2.4), we have

$$J_\nu\left(\boldsymbol{r}_s + \mathrm{d}r\, \boldsymbol{s}\right) = \frac{1}{4\pi} \int_0^{2\pi} \mathrm{d}\varphi \int_{\mu_0}^{1} J_\nu(\boldsymbol{r}_s')\, \psi_\nu\left(\boldsymbol{r}_s', \mu', \varphi'\right)\ \mathrm{d}\mu. \tag{2.42}$$

$\mu_0 = \cos\theta_0 = \left(1 - \left(R_{\mathrm{out}}/(R_{\mathrm{out}} + \mathrm{d}r)\right)^2\right)^{\frac{1}{2}}$ is the cosine of the angle under which the boundary is seen at $\boldsymbol{r}_s + \mathrm{d}r\, \boldsymbol{s}$. $(\boldsymbol{r}_s', \boldsymbol{\Omega}')$ are the local coordinates of the point on the boundary, along the ray $\boldsymbol{\Omega}$. The integral in Eq. (2.42) can be obtained exactly, if we assume the envelope to be spherically symmetric. In this case, J_ν is constant on the boundary and ψ_ν only depends on $\mu' = \cos\theta' = \left((\mu^2 - \mu_0^2)/(1 - \mu_0^2)\right)^{\frac{1}{2}}$, the cosine of the

4. $\int \frac{\mathrm{d}x}{\left(x^2 + ax + b\right)^{\frac{1}{2}}} = \ln\left(\left|a + 2x + 2\left(x^2 + ax + b\right)^{\frac{1}{2}}\right|\right)$

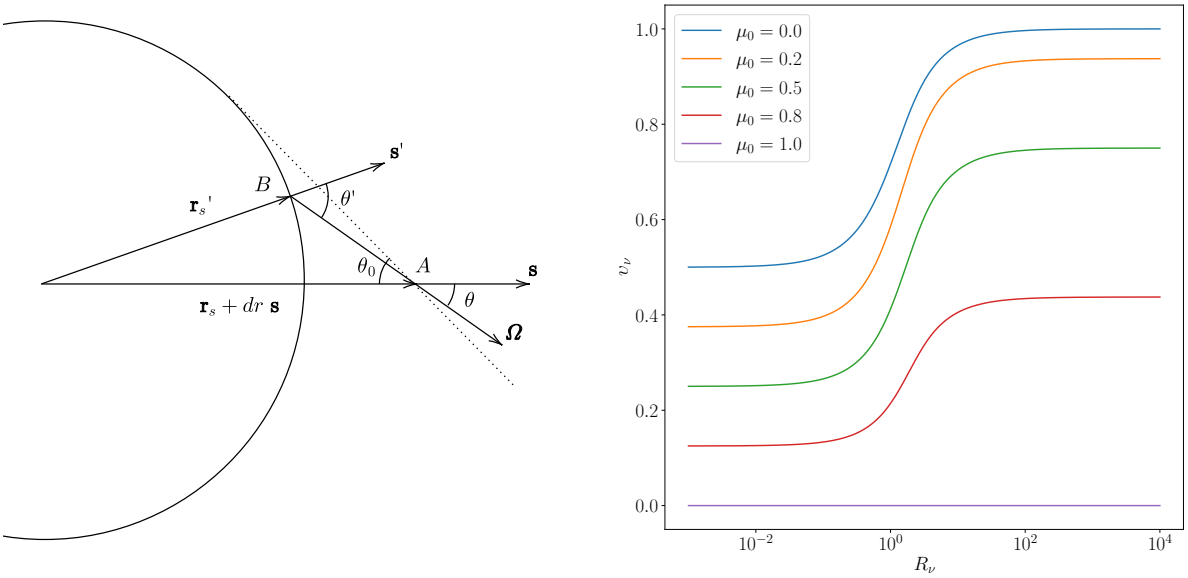

Figure 2.4 – Left: Spherical boundary with a vacuum interface. The intensity, at a given point A, in a direction $\mathbf{\Omega}$, comes directly from the boundary point B. Right: The function υ_ν Eq. (2.48) for different values of μ_0.

angle between $\boldsymbol{s}'$ and $\mathbf{\Omega}$. This assumption gets more and more accurate as $\mathrm{d}r \to 0$ or $\mu_0 \to 0$. The expression is then

$$J_\nu\left(R_{\text{out}} + \mathrm{d}r\right) = \frac{J_\nu(R_{\text{out}})}{2} \int_{\mu_0}^{1} \psi_\nu\left(R_{\text{out}}, \mu'\right)\ \mathrm{d}\mu. \tag{2.43}$$

The integral in Eq. (2.43) is expressed

$$\begin{aligned} \int_{\mu_0}^{1} \psi_\nu\left(R_{\text{out}}, \mu'\right)\ \mathrm{d}\mu &= \frac{\tanh R_\nu}{R_\nu} \int_{\mu_0}^{1} \frac{\mathrm{d}\mu}{1 - \tanh R_\nu \sqrt{\frac{\mu^2 - \mu_0^2}{1 - \mu_0^2}}} \\ &= \frac{\tanh R_\nu \sqrt{1 - \mu_0^2}}{R_\nu} \int_{\mu_0}^{1} \frac{\mathrm{d}\mu}{\sqrt{1 - \mu_0^2} - \tanh R_\nu \sqrt{\mu^2 - \mu_0^2}}. \end{aligned} \tag{2.44}$$

Applying the variable change $x = \mu \tanh R_\nu$ and multiplying the numerator and the denominator by the conjugate of the denominator, yields

$$\int_{\mu_0}^{1} \psi_\nu\left(R_{\text{out}}, \mu'\right)\ \mathrm{d}\mu = \frac{\sqrt{1 - \mu_0^2}}{R_\nu} \int_{\mu_0 \tanh R_\nu}^{\tanh R_\nu} \frac{\sqrt{1 - \mu_0^2} + \sqrt{x^2 - (\mu_0 \tanh R_\nu)^2}}{1 - \mu_0^2\left(1 - \tanh^2 R_\nu\right) - x^2}\ \mathrm{d}x. \tag{2.45}$$

The first term in the integral is

$$\begin{aligned}\int_{\mu_0\,\tanh R_\nu}^{\tanh R_\nu} \frac{\sqrt{1-\mu_0^2}}{1-\mu_0^2\left(1-\tanh^2 R_\nu\right)-x^2}\,\mathrm{d}x &= \sqrt{1-\mu_0^2}\,a_\nu^2 \int_{\mu_0\,\tanh R_\nu}^{\tanh R_\nu} \frac{\mathrm{d}x}{1-(a_\nu\,x)^2} \\ &= \sqrt{1-\mu_0^2}\,a_\nu\left(\operatorname{arctanh}\left(a_\nu\,\tanh R_\nu\right)-\operatorname{arctanh}\left(a_\nu\,\mu_0\,\tanh R_\nu\right)\right), \\ &\text{with}\quad a_\nu = \frac{1}{\sqrt{1-\mu_0^2\left(1-\tanh^2 R_\nu\right)}}.\end{aligned} \tag{2.46}$$

The second term is

$$\begin{aligned}&\int_{\mu_0\,\tanh R_\nu}^{\tanh R_\nu} \frac{\sqrt{x^2-(\mu_0\,\tanh R_\nu)^2}}{1-\mu_0^2\left(1-\tanh^2 R_\nu\right)-x^2}\,\mathrm{d}x \\ &= \sqrt{1-\mu_0^2}\frac{\operatorname{arctanh}\left(b_\nu\right)}{b_\nu} - \operatorname{arctanh}\left(\sqrt{1-\mu_0^2}\right) \text{with}\quad b_\nu = \sqrt{1-\left(\frac{\mu_0}{\cosh R_\nu}\right)^2}.\end{aligned} \tag{2.47}$$

Finally, Eq. (2.43) can be written as,

$$\begin{aligned}J_\nu\left(R_{\text{out}}+\mathrm{d}r\right) &= \upsilon_\nu\, J_\nu(R_{\text{out}}) \\ \text{with}\quad \upsilon_\nu = \frac{\sqrt{1-\mu_0^2}}{2\,R_\nu}&\left(a_\nu\sqrt{1-\mu_0^2}\operatorname{arctanh}\left(\frac{a_\nu\,\tanh R_\nu(1-\mu_0^2)}{1-a_\nu^2\,\tanh^2 R_\nu\,\mu_0}\right)\right. \\ &\left.-\operatorname{arctanh}\left(\sqrt{1-\mu_0^2}\right)+\sqrt{1-\mu_0^2}\frac{\operatorname{arctanh}(b_\nu)}{b_\nu}\right).\end{aligned} \tag{2.48}$$

A representation of the υ_ν function is shown in Fig. 2.4. If the outer boundary is optically-thick ($R_\nu \ll 1$), we have $\upsilon_\nu = (1-\mu_0)/2$, or equivalently

$$J_\nu\left(R_{\text{out}}+\mathrm{d}r\right) = \frac{J_\nu(R_{\text{out}})}{2}\left(1-\sqrt{1-\left(\frac{R_{\text{out}}}{R_{\text{out}}+\mathrm{d}r}\right)^2}\right), \tag{2.49}$$

which corresponds to the expected dilution of the radiation field in vacuum, emitted by an isotropic spherically-symmetric source. When the boundary is optically-thin ($R_\nu \gg 1$), we have $\upsilon_\nu = (1-\mu_0^2)$ or equivalently

$$J_\nu\left(R_{\text{out}}+\mathrm{d}r\right) = J_\nu(R_{\text{out}})\left(\frac{R_{\text{out}}}{R_{\text{out}}+\mathrm{d}r}\right)^2, \tag{2.50}$$

which corresponds to the optically-thin FLD solution $r^2 J_\nu = \text{constant}$.

2.3 Flux-limited diffusion in spherically-symmetric circumstellar envelopes

We now want to use the FLD approximation together with the boundary conditions we derived to solve the problem we described in Sect. 1.2.3. In this section, we consider the

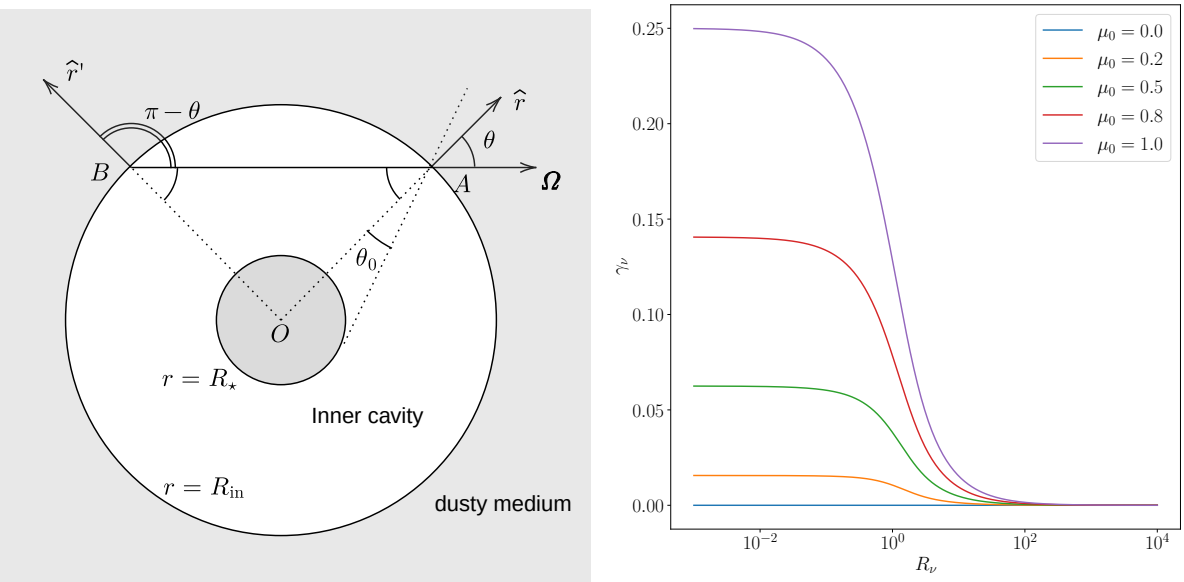

Figure 2.5 – Left: Spherical inner cavity or radius $R_{\rm in}$ enclosing a star of radius $R_\star$. B is the opposite point of A on the cavity, along the $\boldsymbol{\Omega}$ direction. Right: The γ_ν Eq. (2.56) function for several values of μ_0. For optically-thick envelopes ($R_\nu \ll 1$), $\gamma_\nu \to \mu_0^2/4$ while for optically-thin envelopes ($R_\nu \gg 1$), $\gamma_\nu \to 0$.

simplified case of a spherically-symmetric envelope. We assume the opacities $\kappa_\nu^{\rm ext}$, $\kappa_\nu^{\rm abs}$ and $\kappa_\nu^{\rm sca}$ to only depend on the radial variable r. We note that for the radiative transfer problem to be completely spherically-symmetric, both the opacities and the boundary conditions (or stellar sources) have to be independent of the angle φ. In such cases, the specific intensity I_ν only depends on the radius r and the cosine angle μ. Consequently, the mean intensity J_ν only depends on the radial coordinate r. By symmetry, the radiative flux $\boldsymbol{H}_\nu$ is aligned along the radial direction $\hat{r}$ and we expect the angular dependence of I_ν to be well-reproduced by ψ_ν expressed as Eq. (2.19). In contrast to Sect. 1.2.3, the stellar and envelope specific intensities $I_\nu^\star$ and $I_\nu^{\rm env}$ have the same spherical symmetry and we do not decouple the radiation field according Eq. (1.67). In doing so, this allows us to treat, in a simple way, the star as an extended source from which we will include its flux in the boundary conditions.

With all the previous assumptions, the radiative transfer problem is described by the time-independent, one-dimensional FLD equation (see Eq. 2.23),

$$-\frac{1}{r^2}\partial_r\left(r^2\, D_\nu\, \partial_r J_\nu\right) + \kappa_\nu^{\rm abs}\, J_\nu = \kappa_\nu^{\rm abs}\, B_\nu\left(T\right). \tag{2.51}$$

2.3.1 Boundary condition on a spherical inner cavity enclosing a star

We want to specify the boundary condition we derived Eq. (2.34) at an inner spherical cavity located at a distance $R_{\rm in}$ ($\boldsymbol{r}_s = R_{\rm in}\,\hat{r}$) from the centre of a star of radius $R_\star$ and surface temperature $T_\star$. Given the spherical symmetry, the vector $\boldsymbol{R}_\nu$ is aligned along the radial direction $\boldsymbol{s} = -\hat{r}$ which corresponds to the case $|\mu_{R_\nu}| = 1$. The α_ν coefficient,

defined in Eq. (2.33), is rewritten

$$\alpha_\nu \left(|\mu_{R_\nu}| = 1\right) = \frac{\ln\left(\cosh R_\nu\right)}{2\, R_\nu\, \tanh R_\nu}. \tag{2.52}$$

Then, we need to specify the incident flux upon the surface $H_\nu^{\rm inc}$. It is made of two contributions,

$$H_\nu^{\rm inc} = \frac{1}{4\pi} \int\limits_{\boldsymbol{s}.\boldsymbol{\Omega}\leq 0} |\boldsymbol{s}.\boldsymbol{\Omega}| \left(B_\nu\left(T_\star\right) + I_\nu\left(\boldsymbol{r}'_s, \boldsymbol{\Omega}'\right)\right)\, {\rm d}\boldsymbol{\Omega}. \tag{2.53}$$

The first contribution comes from the star and the other from the self-heating of the inner cavity and is expressed as $I_\nu\left(\boldsymbol{r}'_s, \boldsymbol{\Omega}'\right) = J_\nu\left(\boldsymbol{r}'_s\right)\, \psi_\nu\left(\boldsymbol{r}'_s, \boldsymbol{\Omega}'\right)$ in the FLD approximation. As shown in Fig. 2.5-left, the vector $\boldsymbol{r}'_s = R_{\rm in}\, \hat{r}'$ corresponds to the opposite point on the inner cavity (***OB*** on the figure). Because of this dependence, this boundary condition is no longer local and cannot be expressed in a closed form, except in the spherical symmetry where $J_\nu(\boldsymbol{r}'_s) = J_\nu(\boldsymbol{r}_s)$ and $\psi_\nu(\boldsymbol{r}'_s, \boldsymbol{\Omega}') = \psi_\nu(\boldsymbol{r}'_s, \mu') = \psi_\nu(\boldsymbol{r}_s, -\mu)$. To perform the angular integration in Eq. (2.53), we align the z axis with the unitary vector $\hat{r}$. For the star, the integration on $\mu = \cos(\theta)$ (θ being the angle between n_z and $\boldsymbol{\Omega}$) spans from $\mu_0 = \cos\theta_0 = \left(1 - \left(R_\star/R_{\rm in}\right)^2\right)^{1/2}$ to 1, and for the inner cavity, it spans from 0 to μ_0 (see Fig. 2.5-left),

$$H_\nu^{\rm inc} = \frac{1}{2}\left(\int\limits_{\mu_0}^{1} \mu\, B_\nu(T_\star)\, {\rm d}\mu + J_\nu(R_{\rm in}) \int\limits_{0}^{\mu_0} \mu\, \psi_\nu\left(R_{\rm in}, -\mu\right)\, {\rm d}\mu\right). \tag{2.54}$$

The incident flux $H_\nu^{\rm inc}$ is then expressed as,

$$H_\nu^{\rm inc} = \frac{1}{4}\, B_\nu(T_\star) \left(\frac{R_\star}{R_{\rm in}}\right)^2 + \gamma_\nu\, J_\nu\left(R_{\rm in}\right), \tag{2.55}$$

with,

$$\begin{aligned} \gamma_\nu = \frac{1}{2}\int\limits_0^{\mu_0} \mu\, \psi_\nu\left(R_{\rm in}, -\mu\right)\, {\rm d}\mu &= \frac{1}{2\, R_\nu\, \tanh R_\nu} \int\limits_0^{\mu_0\, \tanh R_\nu} \frac{x}{1-x}\, {\rm d}x \\ &= \frac{\mu_0\, \tanh R_\nu - \ln\left(1 + \mu_0\, \tanh R_\nu\right)}{2\, R_\nu\, \tanh R_\nu}. \end{aligned} \tag{2.56}$$

A representation of γ_ν is shown in Fig. (2.5)-right. For optically-thick envelopes ($R_\nu \ll 1$), $\gamma_\nu \to \mu_0^2/4$ while $\gamma_\nu \to 0$ as $R_\nu \to \infty$, as expected. The boundary condition for the FLD equation Eq. (2.34) in the case of an inner spherical cavity enclosing a star is,

$$\left(\alpha_\nu - \gamma_\nu\right)\, J_\nu\left(R_{\rm in}\right) - \frac{D_\nu}{2}\, \partial_r J_\nu|_{r=R_{\rm in}} = \frac{1}{4}\, B_\nu(T_\star) \left(\frac{R_\star}{R_{\rm in}}\right)^2, \tag{2.57}$$

with α_ν as defined in Eq. (2.52). In the optically-thin limit ($R_\nu \gg 1$, $\kappa_\nu^{\rm abs} \to 0$), the FLD Eq. (2.51) and the boundary condition Eq. (2.57) reduce to

$$r^2 J_\nu = {\rm const} = R_{\rm in}^2\, J_\nu\left(R_{\rm in}\right) \quad \text{and} \quad J_\nu\left(R_{\rm in}\right) = \frac{1}{4}\, B_\nu(T_\star) \left(\frac{R_\star}{R_{\rm in}}\right)^2, \tag{2.58}$$

respectively. The solution of the FLD equation in this limit is then

$$J_\nu = \frac{1}{4}\, B_\nu(T_\star) \left(\frac{R_\star}{r}\right)^2 . \tag{2.59}$$

We can compare Eq. (2.59) with the known analytical solution of the mean specific intensity in free space

$$J_\nu = \frac{1}{2} \int_{\sqrt{1-\left(\frac{R_\star}{r}\right)^2}}^{1} B_\nu(T_\star)\, \mathrm{d}\mu = \frac{1}{2} B_\nu(T_\star) \left(1 - \sqrt{1 - \left(\frac{R_\star}{r}\right)^2}\right) . \tag{2.60}$$

Both equations agree when $(R_\star/r)^2 \ll 1$. The relative difference in temperature ($T = (\pi \int J_\nu \, \mathrm{d}\nu/\sigma)^{1/4}$) between Eq. (2.60) and the FLD solution Eq. (2.59) is ≈ 15 % at the star surface, 1 % at $r \approx 2.5\ R_\star$. For $r \geq 10\ R_\star$ (such as the test cases presented in Sect. 2.3.6), this difference becomes negligible (≤ 0.06 %). Note that this difference is due to the FLD solution in the optically-thin limit Eq. (2.58) and not the boundary condition itself.

2.3.2 Vacuum boundary on the outer edge of the envelope

We directly use the boundary condition Eq. (2.41) we derived, where $\boldsymbol{s} = \hat{r}$. The coefficient ζ_ν is written, in spherical symmetry

$$\zeta_\nu(\mu_{R_\nu} = 1) = \frac{\frac{1}{2} + \alpha_\nu \tanh(R_\nu)}{\alpha_\nu + \frac{1}{2}\lambda_\nu R_\nu}, \tag{2.61}$$

with α_ν defined in Eq. (2.52). The boundary condition at the vacuum outer shell of the envelope is then

$$J_\nu(R_{\rm out}) + \zeta_\nu(R_\nu^{\rm e})\, D_\nu(R_\nu^{\rm e})\, \partial_r J_\nu|_{r=R_{\rm out}} = 0, \tag{2.62}$$

with $R_\nu^{\rm e}$, an extrapolated value of R_ν, estimated from the interior values of R_ν.

2.3.3 Approximation of the emergent flux

Additionally, we need to estimate the radiative flux $H_\nu^{\rm out}$ that emerges at a given point on the outer shell $r = R_{\rm out}$. Formally, at a vacuum boundary with no incident flux, it is

$$H_\nu^{\rm out} = \hat{r}.\boldsymbol{H}_\nu = \frac{1}{4\pi} \int_{4\pi} \boldsymbol{\Omega}.\hat{r}\, I_\nu(R_{\rm out}, \mu)\, \mathrm{d}\boldsymbol{\Omega} = \frac{1}{2} \int_0^1 \mu\, I_\nu(R_{\rm out}, \mu)\, \mathrm{d}\mu \tag{2.63}$$

We note that in the exact problem, the net flux H_ν (integrated over all directions) is equal to the emerging flux $H_\nu^{\rm out}$, as $I_\nu = 0, \forall\, \mu < 0$. However, the FLD approximation cannot reproduce this angular dependence for the specific intensity since it is constrained by the shape of the normalised intensity ψ_ν. Hence at a vacuum boundary, the net flux is not equal to the emerging flux, in the FLD approximation. Since it is the net flux that

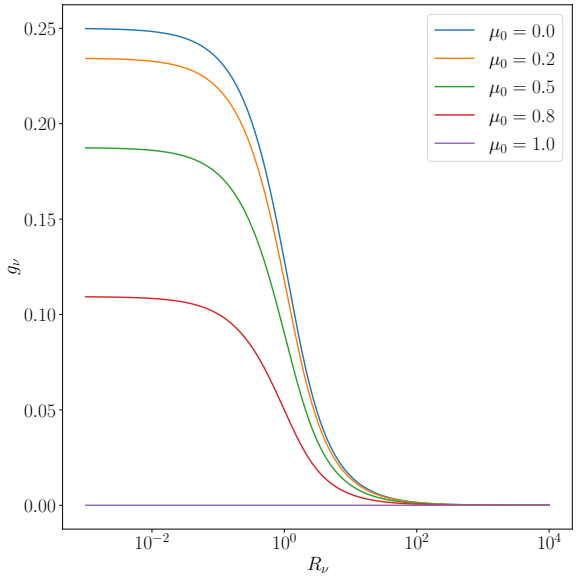

Figure 2.6 – The function g_ν Eq. (2.67) for several values of μ_0.

is conserved ($\boldsymbol{\nabla}.\boldsymbol{H} = 0$), we use the FLD expression for $\boldsymbol{H}_\nu$ Eq. (2.20) to compute the emerging flux,

$$H_\nu^{\rm out} \approx \hat{r}.\boldsymbol{H}_\nu(R_{\rm out}) = -D_\nu\left(R_\nu\right)\ \partial_r J_\nu|_{r=R_{\rm out}}\ . \tag{2.64}$$

In order to be consistent with the vacuum boundary condition Eq. (2.62), we use an extrapolation value to compute the non-linear diffusion coefficient D_ν,

$$H_\nu^{\rm out} = -D_\nu\left(R_\nu^{\rm e}\right)\ \partial_r J_\nu|_{r=R_{\rm out}}\,. \tag{2.65}$$

We note that with this approximation, the emerging flux $H_\nu^{\rm out}$ is a direct result of the FLD solution, hence no further computations are needed to obtain it (such as ray-tracing calculations).

2.3.4 Radiative equilibrium and warming of the stellar surface

In all of our calculations, we assume radiative equilibrium from the stellar surface up to the outer radius of the circumstellar envelope. Let us consider the effective temperature at the stellar surface; the effective temperature $T_{\rm eff}$ is, by definition, related to the net flux $\boldsymbol{H}$ via the relation $|\boldsymbol{H}| = \sigma\, T_{\rm eff}^4/(4\pi)$. However, under the black body assumption, the stellar temperature is linked to the emerging flux from the stellar surface $H_\star^{\rm out}$,

$$H_\star^{\rm out} = \int_0^\infty \left(\frac{1}{2}\int_0^1 \mu\, B_\nu(T_\star)\ {\rm d}\mu\right)\ {\rm d}\nu = \frac{\sigma}{4\pi}T_\star^4. \tag{2.66}$$

We usually make the assumption that $T_{\rm eff} = T_\star$ occurs if we can neglect the radiation from the envelope that falls back onto the star (*e.g* if the star is a point source and/or if the envelope is optically-thin). The radiative flux, at $r = R_{\rm in}$, that falls back from the

inner cavity onto the star (grey disc in Fig. 2.5) is

$$
\begin{aligned}
H_\nu^{\rm fall}(r=R_{\rm in}) &= \frac{1}{4\pi}\int\limits_{\hat{r}.\boldsymbol{\Omega}\leq 0} \hat{r}.\boldsymbol{\Omega}\, I_\nu(R_{\rm in},\boldsymbol{\Omega})\ {\rm d}\boldsymbol{\Omega} \\
&= \frac{1}{2}J_\nu(R_{\rm in})\int\limits_{-1}^{-\mu_0} \mu\,\psi_\nu\,(R_{\rm in},\mu)\ \ {\rm d}\mu = -g_\nu\, J_\nu(R_{\rm in}), \\
\text{with}\quad g_\nu &= \frac{(1-\mu_0)\tanh R_\nu + \ln\left(\frac{1+\mu_0\,\tanh R_\nu}{1+\tanh R_\nu}\right)}{2\,R_\nu\,\tanh R_\nu},
\end{aligned}
\tag{2.67}
$$

R_ν being evaluated at $r = R_{\rm in}$ and μ_0 as defined in Sect. 2.3.1. A representation of g_ν is displayed in Fig. 2.6. When the envelope becomes optically-thick ($R_\nu \ll 1$), $g_\nu \to (1-\mu_0)^2/4$ while $g_\nu \to 0$ when the envelope is thin ($R_\nu \gg 1$). We note that $H_\nu^{\rm fall} < 0$ since the flux is an algebraic quantity. The net flux at the stellar surface is then,

$$
\begin{aligned}
|\boldsymbol{H}|(r=R_\star) &= H_\star^{\rm out} + \left(\frac{R_{\rm in}}{R_\star}\right)^2 \int\limits_0^\infty H_\nu^{\rm fall}\ {\rm d}\nu \\
\text{or equivalently,}\quad T_{\rm eff}^4 &= T_\star^4 + \frac{4\pi}{\sigma}\left(\frac{R_{\rm in}}{R_\star}\right)^2 \int\limits_0^\infty H_\nu^{\rm fall}\ {\rm d}\nu
\end{aligned}
\tag{2.68}
$$

In numerical simulations, we impose $T_{\rm eff}$ and the stellar temperature $T_\star$ can be updated accordingly with the help of Eq. (2.68). In the optically-thin case ($R_\nu \gg 1$) and/or point-source approximation ($\mu_0 \to 1$), Eq. (2.68) reduces to $T_{\rm eff} = T_\star$, as expected.

2.3.5 Numerical implementation

The solution of the complete problem involves the resolution of the FLD equation Eq. (2.51), for each frequency, supplemented with the boundary conditions Eqs. (2.57) and (2.62), coupled with the equation for radiation equilibrium Eq. (1.66) and the equation for updating the stellar temperature Eq. (2.68). This set of equations is discretised on a computational grid and solved using an iterative method.

Discretisation of the equations

We discretise and sample logarithmically the frequency domain into n_ν points, denoted by the subscript k. The radial coordinate r is partitioned into n_x cells and denoted by the subscript i. We use one ghost cell at each boundary to ease the implementation of the boundary conditions. The quantities that are scalars (e.g J_ν) are computed at the cell centres (integer indexes) while the vectors (e.g $\boldsymbol{H}_\nu$) are estimated on the cell walls (half-integer indexes). The set of equations is solved with respect to a new variable $x = f(r)$ on a regular grid of constant step $\Delta x = (x(R_{\rm out}) - x(R_{\rm in}))\,/\,(n_x - 2)$ to allow r to be non-uniformly (logaritmically most of the time) sampled. An illustration of the computational grid used is shown in Fig. 2.7. The differential operators appearing in the

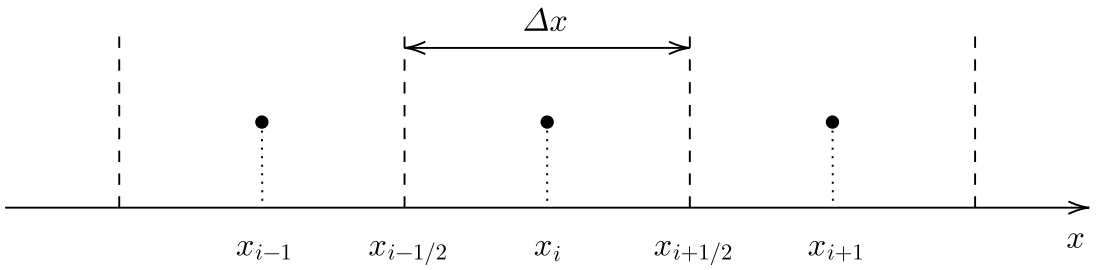

Figure 2.7 – The one-dimensional uniform grid used. The dashed lines correspond the the cell edges while the cell centres are denotes by the dots. Note that the inner radius $R_{\rm in}$ corresponds to the coordinate $x_{1/2}$ while the outer radius $R_{\rm out}$ corresponds to $x_{n_x-3/2}$.

equations are approximated with a second-order finite difference operator

$$\partial_r f|_{r=r_i} = \left.\frac{\mathrm{d}x}{\mathrm{d}r}\right|_{x=x_i} \partial_x f|_{x=x_i} \approx \left.\frac{\mathrm{d}x}{\mathrm{d}r}\right|_{x=x_i} \frac{f(x_{i+1}) - f(x_{i-1})}{2\Delta x} + O(\Delta x^2). \tag{2.69}$$

where f is any function for which we want to estimate its derivative. Accordingly, the FLD Eq. (2.51) is approximated by the following system of non-linear equations (omitting the frequency dependence for simplicity)

$$\begin{aligned} -a_{i+\frac{1}{2}}\, J_{i+1} + a_i\, J_i - a_{i-\frac{1}{2}}\, J_{i-1} &= b_i\, B(T_i), \\ \text{with} \quad a_{i\pm\frac{1}{2}} &= \left.\frac{\mathrm{d}x}{\mathrm{d}r}\right|_{x_{i\pm\frac{1}{2}}} r^2_{i\pm\frac{1}{2}}\, D_{i\pm\frac{1}{2}}, \\ b_i &= \Delta x^2 \left(\left.\frac{\mathrm{d}x}{\mathrm{d}r}\right|_{x_i}\right)^{-1} r_i^2\, \kappa_i^{\rm abs}, \\ a_i &= a_{i+\frac{1}{2}} + b_i + a_{i-\frac{1}{2}}. \end{aligned} \tag{2.70}$$

The non-linearity of Eq. (2.70) arises both from the expression of the coefficients $a_{i\pm1/2}$ and b_i. They implicitly depend on J_ν, through the diffusion coefficient D_ν and the radiative equilibrium Eq. (1.66), respectively. The non-linear coefficients, present in all our equations, require an estimation of J_ν and its gradient (see Eqs. 2.20 and 2.11) at the cell walls. We use the following second-order approximation,

$$J_{k,i+\frac{1}{2}} \approx \frac{1}{2}\left(J_{k,i+1} + J_{k,i}\right), \quad \partial_r J_\nu|_{k,i+\frac{1}{2}} \approx \left.\frac{dx}{\mathrm{d}r}\right|_{i+\frac{1}{2}} \frac{J_{k,i+1} - J_{k,i}}{\Delta x} \quad . \tag{2.71}$$

For the boundary conditions, we use two ghosts cells (one at each boundary of the domain) in order to simplify their implementation. In doing so, Eq. (2.57) is imposed at the wall between the first ($i = 0$) and second cell ($i = 1$), and between the last ($i = n_x - 1$) and

penultimate cell ($i = n_x - 2$) for Eq. (2.62). The value of J_ν in the ghost cell at the inner cavity is

$$J_0 = \frac{\frac{1}{2}\,B(T_\star)\left(\frac{R_\star}{R_{\rm in}}\right)^2 - \left(\alpha - \gamma - \frac{D_{\frac{1}{2}}}{\Delta x}\frac{\mathrm{d}x}{\mathrm{d}r}|_{x_{\frac{1}{2}}}\right) J_1}{\alpha - \gamma + \frac{D_{\frac{1}{2}}}{\Delta x}\frac{\mathrm{d}x}{\mathrm{d}r}|_{x_{\frac{1}{2}}}} \qquad \text{and} \quad J_{n_x-1} = \frac{\zeta(R^{\rm e})\frac{D(R^{\rm e})}{\Delta x}\frac{\mathrm{d}x}{\mathrm{d}r}|_{x_{n_x-\frac{3}{2}}} - \frac{1}{2}}{\zeta(R^{\rm e})\frac{D(R^{\rm e})}{\Delta x}\frac{\mathrm{d}x}{\mathrm{d}r}|_{x_{n_x-\frac{3}{2}}} + \frac{1}{2}} J_{n_x-2} \tag{2.72}$$

with α and γ defined by Eqs. (2.52) and (2.56) and evaluated at the boundaries of the domain. For the extrapolated value $R^{\rm e}$ used in $\zeta(R^{\rm e})$ and $D(R^{\rm e})$, we use a second-order Lagrange extrapolation,

$$R^{\rm e} = 3\left(R_{n_x-\frac{5}{2}} - R_{n_x-\frac{7}{2}}\right) + R_{n_x-\frac{9}{2}}\ . \tag{2.73}$$

For the discretisation of the radiative equilibrium Eq. (1.66), we replace the frequency integration by a quadrature formula with the associated weights W_k,

$$\sum_{k=0}^{n_\nu-1} W_k\,\kappa^{\rm abs}_{k,i}\,J_{k,i} = \sum_{k=0}^{n_\nu-1} W_k\,\kappa^{\rm abs}_{k,i}\,B_k(T). \tag{2.74}$$

For the quadrature weights, we use a simple trapezoidal rule, on the logarithm of ν. We note that we observed a super-convergence behaviour (Trefethen and Weideman, 2014) when computing the quadrature, hence a limited number of frequency points is needed to accurately impose radiative equilibrium. The right-hand side of Eq. (2.74) is pre-computed and stored in a table, with the help of Eq. (1.7), for a wide range of temperatures, allowing the left-hand side to be linearly interpolated in this table (we use the logarithm of the integral for better accuracy). By doing so, we avoid the use of an iterative method to determine the new temperature.

In the same way, the equation for the update of the stellar temperature Eq. (2.68) is approximated,

$$T_\star = \left(T_{\rm eff}^4 + \frac{4\pi}{\sigma}\left(\frac{R_{\rm in}}{R_\star}\right)^2 \sum_{k=0}^{n_\nu-1} W_k\,g_k\,\frac{J_{k,0}+J_{k,1}}{2}\right)^{\frac{1}{4}}\ . \tag{2.75}$$

with g_k given by Eq. (2.67) and evaluated a $r = R_{\rm in}$.

Iterative method

Several strategies are possible in order to solve the set of discretised equations Eqs. (2.70), (2.72), (2.74), (2.75). The complete solution requires the knowledge of the mean specific intensity at all spatial/frequency points, the temperature at all spatial points and the stellar temperature, hence our solution vector is $\boldsymbol{X} = [J_{0,0}, ..., J_{k,i}, ..., J_{n_\nu-1,n_x-1}, T_0, ..., T_i, ..., T_{n_x-1}, T_\star]$.

The numerical scheme Eq. (2.70) and the boundary conditions Eq. (2.72) can be put into the following matrix form,

$$\mathcal{A}_k(\boldsymbol{J})\boldsymbol{J}_k = \boldsymbol{B}_k\left(\boldsymbol{J}\right). \tag{2.76}$$

$\boldsymbol{J}_k = [J_{k,1}, ..., J_{k,i}, ..., J_{k,n_x-2}]^t$ is the mean specific intensity at all spatial points, at frequency ν_k. $\mathcal{A}^k$ is a tri-diagonal matrix of size $n_x - 2 \times n_x - 2$ coupling the solutions points in $\boldsymbol{J}_k$, and $\boldsymbol{B}_k$ the vector containing the right hand side of Eq. (2.70). We indicated the non-linear dependence of $\mathcal{A}^k$ and $\boldsymbol{B}^k$ with $\boldsymbol{J}$, the mean specific intensity at all spatial/frequency points.

One solution is to start with an initial guess of $\boldsymbol{X}$ and to compute and "freeze" $\mathcal{A}_k$ and $\boldsymbol{B}_k$ for all ν_k. Eq. (2.76) then becomes a linear system and can be solved with a standard direct or iterative method. When the solution is found, we can update $\mathcal{A}_k$ and $\boldsymbol{B}_k$, via Eqs. (2.72), (2.74), (2.75) and start again and solve Eq. (2.76) with the updated coefficients. This procedure shows similarities with the so-called the Λ-iteration in the literature (see e.g Hubeny and Mihalas, 2014), and becomes very slow and does not converge inside optically-thick regions.

Our strategy is to solve Eq. (2.76) with an iterative method while updating $\mathcal{A}_k$ and $\boldsymbol{B}_k$ at each iteration. It proceeds as follows: if we denote by the superscript n, the iteration index of the method, we start with an initial guess of our solution vector X^n $(n = 0)$ and compute the all the non-linear coefficients $\mathcal{A}_k$ and $\boldsymbol{B}_k$. We first update the values of the mean specific intensity, for all frequency ν_k with the help of Eq. (2.70) which we rewrite

$$J^{n+1}_{k,i} = \frac{b_{k,i}\, B_k(T^n_i) + a^n_{k,i+\frac{1}{2}}\, J^n_{k,i+1} + a^n_{k,i-\frac{1}{2}}\, J^{n+1}_{k,i-1}}{a^n_{k,i}}. \tag{2.77}$$

Eq. (2.77) corresponds to a Gauss-Seidel forward sweep (see Appendix B.2 for a short review of the Gauss-Seidel method), starting from $i = 1$ to $i = n_x - 2$. Once the J_ν is updated, we consequently compute the values $J^{n+1}_{k,0}$ and J^{n+1}_{k,n_x-1} inside the ghost cells, with the help of Eq. (2.72). The stellar and dust temperature $T^{n+1}_\star$ and T^{n+1} are then updated via Eqs. (2.74) and (2.75). Finally, we repeat the procedure until the maximal values of relative differences between two consecutive iterates $\max_{k,i}(|J^{n+1}_{k,i} - J^n_{k,i}|/J^n_{k,i})$ falls below a small arbitrary number ϵ.

Initial conditions

Initial conditions for both J_ν and T must be provided in order to solve the problem. As an initial guess, we use the analytic solution of the FLD in the optically-thin limit Eq. (2.24), and we write

$$J^0_{k,i} = \frac{1}{4}\left(\frac{R_\star}{r_i}\right)^2 B_k(T_\star)\ , \tag{2.78}$$

from which we deduce the corresponding temperature profile T^0 with the help of Eq. (2.74).

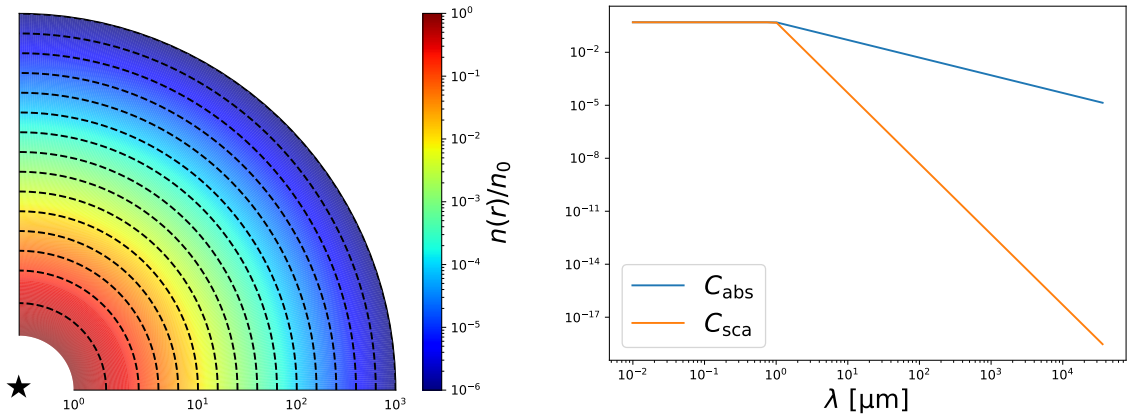

Figure 2.8 – Left: Normalised density structure of the benchmark from Ivezic et al. (1997). The dashed lines represent the iso-density curves. Right: Optical coefficients mimicking the behaviour of spherical dust grains.

2.3.6 Numerical tests

Benchmarks from Ivezic et al. (1997)

We tested the accuracy of our FLD code with our mixed boundary conditions in a realistic case, by comparing it with the 1D benchmark problems realised by Ivezic et al. (1997). We recall the conditions of the test and refer to the original paper for further information.

A point-like star, embedded in a spherically symmetric envelope of matter at radiative equilibrium, irradiates as a black body at the temperature $T_\star = 2\,500$ K. This envelope extends from the inner radius $R_{\rm in}$ to the outer radius $R_{\rm out} = 1\,000\ R_{\rm in}$. The inner radius is set so that the temperature at the inner radius is always $T_{\rm in} = T(R_{\rm in}) = 800$ K. The number density of dust grain $n(r)$ is assumed to be a power law of the form $n(r) = n_0\,(R_{\rm in}/r)^p$ (see Fig. 2.8-left). The radial optical depth τ_ν of the envelope is linked to the density profile by

$$\tau_\nu = \int_{R_{\rm in}}^{R_{\rm out}} \kappa_\nu^{\rm ext}\ {\rm d}r = \int_{R_{\rm in}}^{R_{\rm out}} C_\nu^{\rm ext}\, n(r)\ {\rm d}r, \tag{2.79}$$

where $C_\nu^{\rm ext}$ is the extinction cross-section coefficient. It is defined by

$$\begin{aligned} &C_\nu^{\rm abs} = C_{\nu_0}^{\rm abs}, \quad C_\nu^{\rm sca} = C_{\nu_0}^{\rm sca} && \text{if } \nu \geq \nu_0, \\ &C_\nu^{\rm abs} = C_{\nu_0}^{\rm abs} \left(\frac{\nu}{\nu_0}\right), \quad C_\nu^{\rm sca} = C_{\nu_0}^{\rm sca} \left(\frac{\nu}{\nu_0}\right)^4 && \text{if } \nu \leq \nu_0, \\ &C_\nu^{\rm ext} = C_\nu^{\rm abs} + C_\nu^{\rm sca}, \end{aligned} \tag{2.80}$$

with $C_{\nu_0}^{\rm abs} = (1-\epsilon_{\nu_0})\, C_{\nu_0}^{\rm ext}$ and $C_{\nu_0}^{\rm sca} = \epsilon_{\nu_0}\, C_{\nu_0}^{\rm ext}$. $C_{\nu_0}^{\rm ext} = 1$ is the extinction cross section at ν_0, the frequency corresponding to $\lambda_0 = 1\ \mu$m and ϵ_{ν_0} the albedo at ν_0, set to 1/2 for these tests. The optical data are represented in Fig. 2.8-right. These optical coefficients aims at mimicking the behaviour of spherical dust grains with radius proportional to the transition wavelength λ_0.

τ_{ν_0}	$\epsilon(T)$		$\epsilon\left(\lambda F_\lambda / F\right)$	
	$p=0$	$p=2$	$p=0$	$p=2$
1	0/0/1	0/0/1	1/1/4	1/1/3
10	0/0/1	1/1/3	2/3/14	2/2/10
100	1/0/1	1/1/3	1/1/8	1/2/11
1 000	2/1/4	1/1/4	6/8/30	3/2/9

Table 2.2 – Results from the comparison with DUSTY. Relative differences ϵ (in %) for the temperature profiles $\epsilon(T)$ and for the SEDs $\epsilon\left(\lambda F_\lambda / F\right)$ shown in Fig. 2.9. The results are presented in the form mean(ϵ) / std(ϵ) / max(ϵ) and rounded to the closest percent.

The benchmark problems are thus completely defined by two parameters: (i) the exponent in the density power law $p = 0, 2$, and (ii) the radial optical depth of the envelope at ν_0, $\tau_{\nu_0} = 1, 10, 100,$ and 1 000. This creates eight different cases to test the accuracy of our code. The coefficient n_0 in the density profile is determined with the help of τ_{ν_0} and p,

$$n_0 = \frac{(p-1)\,\tau_{\nu_0}}{C_{\nu_0}^{\mathrm{ext}} R_{\mathrm{out}}} \left(\frac{R_{\mathrm{out}}}{R_{\mathrm{in}}}\right)^p \left[\left(\frac{R_{\mathrm{out}}}{R_{\mathrm{in}}}\right)^{p-1} - 1\right]^{-1}. \tag{2.81}$$

The normalised temperature profile T/T_{in} and the normalised SED $\lambda F_\lambda / F$ ($F = \int_0^\infty F_\lambda \, d\lambda$) of the envelope are shown in Fig. 2.9 for each case. We compute our normalised SEDs with the help of Eq. (2.65),

$$\left.\frac{\lambda F_\lambda}{F}\right|_{\lambda_k} \approx \frac{\nu_k \, H_k^{\mathrm{out}}}{\sum_{k=0}^{n_\nu - 1} W_k \, H_k^{\mathrm{out}}}. \tag{2.82}$$

The Ivezic benchmarks were produced with version 2 of DUSTY [5] (Ivezic and Elitzur, 1997). Because the DUSTY code generates its own computational grid, the spatial and frequency grids are different between both codes. Consequently, we compared the results by linearly interpolating our profiles (in $\log - \log$ scale) onto the DUSTY grids. We used 128 points for space and frequency, with a logarithmic sampling. We also point out that we restricted the comparison, for the normalised SEDs, to the frequency domain where $\lambda F_\lambda / F \geq 10^{-6}$ because of non-physical results of the DUSTY code below this threshold, for the smallest wavelengths.

DUSTY treats the star in the point-source approximation, hence it makes no distinction between T_{eff} and $T_\star$ (see Sect. 2.3.4). In our code, because we treat the star as an extended source, we impose T_{eff} and update the stellar temperature $T_\star$. Amongst all the benchmarks, this effect is the biggest for $p = 2$ and $\tau_{\nu_0} = 1\,000$ where we obtain $T_\star - T_{\mathrm{eff}} \approx 6$ K.

The FLD results and the benchmarks agree well. The main results, showing the relative differences between the two codes, are displayed in Table 2.2. The average relative differences in the temperature profiles mean($\epsilon(T)$) is of the order of 1 %, with a maximum value of approximately 4 %, achieved by the most optically thick envelopes ($\tau_{\nu_0} = 1\,000$). We note that the biggest discrepancies occurs inside the domain and not at the boundaries, highlighting the accuracy of the boundary conditions.

5. available at http://faculty.washington.edu/ivezic/dusty_web/

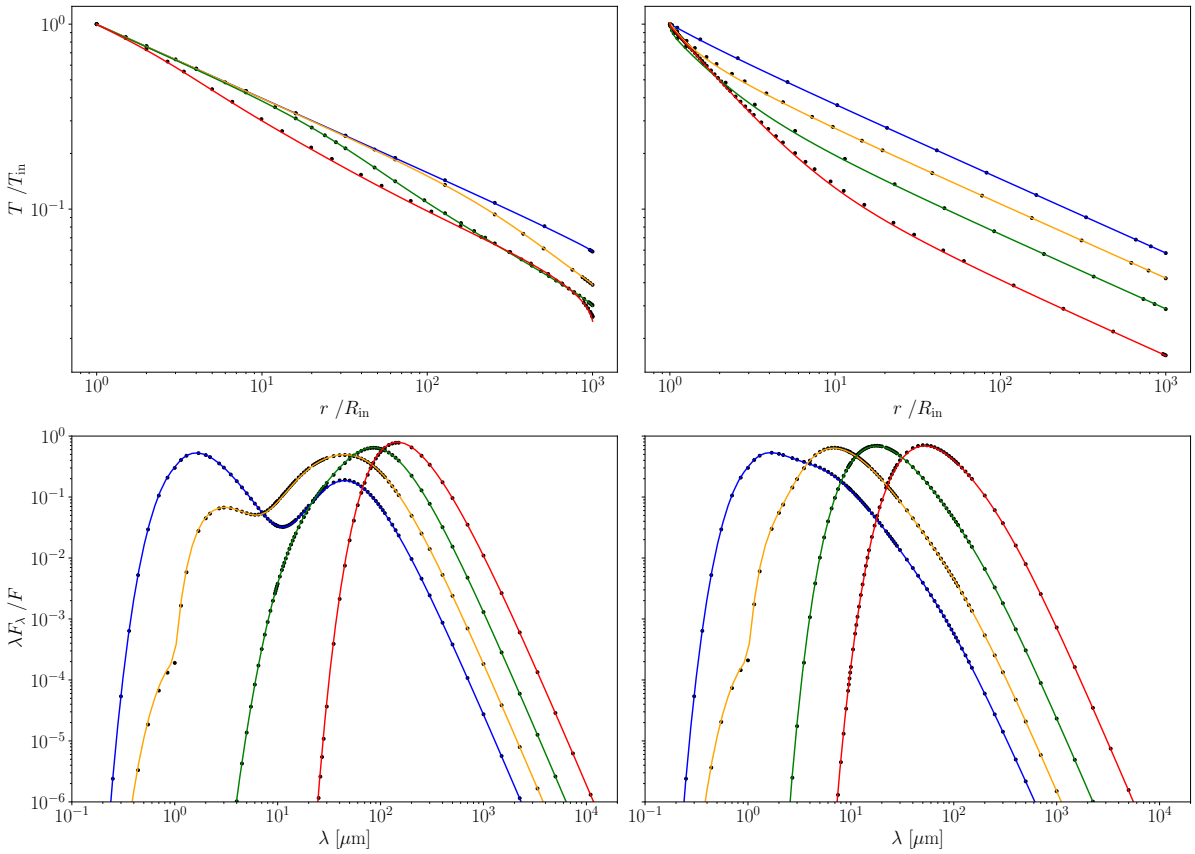

Figure 2.9 – Non-grey case : Normalised temperature profiles (*upper panels*) and SEDs (*lower panels*) for four different opacities $\tau_{\nu_0} = 1, 10, 100,$ and $1\,000$ (blue, orange, green and red, respectively) and two density power laws: $p = 0$ (*left panels*) and $p = 2$ (*right panels*). The solid lines represent the FLD curves, and the black dots indicate the benchmark profiles from Ivezic et al. (1997).

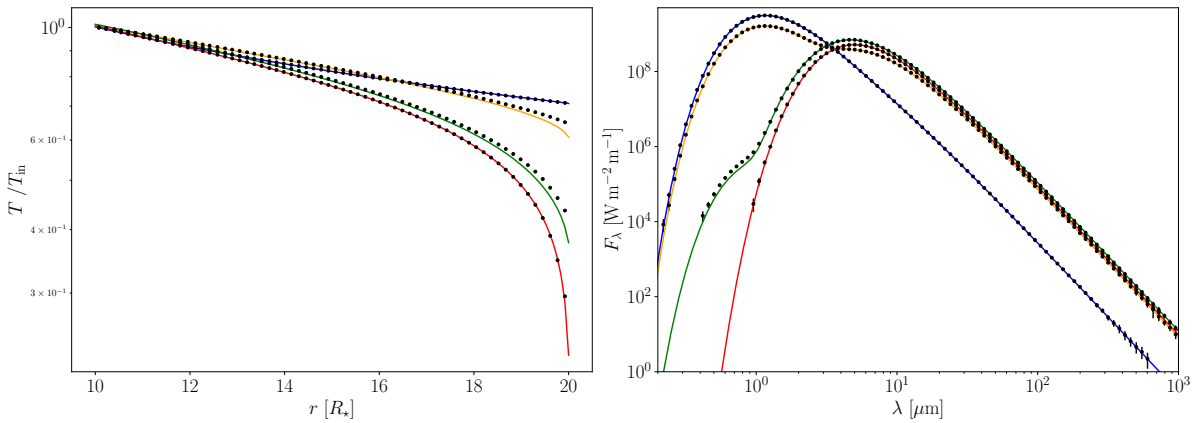

Figure 2.10 – Grey case : Normalised temperature profiles (*left panel*) and emerging fluxes (*right panel*) for four different opacities $\tau = 0.01, 1, 10,$ and 100 (blue, orange, green and red, respectively) with a constant density profile (p = 0). The solid lines represent the FLD curves, and the black dots with the error bars σ indicate the MC profiles from Niccolini and Alcolea (2006).

The average of the relative differences in the normalised SEDs mean($\epsilon\,(\lambda F_\lambda/F)$) always stays below 3 %, except for the optically-thick envelope with a constant density profile, where this difference reaches 6 %. Note that both the peak from the star, at around 1.1 μm (visible for the most optically-thin cases) and the envelope contribution are well reproduced. These results highlight that using Eq. (2.65) is pertinent and that, in this case, no further calculations is needed to compute the SED, such as a ray tracing computations.

Grey spherical shell with the Monte Carlo code from Niccolini & Alcolea (2006)

We now test the boundary conditions in the less realistic but more extreme case of a "spatially thin" spherically symmetric grey envelope. We expect the boundary effects to play a major role for this setup. The inner radius is set to $R_{\rm in} = 10\ R_\star$ and the outer radius $R_{\rm out} = 20\ R_\star$. We assume a constant density profile ($p = 0$) in the envelope. After running some tests, we noted that DUSTY is unable to accurately treat this kind of envelopes, and thus we rather used the 3D Monte Carlo radiative transfer code of Niccolini and Alcolea (2006) for comparison. Our test cases consisted in determining the normalised temperature profiles $T/T_{\rm in}$ and the emerging fluxes F_λ for several cases, ranging from optically thin ($\tau = 0.01$) up to the optically thick envelopes ($\tau = 100$). The corresponding profiles are shown in Fig. 2.10.

The spatial and frequency grid are again different between both codes, so we interpolated our results linearly (in $\log - \log$ scale) onto the Monte Carlo grids. The relative differences between the two codes, are displayed in Table 2.3. As an additional feature, the Monte Carlo code also provides an estimation of the errors on the temperature $\sigma(T)$ and on the emerging flux $\sigma(F_\lambda)$, computed from the Monte Carlo noise (Niccolini and Alcolea, 2006).

τ	$\epsilon(T)$	$\epsilon\,(F_\lambda)$
0.01	0/0/0	0/3/17
1	1/1/5	0/3/17
10	1/1/7	1/8/33
100	0/0/3	1/2/13

Table 2.3 – Results from the comparison with the Monte Carlo code from Niccolini and Alcolea (2006). Relative differences ϵ (in %) for the temperature profile $\epsilon(T)$ and for emerging flux $\epsilon\,(F_\lambda)$ shown in Fig. 2.10. The differences are presented in the form mean(ϵ) / std(ϵ) / max(ϵ) and rounded to the closest percent. mean(ϵ) is given by Eq. (2.83).

We used this information to compute a more relevant mean value for $\epsilon(T)$ and $\epsilon(F_\lambda)$,

$$\text{mean}(\epsilon(T)) = \frac{\sum_{i=0}^{N_x} W_i\,\epsilon(T_i)}{\sum_{i=0}^{N_x} W_i}, \quad \text{mean}(\epsilon(F_\lambda)) = \frac{\sum_{k=0}^{N_\lambda} W_k\,\epsilon(F_k)}{\sum_{k=0}^{N_\lambda} W_k}, \tag{2.83}$$

where N_x (N_λ) is the number of spatial (wavelength) points of the MC grid, $\epsilon(T_i)$ ($\epsilon(F_k)$) is the relative error (in %) on the temperature (emerging flux) between our results and the MC results, and W_i (W_k) is the inverse square of the MC relative errors, defined as

$$W_i = \left(\frac{\sigma(T_i)}{T_i}\right)^{-2}, \; W_k = \left(\frac{\sigma(F_k)}{F_k}\right)^{-2}. \tag{2.84}$$

This time, the flux that falls back onto the star, from the inner cavity, is significant. We find that, for the most optically-thick case ($\tau = 100$), $T_\star - T_{\rm eff} \approx 300$ K. The average of the relative differences of the temperature profile mean($\epsilon(T)$), remains of the order of 1 % for all the cases we tested. The largest differences are reached for the intermediate cases ($\tau = 1, 10$) and are located on the external edge of the envelope. This is expected because the FLD approximation is known to perform well in the optically thin and thick regimes, but it is less well suited to describe these intermediate cases. Nevertheless, the temperature profile is still quite well reproduced and the emerging flux is not affected by the small errors on the temperature close to the outer edge. We point out that the boundary conditions derived in this paper allow us to successfully reproduce the correct behaviour of the temperature profile for the optically thick envelope where it shows a quite steep decrease at the outer surface, as shown by Fig. 2.10. The emerging fluxes F_λ agree within 1 % on average, except for the optically thick case ($\tau = 100$), where mean($\epsilon(F_\lambda)$) reaches about 5 %.

We conclude this section with a comparison of the vacuum boundary from this study Eq. (2.62) and the original BC Eq. (56) from Levermore and Pomraning (1981) given by,

$$J_\nu(R_{\rm out}) + 2\,D_\nu \boldsymbol{s}.\,\boldsymbol{\nabla}\,J_\nu|_{r=R_{\rm out}} = 0 \tag{2.85}$$

It is important to notice that the boundary condition Eq. (2.85) was not originally intended to describe this class of problems, but the comparison still remains instructive

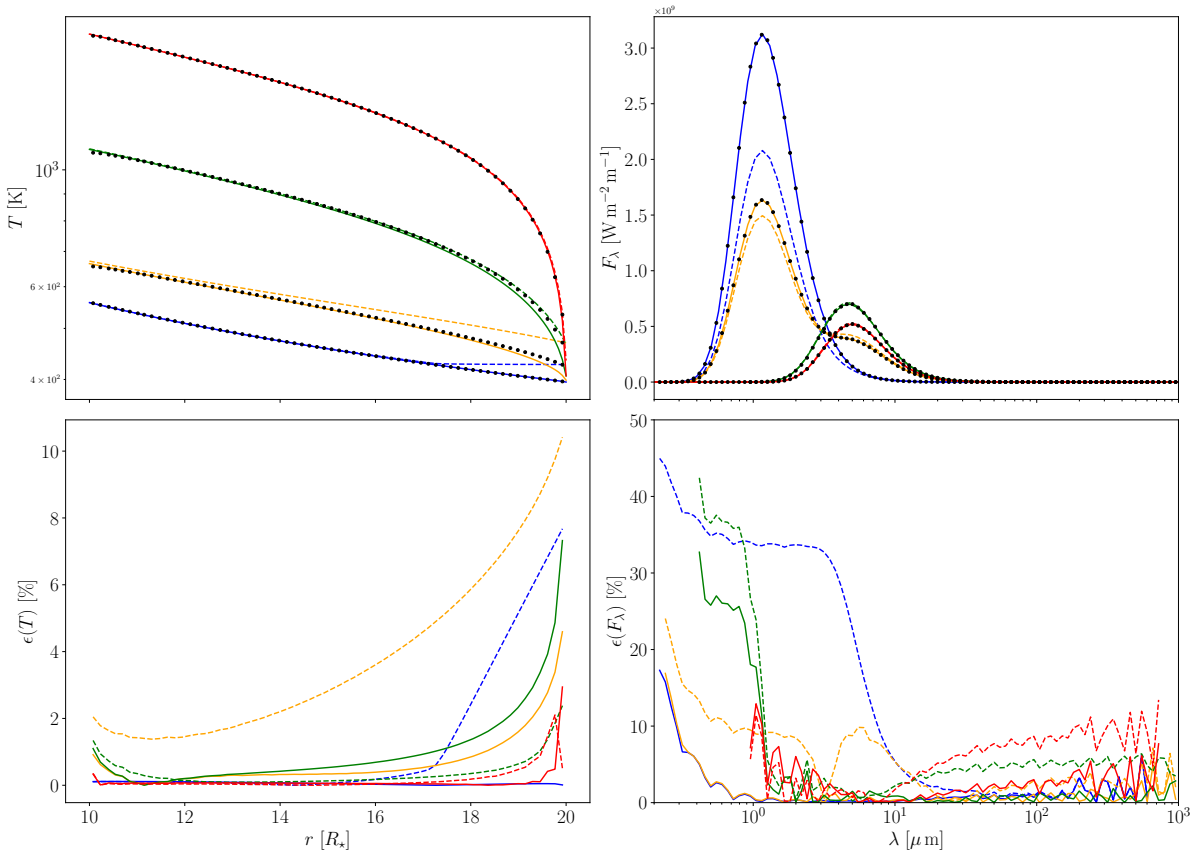

Figure 2.11 – Comparison of the outer boundary conditions presented here (solid lines) and from Levermore and Pomraning (1981) (dashed lines) for the test case presented in Sect. 2.3.6. The colour code is the same as in Fig. 2.10. The emerging fluxes are displayed in semi-log scale to highlight the differences between the boundary conditions. The lower panels show the relative differences profiles with respect to the Monte Carlo code from Niccolini and Alcolea (2006) in temperature (*left*) and in emerging flux (*right*).

for studying the importance of the boundary conditions for the accuracy of the solution. In Eq. (2.85), the factor two was originally used to give the correct ratio of the energy density over the emerging radiative flux in plane-parallel geometry for an optically-thin slab illuminated on the other side by an isotropic incident radiation field. However, for the special case of a spherical envelope surrounding a black-body star, this ratio becomes

$$\frac{\int_{\mu_0}^{1} B_\nu(T_\star)\,\mathrm{d}\mu}{\int_{\mu_0}^{1} \mu\, B_\nu(T_\star)\,\mathrm{d}\mu} = \frac{2\,(1-\mu_0)}{1-\mu_0^2} = \frac{2}{1+\mu_0} \tag{2.86}$$

with $\mu_0 = (1-(R_\star/R_{\rm out})^2)^{1/2}$, the cosine of the stellar angular size at $R_{\rm out}$. As $\mu_0 \to 0$ or equivalently $R_\star/R_{\rm out} \to 1$, this ratio increases to 2, as in Eq. (2.85), because we recover the case of a plane-parallel geometry with an isotropic incident radiation field. Far from the star ($\mu_0 \to 1$ or $R_\star/R_{\rm out} \to 0$), the ratio tends to 1, associated with an incoming sharp-peaked radiation. Hence, Eq. (2.85) will strongly deviate from the analytic limit 1, in the optically-thin limit.

This is what we observe in Fig. 2.11 that displays the relative differences, in the temperature profiles $\epsilon(T)$ and in the emerging fluxes $\epsilon(F_\lambda)$ for the same test case as presented at the beginning of this section. We note that this test case is not realistic, however, it allows to compare different optical regimes, compared to a more realistic problem in which the radiation is free at the external regions most of the time, such as for the test case presented in Sect. 2.3.6. We recall that Eq. (2.85) is a limiting case of the boundary condition we derived Eq. (2.41), hence it is not surprising that the results converge to the same profile, for a optically-thick grey envelope ($\tau = 100$). On the other-hand, in the optically-thin case ($\tau = 0.01$) where we would expect the ζ (see Eq. (2.61)) to be close to unity, Eq. (2.85) performs poorly, as expected. For intermediates regimes ($\tau = 1, 10$), the entanglement of the error of the boundary condition and FLD approximation itself makes any comparison very hard. We note that although the temperature profile is closer to the benchmark for $\tau = 10$ with Eq. (2.85), this is not the case for the associated emerging flux. We also note that in general, a boundary condition, although defined locally, can have a global influence on the whole solution, as shown by the temperature profile of the test case $\tau = 1$. To conclude, we also point out that we tried to implement Eq. (2.85) in the non-grey cases (Sect. 2.3.6) but we were unable to reach a satisfying convergence of the computations.

2.4 Flux-limited diffusion in axis-symmetric circumstellar envelope

In the spherical case, we expected and saw that the FLD approximation, when provided with appropriate boundary conditions, can quite well reproduce the radiation field. Apart from the boundary conditions, this success is mostly due to the fact that, in spherically symmetric envelopes, the form of specific intensity in the FLD (see Eq. 2.3) and the true radiation field share the same axial symmetry around the radial unitary vector $\hat{r}$. We now

want to know how accurate can the FLD approximation and our boundary conditions be in multi-dimensional configurations, where this symmetry no longer occurs. The mean intensity $J_\nu(\boldsymbol{r})$ is now a function of the radius r and the polar angle Θ (see Fig. 1.7). This time, we make use of the decomposition of the radiation field we presented in Sect. 1.2.3. We treat the star in the point source approximation and we can easily compute the stellar term $J_\nu^\star$ in Eq. (1.67), directly from a numerical estimation of Eq. (1.69). Then we only solve for, in the FLD approximation, the envelope component of the radiation $I_\nu^{\rm env}$. We apply the FLD formalism presented in Sect. 2.1 to Eq. (1.67) for $I_\nu^{\rm env}$. The mean specific intensity $J_\nu^{\rm env}$ then verifies the time-independent two-dimensional FLD equation

$$-\frac{1}{r^2}\partial_r\left(r^2\,D_\nu\,\partial_r J_\nu^{\rm env}\right)-\frac{1}{r^2\,\sin\Theta}\,\partial_\Theta\left(\sin\Theta\,D_\nu\,\partial_\Theta J_\nu^{\rm env}\right)+\kappa_\nu^{\rm abs}\,J_\nu^{\rm env}=\kappa_\nu^{\rm abs}B_\nu\left(T\right)+\kappa_\nu^{\rm sca}\,J_\nu^\star, \tag{2.87}$$

with D_ν, the non-linear diffusion coefficient given by Eq. (2.20) and computed with the help of $\boldsymbol{R}_\nu$ Eq. (2.11) which is expressed, in axis-symmetric configuration,

$$\boldsymbol{R}_\nu=-\frac{\partial_r J_\nu^{\rm env}\;\hat{r}+\frac{1}{r}\partial_\Theta J_\nu^{\rm env}\;\hat{\Theta}}{\omega_\nu\,\kappa_\nu^{\rm ext}\,J_\nu^{\rm env}},\ \text{with}\quad \omega_\nu=\frac{\kappa_\nu^{\rm abs}\,B_\nu+\kappa_\nu^{\rm sca}\left(J_\nu^\star+J_\nu^{\rm env}\right)}{\kappa_\nu^{\rm ext}\,J_\nu^{\rm env}}. \tag{2.88}$$

2.4.1 Boundary conditions

We need to specify the boundary conditions for Eq. (2.87) at each surface of the spatial domain $[R_{\rm in},R_{\rm out}]\times]0,\pi/2]$. On the inner cavity, we directly use the Marshak-type boundary condition Eq. (2.34) we derived in Sect. 2.2.1 and write ($\boldsymbol{s}=-\hat{r}$)

$$\alpha_\nu\,J_\nu^{\rm env}(R_{\rm in},\Theta)-\frac{D_\nu}{2}\,\partial_r J_\nu^{\rm env}|_{r=R_{\rm in},\Theta}=H_\nu^{\rm inc}(R_{\rm in},\Theta),\quad\forall\,\Theta\in]0,\pi/2]. \tag{2.89}$$

We need to specify the incident flux $H_\nu^{\rm inc}$ for $I_\nu^{\rm env}$. The only contribution comes from the self-heating of the cavity and the incident flux is written

$$H_\nu^{\rm inc}=\frac{1}{4\pi}\int\limits_{\boldsymbol{s}.\boldsymbol{\Omega}\leq 0}|\boldsymbol{s}.\boldsymbol{\Omega}|\;I_\nu^{\rm env}\left(\boldsymbol{r}_s',\boldsymbol{\Omega}'\right)\;{\rm d}\boldsymbol{\Omega}=\frac{1}{4\pi}\int\limits_{\boldsymbol{s}.\boldsymbol{\Omega}\leq 0}|\boldsymbol{s}.\boldsymbol{\Omega}|\;J_\nu^{\rm env}(\boldsymbol{r}_s')\,\psi_\nu^{\rm env}\left(\boldsymbol{r}_s',\boldsymbol{\Omega}'\right)\;{\rm d}\boldsymbol{\Omega} \tag{2.90}$$

$(\boldsymbol{r}_s',\boldsymbol{\Omega}')$ are the local coordinates of the opposite point of $\boldsymbol{r}_s$ on the boundary, along the ray $\boldsymbol{\Omega}$ (see Fig. 2.5). We use the same convention as in Sect. 2.3.1 to perform the angular integration in Eq. (2.90),

$$H_\nu^{\rm inc}=\frac{1}{4\pi}\int_0^{2\pi}{\rm d}\varphi\int_0^{\mu 0}\mu\,J_\nu^{\rm env}\left(R_{\rm in},\Theta'\right)\,\psi_\nu^{\rm env}\left(R_{\rm in},\Theta',\mu',\varphi'\right)\;{\rm d}\mu. \tag{2.91}$$

$\mu_0=(1-(R_\star/R_{\rm in})^2)^{1/2}$ is the cosine of the angle under which the star is seen from a point on the inner cavity and $(R_{\rm in},\Theta',\mu',\varphi')$ are the coordinates of the opposite point. Their expression is given in Appendix A. This time, because $J_\nu^{\rm env}$ and $\psi_\nu^{\rm env}$ are no longer constant on the inner cavity, the integral can only be estimated numerically. Eq. (2.91) can be rewritten in term of the general quadrature formula

$$H_\nu^{\rm inc}\approx\frac{1}{4\pi}\sum_{m=0}^{M-1}\sum_{n=0}^{N-1}W_{\mu_m}\,W_{\varphi_n}\,\mu_m\,J_\nu^{\rm env}\left(R_{\rm in},\Theta'_{m,n}\right)\,\psi_\nu^{\rm env}\left(R_{\rm in},\Theta'_{m,n},\mu'_m,\varphi'_{m,n}\right), \tag{2.92}$$

with M, N, the number of points along the μ, φ, direction, and W_{μ_m}, W_{φ_n}, the corresponding quadrature weights. From the numerical test we performed, we found out that using a simple mid-point rule is enough since $J_\nu^{\rm env}\,\psi_\nu^{\rm env}$ gently varies along the inner cavity. Because $J_\nu^{\rm env}$ and ψ_ν are in practice computed on a discrete grid, we need to linearly interpolate these quantities on the inner cavity, to obtain $J_\nu^{\rm env}\left(R_{\rm in}, \Theta'_{m,n}\right)$ and $\psi_\nu^{\rm env}\left(R_{\rm in}, \Theta'_{m,n}, \mu'_m, \varphi'_{m,n}\right)$.

To treat the vaccum boundary at the outer edge ($r = R_{\rm out}$), we directly use the boundary condition Eq. (2.48) and write

$$J_\nu^{\rm env}(R_{\rm out} + {\rm d}r, \Theta) = \upsilon_\nu\, J_\nu^{\rm env}(R_{\rm out}, \Theta), \quad \forall\, \Theta \in]0, \pi/2]. \tag{2.93}$$

Finally, the polar and equatorial symmetries impose that no flux is flowing thought the polar axis and the equatorial plane. Consequently we have,

$$\hat{\Theta}.\boldsymbol{H}_\nu^{\rm env}\Big|_{r,\Theta=0,\frac{\pi}{2}} = 0 \quad \text{or equivalently} \quad \partial_\Theta J_\nu^{\rm env}|_{r,\Theta=0,\frac{\pi}{2}} = 0, \quad \forall\, r \in [R_{\rm in}, R_{\rm out}]. \tag{2.94}$$

2.4.2 Emerging flux and images

For the numerical tests, we need to estimate the total flux $f_\nu^{\rm obs}$ that an observer receives from the object, situated at a distance $d \gg R_{\rm out}$ and doing an angle i with the polar axis.

Since we decouple the stellar from the envelope radiation (see Eq. 1.67), the total flux is made of the stellar and envelope total flux

$$f_\nu^{\rm obs}(i, d) = f_\nu^{\rm obs,\star} + f_\nu^{\rm obs,env}. \tag{2.95}$$

If we assume the star to be an unresolved black body point source, the stellar flux at distance d is the flux of the star at the stellar surface attenuated by the circumstellar matter present in the direction of the line of sight (red line in Fig. 2.12) , and with the dilution factor $(R_\star/d)^2$,

$$f_\nu^{\rm obs,\star}(i, d) = \pi \left(\frac{R_\star}{d}\right)^2 B_\nu(T_\star)\, \exp\{-\tau(i)\}, \tag{2.96}$$

with $\tau(i) = \int_{R_{\rm in}}^{R_{\rm out}} \kappa_\nu^{\rm ext}(r, i)\, {\rm d}r$, the integrated radial optical depth in the direction of the line of sight.

To compute the envelope flux and images, we define an image plane $(\hat{x}, \hat{y})$, at a distance $d \gg R_{\rm out}$ from the star and tilted with an angle i with respect to the polar axis (see Fig. 2.12). The x and y axes are oriented with the help of the spherical coordinates system $(\hat{r}, \hat{\Theta}, \hat{\Phi})$. In this plane, we can construct images of any geometry but we only consider the explicit case of a square image of width L and a circular image of radius R.

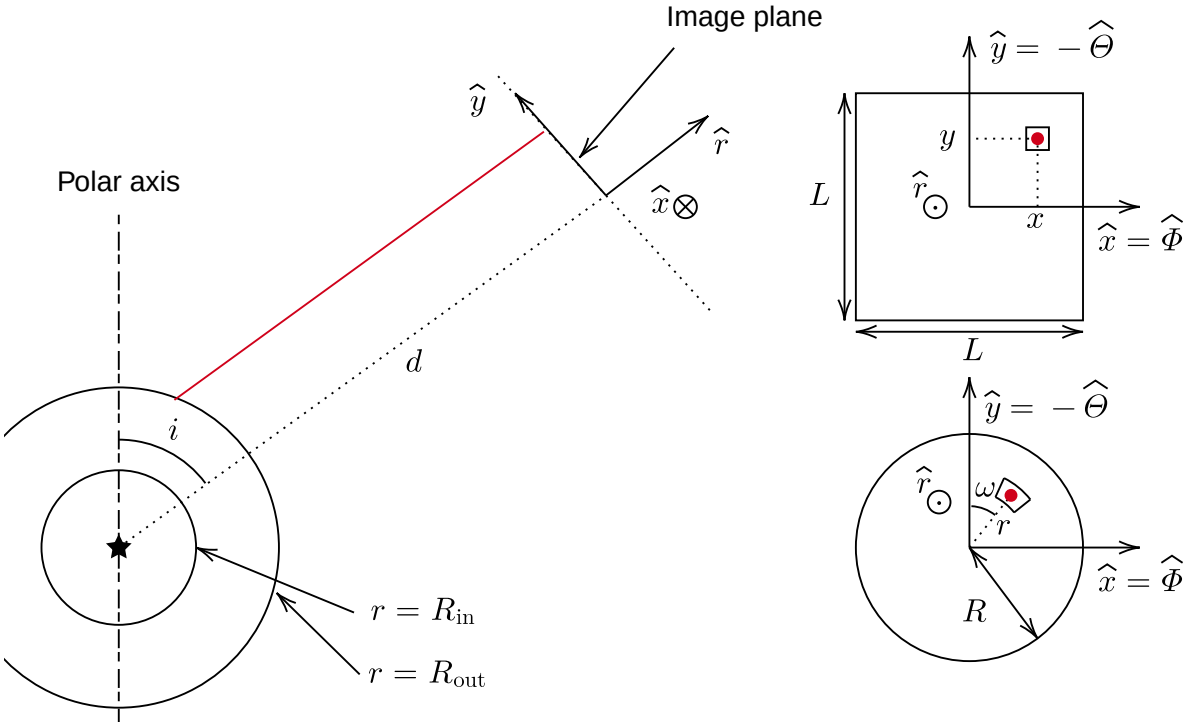

Figure 2.12 – Left: image plane situated at a distance $d \gg R_{\rm out}$, and tilted with an angle i with respect to the polar axis. The red line is an example of a ray, emerging from the envelope, and arriving normal to the image plane. Right: Examples of a square and a circular image with their associated pixel geometry.

Since $d \gg R_{\rm out}$, the flux inside the image can formally be written

$$\begin{aligned} f_\nu^{\rm obs,env}(i) &= \int_{-\frac{L}{2}}^{\frac{L}{2}} \int_{-\frac{L}{2}}^{\frac{L}{2}} I_\nu^{\rm env}(x,y,\hat{r})\ \frac{{\rm d}x\,{\rm d}y}{d^2}, \\ \text{or} \quad f_\nu^{\rm obs,env}(i) &= \int_0^{2\pi} \int_0^{R} I_\nu^{\rm env}(r,\omega,\hat{r})\ \frac{r\,{\rm d}\omega\,{\rm d}r}{d^2}. \end{aligned} \tag{2.97}$$

In practice, images are made of a collection of pixels in which we evaluate the emerging specific intensity at the pixel centre. A square (circular) image, is divided into $N \times N$ ($N_r \times N_\omega$) pixels and the flux in the image can then be rewritten

$$\begin{aligned} f_\nu^{\rm obs,env}(i) &\approx \sum_{i=0}^{N-1} \sum_{j=0}^{N-1} I_\nu^{\rm env}(x_i,y_j,\hat{r})\ \frac{\Delta x_i\,\Delta y_i}{d^2}, \\ \text{or} \quad f_\nu^{\rm obs,env}(i) &\approx \sum_{i=0}^{N_r} \sum_{j=0}^{N_\omega} I_\nu^{\rm env}(r_i,\omega_j,\hat{r})\ \frac{r_i\,\Delta\omega_j\,\Delta r_i}{d^2}, \end{aligned} \tag{2.98}$$

with $\Delta x_i \Delta y_i$ ($r_i\,\Delta\omega_j\,\Delta r_i$) the pixel size of the square (circular) image. We note that the circular image is particularly well-suited for the computation of $f_\nu^{\rm obs,env}(i)$ since we can easily increase the number of pixels in the centre of the image in order to resolve the disc inner parts.

The emerging specific intensity, crossing each pixel centre $\boldsymbol{r}_0 = x_i\ \hat{x} + y_j\ \hat{y} + d\ \hat{r}$ ($\boldsymbol{r}_0 = r_i\ \sin\omega_j\ \hat{x} + r_i\ \cos\omega_j\ \hat{y} + d\ \hat{r}$ for a circular image), along the ray normal to the image plane (red line in Fig. 2.13), is computed via a ray tracing technique. Formally, this intensity is written, by integration of the time-independent radiative transfer equation version of Eq. (1.33), along the ray $\boldsymbol{r} = \boldsymbol{r}_0 - s\,\hat{r}$,

$$I_\nu^{\rm env}(\boldsymbol{r}_0,\hat{r}) = \int_{s_{min}}^{s_{max}} \eta_\nu\ \exp\left\{-\tau_\nu(s)\right\}\ {\rm d}s, \text{with} \quad \tau_\nu(s) = \int_{s_{min}}^{s} \kappa_\nu^{\rm ext}\ {\rm d}s'. \tag{2.99}$$

s is the distance from $\boldsymbol{r}_0$ to a given point on the ray. η_ν and $\kappa_\nu^{\rm ext}$ are the emissivity and the extinction coefficient, respectively, as defined in Eq. (1.33). Note that the emissivity is already known from previous calculations of the radiative transfer problem. s_{min} and s_{max} correspond to the two intersections of the ray with the outer sphere of radius $R_{\rm out}$.

In practice, η_ν and $\kappa_\nu^{\rm ext}$ are defined on a discrete grid and the previous integral can be rewritten as

$$I_\nu^{\rm env}(\boldsymbol{r}_0,\hat{r}) = \sum_{i=0}^{n-2} \int_{s_i}^{s_{i+1}} \eta_\nu\ \exp\left\{-\tau_\nu(s)\right\}\ {\rm d}s. \tag{2.100}$$

The $\{s_i\}_{i=0}^{n-1}$ are the n intersections of the ray with the grid (red crosses in Fig. 2.13), with $s_0 = s_{min}$ and $s_{n-1} = s_{max}$. The coordinates of all intersections can be computed by looking at the solution of the intersection of the ray $\boldsymbol{r}_0 - s\,\hat{r}$ with the cones and the

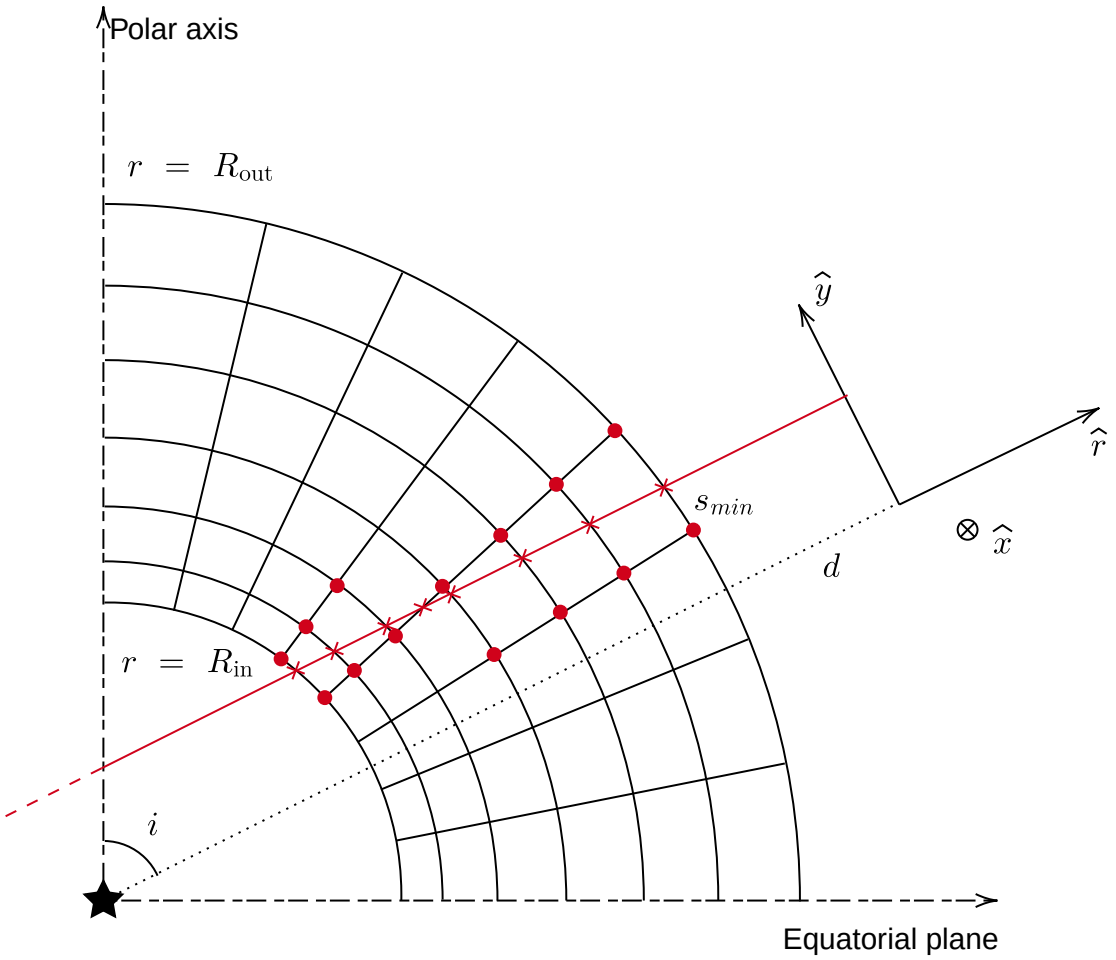

Figure 2.13 – Example of a ray (red line) normal to the image plane, crossing the spherical grid. The red crosses represent the intersections between the ray and the grid. The values of $\kappa_\nu^{\rm ext}$ and S_ν at these intersections are linearly interpolated from the grid-adjacent values (red dots).

concentric shells that define the grid. We can express ΔI_ν^i, the contribution to the total intensity $I_\nu(x, y, \hat{r})$ of each portion between two consecutive intersections as,

$$I_\nu^{\rm env}(\boldsymbol{r}_0, \hat{r}) = \sum_{i=0}^{n-2} \exp\left\{-\tau_\nu^i\right\} \Delta I_\nu^i,$$
$$\text{with} \quad \Delta I_\nu^i = \int_{s_i}^{s_{i+1}} \eta_\nu \exp\left\{-\int_{s_i}^{s} \kappa_\nu^{\rm ext}\, {\rm d}s'\right\} {\rm d}s \quad \text{and} \quad \tau_\nu^i = \int_{s_{min}}^{s_i} \kappa_\nu^{\rm ext}\, {\rm d}s'. \tag{2.101}$$

In order to evaluate the integrals, we need a suitable approximation for η_ν and $\kappa_\nu^{\rm ext}$ between each s_i and s_{i+1}. The simplest approach is assume they are constant, e.g to take an average value $\eta_\nu = (\eta_\nu(s_i)+\eta_\nu(s_{i+1}))/2$. However, in regions where the source function has a quadratic behaviour, it leads to an over-estimation of the intensity. Following Olson et al. (1986), we assume that η_ν and $\kappa_\nu^{\rm ext}$ are linear functions between two consecutive intersections. Higher order of approximation can be used, for better accuracy, they however in some cases lead to pathological flaws (e.g negative intensity values) that requires specific techniques to circumvent them. For the cases we consider, we found that the linear approximation was accurate enough. Each contribution ΔI_ν^i is then given by

$$\Delta I_\nu^i \approx \left(1 - \exp\left\{-\Delta\tau_\nu^i\right\} - \beta\right) S_\nu(s_i) + \beta\, S_\nu(s_{i+1})\,,$$
$$\text{with} \quad \beta = \frac{\Delta\tau_\nu^i - 1 + \exp\left\{-\Delta\tau_\nu^i\right\}}{\Delta\tau_\nu^i} \quad \text{and} \quad \Delta\tau_\nu^i = \frac{\kappa_\nu^{\rm ext}(s_i) + \kappa_\nu^{\rm ext}(s_{i+1})}{2}\,(s_{i+1} - s_i)\,, \tag{2.102}$$

with $S_\nu = \eta_\nu/\kappa_\nu^{\rm ext}$. The values of S_ν and $\kappa_\nu^{\rm ext}$ at the intersections s_i and s_{i+1} are estimated by linear interpolation from the grid-adjacent values (red dots in Fig. 2.13). Note that τ_ν^i is computed recursively,

$$\tau_\nu^{i+1} = \tau_\nu^i + \int_{s_i}^{s_{i+1}} \kappa_\nu^{\rm ext} {\rm d}s' = \tau_\nu^i + \Delta\tau_\nu^i\,, \tag{2.103}$$

with $\tau_\nu^0 = 0$ and $\Delta\tau_\nu^i$ defined in Eq. (2.102).

2.4.3 Numerical implementation

We proceed to the two-dimensional generalisation of the implementation described in Sect. 2.3.5. Eqs. (2.87), (2.89), (2.93) , (2.94) and (1.66) are discretised on a computational grid and solved via the iterative method presented in Sect. 2.3.5.

Again, the equations are solved with respect to the uniformly sampled variables $x = f(r)$ and $y = g(\Theta)$ in order to non-uniformly sample the radial r and angular Θ coordinates. The domain $[R_{\rm in}, R_{\rm out}]\times]0, 2\pi]$ is decomposed into $N_r \times N_\Theta$ cells. We compute the vectors on the cells walls and the scalars on the cell centres (see Fig. 2.14). We use the same finite difference operator Eq. (2.69) to approximate the derivatives. The FLD Eq. (2.87)

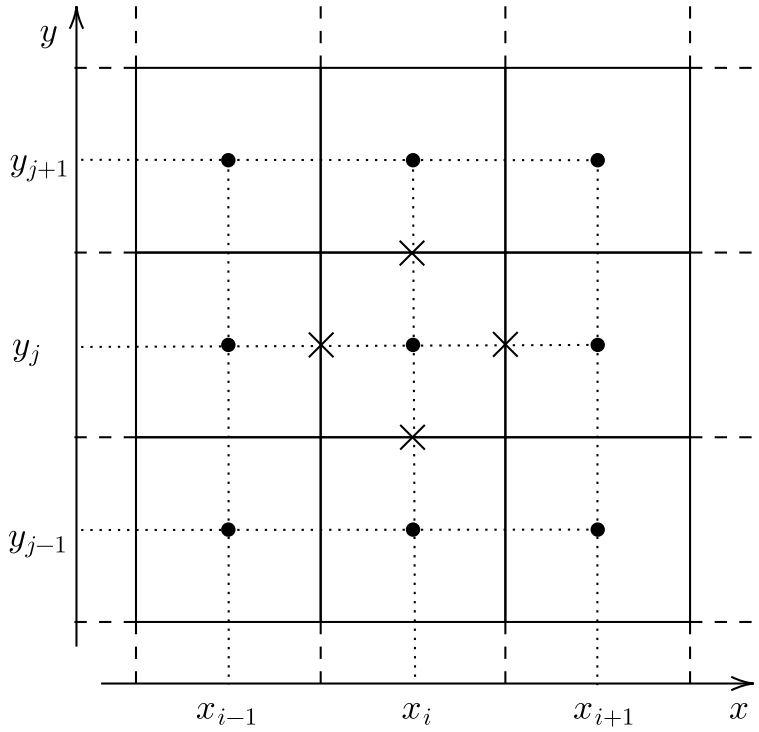

Figure 2.14 – Illustration of two-dimensional computational grid used to solve the discretised FLD Eq. (2.104). The non-linear coefficients and vectors are computed at the cell edges (crosses) while the values of $J_\nu^{\rm env}$ and B_ν are computed at the cell centres (dots).

is then approximated with the following numerical scheme

$$
\begin{aligned}
-a_{i+1/2,j}\,J^{\rm env}_{i+1,j} - a_{i,j+1/2}\,J^{\rm env}_{i,j+1} + a_{i,j}\,J^{\rm env}_{i,j} - a_{i-\frac{1}{2},j}\,J^{\rm env}_{i-1,j} - a_{i,j-1/2}\,J^{\rm env}_{i,j-1} &= \\
b_{i,j}\left(\kappa^{\rm abs}_{i,j}\,B_{i,j} + \kappa^{\rm sca}_{i,j}\,J^{\star}_{i,j}\right)& \\
\text{with,} \qquad a_{i\pm1/2,j} = \Delta y^2\,\frac{{\rm d}y}{d\Theta}\bigg|_j\,\frac{{\rm d}x}{{\rm d}r}\bigg|_{i\pm1/2}\,r^2_{i\pm1/2}\,\sin\Theta_j\,D_{i\pm1/2,j},& \\
a_{i,j\pm1/2} = \Delta x^2\,\frac{{\rm d}x}{{\rm d}r}\bigg|_i\,\frac{{\rm d}y}{d\Theta}\bigg|_{j\pm1/2}\,\sin\Theta_{j\pm1/2}\,D_{i,j\pm1/2},& \\
b_{i,j} = \Delta x^2\,\Delta y^2\,\frac{{\rm d}x}{{\rm d}r}\bigg|_i\,\frac{{\rm d}y}{d\Theta}\bigg|_j\,r^2_i\,\sin\Theta_j,& \\
a_{i,j} = a_{i+1/2,j} + a_{i-1/2,j} + a_{i,j+1/2} + a_{i,j-1/2} + b_{i,j}.&
\end{aligned}
\tag{2.104}
$$

The non-linear coefficients in Eqs. (2.87), (2.89), (2.93) require an estimate of $J^{\rm env}_\nu$ and it's gradient at the cell walls. We adopt the following 6-points stencil, for example for $J^{\rm env}_{i+1/2,j}$

$$
J^{\rm env}_{i+1/2,j} \approx \frac{1}{4}\left(J_{i+1,j} + J_{i,j}\right) + \frac{1}{8}\left(J_{i+1,j+1} + J_{i,j+1} + J_{i+1,j-1} + J_{i,j-1}\right). \tag{2.105}
$$

For the gradient, we need to estimate the two components $\partial_x J^{\rm env}$ and $\partial_y J^{\rm env}$,

$$
\begin{aligned}
\partial_x J^{\rm env}|_{i+1/2,j} &\approx \frac{1}{2\Delta x}\left(J^{\rm env}_{i+1,j} - J^{\rm env}_{i,j}\right) + \frac{1}{4\Delta x}\left(J^{\rm env}_{i+1,j+1} - J^{\rm env}_{i,j+1} + J^{\rm env}_{i+1,j-1} - J^{\rm env}_{i,j-1}\right), \\
\partial_y J^{\rm env}|_{i+1/2,j} &\approx \frac{1}{4\Delta x}\left(J^{\rm env}_{i+1,j+1} - J^{\rm env}_{i,j-1} + J^{\rm env}_{i,j+1} - J^{\rm env}_{i,j-1}\right).
\end{aligned}
\tag{2.106}
$$

The discretisation of the boundary conditions Eqs. (2.89), (2.93) and (2.94) yields

$$
\begin{aligned}
J^{\rm env}_{0,j} &= \frac{H^{\rm inc} - \left(\alpha_{1/2,j} - \frac{D_{1/2,j}}{\Delta x}\frac{{\rm d}x}{{\rm d}r}|_{x_{1/2}}\right)J^{\rm env}_{1,j}}{\alpha_{1/2,j} + \frac{D_{1/2,j}}{\Delta x}\frac{{\rm d}x}{{\rm d}r}|_{x_{1/2}}}, \\
J^{\rm env}_{N_r-1,j} &= \frac{\upsilon_{N_r-3/2,j}}{2-\upsilon_{N_r-3/2,j}}J^{\rm env}_{N_r-2,j}, \\
J^{\rm env}_{i,0} &= J^{\rm env}_{i,1} \quad \text{and} \quad J^{\rm env}_{i,N_\Theta-1} = J^{\rm env}_{i,N_\Theta-2}.
\end{aligned}
\tag{2.107}
$$

Finally, the radiative Equilibrium Eq. (1.66) is rewritten, using the subscript k to denote the frequency dependence,

$$
\sum_{k=0}^{N_\nu-1} W_k\,\kappa^{\rm abs}_{k,i,j}\left(J^{\rm env}_{k,i,j} + J^{\star}_{k,i,j}\right) = \sum_{k=0}^{N_\nu-1} W_k\,\kappa^{\rm abs}_{k,i,j}\,B_k(T). \tag{2.108}
$$

We use the same iterative method as in Sect. (2.3.5) in order to solve the system of Eqs. (2.104), (2.107) and (2.108). The solution vector is now $\boldsymbol{X} = [J^{\rm env}_{0,0,0}, ..., J^{\rm env}_{k,i,j}, ..., J^{\rm env}_{N_\nu-1,N_r-1,N_\Theta-1}, T_{0,0}, ..., T_{i,j}, ..., T_{N_r-1,N_\Theta-1}]$. If we call n, the superscript index of iteration

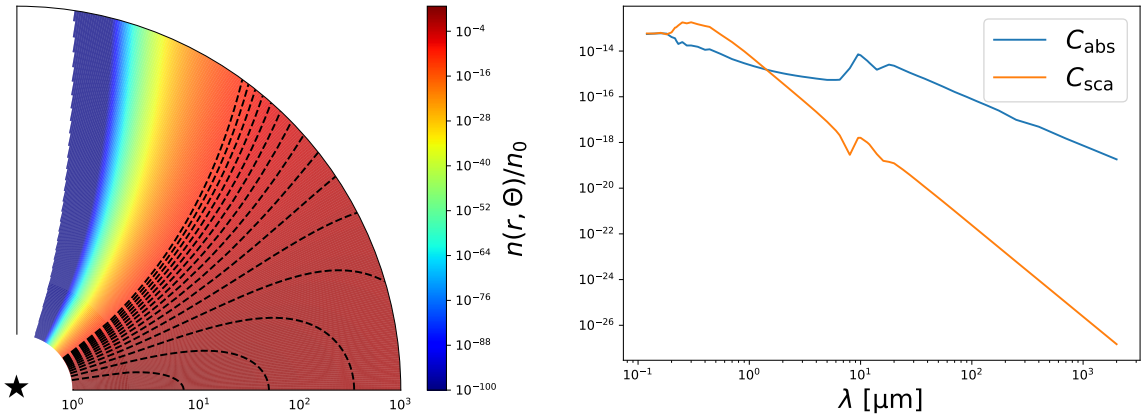

Figure 2.15 – Left: Normalised density map of the disc. The dashed lines represent the iso-density contours highlighting the disc geometry. Right: Optical data of spherical astronomical silicate grains, taken from Draine and Lee (1984).

of the method, we update first update the values of $J_\nu^{\rm env}$, using a Gauss-Seidel forward sweep (see Appendix B.2)

$$\begin{aligned}\left[J_{i,j}^{\rm env}\right]^{n+1} = \frac{1}{A_{i,j}^n}\Big(b_{i,j}\left(\kappa_{i,j}^{\rm abs}\left[B_{i,j}\right]^n + \kappa_{i,j}^{\rm sca} J_{i,j}^\star\right) + A_{i+1/2,j}^n\left[J_{i+1,j}^{\rm env}\right]^n \\ - A_{i,j+1/2}^n\left[J_{i,j+1}^{\rm env}\right]^n + A_{i-\frac{1}{2},j}^n\left[J_{i-1,j}^{\rm env}\right]^{n+1} - A_{i,j-1/2}^n\left[J_{i,j-1}^{\rm env}\right]^{n+1}\Big)\end{aligned} \tag{2.109}$$

starting from $(i,j) = (1,1)$ to $(N_r - 2, N_\Theta - 2)$. Doing this for all frequencies ν_k yields the complete update of the mean radiation field $J_\nu^{\rm env}$ in the domain $[R_{\rm in}, R_{\rm out}]\times]0,\pi/2]$. We consequently update the values of $J_\nu^{\rm env}$ inside the ghost cells via Eq. (2.107) and update the values of all the non-linear coefficients. Finally, we update the dust temperature via Eq. (2.108).

2.4.4 Numerical tests

We make use of the axis-symmetric benchmark published by Pascucci et al. (2004). The authors consider the general case of a point-like star embedded in a circumstellar disc with an inner cavity free of dust. The star radiates as a black body at the temperature $T_\star = 5\,800$ K. In order for the circumstellar material to be dust, it needs to lie outside of the sublimation radius, where the temperature is low enough. The disc extends from an inner radius of $R_{\rm in} = 1$ AU to a distance of $R_{\rm out} = 1\,000$ AU, guaranteeing an inner dust temperature to be around ~ 400 K, for the test cases we consider. The disc is supposed to be exclusively made of spherical astronomical silicate grains with an isotropic and coherent scattering profile. The optical data are taken from Draine and Lee (1984) and their profile is represented in Fig. 2.15-right. Note that the scattering dominates between 0.2 and 1 μm and that there is a emission peak at ~ 10 μm. The number density profile

(see Fig. 2.15-left) $n^{\rm disc}$ is assumed to be that of a Keplerian disc

$$\begin{aligned} n^{\rm disc}(r,\Theta) &= n_0^{\rm disc}\frac{r_d}{r\sin\Theta}\exp\left\{-\frac{\pi}{4}\left(\frac{r\cos\Theta}{h}\right)^2\right\}, \\ \text{with} \qquad h &= z_d\left(\frac{r\sin\Theta}{r_d}\right)^{9/8} \quad \text{and} \quad r_d = \frac{R_{\rm out}}{2}, \quad z_d = \frac{R_{\rm out}}{8}. \end{aligned} \tag{2.110}$$

The constant $n_0^{\rm disc}$ is determined to set $\tau_{\nu_0} = \int_{R_{\rm in}}^{R_{\rm out}} C_{\nu_0}^{\rm ext}\, n^{\rm disc}\, {\rm d}r$, the radial optical depth, integrated though the disc mid-plane ($\Theta = \pi/2$), at frequency $\nu_0 = c/\lambda_0$ with $\lambda_0 = 0.55$ μm,

$$n_0^{\rm disc} = \frac{\tau_{\nu_0}}{C_{\nu_0}^{\rm ext}\, r_d\, \ln\left(\frac{R_{\rm out}}{R_{\rm in}}\right)}. \tag{2.111}$$

We explore the case of an optically-thin and thick disc $\tau_{\nu_0} = 0.1, 100$, respectively. We do not display the intermediate cases as we expect (and verified) that the discrepancies in the results are smaller than the most optically-thick case.

A numerical flaw of the FLD approximation appears in vacuum regions, where the extinction coefficient goes to zero $\kappa_\nu^{\rm ext} \to 0$ and the quantity R_ν goes to infinity $R_\nu \to \infty$. This is a problem in a numerical implementation where we only deal with finite values of quantities. The FLD approximation requires a special treatment for these regions. One way to circumvent this problem is to introduce an additional shell to mimic the vacuum behaviour of the FLD solution in these regions. The disc is embedded in this extremely-optically-thin ($\tau_{\nu_0}^{\rm shell} = 10^{-5}$) circumstellar shell, made of the same dust as the disc and with a constant number density profile $n^{\rm shell}$. The total number density is then

$$\begin{aligned} n(r,\Theta) &= n^{\rm disc}(r,\Theta) + n^{\rm shell}, \\ \text{with} \qquad n^{\rm shell} &= \frac{\tau_{\nu_0}^{\rm shell}}{C_{\nu_0}^{\rm ext}\,(R_{\rm out}-R_{\rm in})}. \end{aligned} \tag{2.112}$$

Eq. (2.112) insures to have a minimal density floor that keeps finite the values for R_ν.

The original benchmark compares the results of five different radiative transfer codes. The codes are of different nature; three are Monte Carlo code, one relies on short characteristics and the last one is based on finite difference (see Sect. 1.1.5 for a presentation of the different type of methods). We refer to the original article from Pascucci et al. (2004) for a list of the codes and their specific features. New radiative transfer codes emerged or existent ones were improved since the original study, hence we decided to rather compare our results with RADMC-3D [6], a more recent Monte Carlo radiative transfer code from Dullemond et al. (2012). RADMC-3D is mainly written to solve the continuum radiative transfer problem in dusty media. It computes the dust temperature from a user-input dust density distribution. It is available in one, two or three-dimensional geometries. It also includes a ray-tracing module to compute images and spectra from the user-input/computed emissivity η_ν (see Eq. 1.31).

In Fig. 2.16, we show the temperature profiles of the two codes, in the disc mid-plane at $\Theta = \pi/2$ and at the radius $r \approx 2$ AU. The optically-thin disc is well reproduced by

6. available at https://www.ita.uni-heidelberg.de/ dullemond/software/radmc-3d/

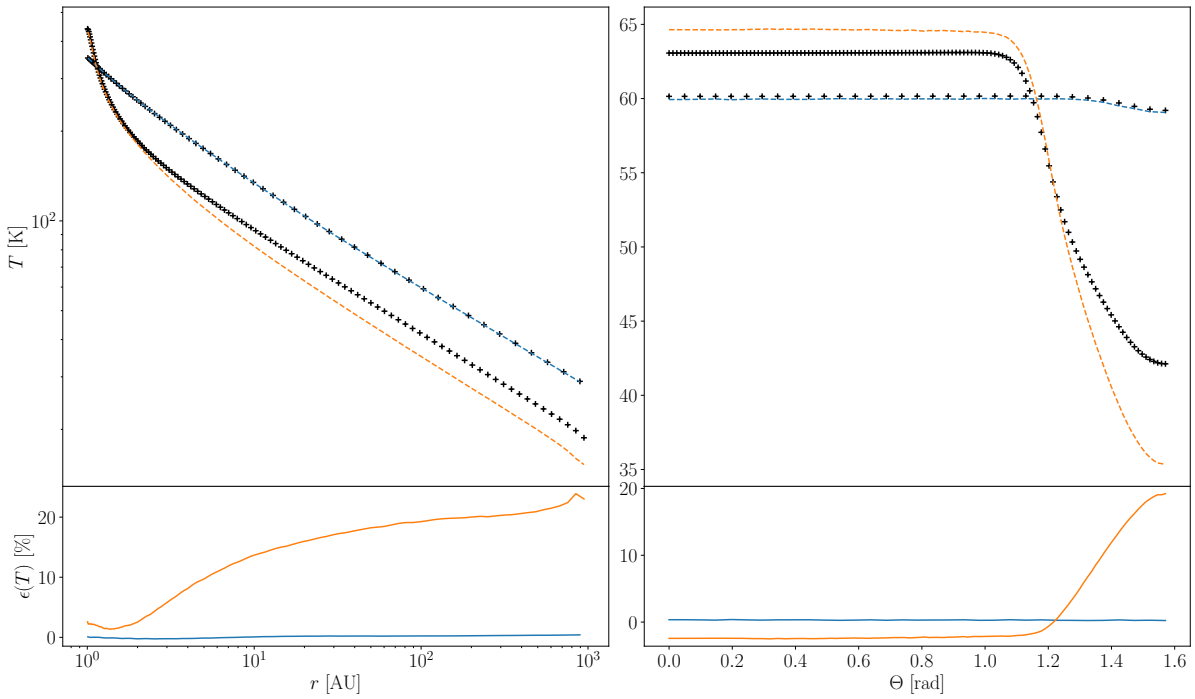

Figure 2.16 – Temperature profiles for the axis-symmetric envelope with $\tau_{\nu_0} = 0.1$ (blue curve) and $\tau_{\nu_0} = 100$ (orange curve), in the disc-mid-plane (left panel) and at $r \approx 100$ AU (right panel). The cross marks represent the FLD solution from this study and the solid curves are computed with RADMC-3D. The lower panels display the relative differences between the two codes

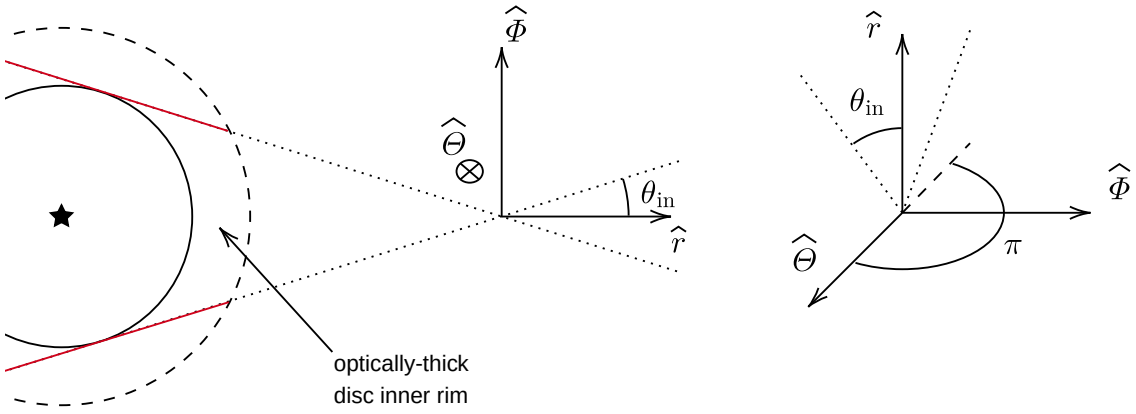

Figure 2.17 – The influence of the optically-thick inner-disc rim on the radiation field at large radii, in the disc mid-plane. The main contribution comes from peaks (dashed lines) where the integrated emissivty is the largest (red lines). The two peaks are in the direction corresponding to $\mu = \cos\theta_{\rm in} = (1 - (R_{\rm in}/r)^2)^{1/2}$ and $\varphi = 0, \pi$, as pictured by the right figure.

the FLD code, with discrepancies less than 1 %. It is not surprising since, for this case, the mean radiation field is dominated by the stellar mean radiation field $J^\star_\nu$, which is computed exactly (at the precision of the numerical integration). The agreement for the optically-thick disc is more mitigated. The biggest discrepancies are found in the disc-mid plane, after the optically-thick regions (after $\sim$ 2 AU), where the stellar radiation is shadowed by the optically-thick disc inner-parts. In these regions, the temperature of the FLD is over-estimated (up to $\sim$ 25 %).

It was previously reported in the literature that the FLD approximation is unable to cast shadows (see e.g Kuiper and Klessen, 2013). One of the invoked reasons is that the FLD radiative flux is oriented along the gradient of J_ν, leading to an unrealistic diffusion around the optically-thick inner disc rim and resulting in an over-heating of the disc mid-plane at larger radii. We would like to bring another qualitative insight, based on the symmetries of the problem, in order to explain why the FLD is unable to accurately compute the radiation field in the disc mid-plane.

Consider the situation in the equatorial plane, pictured in Fig. 2.17. If we look at the radiation field at a given radius, after the disc inner rim, the main contribution to the specific intensity comes from two peaks (dotes lines) where the integrated emissivity (red lines) is the biggest. If we look at the angular coordinates of these peaks, they are at a $\mu = \cos\theta_{\rm in} = (1 - (R_{\rm in}/r)^2)^{1/2}$ and $\varphi = 0, \pi$. Now, the angular dependence of the specific intensity, in the FLD approximation, is given by the function ψ_ν Eq. (2.19) which is symmetric around the gradient of J_ν (or equivalently R_ν). In the equatorial plane, because of the equatorial symmetry, $\partial_\Theta J_\nu = 0$ and the gradient is aligned along the radial direct $\hat{r}$. Hence, in the FLD approximation, the radiation field is symmetric around $\hat{r}$

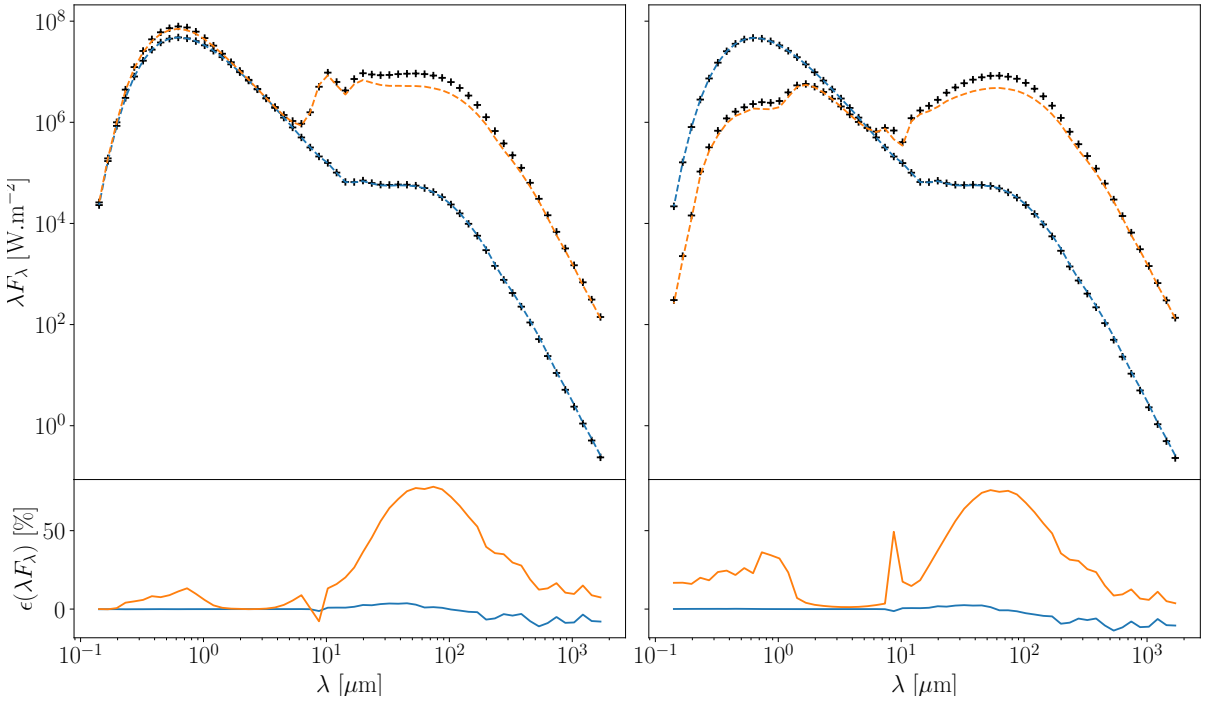

Figure 2.18 – Spectral energy distributions for the axis-symmetric envelope with $\tau_{\nu_0} = 0.1$ (blue curve) and $\tau_{\nu_0} = 100$ (orange curve). The left and right panels correspond to $i = 12.5, 77.5$ deg, respectively. The cross marks represent the solution from this study and the solid curves are computed with RADMC-3D. The lower panels display the relative differences between the two codes.

which is in strong disagreement with the angular dependence of the true radiation field. Hence the FLD, cannot reproduce the two peaks we would expect in these regions, which could explain the observed disagreement in Fig. 2.16.

In contrast, on the inner-cavity, the temperature is very-well reproduced which shows that the inner boundary condition Eq. (2.89) plus the FLD approximation accurately describes the inner disc regions. On the outer edge, while there is a temperature bias inherent to the FLD method as we just explained it, the temperature slope however agrees well, which again confirm the accuracy of the vacuum boundary condition Eq. (2.93).

In Fig. 2.18, we show the spectral energy distributions (SED) for the two test cases, for two inclination angles $i = 12.5, 77.5$ deg with respect to the polar axis and computed via the ray-tracing technique we explained in Sect. 2.4.2. The SEDs is made of the stellar and envelope contributions. The stellar component peaks at around $\lambda \approx 0.6$ μm is computed exactly and the discrepancies are always < 1 % when this part dominates. The optically-thin SED is well-reproduced by the FLD code, even after $\lambda \approx 10$ μm where the contribution for the envelope dominates. The differences with respect to RADMC-3D are always < 15 %, for all inclinations. The SEDs from the optically-tick enveloped is not very-well reproduced. The over-estimation of temperature we discussed previously results in an over-estimation of the dust emission of the disc-mid plane outer regions, that we observe in the SEDs, between 10 and 500 μm. We also note a little over-estimation

at short wavelengths ($\lambda < 1$ μm), where scattering dominates.

We end this section with a comparison of intensity maps of the disc inner 10 AU regions. As we saw it, the temperature in the inner disc regions is quite well reproduced (see Fig. 2.16) and we would like to see if this agreement is reflected in the images we see. In Fig. 2.19, we show the intensity maps of the 10 AU disc inner regions, seen at an inclination of 77.5 deg and at $\lambda = 2.3$, 4.5 and 12 μm. These wavelengths are characteristic of the operating spectral bands of instruments such as GRAVITY (Gravity Collaboration et al., 2017) and MATISSE (Lopez et al., 2022). At $\lambda = 2.3$ μm, the agreement is very good, with discrepancies in the radiation from disc inner rim < 6 %. They increase to 20 % at $\lambda = 4.5$ μm. At $\lambda = 13$ μm, the disagreement is the biggest, especially in the rim outer regions at 4 AU (green curve). We however note that the radiation from the inner radius (centre of the images) is quite well reproduced (~ 10 %).

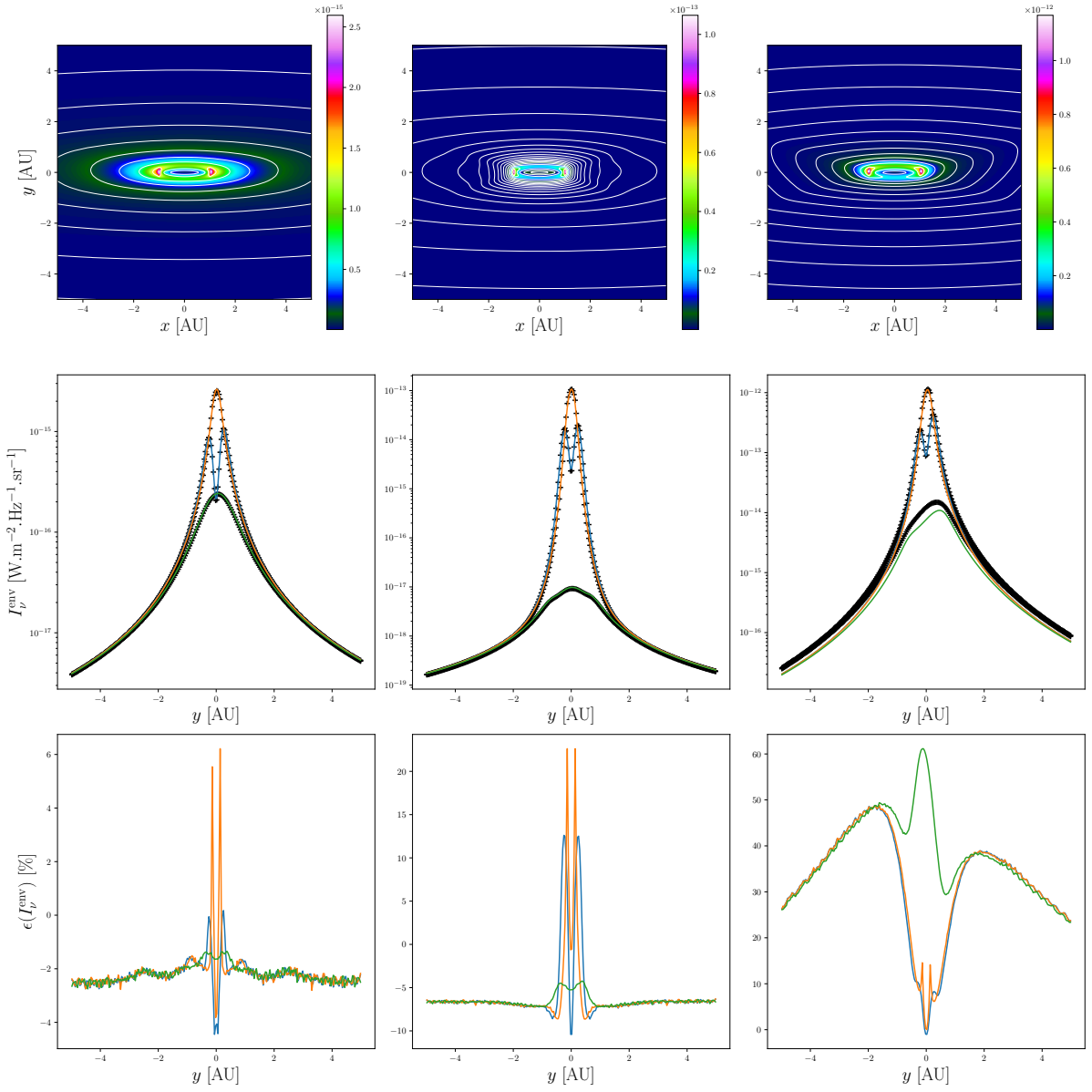

Figure 2.19 – Intensity maps of the 10 AU disc inner regions, seen at an inclination $i = 77.5$ deg and at $\lambda = 2.3$, 4.5 and 12 μm (left, middle and right panels, respectively). The top panels show the intensity maps with white solid lines highlighting the iso-contours of $I_\nu^{\rm env}$. The middle panels represent vertical slices at $x = 0$, 2 and 4 AU (blue, orange and green lines, respectively). The lower panels display the corresponding relative differences between the two codes.

Chapter 3

Discontinuous Galerkin finite element method for the radiative transfer problem inside axis-symmetric circumstellar envelopes

While approximate methods are easier to handle numerically, they often fail to accurately describe the radiation field in complex geometries (Kuiper and Klessen, 2013). In chapter 2, we saw that the FLD approximation, despite being quite accurate in spherical-symmetric systems, is notably less precise in multi-dimensional cases, even provided with mixed non-linear boundary conditions. For these cases, it is necessary to directly numerically solve the radiative transfer equation. In Sect. 1.1.5, we presented the main current techniques used to solve the radiative transfer problem with their inherent advantages and flaws. In this chapter we present another method that did not receive much attention, in the context of astrophysical radiative transfer.

Numerical methods such as finite-elements have already been used to solve the radiative transfer equation. A variant of it, the discontinuous Galerkin finite element method (Reed and Hill, 1973, DG-FEM hereafter), make use of elements and flux integrals along their boundaries, guaranteeing local conservation. However, as opposed to the classical finite-element methods, the reconstructed solution is discontinuous across element edges. The DG-FEM formalism leads to a localised discretisation which offers excellent parallel efficiency as well as efficient adaptive mesh refinement capabilities. Furthermore, the solution present little to no oscillations, even in the cases where the solution displays a non-smooth behaviour (Nair et al., 2011). Likewise finite-differences and ray-tracing techniques, DG-FEM gives direct access to the radiation field and allows to control the error.

The DG-FEM was successfully applied to the one-dimensional spherical neutron transport equation (Machorro, 2007) or more recently to the grey one-dimensional spherical radiative transfer equation in stellar atmospheres (Kitzmann et al., 2016). Extension to the two-dimensional radiative transfer, in cylindrical coordinates, exists in another

context (Cui and Li, 2005).

In this chapter, we explore the capabilities of the method by applying it to the frequency-dependent radiative transfer problem we presented in Sect. 1.2.3. We show that this method can successfully determine the correct temperature profile, and emissivity η_ν, allowing to compute images and spectral energy distributions (SEDs) via ray-tracing techniques. The chapter is organised as follows: in Sect. 3.1, we present the method, applied to a simple equation, in order to introduce the theory and our notations, and in Sect. 3.2, we apply the technique to the radiative transfer problem for axis-symmetric configurations. In Sect. 3.3 we present details concerning numerical aspects of the method. Finally, in Sect. 3.4, we show some numerical tests.

3.1 Presentation of the method

Consider the following conservation law

$$\partial_t u + \boldsymbol{\nabla}.\boldsymbol{F}(u) = S(u). \tag{3.1}$$

$\boldsymbol{F}(u)$ is called the flux of u and $S(u)$ is a source term. Integration of Eq. (3.1) over a volume express the conservation of the quantity u flowing though this volume. Conservation laws are common and describe a wide variety of phenomena (e.g in electromagnetism, fluid mechanics, etc.). In this thesis, we only deal with time-independent problems, and we present the DG-FEM in such context. A more general formulation can be found in Hesthaven and Warburton (2007) or Nair et al. (2011). The radiative transfer equation is a transport equation for photons, hence we only consider the explicit case of a linear advection problem $F(u) = au$. We introduce the DG-FEM and our notations by considering the following time-independent one-dimensional conservation law

$$\begin{aligned} a\,\partial_x u(x) + b\,u(x) = c, \quad & x \in [0,1] = D, \\ & \text{with} \quad u(0) = 0. \end{aligned} \tag{3.2}$$

with a, b, $c > 0$, constant coefficients in D. Eq. (3.2) is identical to the radiative transfer equation Eq. (1.31) along a given ray, inside a static homogeneous medium with a constant source ($b = \kappa_\nu^{\text{ext}}$, $c = \eta_\nu$) and with no boundary inflow, $I_\nu(s = 0) = 0$. For this simple case, we know the solution of Eq. (3.2) is,

$$u(x) = \frac{c}{b}\left(1 - \exp\left\{-\frac{b}{a}x\right\}\right). \tag{3.3}$$

Similarly to standard finite elements methods, we decompose the domain D into N non-overlapping domains $D^k = [x_l^k, x_r^k]$ called "elements", with x_l^k and x_r^k the left and right edges of D^k, respectively. The domain D is then $D = \bigcup_{k=0}^{N-1} D^k$ with $k = 0, ..., N-1$. An illustration of this decomposition is shown in Fig. 3.1-left. Unlike standard finite elements, in the DG-FEM we allow the solution to be discontinuous across elements and we assume that we can approximate the global solution (spanning over the entire domain D) as the direct sum of local piece-wise continuous functions inside each element

$$u(x) \approx u_h(x) = \bigoplus_{k=0}^{N-1} u_h^k(x), \tag{3.4}$$

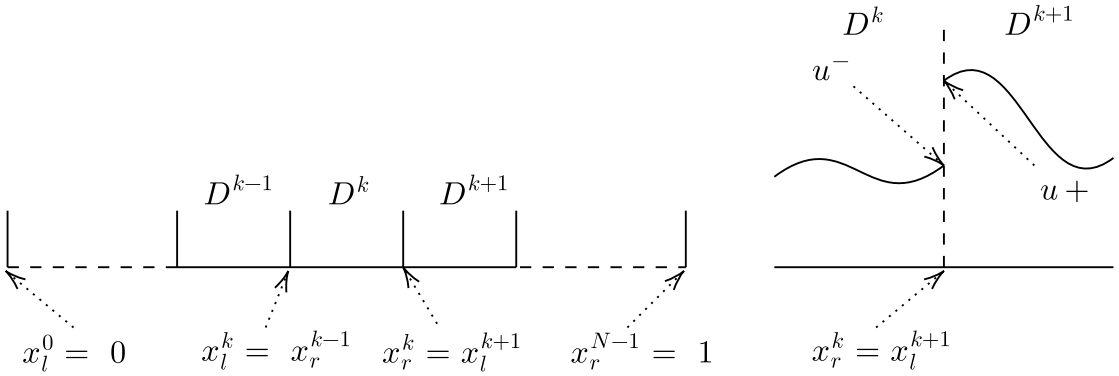

Figure 3.1 – Left: Example of decomposition of the domain D into N non-overlapping one-dimensional elements $D^k = [x_l^k, x_r^k]$. Right: Zoom at the right interface of the D^k element, picturing the discontinuity of the solution u at $x_{k+1/2}$. The numerical flux $F^*(u)$, used to estimate the flux flowing through the element edge, is in general a function of the left and right values u^- and u^+, respectively.

where $u_h^k(x)$ is the local representation of $u(x)$, i.e the numerical approximation of u, inside the element D^k. Within each element, we express the local solution as a polynomial of order n,

$$u_h^k(x) = \sum_{i=0}^{n-1} \hat{u}_i^k \, \psi_i(x) = \sum_{i=0}^{n-1} u_i^k \, h_i^k(x). \tag{3.5}$$

The two representations in Eq. (3.5) are called the modal and nodal forms. In the modal form, we use a basis $\{\psi_0(x), ..., \psi_i(x), ..., \psi_{n-1}(x)\}$. The choice of this basis is problem-dependent. In general, the Legendre polynomials are quite commonly used, but for some specific problems such as, for example, equations on the sphere, spherical harmonics are often used (Fletcher, 2012). In the nodal approach, we define n local grid points $\left\{x_0^k, ..., x_i^k, ..., x_{n-1}^k\right\}$ and the polynomials are defined with the n interpolating Lagrange polynomial $\left\{h_0^k(x), ..., h_i^k(x), ..., h_{n-1}^k(x)\right\}$ passing through these nodes. In this thesis we only consider the nodal representation and refer for example to Nair et al. (2011) for further details on the modal approach. The interpolating Lagrange polynomials are defined as

$$h_i^k(x) = \prod_{\substack{\alpha=0 \\ \alpha \neq i}}^{n-1} \frac{x - x_\alpha^k}{x_i^k - x_\alpha^k}, \tag{3.6}$$

where $\left\{x_0^k, \; ..., \; x_\alpha^k, \; ..., \; x_{n-1}^k\right\}$ are n the arbitrary nodes, in the element D^k, defining the Lagrange polynomials. The choice for these nodes is free and we will discuss this matter later. By definition, the coefficients $u_i^k = u_h^k(x_i^k)$ in Eq. (3.5) correspond to the value of $u_h^k(x)$ at the node of coordinate $x = x_i^k$, since the Lagrange polynomials verifies

$$h_i(x_j) = \delta_{i,j}, \tag{3.7}$$

with $\delta_{i,j}$, the Kronecker delta.

If we insert the form Eq. (3.5) in Eq. (3.2), we obtain the residual $\mathcal{R}_h^k$ of Eq. (3.2) inside each element D^k

$$\mathcal{R}_h^k(x) = \partial_x F(u_h^k(x)) + b\, u_h^k(x) - c, \tag{3.8}$$

with $F(u_h^k(x)) = a\, u_h^k(x)$. Note that $\mathcal{R}_h^k(x)$ is non zero, because we do not insert the true solution Eq. (3.3). In general, a numerical method consists in finding a way to cancel this residual. For example, in standard finite difference methods, we set this residual to be zero on a discrete grid. In the DG-FEM or other standard finite element methods, we use the weak formulation of Eq. (3.2) that consists in cancelling the residual Eq. (3.8), in some integral sense, over the element D^k,

$$\int_{D^k} \mathcal{R}_h^k(x)\, \phi(x)\, \mathrm{d}x = 0 \quad \forall\, D^k, \tag{3.9}$$

where $\phi(x)$ is some weight function, also called the test function. The flux term in Eq. (3.9) can be rewritten, if we integrate it by parts, yielding

$$\int_{D^k} \left(b\, u_h^k(x) - c\right) \phi(x) - F(u_h^k(x)) \partial_x\, \phi(x)\, \mathrm{d}x + \left[F(u_h^k(x))\, \phi(x)\right]_{x_l^k}^{x_r^k} = 0 \quad \forall\, D^k. \tag{3.10}$$

It expresses the requirement of orthogonality between the residual $\mathcal{R}_h^k(x)$ and the test function $\phi(x)$. The integral term in Eq. (3.10) is purely local; it only depends on the solution inside the element D^k. The second term is proportional to the flux at the edge of the element D^k and represents the coupling with the neighbouring elements $D^{k\pm1}$. Unlike standard finite element methods, each element D^k has its own approximate local solution $u_h^k(x)$ and the global solution u_h, over D, is allowed to be discontinuous at the element edges. For example, as pictured by Fig. 3.1-right, at the element right interface x_r^k, there are two different possible values for the solution, when computing the flux function: the left and right value $F(u^-)$ and $F(u^+)$, respectively. This discontinuity must be addressed if we want to compute the flux flowing through the element edge. The way to deal with it is to employ a numerical flux which is a general function of the values adjacent to the discontinuity, $F(u) \approx F^*(u^-, u^+)$. Several choices for this numerical flux are possible, depending on the nature of problem (Cockburn, 2003). In practice, for a linear advection problem $F(u) = au$, the Lax-Friedrichs numerical flux is widely used and is

$$F^*(u^-, u^+) = \frac{1}{2}\left(F(u^-) + F(u^+) - |a|\left(u^+ - u^-\right)\right). \tag{3.11}$$

As it can be seen from Eq. (3.11), if $a > 0$, $F^*(u^-, u^+) = F(u^-)$ and $F^*(u^-, u^+) = F(u^+)$ if $a < 0$, and it reproduces the correct propagation of information for a linear advection problem, characteristic of hyperbolic equations.

The Galerkin formulation consists in assuming that $u_h^k(x)$ and $\phi(x)$ belong to the same finite-dimensional space of functions, hence $\phi(x) = h_i^k(x)$ in our specific case. The weak formulation Eq. (3.10) is then rewritten

$$\begin{aligned} &\int_{D^k} \left(b\, u_h^k(x) - c\right) h_i^k(x) - F(u_h^k(x))\, \partial_x h_i^k(x)\, \mathrm{d}x \\ &+F^*(u_h^-, u_h^+)\, h_i^k(x_r^k) - F^*(u_h^-, u_h^+)\, h_i^k(x_l^k) = 0 \quad \forall\, D^k \text{ and } \forall\, i = 0, ..., n-1. \end{aligned} \tag{3.12}$$

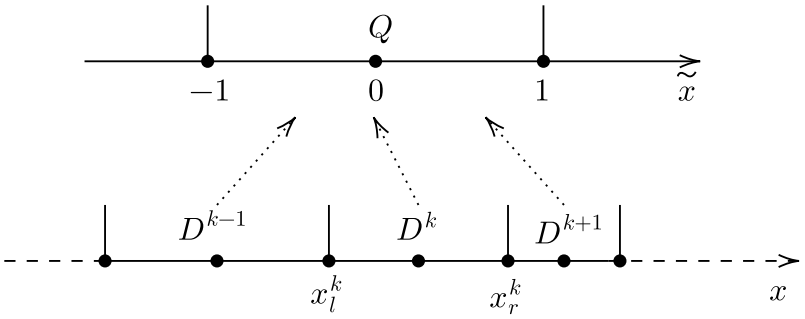

Figure 3.2 – Example of the linear mapping Eq. (3.13) between each element $D^k = [x_l^k, x_r^k]$ and an unique reference element $Q = [-1, 1]$. We show here the special case of the Gauss-Lobatto quadrature nodes (n=3). Note that, with the Gauss-Lobatto quadrature, the end-nodes of a given element D^k coincide with the neighbouring ones. The solution is readily available at the edges for the computation of the numerical flux needed in Eq. (3.12).

Eq. (3.12) is the discontinuous Galerkin formulation of the problem given by Eq. (3.2). It provides us with a system of $N' = N \times n$ [1] equations relating the node coefficients $u_i^k = u_h^k(x_i^k)$ defined in Eq. (3.5). The integral term in Eq. (3.12) can be numerically estimated with the help of quadrature formulae. For computational efficiency, we choose the quadrature roots and the polynomials nodes to be the same. The choice of the quadrature, with the associated roots (nodes) is not unique and is usually problem-dependent (for an extensive review see e.g Kopriva and Gassner, 2010).

Throughout this chapter, we consider the Gauss-Legendre and the Gauss-Lobatto quadrature with the same number of nodes within each elements D^k. All the elements will be mapped to a unique reference element Q, via the following linear transformation

$$\tilde{x} = \frac{2\left(x - \frac{x_l^k + x_r^k}{2}\right)}{\Delta x^k}, \quad \partial_{\tilde{x}} = \frac{\Delta x^k}{2}\partial_x. \tag{3.13}$$

$\tilde{x}$ is the local coordinate ($\tilde{x} \in [-1, 1] = Q$) and $\Delta x^k = x_r^k - x_l^k$ the element width of D^k. The nodes of the quadrature are defined with respect to this local coordinate, $\{\tilde{x}_0, ..., \tilde{x}_i, ..., \tilde{x}_{n-1}\}$. An example of this mapping is shown in Fig. 3.2 for the Gauss-Lobatto quadrature with $n = 3$. The Gauss-Lobatto quadrature is less accurate than the standard Gauss-Legendre quadrature; it can integrate exactly polynomials up to $2n - 3$ degree, whereas the Gauss-Legendre quadrature is exact up to polynomials of $2n - 1$ degree. However, the Gauss-Lobatto quadrature has the numerical advantage of having roots that include the end-points of the element ($\tilde{x}_0 = -1$, $\tilde{x}_{n-1} = 1$), which avoids the need of an interpolation procedure when computing the solution at the element edges, needed for the numerical flux in Eq. (3.12). We give, in Table 3.1, the roots and the associated weights of the Gauss-Legendre and the Gauss-Lobatto quadratures, for the first four orders n.

1. number of elements × number of nodes in each element.

n	Gauss-Legendre		Gauss-Lobatto	
	$\tilde{x}_i$	W_i	$\tilde{x}_i$	W_i
1	0	2	/	/
2	$\pm\frac{1}{\sqrt{3}}$	1	±1	1
3	$\pm\sqrt{\frac{3}{5}}, 0$	$\frac{5}{9}, \frac{8}{9}$	$\pm1, 0$	$\frac{1}{3}, \frac{4}{3}$
4	$\pm\sqrt{\frac{3}{7}+\frac{2}{7}\sqrt{\frac{6}{5}}}, \pm\sqrt{\frac{3}{7}-\frac{2}{7}\sqrt{\frac{6}{5}}}$	$\frac{18-\sqrt{30}}{36}, \frac{18+\sqrt{30}}{36}$	$\pm1, \pm\frac{1}{\sqrt{5}}$	$\frac{1}{6}, \frac{5}{6}$

Table 3.1 – The roots $\tilde{x}_i$ and associated weights W_i for the Gauss-Legendre and Gauss-Lobatto quadratures, for the first four orders n. For the Gauss-Legendre quadrature, the abscissas $\{\tilde{x}_i\}$ $i = 0, ..., n-1$ are the zeros of the Legendre Polynomials $P_n(\tilde{x})$ and the weights are given by $W_i = 2\left[(1-\tilde{x}_i^2)P_n'(\tilde{x}_i)\right]^{-1}$, with $P_n'(\tilde{x}_i)$ the derivative of the Legendre polynomials at $\tilde{x}_i$. For the Gauss-Lobatto quadrature, the abscissas are given by the end-point $\tilde{x}_{0,n-1} = \pm1$ plus the $n-2$ first zeros of the derivative of the Legendre Polynomials $P_{n-1}'(\tilde{x})$. The weights are $W_{0,n-1} = 2[n(n-1)]^{-1}$ for the end-points and $W_i = 2[n(n-1)P_{n-1}(\tilde{x}_i)]^{-1}\,\forall i \neq 0 \,\text{or}\, n-1$.

To compute Eq. (3.12), we first rewrite the DG-FEM formulation with respect to the local coordinate $\tilde{x}$, using Eq. (3.13)

$$\begin{aligned}\frac{\Delta x^k}{2}\int_{-1}^{1}\left(b\,u_h^k(\tilde{x})-c\right)h_i(\tilde{x})\;\mathrm{d}\tilde{x} - \int_{-1}^{1}F(u_h^k)\,\partial_{\tilde{x}}h_i(\tilde{x})\;\mathrm{d}\tilde{x} + F^*(u_h^-,u_h^+)|_{\tilde{x}=1}\,h_i(\tilde{x}=1)\\ -F^*(u_h^-,u_h^+)|_{\tilde{x}=-1}\,h_i(\tilde{x}=-1) = 0, \quad \forall\, D^k \quad \text{and} \quad \forall\, i = 0,\ ...,\ n-1.\end{aligned} \tag{3.14}$$

Second, we use the Gauss-Lobatto quadrature and use the quadrature roots as our node in defining the interpolating Lagrange polynomials Eq. 3.6. The property Eq. (3.7) allows us to write $h_i(\tilde{x}=1) = \delta_{i,n-1}$ and $h_i(\tilde{x}=-1) = \delta_{i,0}$, since the nodes include the element end-points.

For the numerical flux $F^*(u_h^-, u_h^+)$ at the cell edges, we directly use the Lax-Friedrichs numerical flux Eq. (3.11). Since a is a constant and positive throughout the entire computational domain D, Eq. (3.11) simply reduces to $F^*(u_h^-, u_h^+) = F(u_h^-)$, hence we use the left value of the solution, at each element edge (see Fig. 3.1-right). The use of the Gauss-Lobatto quadrature, which includes the element end-points as nodes, allows us to directly write $F^*(u_h^-, u_h^+)|_{\tilde{x}=1} = a\,u_{n-1}^k$ and $F^*(u_h^-, u_h^+)|_{\tilde{x}=-1} = a\,u_{n-1}^{k-1}$.

We compute the integrals in Eq. (3.14) with the help of the Gauss-Lobatto quadrature. The first term is

$$\begin{aligned}\int_{-1}^{1}\left(b\,u_h^k(\tilde{x})-c\right)h_i(\tilde{x})\;\mathrm{d}\tilde{x} &\approx \sum_{j=0}^{n-1}W_j\left(b\,u_h^k(\tilde{x}_j)-c\right)h_i(\tilde{x}_j)\\ &\approx \sum_{j=0}^{n-1}W_j\left(b\,u_j^k-c\right)\delta_{i,j}.\end{aligned} \tag{3.15}$$

We used the property Eq. (3.7) and the definition of the nodal coefficients in $u_h^k(\tilde{x}_j) = u_j^k$. The W_j's are the Gauss-Lobatto quadrature weights (see Table 3.1). In the same way,

the second term is

$$\int_{-1}^{1} F(u_h^k)\,\partial_{\tilde{x}} h_i(\tilde{x})\;\mathrm{d}\tilde{x} \approx a \sum_{j=0}^{n-1} W_j\, u_j^k\, \partial_{\tilde{x}} h_i(\tilde{x}_j), \tag{3.16}$$

$\partial_{\tilde{x}} h_i(\tilde{x}_j)$ are the coefficients of the "differentiation matrix". Their expressions are

$$\partial_{\tilde{x}} h_i(\tilde{x}_j) = \sum_{\substack{\alpha=0 \\ \alpha\neq i}}^{n-1} \frac{1}{\tilde{x}_i - \tilde{x}_\alpha} \prod_{\substack{\beta=0 \\ \beta\neq i \\ \beta\neq\alpha}}^{n-1} \frac{\tilde{x}_j - \tilde{x}_\beta}{\tilde{x}_i - \tilde{x}_\beta}. \tag{3.17}$$

Finally, Eq. (3.14) is then rewritten, regrouping all the terms,

$$\begin{aligned} \sum_{j=0}^{n-1} \left[\left(\frac{\Delta x^k}{2}\, b\, \delta_{i,j} - a\, \partial_{\tilde{x}} h_i(\tilde{x}_j) \right) W_j + a\, \delta_{n-1,j}\, \delta_{i,n-1} \right] u_j^k - a\, \delta_{n-1,j}\, \delta_{i,0}\, u_j^{k-1} \\ = \frac{\Delta x^k}{2} c\, W_i \end{aligned} \tag{3.18}$$

In general Eq. (3.18) can be put in the form of the following linear system

$$\mathcal{A}\, \boldsymbol{u}_h = \boldsymbol{c}. \tag{3.19}$$

$\boldsymbol{u}_h = (u_0^0, ..., u_i^k, ..., u_{n-1}^{N-1})$ is the solution vector, of size N', containing the values of $u_h(x)$ at all the nodes. $\mathcal{A}$ is a sparse matrix of size $N' \times N'$ coupling the elements of $\boldsymbol{u}_h$. $\boldsymbol{c}$ is a vector containing the source term. To put Eq. (3.18) in such a form, we need to combine the element index k and the node index i into one global index. We define the global row index $\alpha = k\,n + i$ and the global column index $\beta = k'\,n + j$ (row major ordering in computer science). This global indices run across all nodes, α, $\beta = 0$, ..., $N' = N \times n$. Summation of Eq. (3.18) over k' yields

$$\begin{aligned} \sum_{k'=0}^{N-1} \sum_{j=0}^{n-1} \Bigg(\left[\left(\frac{\Delta x^k}{2} b\, \delta_{i,j} - a\, \partial_{\tilde{x}} h_i(\tilde{x}_j) \right) W_j + a\, \delta_{n-1,j}\, \delta_{i,n-1} \right] \delta_{k,k'} \\ - a\, \delta_{n-1,j}\, \delta_{i,0}\, \delta_{k-1,k'} \Bigg) u_\beta = \frac{\Delta x^k}{2} c\, W_i. \end{aligned} \tag{3.20}$$

We recognise the following standard matrix-vector product

$$\begin{aligned} \sum_{\beta=0}^{N'-1} \mathcal{A}_{\alpha,\beta}\, u_\beta = c_\alpha, \\ \text{with} \quad \mathcal{A}_{\alpha,\beta} = \left[\left(\frac{\Delta x^k}{2} b\, \delta_{i,j} - a\, \partial_{\tilde{x}} h_i(\tilde{x}_j) \right) W_j + a\, \delta_{n-1,j}\, \delta_{i,n-1} \right] \delta_{k,k'} \\ - a\, \delta_{n-1,j}\, \delta_{i,0}\, \delta_{k-1,k'} \\ \text{and} \quad c_\alpha = \frac{\Delta x^k}{2} c\, W_i. \end{aligned} \tag{3.21}$$

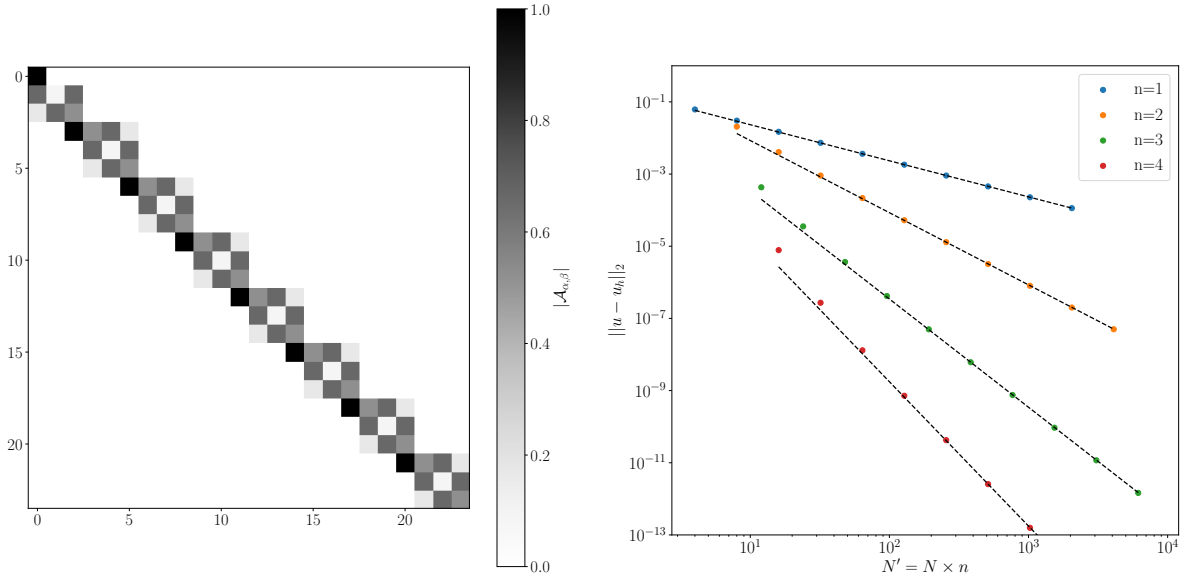

Figure 3.3 – Left: Example of the sparse matrix $\mathcal{A}$ Eq. (3.21) (with $a = b = c = 1$) with $N = 8$ elements and $n = 3$ nodes per element (N' = 24) , illustrating its blocks $(n \times n)$ structure . The only blocks containing non-zero values are the diagonal blocks $A^{k,k}$ and the first lower off-diagonal $A^{k,k-1}$. Right: L_2 norm of the estimate of the error Eq. (3.24) versus the total number of nodes N', for several values of n. The dashed lines show the convergence behaviour $\propto N^{-n}$.

An example of the matrix $\mathcal{A}$ with associated coefficients Eq. (3.21) is shown in Fig. 3.3-left. Eq. (3.19) can be solved with standard iterative or direct methods.

The matrix $\mathcal{A}$ can become very large, especially in the radiative transfer context, and directly storing and solving Eq. (3.19) can become numerically tedious or even impossible. Hopefully, as pictured by Fig. 3.3-left, the matrix $\mathcal{A}$ has a sparse structure. This structure comes from the fact that the DG-FEM is a local formulation i.e, the nodes values u_i^k inside a given element D^k only depend on the other nodes within the same element and the nodes inside the neighbouring ones. This feature makes that $\mathcal{A}$ has a block structure. Consequently $\mathcal{A}$ can be divided into blocks $\mathcal{A}^{k,k'}$ of size $n \times n$, where k', k are the row and column indices defining the position of the block inside $\mathcal{A}$. With this block formulation, we can rewrite Eq. (3.18), taking into account the boundary at element D^0,

$$\begin{aligned} \mathcal{A}^{0,0}\,\boldsymbol{u}_h^0 &= \boldsymbol{c}^0, \\ \mathcal{A}^{k,k}\,\boldsymbol{u}_h^k + \mathcal{A}^{k,k-1}\,\boldsymbol{u}_h^{k-1} &= \boldsymbol{c}^k, \quad \forall\, k = 1, .., N-1, \\ \text{with} \quad \mathcal{A}_{i,j}^{k,k} &= \left(\frac{\Delta x_k}{2} b\,\delta_{i,j} - a\,\partial_{\tilde{x}} h_i(\tilde{x}_j)\right) W_j + a\,\delta_{n-1,j}\,\delta_{i,n-1} \\ \text{and} \quad \mathcal{A}_{i,j}^{k,k-1} &= -a\,\delta_{n-1,j}\,\delta_{i,0}. \end{aligned} \tag{3.22}$$

$\boldsymbol{u}_h^k = (u_0^k, u_1^k, ..., u_{n-1}^k)$ ($\boldsymbol{c}^k = (c_0^k, c_1^k, ..., c_{n-1}^k)$) is the sub-vector of $\boldsymbol{u}_h$ ($\boldsymbol{c}$) of size n containing the nodes values inside the element D^k. $A^{k,k}$ is the diagonal block of $\mathcal{A}$ of size $n \times n$ coupling nodes inside $\boldsymbol{u}_h^k$. $\mathcal{A}^{k,k-1}\boldsymbol{u}_h^{k-1}$ is the coupling term between the element D^k and neighbouring element D^{k-1}. The block structure of the matrix $\mathcal{A}$ clearly appears

in Fig. 3.3-left. The formulation Eq. (3.22) is more efficient to solve numerically and requires less memory than Eq. (3.19), because only the diagonal and first lower off-diagonal blocks are stored and computed rather than the global matrix $\mathcal{A}$.

In general, the boundary conditions can be imposed by modifying the block $\mathcal{A}^{0,0}$ and the sub-vector $\boldsymbol{c}^0$. In our case, we just need to set $\mathcal{A}^{0,0}_{0,0} = 1$, $\mathcal{A}^{0,0}_{0,j} = 0, \quad \forall j = 1, ..., n-1$ and $c^0_0 = 0$ to impose $u(0) = u^0_0 = 0$. Then the system can be simply solved, rewriting Eq. (3.22)

$$\begin{aligned} \mathcal{A}^{0,0}\,\boldsymbol{u}^0_h &= \boldsymbol{c}^0, \\ \mathcal{A}^{k,k}\,\boldsymbol{u}^k_h = \boldsymbol{c}^k - \mathcal{A}^{k,k-1}\,\boldsymbol{u}^{k-1}_h, &\quad k = 1, ..., N-1. \end{aligned} \tag{3.23}$$

which gives us a series of N successive linear systems to solve, starting from $k = 0$ up to $k = N-1$. These linear systems can be efficiently solved with a Gauss elimination method (see Appendix B.1 for a short review of the method).

The numerical solution u_h, given by Eq. (3.23) can be compared with the analytic expression Eq. (3.3). An estimate of the error can be derived, by computing the L_2 norm of the difference between u_h and u

$$\begin{aligned} ||u - u_h||_2 &= \left(\sum_{k=0}^{N-1} \frac{\Delta x_k}{2} \int_{-1}^{1} \left(u^k(\tilde{x}) - u^k_h(\tilde{x}) \right)^2 \, \mathrm{d}\tilde{x} \right)^{\frac{1}{2}}, \\ &\approx \left(\sum_{k=0}^{N-1} \frac{\Delta x_k}{2} \sum_{j=0}^{n-1} W_j \left(u^k(\tilde{x}_j) - u^k_j \right)^2 \right)^{\frac{1}{2}}, \end{aligned} \tag{3.24}$$

with $u^k(\tilde{x}_j)$, the analytic solution evaluated inside the D^k element, at node $\tilde{x}_j$.

We ran several simulations, setting $a = b = c = 1$, for different values of N and n. In Fig. (3.3)-right, we display the estimate of the error Eq. (3.24) with respect to the total number of nodes $N' = N \times n$, for several values of n. We can see that the error descreases as N^{-n}. This result reveals the advantage of having a high-order numerical scheme; for a given error threshold, it is often better to choose a higher-order scheme (higher value of n), since it demands less computer resources (number of nodes) to achieve this threshold. The possibility for the DG-FEM to the control of the order of the numerical scheme is a very desirable property in the radiative transfer context, where we are often limited by numerical resources.

3.2 Solving the radiative transfer equation with the discontinuous Galerkin finite element method

We now present the DG-FEM applied to the radiative transfer equation. A derivation for the one-dimensional spherical-symmetric equation can be found in Kitzmann et al. (2016). We recall the radiative transfer equation, in the spherical coordinate system,

$$\begin{aligned} \mu\,\partial_r I_\nu + \frac{\sqrt{1-\mu^2}\cos\varphi}{r}\partial_\Theta I_\nu + \frac{1-\mu^2}{r}\partial_\mu I_\nu - \frac{\cot\Theta\sqrt{1-\mu^2}\sin\varphi}{r}\partial_\varphi I_\nu \\ + \kappa^{\mathrm{ext}}_\nu\, I_\nu = \eta_\nu, \end{aligned} \tag{3.25}$$

with the coordinates $\boldsymbol{x} = (r, \Theta, \mu = \cos\theta, \varphi)$ as defined in Fig. 1.7. Eq. (3.25) is a four-dimensional equation that we want to solve on the domain $D = [R_{\rm in}, R_{\rm out}] \times]0, \pi/2] \times [-1, 1] \times [0, \pi]$. Note that the radiative transfer equation is not defined at the pole $\Theta = 0$ due to the use of the spherical coordinate system. Also note that in solving Eq. (3.25), we assume that the emissivity term η_ν is known. In this context, solving the equation with the DG-FEM is identical to perform a formal solution to compute the radiation field from the known emissivity (see Sect. 1.1.5). In practice, the scattering term in the emissivity could be treated explicitly, by putting it in the left-hand side of Eq. (3.25), but at the expense of changing the morphology of the matrix of the linear system resulting from the DG-FEM formulation.

In the following, we omit the frequency subscript for simplicity. We first rewrite Eq. (3.25) in the form of a four-dimensional conservation law such as Eq. (3.1)

$$\nabla_{\boldsymbol{x}}.\boldsymbol{F}(\tilde{I}) + \kappa^{\rm ext}\,\tilde{I} = \tilde{\eta}, \tag{3.26}$$

with $\tilde{\eta} = r^2 \sin\Theta\,\eta$. We introduce the quantity $\tilde{I} = r^2 \sin\Theta\, I$, conserved in Eq. (3.26). Using this quantity instead of I is important because it improves the numerical stability, especially near the polar axis at $\Theta = 0$, because the associated flux $\boldsymbol{F}(\tilde{I})$ has smaller variations than $\boldsymbol{F}(I)$. $\nabla_{\boldsymbol{x}}.\boldsymbol{F}(\tilde{I})$ is the Cartesian divergence operator with respect to $\boldsymbol{x} = (r, \Theta, \mu, \varphi)$, acting on the flux vector $\boldsymbol{F}(\tilde{I})$

$$\boldsymbol{F}(\tilde{I}) = \boldsymbol{a}\tilde{I} = \begin{bmatrix} a_r \\ a_\Theta \\ a_\mu \\ a_\varphi \end{bmatrix} \tilde{I} = \begin{bmatrix} \mu \\ \sqrt{1-\mu^2}\cos\varphi/r \\ (1-\mu^2)/r \\ -\cot\Theta\sqrt{1-\mu^2}\sin\varphi/r \end{bmatrix} \tilde{I}. \tag{3.27}$$

We decompose the domain D into $N = N_r \times N_\Theta \times N_\mu \times N_\varphi$ non-overlapping rectangular elements $D^{i,j,k,l}$ with N_r, N_Θ, N_μ, N_φ, the number of elements along the r, Θ, μ, φ coordinate, respectively. Each element is identified with four indices i, j, k, l, ranging from 0 to $N_r - 1$, $N_\Theta - 1$, $N_\mu - 1$, $N_\varphi - 1$. The global approximation of the solution $\tilde{I}_h$ across the domain D is formed by the direct sum of the N piece-wise continuous solution inside each element,

$$\tilde{I}(\boldsymbol{x}) \approx \tilde{I}_h(\boldsymbol{x}) = \bigoplus_{i=0}^{N_r-1} \bigoplus_{j=0}^{N_\Theta-1} \bigoplus_{k=0}^{N_\mu-1} \bigoplus_{l=0}^{N_\varphi-1} \tilde{I}_h^{i,j,k,l}(\boldsymbol{x}). \tag{3.28}$$

Within each element $D^{i,j,k,l}$, we use the nodal representation and express the local solution with the four-dimensional Lagrange polynomials

$$\tilde{I}_h^{i,j,k,l}(\boldsymbol{x}) = \sum_{a=0}^{n_a-1} \sum_{b=0}^{n_b-1} \sum_{c=0}^{n_c-1} \sum_{d=0}^{n_d-1} \tilde{I}_{a,b,c,d}^{i,j,k,l}\, h_{a,b,c,d}(\boldsymbol{x}). \tag{3.29}$$

$h_{a,b,c,d}$ is the four-dimensional Lagrange polynomial defined as

$$\begin{aligned} h_{a,b,c,d}(\boldsymbol{x}) &= h_a(r)\, h_b(\Theta)\, h_c(\mu)\, h_d(\varphi) \\ &= \prod_{\substack{\alpha=0 \\ \alpha\neq a}}^{n_a-1} \frac{r - r_\alpha}{r_a - r_\alpha} \prod_{\substack{\beta=0 \\ \beta\neq b}}^{n_b-1} \frac{\Theta - \Theta_\beta}{\Theta_b - \Theta_\beta} \prod_{\substack{\gamma=0 \\ \gamma\neq c}}^{n_c-1} \frac{\mu - \mu_\gamma}{\mu_c - \mu_\gamma} \prod_{\substack{\delta=0 \\ \delta\neq d}}^{n_d-1} \frac{\varphi - \varphi_\delta}{\varphi_d - \varphi_\delta}. \end{aligned} \tag{3.30}$$

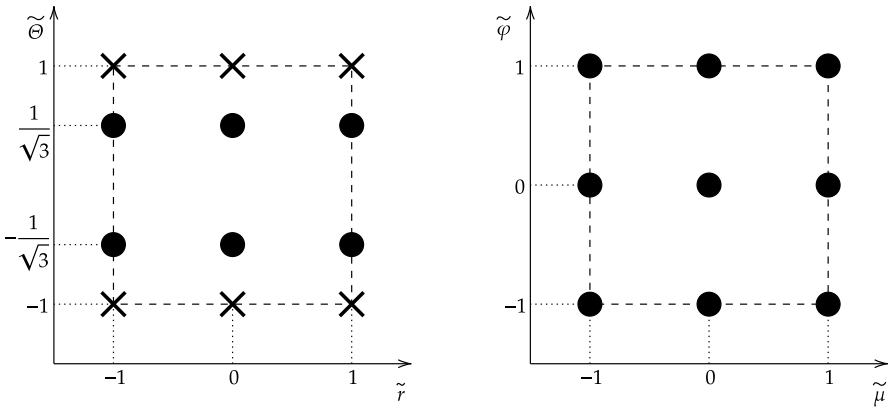

Figure 3.4 – Example of the unique reference element Q (dashed lines) using $n_a = n_c = n_d = 3$ and $n_b = 2$ points. The left and right panels correspond to two-dimensional slices in the (r, Θ) and (μ, φ) planes, respectively. The black dots correspond to the nodes where the coefficients $\tilde{I}^{i,j,k,l}_{a,b,c,d}$ are computed while the crosses correspond to the interpolated value of $\tilde{I}$ used to compute the numerical flux F^* at the interface, along the $\tilde{\Theta}$-coordinate.

with n_a, n_b, n_c, n_d, the number of nodes in each element $D^{i,j,k,l}$, along the r, Θ, μ, φ coordinate, respectively. As we saw it in Sect. 3.1, the coefficients $\tilde{I}^{i,j,k,l}_{a,b,c,d} = \tilde{I}^{i,j,k,l}_h(\boldsymbol{x}^{i,j,k,l}_{a,b,c,d})$ correspond to the value of $\tilde{I}^{i,j,k,l}_h$ at the nodes of coordinates $\boldsymbol{x}^{i,j,k,l}_{a,b,c,d} = (r^i_a, \Theta^j_b, \mu^k_c, \varphi^l_d)$.

As in Sect. 3.1, we use the linear transformation Eq. (3.13) to map each element $D^{i,j,k,l}$ to a unique reference element $Q = [-1,1]\times[-1,1]\times[-1,1]\times[-1,1]$ where the quadrature with the associated nodes are defined. Q is described with the local coordinate $\tilde{\boldsymbol{x}} = (\tilde{r}, \tilde{\Theta}, \tilde{\mu}, \tilde{\varphi})$, with each coordinate defined as in Eq. (3.13). We choose the nodes corresponding to the Gauss-Lobatto quadrature for the r, μ, φ coordinates. In order to avoid the polar singularity at $\Theta = 0$, due to the spherical coordinate system, we use the standard Gauss-Legendre quadrature for the Θ coordinate, which does not include the end-points in each element. An example of Q with the associated nodes is shown in Fig. 3.4.

Let us introduce $\mathcal{R}^{i,j,k,l}_h$, the residual of Eq. (3.26) in the $D^{i,j,k,l}$ element,

$$\mathcal{R}^{i,j,k,l}_h(\boldsymbol{x}) = \nabla_{\boldsymbol{x}}.\boldsymbol{F}(\tilde{I}^{i,j,k,l}_h(\boldsymbol{x})) + \kappa^{\text{ext}}\,\tilde{I}^{i,j,k,l}_h(\boldsymbol{x}) - \tilde{\eta}(\boldsymbol{x}). \tag{3.31}$$

As in Eq. (3.12) we form the Discontinuous Galerkin formulation by multiplying the residual with the test function belonging to the Lagrange polynomials and integrating over the element,

$$\int_{D^{i,j,k,l}} \mathcal{R}^{i,j,k,l}_h(\boldsymbol{x})\; h_{a',b',c',d'}(\boldsymbol{x})\; \mathrm{d}^4\boldsymbol{x} = 0, \quad \forall\, D^{i,j,k,l} \quad \text{and} \quad \forall\, h_{a',b',c',d'}. \tag{3.32}$$

The divergence term in Eq. (3.32) can be recast, with the help of the divergence theorem

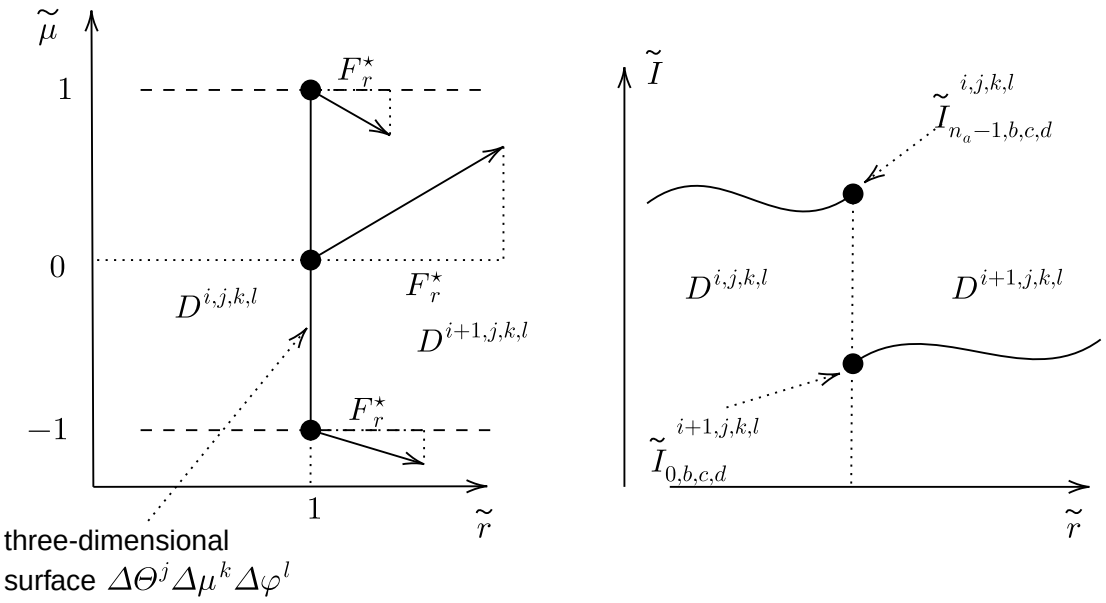

Figure 3.5 – Left: Example of a two-dimensional view $(\tilde{r}, \tilde{\mu})$ of the element $D^{i,j,k,l}$ and its neighbour $D^{i+1,j,k,l}$. The radial numerical flux must be evaluated at the nodes of the quadrature $(\tilde{r} = 1, \tilde{\Theta}_b, \tilde{\mu}_c, \tilde{\varphi}_d)$ lying on the three-dimensional surface at $\tilde{r} = 1$. Right: Zoom on one of these nodes. The value of $\tilde{I}$ is discontinuous and the numerical flux is computed using Eq. (3.36).

(Green-Ostrogradsky), into

$$\int_{D^{i,j,k,l}} \left(\kappa^{\text{ext}}\,\tilde{I}_h^{i,j,k,l} - \tilde{\eta}\right) h_{a',b',c',d'} - \boldsymbol{F}(\tilde{I}_h^{i,j,k,l}).\,\boldsymbol{\nabla}_{\boldsymbol{x}}\, h_{a',b',c',d'}\ \mathrm{d}^4\boldsymbol{x} + \oint_{\partial D^{i,j,k,l}} \boldsymbol{s}.\boldsymbol{F}^*(\tilde{I}^-,\tilde{I}^+)\, h_{a',b',c',d'}\ \mathrm{d}^3\boldsymbol{x} = 0, \quad \forall\, D^{i,j,k,l} \quad \text{and} \quad \forall\, h_{a',b',c',d'}. \tag{3.33}$$

As in Eq. (3.12), we identify the first integral as the local one. $\boldsymbol{\nabla}_{\boldsymbol{x}}\, h_{a',b',c',d'}$ is the four-dimensional gradient of the Lagrange polynomial $h_{a',b',c',d'}$. The second term in Eq. (3.33) is a surface integral and represents the coupling between $D^{i,j,k,l}$ and its neighbours. This time, instead of Eq. (3.12), it is a three-dimensional surface integral over the boundaries of the four-dimensional element $D^{i,j,k,l}$. $\boldsymbol{s}$ is the outward normal vector to the surface element and $\boldsymbol{s}.\boldsymbol{F}^*(\tilde{I}^-,\tilde{I}^+)$ is the normal component of the numerical flux, arising because the solution is discontinuous at the element edges. We note that since each element $D^{i,j,k,l}$ is a four-dimensional cube, the surface integral is made of $2\times 4 = 8$ contributions. To have a better understanding of this term, let us give an example by computing one on the contributions, e.g for the radial surface edge $\tilde{r} = 1$ ($\boldsymbol{s} = \hat{r}$). The radial flux $F_r^\star(\tilde{I}^-,\tilde{I}^+) = \boldsymbol{s}.\boldsymbol{F}^*(\tilde{I}^-,\tilde{I}^+)$ flowing across the three-dimensional surface $\Delta\Theta^j\Delta\mu^k\Delta\varphi^l$ is

$$\frac{\Delta\Theta^j\,\Delta\mu^k\,\Delta\varphi^l}{8}\int_{-1}^{1} F_r^\star(\tilde{I}^-,\tilde{I}^+)\, h_{a',b',c',d'}(\tilde{r}=1)\ \mathrm{d}\tilde{\Theta}\,\mathrm{d}\tilde{\mu}\,\mathrm{d}\tilde{\varphi}. \tag{3.34}$$

Performing, the integration, with the help of the quadrature formulae, Eq. (3.34) is rewritten, using also the property Eq. (3.7),

$$\frac{\Delta\Theta^j\,\Delta\mu^k\,\Delta\varphi^l}{8}\sum_{b,c,d} W_b\,W_c\,W_d\,F^\star_{r\,\tilde{r}=1,b,c,d}(\tilde{I}^-,\tilde{I}^+)\,\delta_{na-1,a}\,\delta_{b',b}\,\delta_{c',c}\,\delta_{d',d}. \tag{3.35}$$

The situation is pictured in Fig. 3.5. We must evaluate $F^\star_{r\,\tilde{r}=1,b,c,d}$, the radial numerical flux at the nodes of coordinates $(\tilde{r}=1,\tilde{\Theta}_b,\tilde{\mu}_c,\tilde{\varphi}_d)$. We use the Lax-Friedrichs numerical flux, as defined in Eq. (3.11), that we rewrite

$$F^\star_{r\,\tilde{r}=1,b,c,d}(\tilde{I}^-,\tilde{I}^+) = \max\left(a_r{}^{i,j,k,l}_{na-1,b,c,d},\,0\right)\tilde{I}^{i,j,k,l}_{na-1,b,c,d} + \min\left(a_r{}^{i+1,j,k,l}_{0,b,c,d},\,0\right)\tilde{I}^{i+1,j,k,l}_{0,b,c,d}. \tag{3.36}$$

Eqs. (3.35) and (3.36) give the flux of $\tilde{I}$ flowing through the upper radial surface of the element $D^{i,j,k,l}$. Doing the previous derivation for all the other seven surfaces yields the complete surface term in Eq. (3.33).

Eq. (3.33) is a system of $N' = N\times n = N\times n_a\times n_b\times n_c\times n_d$ equations, relating the coefficients $\tilde{I}^{i,j,k,l}_{a,b,c,d}$. The system Eq. (3.33) can be formally written

$$\mathcal{A}\,\tilde{\boldsymbol{I}}_h = \boldsymbol{\mathcal{B}}, \tag{3.37}$$

with $\tilde{\boldsymbol{I}}_h = (\tilde{I}^{0,0,0,0}_{0,0,0,0},\ldots,\tilde{I}^{i,j,k,l}_{a,b,c,d},\ldots,\tilde{I}^{N_r-1,N_\Theta-1,N_\mu-1,N_\varphi-1}_{n_a-1,n_b-1,n_c-1,n_d-1})$ the vector of size N' containing the solution points of the full domain D, $\mathcal{A}$ a sparse matrix of size $N'\times N'$ coupling the elements of $\tilde{\boldsymbol{I}}_h$ and $\boldsymbol{\mathcal{B}}$ a vector containing the emissivity term $\tilde{\eta}$.

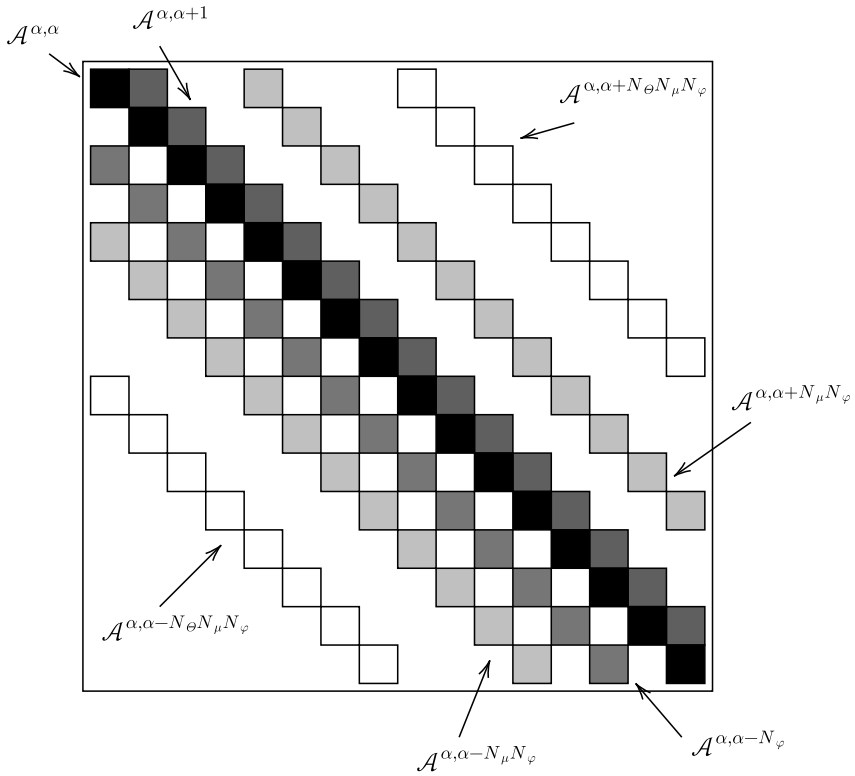

Figure 3.6 – Example of the sparse structure of $\mathcal{A}$ with $N_r = N_\Theta = N_\mu = N_\varphi = 2$. The squares represent the blocks of size $n \times n$ containing non-zero values. The matrix has banded corresponding to the coupling terms $\mathcal{A}^{\alpha,\alpha}$, $\mathcal{A}^{\alpha,\alpha+1}$, $\mathcal{A}^{\alpha,\alpha-N_\varphi}$, $\mathcal{A}^{\alpha,\alpha\pm N_\mu N_\varphi}$, $\mathcal{A}^{\alpha,\alpha\pm N_\Theta N_\mu N_\varphi}$ blocks.

In practice, for most applications the matrix $\mathcal{A}$ is too big to be stored on a computer. For example, in our numerical tests in Sect. 3.4, we use 16^4 elements, with $3\times2\times3\times3$ nodes in each, resulting in a matrix $\mathcal{A}$ of $\sim 1.25\times10^{13}$ elements, or 728 TB of computer memory in double precision. We already discussed in Sect. (3.1) about the local formulation inherent to the DG-FEM method, where the solution points $\tilde{I}^{i,j,k,l}_{a,b,c,d}$ within a given element $D^{i,j,kl}$ only depend on the other points within the same element and the neighbouring cells $D^{i\pm1,j\pm1,k-1,l+1}$. We note that the elements $D^{i,j,k+1,l}$ and $D^{i,j,k,l-1}$ do not contribute because we use the Lax-Friedrichs numerical flux Eq. (3.11) and $a_\mu \geq 0$, $a_\varphi \leq 0$, $\forall\, \boldsymbol{x} \in D$ (see Eq. 3.36). We can rewrite Eq. (3.37) as a block formulation, similar to Eq. (3.22) with the help of the block index $\alpha = i\,N_\Theta N_\mu N_\varphi + j\,N_\mu N_\varphi + k\,N_\varphi + l$ to identify the position of each block in $\mathcal{A}$

$$\begin{aligned}\mathcal{A}^{\alpha,\alpha}\,\tilde{\boldsymbol{I}}^{\alpha}_h + \mathcal{A}^{\alpha,\alpha+N_\Theta N_\mu N_\varphi}\,\tilde{\boldsymbol{I}}^{\alpha+N_\Theta N_\mu N_\varphi}_h + \mathcal{A}^{\alpha,\alpha-N_\Theta N_\mu N_\varphi}\,\tilde{\boldsymbol{I}}^{\alpha-N_\Theta N_\mu N_\varphi}_h \\ +\mathcal{A}^{\alpha,\alpha+N_\mu N_\varphi}\,\tilde{\boldsymbol{I}}^{\alpha+N_\mu N_\varphi}_h + \mathcal{A}^{\alpha,\alpha-N_\mu N_\varphi}\,\tilde{\boldsymbol{I}}^{\alpha-N_\mu N_\varphi}_h + \mathcal{A}^{\alpha,\alpha-N_\varphi}\,\tilde{\boldsymbol{I}}^{\alpha-N_\varphi}_h \\ +\mathcal{A}^{\alpha,\alpha+1}\,\tilde{\boldsymbol{I}}^{\alpha+1}_h = \boldsymbol{\mathcal{B}}^{\alpha}.\end{aligned} \tag{3.38}$$

$\tilde{\boldsymbol{I}}^{\alpha}_h = (\tilde{I}^{\alpha}_{0,0,0,0}, ..., \tilde{I}^{\alpha}_{a,b,c,d}, ..., \tilde{I}^{\alpha}_{n_a-1,n_b-1,n_c-1,n_d-1})$ is a sub-vector of $\tilde{\boldsymbol{I}}_h$ of size n, containing the solution nodes inside the element $D^\alpha = D^{i,j,k,l}$. $\mathcal{A}^{\alpha,\alpha}$ is the diagonal block of $\mathcal{A}$ of size $n\times n$ coupling the nodes in D^α. $\boldsymbol{\mathcal{B}}^\alpha$ is the term proportional to the emissivity in the element D^α and the other terms are the communication terms with the adjacent elements. An example of the structure of the matrix $\mathcal{A}$ with the associated blocks is shown in Fig. 3.6. As it can be seen the matrix $\mathcal{A}$ has a block-banded structure. The formulation Eq. (3.38) allows us to only store the blocks containing non-zero values in $\mathcal{A}$.

We note that in our case the system Eq. (3.38) is non-linear because the $\boldsymbol{\mathcal{B}}^\alpha$ term contains the emissivity $\eta_\nu = \kappa^{\rm abs}_\nu\, B_\nu(T) + \kappa^{\rm sca}_\nu\, J_\nu$ which depends implicitly on $\tilde{I}$, via the mean specific intensity J_ν (see Eq. 1.5) and via $B_\nu(T)$ through the radiative equilibrium equation Eq. (1.66).

3.3 Solution strategy and numerical considerations

The solution of the complete problem presented in Sect. 1.2.3 involves the determination of the full radiation field I_ν Eq. (1.65) for all frequency points, coupled with the equation of radiative equilibrium Eq. (1.66). We solve the radiative transfer problem on a discrete, logarithmically spaced [2], frequency grid ν_m, with $m = 0, ..., N_\nu - 1$ and N_ν the number of frequency points. For the test cases we consider in Sect. 3.4, the star is treated in the point source approximation, hence we directly use Eqs. (1.68) and (1.69) to treat $I^\star_\nu$, the stellar component of the radiation field. The radiation field of the envelope $I^{\rm env}_\nu$ Eq. (1.67) is solved with the DG-FEM presented in Sect. 3.2, via Eq. (3.38). For simplicity, we omit the envelope superscript but implicitly refer to this contribution below.

The solution vector is now composed of the radiation field at all the spatial-angular nodes $(r^i_a, \Theta^j_b, \mu^k_c, \varphi^l_d)$, plus the dust temperature at all spatial nodes (r^i_a, Θ^j_b), $\boldsymbol{X} = ((\tilde{\boldsymbol{I}}^0_h)^0, (\tilde{\boldsymbol{I}}^\alpha_h)^m, ..., (\tilde{\boldsymbol{I}}^{N-1}_h)^{N_\nu-1}, T^{0,0}_{0,0}, ..., T^{i,j}_{a,b}, ..., T^{N_r-1,N_\Theta-1}_{n_a-1,n_b-1})$. We use the same method as the one presented in Sect. 2.3.5. Let us call n, the iteration of the method.

2. To account for the important dynamic of the solution with respect to this variable.

For the initial condition $\boldsymbol{X}^0$ ($n=0$), we assume the radiation field of the envelope to be zero everywhere, $(\tilde{\boldsymbol{I}}_h^\alpha)^m = \boldsymbol{0}$. Accordingly, the initial dust temperature is computed with the help of the following discrete version of the radiative equilibrium Eq. (1.66),

$$\sum_{m=0}^{N_\nu-1} W_m \left(\kappa^{\mathrm{abs}\,i,j}_{a,b}\right)^m \left(\left(J^{i,j}_{a,b}\right)^m + \left(J^{\star\,i,j}_{a,b}\right)^m\right) = \sum_{m=0}^{N_\nu-1} W_m \left(\kappa^{\mathrm{abs}\,i,j}_{a,b}\right)^m B_m(T). \tag{3.39}$$

where W_m are the quadrature weights used for the numerical estimate of the integral. $J^{\star\,i,j}_{a,b}$ is computed directly using Eq. (1.69). As in Eq. (2.108), the right-hand side of Eq. (3.39) is pre-computed in a table for a large range of temperatures, and the temperature at the spatial node $T^{i,j}_{a,b}$ is found by interpolation of the left-hand side in this table. We then use the Planck law Eq. (1.7) to compute the corresponding $B^{i,j}_{a,b}$.

Then, for each frequency, we update the radiation field of the envelope, by performing a Gauss-Seidel forward sweep (see Appendix B.2), on all elements D^α to compute $(\tilde{\boldsymbol{I}}_h^\alpha)^m$ at the next iterate $n+1$

$$\begin{aligned}
\mathcal{A}^{\alpha,\alpha}\left[\tilde{\boldsymbol{I}}_h^\alpha\right]^{n+1} &= [\boldsymbol{b}^\alpha]^{n,n+1} \\
\text{with}\quad [\boldsymbol{b}^\alpha]^{n,n+1} &= [\boldsymbol{\mathcal{B}}^\alpha]^n - \mathcal{A}^{\alpha,\alpha+N_\Theta N_\mu N_\varphi}\left[\tilde{\boldsymbol{I}}_h^{\alpha+N_\Theta N_\mu N_\varphi}\right]^n \\
&- \mathcal{A}^{\alpha,\alpha-N_\Theta N_\mu N_\varphi}\left[\tilde{\boldsymbol{I}}_h^{\alpha-N_\Theta N_\mu N_\varphi}\right]^{n+1} - \mathcal{A}^{\alpha,\alpha+N_\mu N_\varphi}\left[\tilde{\boldsymbol{I}}_h^{\alpha+N_\mu N_\varphi}\right]^n \\
&- \mathcal{A}^{\alpha,\alpha-N_\mu N_\varphi}\left[\tilde{\boldsymbol{I}}_h^{\alpha-N_\mu N_\varphi}\right]^{n+1} - \mathcal{A}^{\alpha,\alpha-N_\varphi}\left[\tilde{\boldsymbol{I}}_h^{\alpha-N_\varphi}\right]^{n+1} - \mathcal{A}^{\alpha,\alpha+1}\left[\tilde{\boldsymbol{I}}_h^{\alpha+1}\right]^n.
\end{aligned} \tag{3.40}$$

This gives us a series of N linear systems to solve, starting from $\alpha=0$ to $\alpha=N-1$. They are successively solved, using a Gauss elimination method (see Appendix B.1). The blocks of $\mathcal{A}$ depend on the geometry of the problem and on the absorption and scattering coefficients. They are thus computed once and for all. We give in Appendix C the expressions for $\mathcal{A}^{\alpha,\alpha}$ and for $\boldsymbol{b}$ in Eq. (3.40).

To insure the boundary conditions Eqs. (1.70), (1.71) and (1.72), we need to modify the block $\mathcal{A}^{\alpha,\alpha}$ and the right-hand side $\boldsymbol{b}$ when an element D^α is touching the boundaries of the computational domain.

Once the envelope radiation field $(\tilde{\boldsymbol{I}}_h^\alpha)^m$ has been updated, $\forall\,\alpha, m$, we need to update the source term $\mathcal{B}^\alpha$ for the next iteration. This requires the computation of the emissivity $\eta_\nu = \kappa_\nu^{\mathrm{abs}}\,B_\nu(T) + \kappa_\nu^{\mathrm{sca}}(J_\nu^\star + J_\nu)$ and thus the computation of J_ν and the dust temperature T at each spatial node (r_a^i, Θ_b^j). For J_ν it is directly estimated from the envelope radiation field at the node, following the definition Eq. (1.5)

$$\begin{aligned}
J^{i,j}_{a,b} &= \frac{1}{2\pi\, {r_a^i}^2\,\sin\Theta_b^j}\int_0^\pi \mathrm{d}\varphi \int_{-1}^1 \tilde{I}_h^\alpha(r_a^i,\Theta_b^j,\mu,\phi)\;\mathrm{d}\mu \\
&= \frac{1}{2\pi\, {r_a^i}^2\,\sin\Theta_b^j}\sum_{k=0}^{N_\mu-1}\sum_{l=0}^{N_\varphi-1}\frac{\Delta\mu_k\,\Delta\phi_l}{4}\int_{-1}^1 \mathrm{d}\tilde{\varphi}\int_{-1}^1 \tilde{I}_h^\alpha(r_a^i,\Theta_b^j,\tilde{\mu},\tilde{\varphi})\;\mathrm{d}\tilde{\mu} \\
&\approx \frac{1}{8\pi\, {r_a^i}^2\,\sin\Theta_b^j}\sum_{k=0}^{N_\mu-1}\sum_{l=0}^{N_\varphi-1}\Delta\mu_k\,\Delta\phi_l\sum_{c=0}^{n_c-1}\sum_{d=0}^{n_d-1} W_c W_d\,\tilde{I}^{i,j,k,l}_{a,b,c,d}.
\end{aligned} \tag{3.41}$$

	Ivezic et al. (1997)	Sect. 3.4.1	Pascucci et al. (2004)	Sect. 3.4.2
Optical depth τ_{ν_0}	1	10^2	10^{-1}	10^2
$\epsilon(T)$ (%)	0/0/0	0/0/1	0/0/0	1/0/2
$\epsilon\,(\mathrm{SED})_{i=12.5\mathrm{deg}}$ (%)	-/-/-	-/-/-	2/2/6	2/3/10
$\epsilon\,(\mathrm{SED})_{i=77.5\mathrm{deg}}$ (%)	2/2/8	1/2/2	2/2/5	3/4/24

Table 3.2 – Relative differences for the temperature profiles $\epsilon(T)$ and for the SEDs $\epsilon\,(\mathrm{SED})$ of the two test problems. The results are presented in the form mean($|\epsilon|$) / std($|\epsilon|$) / max($|\epsilon|$) and rounded to the closest percent.

We performed the integration from 0 to π for the φ coordinate, because of the planar symmetry of the radiation field with respect to the plane (r, Θ), due to the axis-symmetry of the disc. We made use of the local coordinate system, defined in Eq. (3.13) and approximated the integrals with the quadrature formulae we used for the μ and φ coordinates, with the corresponding weights W (see Table 3.1). The dust temperature, at the spatial nodes is computed with the help of the radiative equilibrium equation Eq. (3.39).

After this, the solution vector $\boldsymbol{X}$ has been completely updated and we repeat the procedure until convergence. Again, for the convergence criterion, we use is the maximal value of relative differences between two consecutive iterates of the envelope mean radiation field falls below a small arbitrary number ϵ.

$$\max_{m,i,j,a,b}\left(\left|\left[\left(J^{i,j}_{a,b}\right)^m\right]^{n+1} - \left[\left(J^{i,j}_{a,b}\right)^m\right]^{n}\right| \Big/ \left[\left(J^{i,j}_{a,b}\right)^m\right]^{n}\right) \leq \epsilon \tag{3.42}$$

3.4 Numerical tests

We consider the numerical tests we presented in Chapter 2. The first test case we consider in Sect. 3.4.1 is the frequency-dependent radiative transfer problem in a spherically-symmetric envelope, from Ivezic et al. (1997). Then, in Sect. 3.4.2, we treat the frequency-dependent radiative transfer in an axis-symmetric envelope (disc), from Pascucci et al. (2004). A summary of the main results is presented in Table 3.2.

3.4.1 1D spherically symmetric envelope

We refer to Sect. 2.3.6 for the presentation of the benchmark. In this section, we only consider the cases with the $p = 2$ for the exponent in the number density law, and the moderately-thick and thick envelopes $\tau_{\nu_0} = 1$, 100, respectively.

For the DG-FEM grid, we use a grid of $N = N_r \times N_\Theta \times N_\mu \times N_\varphi = 16^4$ elements with each element containing $n_a \times n_b \times n_c \times n_d = 3 \times 2 \times 3 \times 3$ nodes, as pictured by Fig. 3.4. For the radial coordinate, the cell edges are logarithmically spaced, to account for the important dynamic of the solution with respect to the radius. For all others coordinates, we consider a linear sampling of the elements. The frequency grid consists of $N_\nu = 60$ logarithmically spaced points, ranging from $\lambda_{N_\nu - 1} = 10^{-2}$ μm to $\lambda_0 = 3.6 \times 10^4$ μm. The spectral energy distribution (SED), emerging from the envelope, is obtained, via ray-tracing of the emissivity term as explained in Sect. 2.4.2.

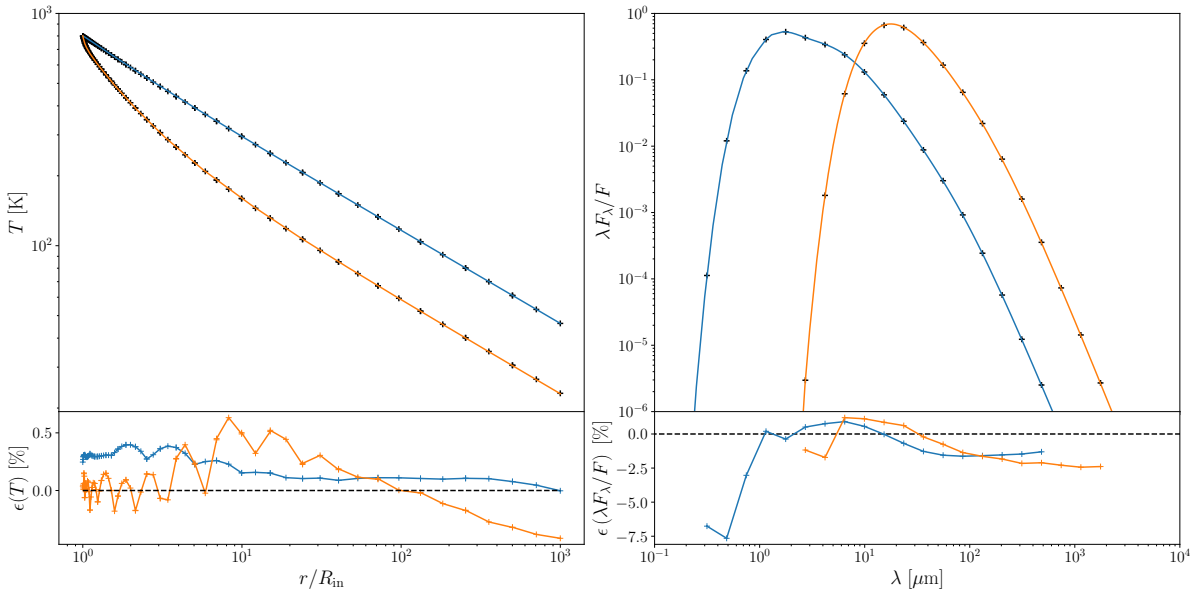

Figure 3.7 – Temperature profiles (left panels) and normalised SEDs (right) for the spherically symmetric envelope, with $\tau_{\nu_0} = 1$ (blue curve) and $\tau_{\nu_0} = 10^2$ (orange curve). The cross marks represent the solution from this study and the solid curves are computed with DUSTY (Ivezic et al., 1997). The lower panels display the relative differences between the two codes.

The radial temperature profile T and the normalised spectral energy distribution (SED) $\lambda F_\lambda / F$ $\left(F = \int_0^\infty F_\lambda \, d\lambda\right)$ of the envelope are shown in Fig. 3.7. For the DG-FEM code, the temperature corresponds to the mean radial profile across all nodal points Θ. The spatial and frequency grids differ between both codes and we perform a linear interpolation (in log-log scaling) of the DUSTY profiles at our grid points for comparison. We observe a good agreement between the two codes. On average, the absolute relative differences stay below 1 % for the temperature and 2 % for the SEDs.

3.4.2 2D axis-symmetric envelope

We refer to Sect. 2.4.4 for the detailed presentation of the test. For the DG-FEM code we use the same spatial, angular, and frequency grid as in Sect. 3.4.1. For RADMC-3D, we also use the same setup as in Sect. 2.4.4.

The temperature T of the disc is displayed in Fig. 3.8. The DG-FEM code successfully reproduces the temperature profile. The temperature regions with steep gradients are always well reproduced, even with a fairly reasonable number of nodes. This result is a direct consequence of having a high-order numerical scheme. The radiation field can exhibit discontinuities, because of boundary conditions or very strong density gradients. Our numerical tests revealed no oscillations and very few negative values for the specific intensity that did not pollute the computation of the mean radiation field. On average, the absolute relative differences stay below one percent for both test cases. The temperature in the disc mid-plane is very-well reproduced, highlighting that the method is able to

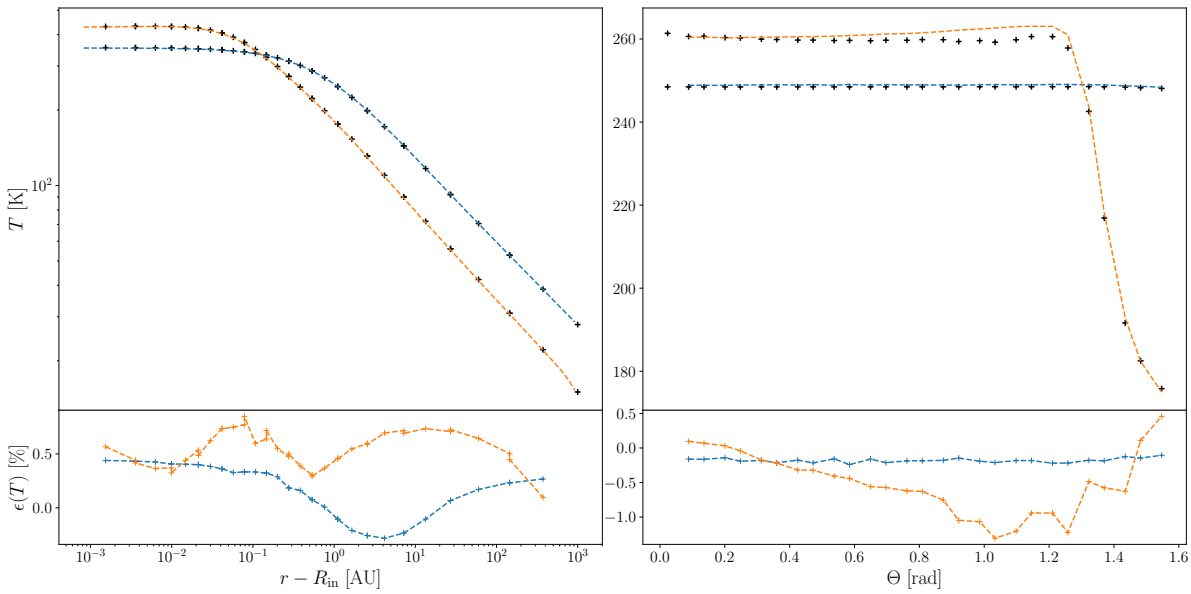

Figure 3.8 – Temperature profiles for the axis-symmetric envelope with $\tau_{\nu_0} = 10^{-1}$ (blue curve) and $\tau_{\nu_0} = 10^2$ (orange curve), in the in the disc-mid-plane (left panel) and at r=2 AU (right panel). The cross marks represent the solution from this study and the solid curves are computed with RADMC-3D. The lower panels display the relative differences between the two codes.

correctly capture the shadow of the disc in the disc mid-plane outer regions (see Sect. 2.4.4 for an explanation of the effect).

In Fig. 3.9, we display the corresponding SEDs, for two inclinations with respect to the polar axis $i = 12.5, 77.5$ deg. Again our SEDs, computed from ray-tracing of the emissivity η_ν derived with the DG-FEM code, show good agreement: around the stellar peak at ~ 0.5 μm as well as the emission of the envelope at wavelengths larger than ~ 10 μm. On average, the absolute relative differences stays below 5 %. We note a peak in the discrepancies for the optically-thick case, between 8.7 and 10.2 μm (according to the resolution of our frequency grid). The same peak is also present when we compare the RADMC-3D SEDs with the ones obtained from the FLD approximation (see Fig. 2.18). Then we conclude that this peak can either be due to our ray-tracer or from the solution of RADMC-3D. We note that the same behaviour was previously observed in Pascucci et al. (2004), between a grid-based and a Monte-Carlo code. The authors suggested that, at these wavelengths, the flux mainly comes from the inner disc regions (between 1 and 2 AU) and the numerical simulations are particularly sensitive to the resolution of the inner parts. However we tried to increase the resolution in these regions which did not result in any improvement.

In Fig. 3.10, we show a set of intensity maps, ray-traced from the DG-FEM solution, of the 10 AU disc inner regions, at $\lambda = 2.3, 4.5, 12.1$ μm and for several inclinations $i = 12.5, 77.5, 90$ deg. These wavelengths are characteristic of the operating spectral bands of instruments such as GRAVITY (Gravity Collaboration et al., 2017) and MATISSE

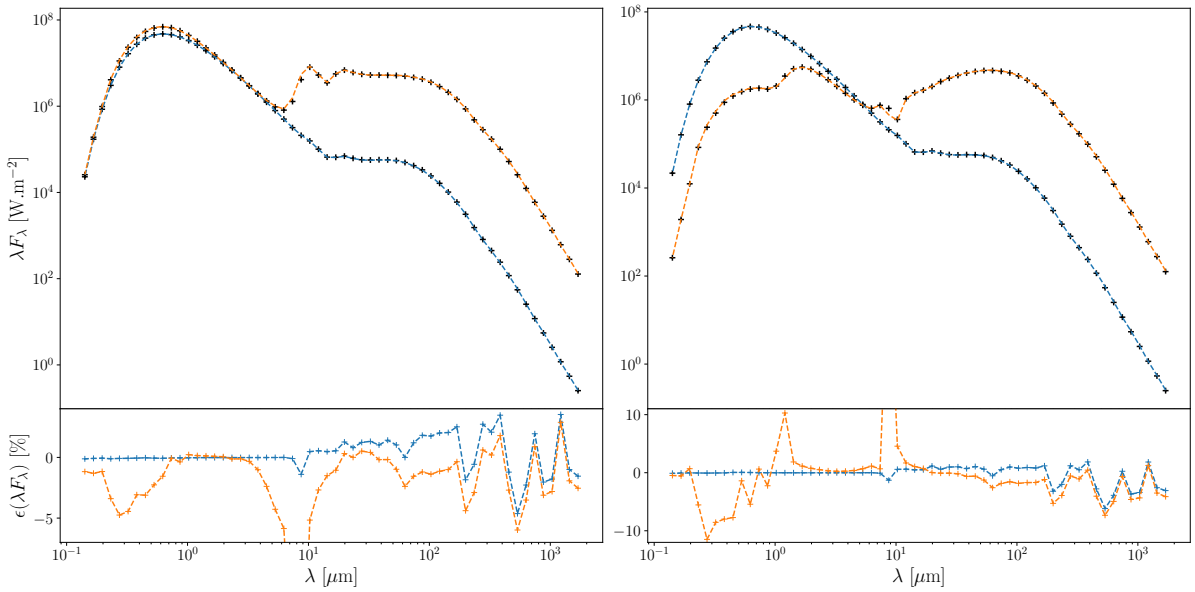

Figure 3.9 – SEDs profiles for the axis-symmetric envelope with $\tau_{\nu_0} = 10^{-1}$ (blue curve) and $\tau_{\nu_0} = 10^2$ (orange curve). The left and right panels correspond to $i = 12.5, 77.5$ deg, respectively. The cross marks represent the solution from this study and the solid curves are computed with RADMC-3D. The lower panels display the relative differences between the two codes.

(Lopez et al., 2022). On average, the agreement between the images from the DG-FEM code and the images from RADMC-3D is around 10 % for all frequencies and inclinations.

We show in Fig. 3.11 the comparison of an image slice at $x = 0$ AU, for two inclinations $i = 12.5, 77.5$ deg and for $\lambda = 2.3, 4.5, 12.1$ μm. In general, the disc emitting inner regions (peaks in Fig. 3.10) are reproduced very well ($\epsilon(I_\nu^{\rm env}) \leq 3$ %). The biggest discrepancies occur in the wings of the peaks, where the gradient is the steepest (in logarithmic scaling).

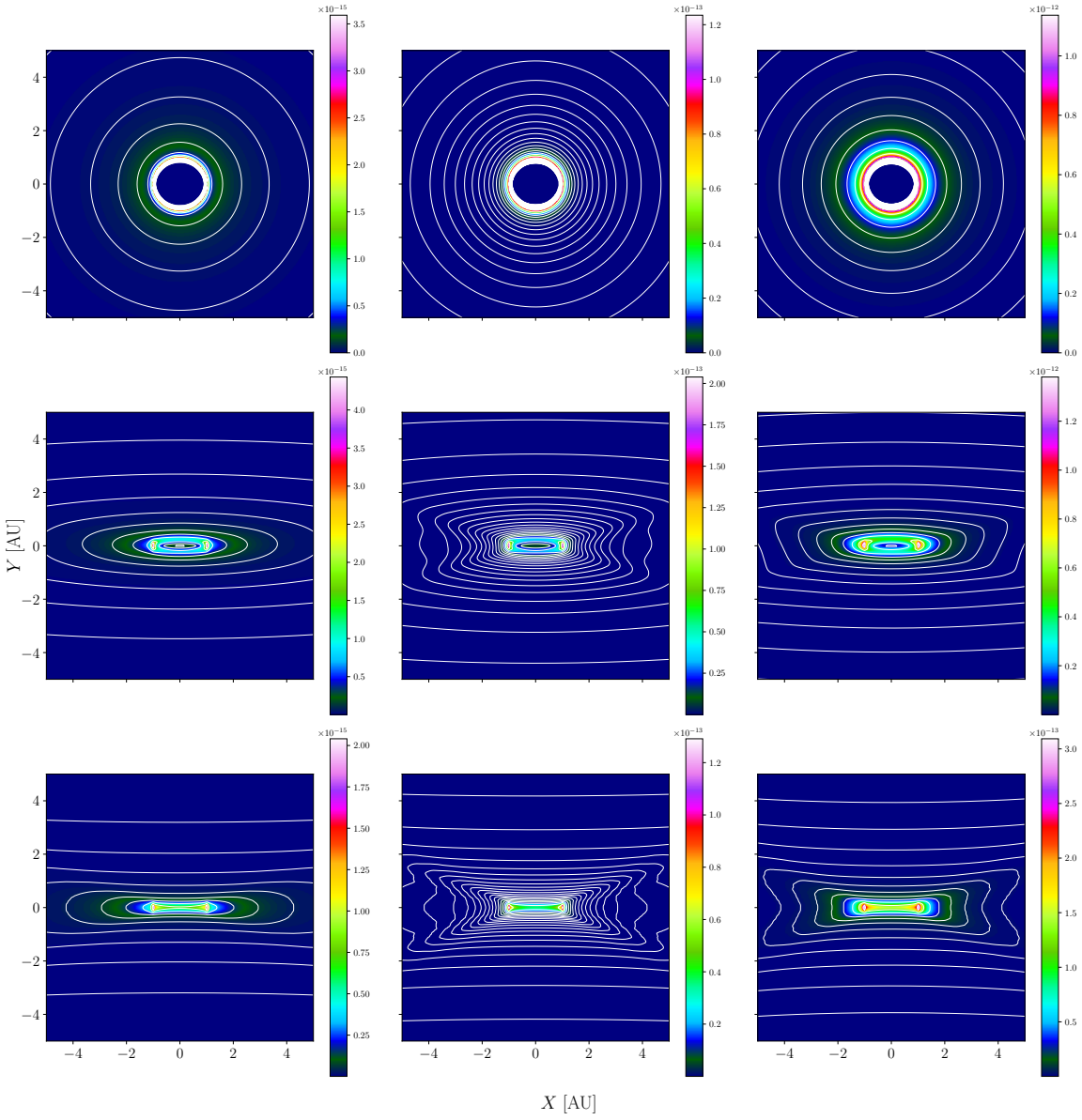

Figure 3.10 – Images at $\lambda = 2.3, 4.5, 12.1$ μm (left, middle, right panels, respectively) of the 10 AU inner regions of the axis-symmetric envelope (Sect. 3.4.2) and computed from the DG-FEM solution with the ray-tracing module (see Sect. 2.4.2). The top middle and bottom panels correspond to the inclinations $i = 12.5, 77.5, 90$ deg, respectively. The color-code shows the specific intensity value (in W.m^{-2}.Hz^{-1}.sr^{-1}) of the envelope $I_\nu^{\rm env}$, inside each pixel. The white solid lines displays the iso-contours of $I_\nu^{\rm env}$.

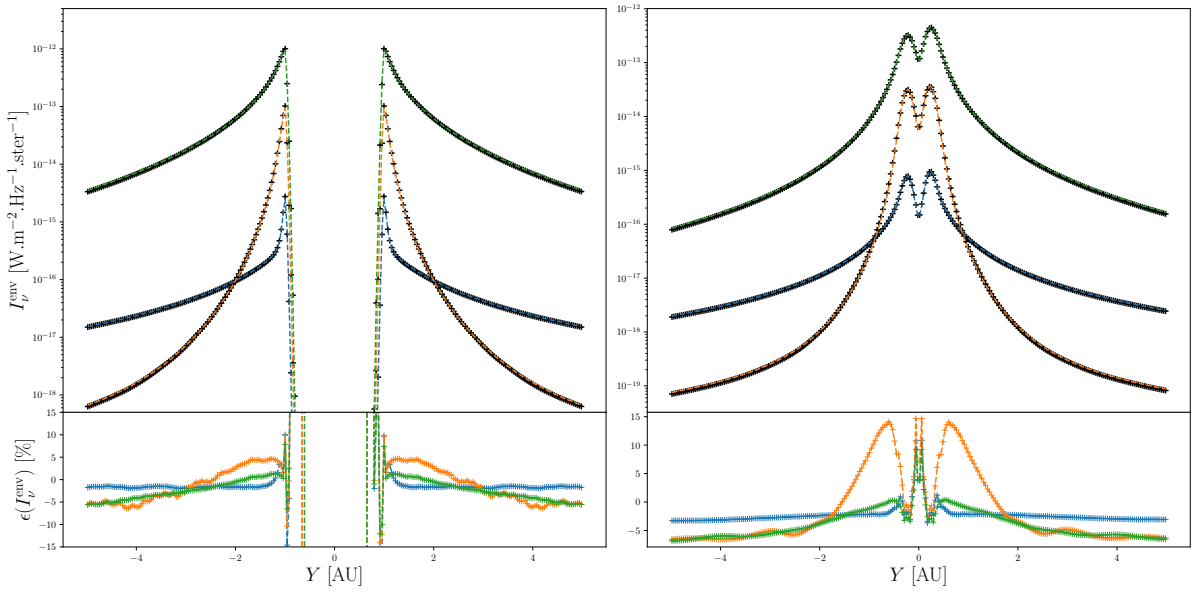

Figure 3.11 – Image slices at $x = 0$ AU, for two inclinations $i = 12.5, 77.5$ deg (left and right panels, respectively). The blue, orange, green curves are the RADMC-3D intensities at $\lambda = 2.3, 4.5, 12.1$ μm, respectively. The cross marks represent the solution from this study. The lower panels display the relative differences between the two codes.

Chapter 4

Conclusions and future work

The work done during this thesis focused on the determination of the radiation field in circumstellar envelopes of dust.

First, we investigated an approximate method of the radiative transfer problem; the Flux-limited diffusion (FLD) approximation. We derived general boundary conditions aimed to be accurate enough in all optical regimes. On a boundary with an incident radiation (e.g an inner cavity surrounding a star), we derived a general Marshak boundary condition with no particular symmetry of the solution at the boundary surface. At a vacuum boundary (e.g outer radius of a circumstellar shell), we constrained, in the FLD formalism, the ratio of emerging intensity over the emerging flux. Alternatively, we derived a vacuum boundary by imposing the value of J_ν in a ghost cell outside the domain. Except for the latter case, we obtained non-linear mixed boundary conditions that relate the mean specific intensity J_ν with its gradient.

We implemented the FLD approximation together with our derived boundary conditions in a one-dimensional spherically-symmetric code. The code solves, using a finite difference method, the FLD equation coupled with the radiative equilibrium equation. It is able to compute the temperature profile of the envelope and the emerging spectral energy distribution (SED). The central star is treated as an extended source and features the possibility of updating the stellar temperature to impose the condition of radiative equilibrium at the stellar surface.

We tested the accuracy of the code by comparing our results with the benchmarks from Ivezic et al. (1997). The temperature profile and the spectral energy distribution are very-well described by the FLD and our boundary conditions. These results were subsequently published in a paper (Perdigon et al., 2021, see Appendix D.1). The FLD approximation, by construction, is compatible with the spherical symmetry and we showed that, when provided with appropriate boundary conditions, it could be used to accurately describe the field in astrophysical applications for objects compatible with this symmetry (e.g AGB stars).

We then extended our study to the two-dimensional axis-symmetric case. We compared the associated results (temperature, SEDs, images) with the benchmarks from Pascucci et al. (2004). The temperature is described well on the disc inner-cavity and the outer

shell, highlighting the accuracy of the boundary conditions. There is, however, an overestimation of the temperature in the disc mid-plane. This effect was previously reported in the literature and justified by the fact that the FLD flux is aligned along the gradient of J_ν (see Eq. 2.20), resulting in the fact that the FLD is unable to correctly reproduce shadows (stellar radiation shadowed by the optically-thick disc inner-rim). Consequently, the spectral energy distributions, computed from ray-tracing of the emissivity, are also showing strong deviations with respect to the benchmark profiles.

We note that several theoretical works modified the original FLD approximation in order for the radiative flux to point in another direction than the gradient of J_ν (Sanchez and Pomraning, 1991; Pomraning, 1992). The authors derived a whole family of flux-limited diffusion approximation, parameterised by a non-linear function χ_ν.

$$\begin{aligned} &\frac{1}{c}\partial_t J_\nu - \boldsymbol{\nabla}.\left(D_\nu\,\boldsymbol{\nabla}\left(\chi_\nu\,J_\nu\right)\right) = \kappa_\nu^{\mathrm{abs}}\left(B_\nu - J_\nu\right), \\ \text{with}\quad &D_\nu = \frac{\lambda(R_\nu)}{\chi_\nu\,\omega_\nu\,\kappa_\nu^{\mathrm{ext}}}\quad\text{and}\quad R_\nu = \frac{\left|\boldsymbol{\nabla}\left(\chi_\nu\,J_\nu\right)\right|}{\omega_\nu\,\kappa_\nu^{\mathrm{ext}}\,\chi_\nu\,J_\nu}. \end{aligned} \tag{4.1}$$

λ_ν and ω_ν remain unchanged and are defined by Eq. (2.18) and Eq. (2.11), respectively. The special case $\chi_\nu = 1$ reduces to the usual FLD approximation. We will not go in the details about how to derive the χ_ν parameter. We briefly indicate that the authors derived an expression for this χ_ν by considering some time-independent transport problems for which exact results are available in the literature, and choose χ_ν such that Eq. (4.1) reproduces these exact results. To our knowledge, this modified FLD has not been yet numerically implemented in a code, in the context of astrophysical radiative transfer. This path deserves some investigations and may be the solution to improve the accuracy of the FLD, in multi-dimensional cases.

We also investigated the Discontinuous Galerkin finite element method (DGFEM) applied to the radiative transfer equation. We applied the DGFEM formulation, with the nodal representation, to the radiative transfer equation in spherical coordinates, with equatorial and polar symmetry. The DG-FEM has not been extensively explored compared to the other more conventional methods. To our knowledge, this is the first time it is implemented in a code for solving the radiative transfer in circumstellar envelopes.

We implemented the method in a code that numerically solve the radiative transfer equation coupled with the radiative equilibrium equation. A useful feature of the code is the possibility for the user to control the order of the method, by choosing how many nodes is used inside each element of the computational domain. A high-order numerical scheme allows to resolve strong spatial and angular gradients with a limited number of points. This feature is particularly appealing in radiative transfer where we often are limited by computer memory. The code compute the radiation field $I_\nu(\boldsymbol{r}, \boldsymbol{\Omega})$ and subsequently the temperature structure and the emissivity, allowing to compute *a posteriori* images and SED's from ray tracing techniques.

We tested the code by comparing the temperature, SED's and images with benchmarks from literature (Pascucci et al., 2004). We found very good agreement between our results and the benchmarks. These results will be published in a forthcoming paper, currently under revision (see Appendix D.2). The method is particularly suited for the treatment of

discontinuities and could be used to create benchmarks featuring density discontinuities or very strong gradients. For instance, a disc with a vacuum gap at a given radius to simulate the formation of planets would be interesting to see how the DG-FEM performs compared to others methods.

Our next goals for the DG-FEM are twofold. The first one concerns numerical optimisation. Since the method heavily relies on the grid used, significant gains of performance could be achieved, with the use of Adaptive Mesh Refinement (AMR) grids. While *a priori* refinement criteria are commonly used, such as the gradient of density and the optical depth, we note that the DG-FEM gives direct access to the residual (see Eq. 3.31), which gives an *a posteriori* criterion of refinement for the grid, based on an estimate of the error.

The second goal is about the physics included in the code. So far, we focused on the isotropic scattering, but extension to any scattering profile is possible and straightforward, by simply changing the expression of the emissivity η_ν. In this thesis, we limited our study to dust, but also plan to include gas. The inclusion of gas does not present a major difficulty, except that the opacities $\kappa_\nu^{\rm abs}$ and $\kappa_\nu^{\rm sca}$ now depend on the temperature of the media, and must be updated accordingly when solving the radiative transfer equation. Finally, we note that the polarisation of light could also be treated with this method.

The DG-FEM yields very promising results and certainly deserves more attention to study astrophysical applications. To continue further, we plan to model the continuum radiation field inside the disc of gas orbiting around Be stars. These geometrically thin viscous Keplerian discs, in vertical hydrostatic equilibrium, are known to be form from the outflowing winds of their central star (Lee et al., 1991). The code will be adapted to treat the central star as an extended sphere. One simple approach is to not perform the decomposition of the radiation Eq. (1.67) and to include the stellar flux as an external source, in the boundary conditions. The optical properties of gas are more complex than those of dust. Since the disc is very close to the star, part of the gas is ionised and free-free and bound-free transitions are important sources of continuum emission and absorption of radiation in these regions. The obtained results will have to be compared with the previous models from the literature (e.g Carciofi and Bjorkman, 2008). We note that since the disc of gas is touching the star itself, the radiative feedback of the disc onto the star may potentially be not negligible (see Sect. 2.3.4). In this context, it may be interesting to study the interactions between the star and the disc, to study if the disc can have any influence on its host star.

To finish, we currently investigated the radiative transfer problem inside circumstellar envelope but we note that the DG-FEM could be applied to other contexts such as multi-dimensional stellar atmospheres or the study of the radiation in the interstellar medium.

Bibliography

L. H. Auer and F. Paletou. Two-dimensional radiative transfer with partial frequency redistribution I. General method. *Astron. Astrophys.*, 285:675–686, May 1994.

J. E. Bjorkman and Kenneth Wood. Radiative Equilibrium and Temperature Correction in Monte Carlo Radiation Transfer. *ApJ*, 554(1):615–623, June 2001. doi: 10.1086/321336.

Craig F. Bohren and Donald R. Huffman. *Absorption and Scattering of Light by Small Particles*. 1998.

C. J. Cannon. Frequency-Quadrature Perturbations in Radiative-Transfer Theory. *ApJ*, 185:621–630, October 1973. doi: 10.1086/152442.

A. Carciofi and J. Bjorkman. Non-lte monte carlo radiative transfer. ii. nonisothermal solutions for viscous keplerian disks. *Astrophysical Journal - ASTROPHYS J*, 684: 1374–1383, 09 2008. doi: 10.1086/589875.

L. Chevallier and B. Rutily. Exact solution of the standard transfer problem in a stellar atmosphere. *J. Quant. Spectr. Rad. Transf.*, 91(4):373–391, April 2005. doi: 10.1016/j.jqsrt.2004.05.065.

B. Cockburn. Discontinuous Galerkin methods. *Zeitschrift Angewandte Mathematik und Mechanik*, 83(11):731–754, November 2003. doi: 10.1002/zamm.200310088.

X. Cui and Ben Q. Li. Discontinuous finite element solution of 2-d radiative transfer with and without axisymmetry. *Journal of Quantitative Spectroscopy and Radiative Transfer*, 96(3):383–407, 2005. ISSN 0022-4073. doi: https://doi.org/10.1016/j.jqsrt.2004.11.007. URL https://www.sciencedirect.com/science/article/pii/S0022407304004807.

B. T. Draine and H. M. Lee. Optical Properties of Interstellar Graphite and Silicate Grains. *ApJ*, 285:89, October 1984. doi: 10.1086/162480.

C. P. Dullemond and J. D. Monnier. The Inner Regions of Protoplanetary Disks. *ARA&A*, 48:205–239, September 2010. doi: 10.1146/annurev-astro-081309-130932.

C. P. Dullemond and R. Turolla. An efficient algorithm for two-dimensional radiative transfer in axisymmetric circumstellar envelopes and disks. *Astron. Astrophys.*, 360: 1187–1202, August 2000.

C. P. Dullemond, A. Juhasz, A. Pohl, F. Sereshti, R. Shetty, T. Peters, B. Commercon, and M. Flock. RADMC-3D: A multi-purpose radiative transfer tool. Astrophysics Source Code Library, record ascl:1202.015, February 2012.

A. S. Eddington. The Internal Constitution of the Stars. *The Scientific Monthly*, 11(4): 297–303, October 1920.

Frank Eisenhauer. Gravity+: Towards faint science, July 2019. URL https://doi.org/10.5281/zenodo.4697646.

C.A.J. Fletcher. *Computational Galerkin Methods*. Scientific Computation. Springer Berlin Heidelberg, 2012. ISBN 9783642859496. URL https://link.springer.com/book/10.1007/978-3-642-85949-6.

H Frisch. *Radiative Transfer An Introduction to Exact and Asymptotic Methods*. Springer Cham, 2022. ISBN 978-3-030-95247-1. URL https://link.springer.com/book/10.1007/978-3-030-95247-1.

Gravity Collaboration, R. Abuter, M. Accardo, A. Amorim, N. Anugu, et al. First light for GRAVITY: Phase referencing optical interferometry for the Very Large Telescope Interferometer. *Astron. Astrophys.*, 602:A94, June 2017. doi: 10.1051/0004-6361/201730838.

Jr. Haisch, Karl E., Elizabeth A. Lada, and Charles J. Lada. Disk Frequencies and Lifetimes in Young Clusters. *ApJ*, 553(2):L153–L156, June 2001. doi: 10.1086/320685.

Jan S. Hesthaven and Tim Warburton. *Nodal Discontinuous Galerkin Methods: Algorithms, Analysis, and Applications*. Springer Science & Business Media, December 2007.

I. Hubeny and D. Mihalas. *Theory of Stellar Atmospheres: An Introduction to Astrophysical Non-equilibrium Quantitative Spectroscopic Analysis*. Princeton Series in Astrophysics. Princeton University Press, 2014. ISBN 9781400852734. URL https://books.google.fr/books?id=VA_rAwAAQBAJ.

Z. Ivezic, M. A. T. Groenewegen, A. Men'shchikov, and R. Szczerba. Benchmark problems for dust radiative transfer. *MNRAS*, 291(1):121–124, October 1997. doi: 10.1093/mnras/291.1.121.

Zeljko Ivezic and Moshe Elitzur. Self-similarity and scaling behaviour of infrared emission from radiatively heated dust - I. Theory. *MNRAS*, 287(4):799–811, June 1997. doi: 10.1093/mnras/287.4.799.

D. Kitzmann, J. Bolte, and A. B. C. Patzer. Discontinuous Galerkin finite element methods for radiative transfer in spherical symmetry. *Astron. Astrophys.*, 595:A90, November 2016. doi: 10.1051/0004-6361/201628578.

David A. Kopriva and Gregor Gassner. On the Quadrature and Weak Form Choices in Collocation Type Discontinuous Galerkin Spectral Element Methods. *Journal of Scientific Computing*, 44:136–155, May 2010.

R. Kuiper and R. S. Klessen. The reliability of approximate radiation transport methods for irradiated disk studies. *Astron. Astrophys.*, 555:A7, July 2013. doi: 10.1051/0004-6361/201321404.

R. Kuiper, H. Klahr, C. Dullemond, W. Kley, and T. Henning. Fast and accurate frequency-dependent radiation transport for hydrodynamics simulations in massive star formation. *Astron. Astrophys.*, 511:A81, February 2010. doi: 10.1051/0004-6361/200912355.

Paul Kunasz and Lawrence H. Auer. Short characteristic integration of radiative transfer problems: formal solution in two-dimensional slabs. *J. Quant. Spectr. Rad. Transf.*, 39:67–79, January 1988. doi: 10.1016/0022-4073(88)90021-0.

Charles J. Lada. Star formation: from OB associations to protostars. In Manuel Peimbert and Jun Jugaku, editors, *Star Forming Regions*, volume 115, page 1, January 1987.

Umin Lee, Hideyuki Saio, and Yoji Osaki. Viscous excretion discs around be stars. *Monthly Notices of the Royal Astronomical Society*, 250(2):432–437, May 1991. ISSN 0035-8711. doi: 10.1093/mnras/250.2.432. Publisher Copyright: © 1991 Royal Astronomical Society. Provided by the NASA Astrophysics Data System.

C. D. Levermore and G. C. Pomraning. A flux-limited diffusion theory. *ApJ*, 248:321–334, August 1981. doi: 10.1086/159157.

B. Lopez, S. Lagarde, R. G. Petrov, W. Jaffe, P. Antonelli, et al. MATISSE, the VLTI mid-infrared imaging spectro-interferometer. *Astron. Astrophys.*, 659:A192, March 2022. doi: 10.1051/0004-6361/202141785.

Eric Machorro. Discontinuous Galerkin finite element method applied to the 1-D spherical neutron transport equation. *Journal of Computational Physics*, 223(1):67–81, April 2007. doi: 10.1016/j.jcp.2006.08.020.

R. Mignon-Risse, M. González, B. Commerçon, and J. Rosdahl. A new hybrid radiative transfer method for massive star formation. *Astron. Astrophys.*, 635:A42, March 2020. doi: 10.1051/0004-6361/201936605.

Ramachandran D. Nair, Michael N. Levy, and Peter H. Lauritzen. *Emerging Numerical Methods for Atmospheric Modeling*, pages 251–311. Springer Berlin Heidelberg, Berlin, Heidelberg, 2011. ISBN 978-3-642-11640-7. doi: 10.1007/978-3-642-11640-7_9. URL https://doi.org/10.1007/978-3-642-11640-7_9.

G. Niccolini and J. Alcolea. 3D continuum radiative transfer. A new adaptive grid construction algorithm based on the Monte Carlo method. *Astron. Astrophys.*, 456(1):1–12, September 2006. doi: 10.1051/0004-6361:20054410.

G. L. Olson and P. B. Kunasz. Short characteristic solution of the non-LTE transfer problem by operator perturbation. I. The one-dimensional planar slab. *J. Quant. Spectr. Rad. Transf.*, 38(5):325–336, January 1987. doi: 10.1016/0022-4073(87)90027-6.

G. L. Olson, L. H. Auer, and J. R. Buchler. A rapidly convergent iterative solution of the non-LTE radiation transfer problem. *J. Quant. Spectr. Rad. Transf.*, 35:431–442, June 1986. doi: 10.1016/0022-4073(86)90030-0.

P.J. Olver. *Introduction to Partial Differential Equations*. Undergraduate Texts in Mathematics. Springer International Publishing, 2016. ISBN 9783319347448. URL https://books.google.be/books?id=-pIHvgAACAAJ.

Joachim Oxenius. *Kinetic theory of particles and photons. Theoretical foundations of Non-LTE plasma spectroscopy*. Springer Berlin, Heidelberg, 1986. doi: 10.1007/978-3-642-70728-5. URL https://link.springer.com/book/10.1007/978-3-642-70728-5.

I. Pascucci, S. Wolf, J. Steinacker, C. P. Dullemond, Th. Henning, G. Niccolini, P. Woitke, and B. Lopez. The 2D continuum radiative transfer problem. Benchmark results for disk configurations. *Astron. Astrophys.*, 417:793–805, April 2004. doi: 10.1051/0004-6361:20040017.

J. Perdigon, G. Niccolini, and M. Faurobert. New boundary conditions for the approximate flux-limited diffusion radiative transfer in circumstellar environments. Test case study for spherically symmetric envelopes. *Astron. Astrophys.*, 653:A139, September 2021. doi: 10.1051/0004-6361/202040236.

G. C. Pomraning. *The equations of radiation hydrodynamics*. 1973.

G. C. Pomraning. On Levermore diffusion theory. *J. Quant. Spectr. Rad. Transf.*, 36(4):325–337, October 1986. doi: 10.1016/0022-4073(86)90056-7.

G. C. Pomraning. Initial and Boundary Conditions for Flux-Limited Diffusion Theory. *Journal of Computational Physics*, 75(1):73–85, March 1988. doi: 10.1016/0021-9991(88)90099-X.

G. C. Pomraning. Multimode flux-limited diffusion theory. *Laser and Particle Beams*, 10(2):239, January 1992. doi: 10.1017/S0263034600004389.

W H Reed and T R Hill. *Triangular mesh methods for the neutron transport equation*. 10 1973. URL https://www.osti.gov/biblio/4491151.

B. Rutily and L. Chevallier. Why is it so difficult to solve the radiative transfer equation? In Philippe Stee, editor, *EAS Publications Series*, volume 18 of *EAS Publications Series*, pages 1–23, January 2006. doi: 10.1051/eas:2006002.

G. B. Rybicki and D. G. Hummer. An accelerated lambda iteration method for multilevel radiative transfer. II. Overlapping transitions with full continuum. *Astron. Astrophys.*, 262:209–215, August 1992.

Richard Sanchez and G. C. Pomraning. A family of flux-limited diffusion theories. *J. Quant. Spectr. Rad. Transf.*, 45:313–337, June 1991. doi: 10.1016/0022-4073(91)90068-2.

C. Sonnhalter, T. Preibisch, and H. W. Yorke. Frequency dependent radiation transfer in protostellar disks. *Astron. Astrophys.*, 299:545, July 1995.

J. Steinacker, A. Bacmann, and T. Henning. Application of adaptive multi-frequency grids to three-dimensional astrophysical radiative transfer. *J. Quant. Spectr. Rad. Transf.*, 75:765–786, December 2002. doi: 10.1016/S0022-4073(02)00042-0.

J. Steinacker, Th. Henning, A. Bacmann, and D. Semenov. 3D continuum radiative transfer in complex dust configurations around stellar objects and active galactic nuclei. I. Computational methods and capabilities. *Astron. Astrophys.*, 401:405–418, April 2003. doi: 10.1051/0004-6361:20021853.

Jürgen Steinacker, Maarten Baes, and Karl D. Gordon. Three-Dimensional Dust Radiative Transfer*. *ARA&A*, 51(1):63–104, August 2013. doi: 10.1146/annurev-astro-082812-141042.

S. Terebey, F. H. Shu, and P. Cassen. The collapse of the cores of slowly rotating isothermal clouds. *ApJ*, 286:529–551, November 1984. doi: 10.1086/162628.

Lloyd N. Trefethen and J. A. C. Weideman. The exponentially convergent trapezoidal rule. *SIAM Review*, 56(3):385–458, 2014. doi: 10.1137/130932132. URL https://doi.org/10.1137/130932132.

P. Woitke, I. Kamp, and W. F. Thi. Radiation thermo-chemical models of protoplanetary disks. I. Hydrostatic disk structure and inner rim. *Astron. Astrophys.*, 501(1):383–406, July 2009. doi: 10.1051/0004-6361/200911821.

Harold W. Yorke and Cordula Sonnhalter. On the Formation of Massive Stars. *ApJ*, 569 (2):846–862, April 2002. doi: 10.1086/339264.

Appendix A

Boundary conditions on a spherical enclosed cavity

The boundary condition in Eq. (1.70) requires to know, for a given point A on the cavity of radius R_{in} and a given incoming direction $\mathbf{\Omega}$ ($\mathbf{\Omega}.\hat{r} > 0$), the coordinates on the opposite point B ($R_{\text{in}}, \Theta', \mu' = \cos\theta', \varphi'$). The situation is illustrated in Fig. A.1. We define the Cartesian coordinate system $(\hat{x}, \hat{y}, \hat{z})$ with $\hat{z}$ aligned along the polar axis and the plane $(\hat{x}, \hat{y})$ coinciding with the equatorial plane. Since the problem is axis-symmetric around the polar axis $\hat{z}$, the coordinates do not depend on the azimutal angle Φ and we can arbitrarily choose A and B to be in the same plane at $\Phi = \pi/2$. This convention simplifies the computations.

First, we see that $\theta' = \pi - \theta$, because the OAB triangle is isosceles, so

$$\mu' = -\mu. \tag{A.1}$$

The position $\boldsymbol{r}_B$ of the point B, is linked to the position $\boldsymbol{r}_A$ of the point A through the relation

$$\boldsymbol{r}_B = \boldsymbol{r}_A - s_{AB}\,\mathbf{\Omega}, \tag{A.2}$$

with s_{AB}, the distance between the point A and B. The direction vector $\mathbf{\Omega}$ is

$$\mathbf{\Omega} = \begin{bmatrix} \mu \\ \sqrt{1-\mu^2}\cos\varphi \\ \sqrt{1-\mu^2}\sin\varphi \end{bmatrix}_{(\hat{r},\hat{\Theta},\hat{\Phi})} = \begin{bmatrix} -\sqrt{1-\mu^2}\sin\varphi \\ \sin\Theta\,\mu + \cos\Theta\sqrt{1-\mu^2}\cos\varphi \\ \cos\Theta\,\mu - \sin\Theta\sqrt{1-\mu^2}\cos\varphi \end{bmatrix}_{(\hat{x},\hat{y},\hat{z})}, \tag{A.3}$$

and Eq. (A.2) is rewritten

$$\begin{aligned} R_{\text{in}} \begin{bmatrix} 0 \\ \sin\Theta' \\ \cos\Theta' \end{bmatrix}_{(\hat{x},\hat{y},\hat{z})} &= R_{\text{in}} \begin{bmatrix} 0 \\ \sin\Theta \\ \cos\Theta \end{bmatrix}_{(\hat{x},\hat{y},\hat{z})} \\ -s_{AB} \begin{bmatrix} -\sqrt{1-\mu^2}\sin\varphi \\ \sin\Theta\,\mu + \cos\Theta\sqrt{1-\mu^2}\cos\varphi \\ \cos\Theta\,\mu - \sin\Theta\sqrt{1-\mu^2}\cos\varphi \end{bmatrix}_{(\hat{x},\hat{y},\hat{z})} &. \end{aligned} \tag{A.4}$$

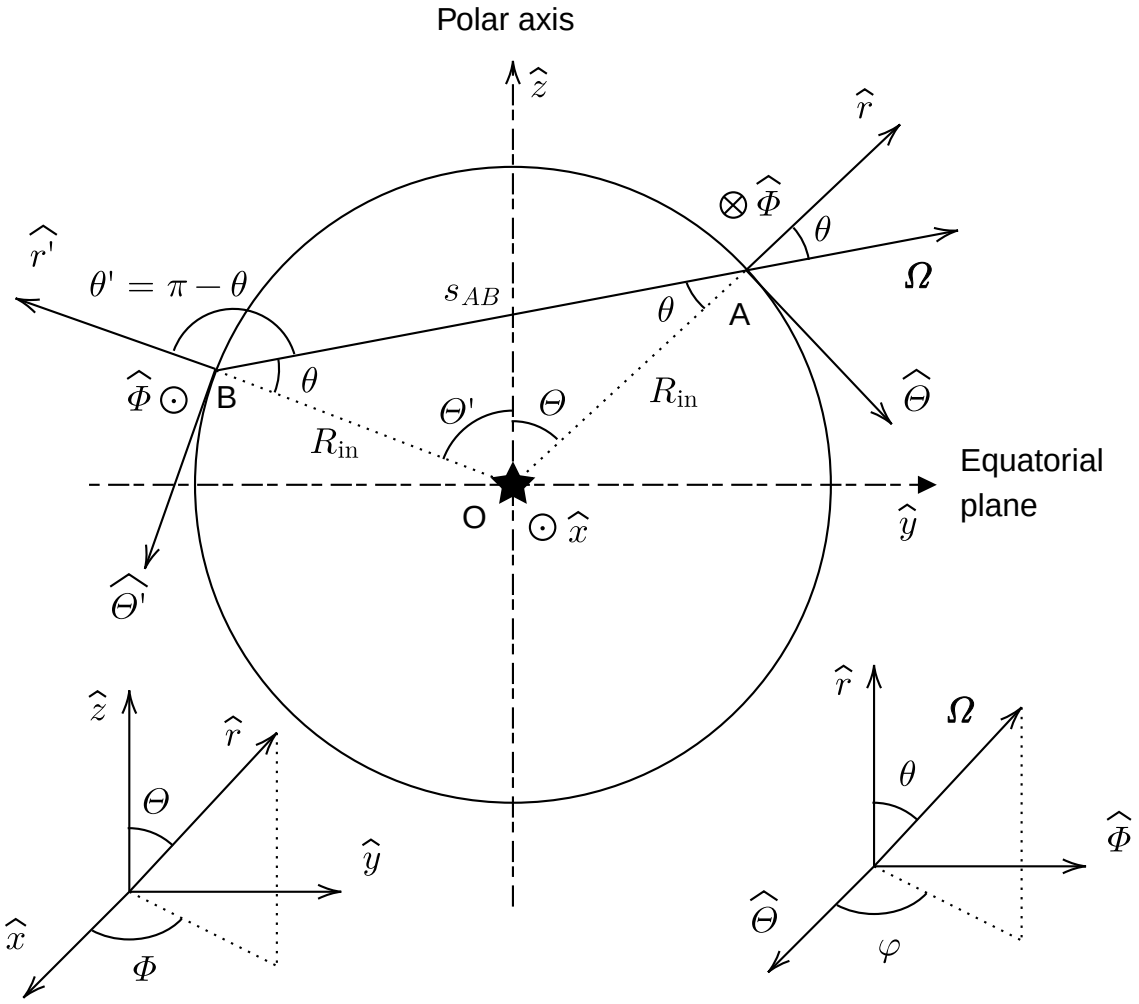

Figure A.1 – Geometry of a ray on the inner cavity. The point B corresponds to the opposite point A, along the direction $\boldsymbol{\Omega}$.

The length $s_{AB} = 2\,\mu\,R_{\text{in}}$ is simply deduced from the length of the base of the isosceles triangle OAB, with $OA = OB = R_{\text{in}}$. A relation between Θ' and the coordinates of the point A is then obtained, rewriting the z-component of Eq. (A.4)

$$\cos\Theta' = \left(1 - 2\,\mu^2\right)\cos\Theta + 2\,\mu\sqrt{1-\mu^2}\cos\varphi\,\sin\Theta, \tag{A.5}$$

and consequently $\Theta' = \arccos|\cos\Theta'|$. The absolute value occurs if we consider the planar symmetry with respect to the equatorial plane.

The angle φ' at the point B verifies

$$\tan\varphi' = \frac{\mathbf{\Omega}.\hat{\Phi}'}{\mathbf{\Omega}.\hat{\Theta}'}, \tag{A.6}$$

with

$$\begin{aligned}
\hat{\Phi}' &= \begin{bmatrix} -1 \\ 0 \\ 0 \end{bmatrix}_{(\hat{x},\hat{y},\hat{z})}, \\
\hat{\Theta}' = \begin{bmatrix} 0 \\ \cos\Theta' \\ -\sin\Theta' \end{bmatrix}_{(\hat{x},\hat{y},\hat{z})} &= \begin{bmatrix} 0 \\ \cos\Theta - 2\,\mu\left(\sin\Theta\mu + \cos\Theta\sqrt{1-\mu^2}\cos\varphi\right) \\ -\sin\Theta + 2\,\mu\left(\cos\Theta\mu - \sin\Theta\sqrt{1-\mu^2}\cos\varphi\right) \end{bmatrix}_{(\hat{x},\hat{y},\hat{z})},
\end{aligned} \tag{A.7}$$

and $\mathbf{\Omega}$ given by Eq. (A.3). Then Eq. (A.6) simplifies

$$\tan\varphi' = \frac{\sin\varphi\,\sin\Theta}{(1-2\mu^2)\cos\varphi\,\sin\Theta - 2\,\mu\sqrt{1-\mu^2}\cos\Theta}. \tag{A.8}$$

Consequently $\varphi' = \arctan\left(|y|/x\right)$ with y and x being the numerator and denominator in Eq. (A.8), respectively. This time, the absolute value is present because of the symmetry around the pole ($\varphi' \in [0,\pi]$). Note that the previous formula breaks for the couples $(\mu,\varphi) = (\sin(\Theta/2), 0)$ and $(\mu,\varphi) = (\cos(\Theta/2), \pi)$, as expected, because it corresponds to the opposite point B on the poles, where $\hat{\Theta}'$ and $\hat{\Phi}'$ are not defined.

Appendix B

Solvers for linear systems

Given a $N \times N$ matrix A with real coefficients and $\boldsymbol{b}$ a real vector of size N, we want to find the vector $\boldsymbol{x}$ such that

$$\mathcal{A}\,\boldsymbol{x} = \boldsymbol{b}. \tag{B.1}$$

There are mainly two classes of linear solvers in order to find $\boldsymbol{x}$, direct and iterative methods. Direct methods essentially consist in finding a way of inverting the matrix $\mathcal{A}$ while iterative methods start from an initial guess $\boldsymbol{x}^0$ and proceed to find new estimates $\boldsymbol{x}^n$, n being the iteration step, until the error $\boldsymbol{x}^n - \boldsymbol{x}$ is sufficiently small. In the following, we review one method of each category that we used over the course of this thesis.

B.1 Direct method: Gauss elimination

The Gauss elimination method can be summarised into three main steps,

— Decomposition of the matrix $\mathcal{A}$

$$\mathcal{A} = L\,U, \tag{B.2}$$

with L and U a lower-left and upper-right triangular matrices (see Fig. B.1).

— Pose $\boldsymbol{y} = U\,\boldsymbol{x}$, then solve for $\boldsymbol{y}$

$$L\,\boldsymbol{y} = \boldsymbol{b}. \tag{B.3}$$

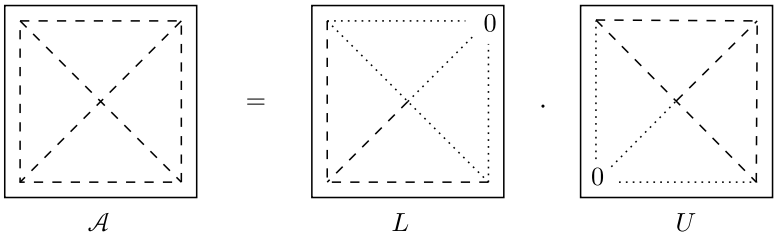

Figure B.1 – Schematic illustrating the decomposition of the matrix $\mathcal{A}$ into the product of a lower-left L and upper-right U triangular matrices. The dotted lines indicate the zones with zeros values.

— Backward solve for $\boldsymbol{x}$

$$U\,\boldsymbol{x} = \boldsymbol{y}. \tag{B.4}$$

The first two steps correspond of the Gauss pivot method. The corresponding algorithm is shown in Algorithm B.1.

Algorithm 1 Perform $L\,U$ decomposition and solve $L\,\boldsymbol{y} = \boldsymbol{b}$

Require: Start with $U = \mathcal{A}$ and $\boldsymbol{y} = \boldsymbol{b}$
  for $k = 0,\ N-2$ **do**
    for $i = k+1,\ N-1$ **do**
      $c_{i,k} = \frac{U_{i,k}}{U_{k,k}}$ $(U_{k,k} \neq 0)$
      for $j = k,\ N-1$ **do**
        $U_{i,j} = U_{i,j} - c_{i,k}\,U_{j,k}$
      end for
      $y_i = y_i - c_{i,k}\,y_k$
    end for
  end for

We note that the requirement in Algorithm B.1 is needed only if one wants to keep the matrix $\mathcal{A}$ and vector $\boldsymbol{b}$ unchanged. In the other case, we can directly perform the $L\,U$ decomposition on $\mathcal{A}$ and $\boldsymbol{b}$ to save computer memory. Once U and $\boldsymbol{y}$ have been computed, $\boldsymbol{x}$ is obtained, starting from $i = N-1$ to 0, by

$$x_i = \frac{1}{U_{i,i}}\left(y_i - \sum_{j=i+1}^{N-1} U_{i,j}\,x_j\right). \tag{B.5}$$

The main flaw of the method happens when the diagonal terms of the matrix $\mathcal{A}_{i,i}$ are very small, leading to a numerical instability and significant errors for $\boldsymbol{x}$. In such cases one way to circumvent this effect is to permute rows of $\mathcal{A}$ and $\boldsymbol{b}$ to insure that diagonal terms remain sufficiently large. The computational cost of the method is $O(N^3)$ for the first two steps and $O(N^2)$ for the third one. When the matrix $\mathcal{A}$ is sparse, it may be more interesting to use an iterative method instead.

B.2 Iterative method: Jacobi and Gauss-Seidel

Consider the linear system given by Eq. (B.1) and we have an initial guess of the solution $\boldsymbol{x}^0$. In general, since $\boldsymbol{x}^0 \neq \boldsymbol{x}$, the residual vector $\boldsymbol{r}^0 = \boldsymbol{b} - \mathcal{A}\,\boldsymbol{x}^0$ is not zero. The Jacobi and Gauss-Seidel methods are an iterative procedure where, from a given estimate $\boldsymbol{x}^n$, we cancel the components of the residual vector at the next iterate $n+1$ and stop until $\boldsymbol{x}^n - \boldsymbol{x}$ is sufficiently small. This requirement is, for each components of $\boldsymbol{r}$,

$$r_i^{n+1} = b_i - \left(\mathcal{A}\,\boldsymbol{x}^{n+1}\right)_i = 0. \tag{B.6}$$

The Jacobi method assumes the term at the next step $\left(\mathcal{A}\,\boldsymbol{x}^{n+1}\right)_i$ is computed from the estimate of $\boldsymbol{x}$ at current step

$$\left(\mathcal{A}\,\boldsymbol{x}^{n+1}\right)_i = \mathcal{A}_{i,i}\,x_i^{n+1} + \sum_{\substack{j=0 \\ j\neq i}}^{N-1} \mathcal{A}_{i,j}\,x_j^n. \tag{B.7}$$

This yields the following iterative formula for the components of the $\boldsymbol{x}$

$$x_i^{n+1} = \frac{1}{\mathcal{A}_{i,i}} \left(b_i - \sum_{\substack{j=0 \\ j \neq i}}^{N-1} \mathcal{A}_{i,j}\, x_j^n \right), \quad \mathcal{A}_{i,i} \neq 0. \tag{B.8}$$

Note that, in this case, the sweeping scheme i.e the order in which we update the x_i components, does not matter. The Gauss-Seidel method is very similar to the Jacobi method, however this time the sweeping scheme is important. For example, consider starting from $i = 0$ to $i = N - 1$ (forward sweep), we can express $\left(\mathcal{A}\,\boldsymbol{x}^{n+1}\right)_i$ as

$$\left(\mathcal{A}\,\boldsymbol{x}^{n+1}\right)_i = \mathcal{A}_{i,i}\, x_i^{n+1} + \sum_{j=0}^{i-1} \mathcal{A}_{i,j}\, x_j^{n+1} + \sum_{j=i+1}^{N-1} \mathcal{A}_{i,j}\, x_j^n. \tag{B.9}$$

We use the freshly computed values of $\boldsymbol{x}$. Then the iterative formula for the components of $\boldsymbol{x}$ becomes

$$x_i^{n+1} = \frac{1}{\mathcal{A}_{i,i}} \left(b_i - \sum_{j=0}^{i-1} \mathcal{A}_{i,j}\, x_j^{n+1} - \sum_{j=i+1}^{N-1} \mathcal{A}_{i,j}\, x_j^n \right), \quad \mathcal{A}_{i,i} \neq 0. \tag{B.10}$$

The computational cost of the Jacobi and Gauss-Seidel methods is $O(n^{\text{iter}} N^2)$, with n^{iter} the number of iterations needed to achieve an error $\boldsymbol{x}^n - \boldsymbol{x}$ sufficiently small.

Appendix C

DG-FEM calculations

The computation of the terms in Eq. (3.33), requires the choice of a particular quadrature in the cell $D^{i,j,k,l}$ for each coordinate $(r, \Theta, \mu, \varphi)$. We recall that for the r, μ, φ coordinates, we make use of the Gauss-Lobatto quadrature which has the advantage of having roots at the end points of the cell. This avoids the use of an interpolation formula when computing the numerical flux $\boldsymbol{F}_h^*$ at the element edges. For the Θ coordinate, we cannot use the Gauss-Lobatto quadrature, at least in the cells that are touching $\Theta = 0$, because the radiative transfer equation is not defined at the polar axis $\Theta = 0$, in spherical coordinates. For this reason and to keep an homogeneous method along the Θ coordinate, we use a Gauss-Legendre quadrature for this coordinate. An example of the associated reference element Q with the chosen nodes is displayed in Fig. 3.4.

In the following, all the superscript indexes refer to the element identification while the subscripts denote each node in the considered element. We start with the volume term in Eq. (3.33),

$$\begin{aligned}\int_{D^{i,j,k,l}} \left(\kappa^{\text{ext}}\, \tilde{I}_h^{i,j,k,l} - \tilde{\eta}\right) h_{a',b',c',d'}\, \mathrm{d}^4\boldsymbol{x} &= \frac{\Delta x^{i,j,k,l}}{16} \int_{-1}^{1} \left(\kappa^{\text{ext}}\, \tilde{I}_h^{i,j,k,l} - \tilde{\eta}\right) h_{a',b',c',d'}\, \mathrm{d}^4\tilde{\boldsymbol{x}} \\ &\approx \frac{\Delta x^{i,j,k,l}}{16} \sum_{a,b,c,d} W_{a,b,c,d} \left(\kappa_{a,b}^{\text{ext}\,i,j}\, \tilde{I}_{a,b,c,d}^{i,j,k,l} - \tilde{\eta}_{a,b}^{i,j}\right) h_{a',b',c',d'}\left(\tilde{\boldsymbol{x}}_{a,b,c,d}\right).\end{aligned} \tag{C.1}$$

$\Delta x^{i,j,k,l} = \Delta r^i\, \Delta\Theta^j\, \Delta\mu^k\, \Delta\varphi^l$ is the four-dimensional volume of the element $D^{i,j,k,l}$. For integration, we used the local coordinate system $(\tilde{r}, \tilde{\Theta}, \tilde{\mu}, \tilde{\varphi})$, defined in Eq. (3.13). $W_{a,b,c,d} = W_r(\tilde{r}_a)\, W_\Theta(\tilde{\Theta}_b)\, W_\mu(\tilde{\mu}_c)\, W_\varphi(\tilde{\varphi}_d)$ are the weights associated with the different quadrature in each direction. Finally, $h_{a',b',c',d'}(\tilde{\boldsymbol{x}}_{a,b,c,d})$ is the four-dimensional Lagrange polynomials, defined in Eq. (3.30), evaluated at the node $\tilde{\boldsymbol{x}}_{a,b,c,d} = (\tilde{r}_a, \tilde{\Theta}_b, \tilde{\mu}_c, \tilde{\varphi}_d)$. From the property Eq. (3.7) we have

$$h_{a',b',c',d'}\left(\tilde{r}_a, \tilde{\Theta}_b, \tilde{\mu}_c, \tilde{\varphi}_d\right) = \delta_{a',a}\, \delta_{b',b}\, \delta_{c',c}\, \delta_{d',d}, \tag{C.2}$$

with $\delta_{a',a}$ the usual delta Kronecker. The other volume term in Eq. (3.33) is expressed

as,

$$
\begin{aligned}
&\int_{D^{i,j,k,l}} \boldsymbol{F}_h.\nabla_{\boldsymbol{x}} h_{a',b',c',d'}\, d^4\boldsymbol{x} \\
&= \int_{D^{i,j,k,l}} \Big(a_r^{i,j,k,l}\, h_{b',c',d'}\, \partial_r h_{a'} + a_\Theta^{i,j,k,l}\, h_{a',c',d'}\, \partial_\Theta h_{b'} + a_\mu^{i,j,k,l}\, h_{a',b',d'}\, \partial_\mu h_{c'} \\
&\qquad + a_\varphi^{i,j,k,l}\, h_{a',b',c'}\, \partial_\varphi h_{d'} \Big)\, \tilde{I}_h^{i,j,k,l}\, \mathrm{d}^4\boldsymbol{x} \\
&= \frac{\Delta x^{i,j,k,l}}{8} \int_{-1}^{1} \Bigg(a_r^{i,j,k,l}\, h_{b',c',d'}\, \frac{\partial_{\tilde{r}} h_{a'}}{\Delta r^i} + a_\Theta^{i,j,k,l}\, h_{a',c',d'}\, \frac{\partial_{\tilde{\Theta}} h_{b'}}{\Delta \Theta^j} + a_\mu^{i,j,k,l}\, h_{a',b',d'}\, \frac{\partial_{\tilde{\mu}} h_{c'}}{\Delta \mu^k} \\
&\qquad + a_\varphi^{i,j,k,l}\, h_{a',b',c'}\, \frac{\partial_{\tilde{\varphi}} h_{d'}}{\Delta \varphi^l} \Bigg)\, \tilde{I}_h^{i,j,k,l}\, \mathrm{d}^4\tilde{\boldsymbol{x}} \\
&\approx \frac{\Delta x^{i,j,k,l}}{8} \sum_{a,b,c,d} W_{a,b,c,d}\, \tilde{I}^{i,j,k,l}_{a,b,c,d} \Bigg({a_r}^{i,j,k,l}_{a,b,c,d}\, \delta_{b',b}\delta_{c',c}\,\delta_{d',d} \frac{\partial_{\tilde{r}} h_{a'}|_{\tilde{r}_a}}{\Delta r^i} \\
&\quad + {a_\Theta}^{i,j,k,l}_{a,b,c,d}\, \delta_{a',a}\,\delta_{c',c}\delta_{d',d} \frac{\partial_{\tilde{\Theta}} h_{b'}|_{\tilde{\Theta}_b}}{\Delta \Theta^j} + {a_\mu}^{i,j,k,l}_{a,b,c,d}\, \delta_{a',a}\,\delta_{b',b}\,\delta_{d',d} \frac{\partial_{\tilde{\mu}} h_{c'}|_{\tilde{\mu}_c}}{\Delta \mu^k} \\
&\qquad + {a_\varphi}^{i,j,k,l}_{a,b,c,d}\, \delta_{a',a}\,\delta_{b',b}\delta_{c',c} \frac{\partial_{\tilde{\varphi}} h_{d'}|_{\tilde{\varphi}_d}}{\Delta \varphi^l} \Bigg).
\end{aligned}
\tag{C.3}
$$

In Eq. (C.3), we used $h_{a',b',c',d'} = h_{a'}(\tilde{r})\, h_{b'}(\tilde{\Theta})\, h_{c'}(\tilde{\mu})\, h_{d'}(\tilde{\varphi})$ and the definition of the flux Eq. (3.27). $\partial_{\tilde{r}} h_{a'}|_{\tilde{r}_a}$ is the partial derivative of the one-dimensional Lagrange polynomial, with respect to the $\tilde{r}$-coordinate, evaluated at the node $\tilde{r}_a$ (with similar definitions for the other coordinates), given by Eq. (3.17).

We already explained how to evaluate the surface integral term in Eq. (3.33). We note that for the flux computation normal to the Θ coordinate, we do not directly have the value of the solution at the element interface because of the Gauss-Legendre quadrature (see Fig. 3.4). We then need to interpolate the solution with the help of Eq. (3.29) to evaluate the numerical flux at the nodes lying on the three-dimensional surface normal to Θ, $\Delta r^i \Delta \mu^k \Delta \varphi^l$, for example

$$
\begin{aligned}
F^*_{\Theta_{a',\tilde{\Theta}=1,c',d'}} = &\sum_b \max\left\{ {a_\Theta}^{i,j,k,l}_{a',\tilde{\Theta}=1,c',d'},\, 0 \right\} \tilde{I}^{i,j,k,l}_{a',b,c',d'} h_b\left(\tilde{\Theta}=1\right) \\
&+ \min\left\{ {a_\Theta}^{i,j,k,l}_{a',\tilde{\Theta}=1,c',d'},\, 0 \right\} \tilde{I}^{i,j+1,k,l}_{a',b,c',d'} h_b\left(\tilde{\Theta}=-1\right).
\end{aligned}
\tag{C.4}
$$

All the terms we derived can be put in the form of the system of equations, we gave in Eq. (3.40)

$$
\mathcal{A}^{\alpha,\alpha}\, \tilde{\boldsymbol{I}}_h^{\alpha} = \boldsymbol{b}^{\alpha}. \tag{C.5}
$$

We denote the elements of $\mathcal{A}^{\alpha,\alpha}$ and $\boldsymbol{b}^{\alpha}$ with the global row index $m = a'\, n_b n_c n_d + b'\, n_c n_d + c'\, n_d + d'$ and the global column index $n = a\, n_b n_c n_d + b\, n_c n_d + c\, n_d + d$. The elements of

$\mathcal{A}^{\alpha,\alpha}$ and $\boldsymbol{b}$ are then

$$
\begin{aligned}
\mathcal{A}^{\alpha,\alpha}_{m,n} &= W_{a,b,c,d}\,\kappa^{\mathrm{ext}\,i,j}_{a,b}\,\delta_{a',a}\,\delta_{b',b}\,\delta_{c',c}\,\delta_{d',d} \\
&+\frac{2}{\Delta r^i}\delta_{b',b}\,\delta_{c',c}\,\delta_{d',d}\,W_{b,c,d}\left(\max\left\{a^{i,j,k,l}_{\tilde{r}\,a,b,c,d},\,0\right\}\delta_{a',n_a-1}\,\delta_{a,n_a-1}\right. \\
&\left.-\min\left\{a^{i,j,k,l}_{\tilde{r}\,a,b,c,d},\,0\right\}\delta_{a',0}\,\delta_{a,0}-W_a\,a^{i,j,k,l}_{\tilde{r}\,a,b,c,d}\,\partial_{\tilde{r}}h_{a'}|_{\tilde{r}_a}\right) \\
&+\frac{2}{\Delta\Theta^j}\,\delta_{a',a}\,\delta_{c',c}\,\delta_{d',d}\,W_{a,c,d}\left(\max\left\{a^{i,j,k,l}_{\tilde{\Theta}\,a,c,d}|_{\tilde{\Theta}=1},\,0\right\}h_{b'}|_{\tilde{\Theta}=1}h_b|_{\tilde{\Theta}=1}\right. \\
&\left.-\min\left\{a^{i,j,k,l}_{\tilde{\Theta}\,a,c,d}|_{\tilde{\Theta}=-1},\,0\right\}h_{b'}|_{\tilde{\Theta}=-1}\,h_b|_{\tilde{\Theta}=-1}-W_b\,a^{i,j,k,l}_{\tilde{\Theta}\,a,b,c,d}\,\partial_{\tilde{\Theta}}h_{b'}|_{\tilde{\Theta}_b}\right) \\
&+\frac{2}{\Delta\mu^k}\,\delta_{a',a}\,\delta_{b',b}\,\delta_{d',d}\,W_{a,b,d}\,a^{i,j,k,l}_{\tilde{\mu}\,a,b,c,d}\,(\delta_{c',n_c-1}\,\delta_{c,n_c-1}-W_c\partial_{\tilde{\mu}}h_{c'}|_{\tilde{\mu}_c}) \\
&-\frac{2}{\Delta\varphi^l}\delta_{a',a}\,\delta_{b',b}\,\delta_{c',c}\,W_{a,b,c}\,a^{i,j,k,l}_{\tilde{\varphi}\,a,b,c,d}\,(\delta_{d',0}\,\delta_{d,0}+W_d\partial_{\tilde{\varphi}}h_{d'}|_{\tilde{\varphi}_d})\,,
\end{aligned}
\tag{C.6}
$$

$$
\begin{aligned}
b^{\alpha}_{m} &= W_{a',b',c',d'}\,\tilde{\eta}^{i,j}_{a',b'} \\
&+\frac{2}{\Delta r^i}W_{b',c',d'}\left(\max\left\{a^{i-1,j,k,l}_{\tilde{r}\,n_a-1,b',c',d'},\,0\right\}\tilde{I}^{i-1,j,k,l}_{n_a-1,b',c',d'}\,\delta_{a',0}\right. \\
&\left.-\min\left\{a^{i+1,j,k,l}_{\tilde{r}\,0,b',c',d'},\,0\right\}\tilde{I}^{i+1,j,k,l}_{0,b',c',d'}\,\delta_{a',n_a-1}\right) \\
&+\frac{2}{\Delta\Theta^j}W_{a',c',d'}\left(\max\left\{a^{i,j-1,k,l}_{\tilde{\Theta}\,a',c',d'}|_{\tilde{\Theta}=1},\,0\right\}h_{b'}|_{\tilde{\Theta}=-1}\sum_b\tilde{I}^{i,j-1,k,l}_{a',b,c',d'}\,h_b|_{\tilde{\Theta}=1}\right. \\
&\left.-\min\left\{a^{i,j+1,k,l}_{\tilde{\Theta}\,a',c',d'}|_{\tilde{\Theta}=-1},\,0\right\}\,h_{b'}|_{\tilde{\Theta}=1}\sum_b\tilde{I}^{i,j+1,k,l}_{a',b,c',d'}\,h_b|_{\tilde{\Theta}=-1}\right) \\
&+\frac{2}{\Delta\mu^k}W_{a',b',d'}\,a^{i,j,k-1,l}_{\tilde{\mu}\,a',b',n_c-1,d'}\,\tilde{I}^{i,j,k-1,l}_{a',b',n_c-1,d'}\,\delta_{c',0} \\
&-\frac{2}{\Delta\varphi^l}W_{a',b',c'}\,a^{i,j,k,l+1}_{\tilde{\varphi}\,a',b',c',0}\,\tilde{I}^{i,j,k,l+1}_{a',b',c',0}\,\delta_{d',n_d-1}.
\end{aligned}
\tag{C.7}
$$

Appendix D

Papers

D.1 New boundary conditions for the approximate flux-limited diffusion radiative transfer in circumstellar environments. Test case study for spherically symmetric envelopes

A&A 653, A139 (2021)
https://doi.org/10.1051/0004-6361/202040236

Astronomy & Astrophysics

New boundary conditions for the approximate flux-limited diffusion radiative transfer in circumstellar environments

Test case study for spherically symmetric envelopes

J. Perdigon, G. Niccolini, and M. Faurobert

Université Côte d'Azur (UCA), Observatoire de la Côte d'Azur (OCA), CNRS, Laboratoire Lagrange, Lagrange, 06304 Nice Cedex 4, France
e-mail: jeremy.perdigon@oca.eu

Received 24 December 2020 / Accepted 2 July 2021

ABSTRACT

Context. In order to constrain the models describing circumstellar environments, it is necessary to solve the radiative transfer equation in the presence of absorption and scattering, coupled with the equation for radiative equilibrium. However, solving this problem requires much CPU time, which makes the use of automatic minimisation procedures to characterise these environments challenging.
Aims. In this context, the use of approximate methods is of primary interest. One promising candidate method is the flux-limited diffusion (FLD), which recasts the radiative transfer problem into a non-linear diffusion equation. One important aspect for the accuracy of the method lies in the implementation of appropriate boundary conditions (BCs). We present new BCs for the FLD approximation in circumstellar environments that we apply here to spherically symmetric envelopes.
Methods. At the inner boundary, the entering flux (coming from the star and from the envelope itself) may be written in the FLD formalism and provides us with an adequate BC. At the free outer boundary, we used the FLD formalism to constrain the ratio of the mean radiation intensity over the emerging flux. In both cases we derived non-linear mixed BCs relating the surface values of the mean specific intensity and its gradient. We implemented these conditions and compared the results with previous benchmarks and the results of a Monte Carlo radiative transfer code. A comparison with results derived from BCs that were previously proposed in other contexts is presented as well.
Results. For all the tested cases, the average relative difference with the benchmark results is below 2% for the temperature profile and below 6% for the corresponding spectral energy distribution or the emerging flux. We point out that the FLD method together with the new outer BC also allows us to derive an approximation for the emerging flux. This feature avoids additional formal solutions for the radiative transfer equation in a set of rays (ray-tracing computations).
Conclusions. The FLD approximation together with the proposed new BCs performs well and captures the main physical properties of the radiative equilibrium in spherical circumstellar envelopes.

Key words. radiative transfer – methods: numerical – circumstellar matter

1. Introduction

The study of circumstellar environments at different stages of stellar evolution is of crucial importance. These environments reflect the physical processes in action, from the star formation with the presence of accretion discs to late stages in the evolution, in which strong stellar winds shape the circumstellar envelopes. Observations at high angular resolution allow to probe and characterise the circumstellar material by determining densities, temperatures, abundances, velocity fields, etc. The exploitation of instruments such as the Multi AperTure mid-Infrared SpectroScopic Experiment[1] (MATISSE), operating in the mid-IR, or the Atacama Large Millimeter Array[2] (ALMA) in the sub-millimetric domain offer complementary views of these environments, that give access to regions close to the central star up to the outer regions using a multi-wavelength approach.

Circumstellar matter is generally composed of a mixture of gas and dust particles that absorbs and scatters the incident stellar radiation. The envelope is then heated by the radiation, and a radiative equilibrium can be reached in which the envelope also emits radiation in the infrared domain.

In order to constrain the models describing circumstellar environments, it is necessary to solve the radiative transfer equation under the assumption of radiative equilibrium. Several numerical techniques exist to solve this problem in one, two, and three dimensions. The Monte Carlo method is popular because it can be adapted to any geometry and can handle many physical processes (see Steinacker et al. 2013 for a thorough review). However, solving the radiative transfer problem requires much CPU time, which makes the use of any automatic minimisation procedure to characterise these environments challenging.

In this context, the use of approximate methods is of primary interest. One promising candidate is the flux-limited diffusion (FLD), introduced by Levermore & Pomraning (1981) (L&P hereafter). This description numerically simplifies the problem by recasting the radiative transfer equation into a non-linear diffusion equation for the mean specific intensity of the radiation field (see Sect. 2).

Physically, the boundary conditions (BCs) for the radiative transfer equation are obtained from the known specific intensity

[1] http://www.eso.org/public/teles-instr/paranal-observatory/vlt/vlt-instr/matisse
[2] http://www.almaobservatory.org

incident on the surface of the object. However, the outgoing intensity is not known a priori and has to be obtained from the solution of the radiative transfer problem. It is thus not obvious to find a BC for the mean specific intensity at the surface of the object. A consequent theoretical work has already been done in finding satisfying BCs for the FLD method (Pomraning 1986, 1988). These BCs were derived with the assumption that a boundary layer could be defined, which might not be true in astrophysical applications where the media may not be seen as an infinite half-space by the radiation for some frequencies. Furthermore, as far as we know, they have never been numerically tested in an astrophysical context.

The FLD approximation has already been implemented in several astrophysical applications. Sonnhalter et al. (1995), Yorke & Sonnhalter (2002) used the FLD to solve the frequency-dependent radiative transfer to model protostellar discs and massive star formation, respectively. In these studies, the central star was treated as an additional source and the specific mean intensity J_ν at the outer edge of the media was set to be equal to the Planck function $B_\nu(T_{\rm out})$, with a prescribed temperature $T_{\rm out}$ at the boundary. Some improvements were made later, in the context of the radiation hydrodynamics problem for massive star formation (see Kuiper et al. 2010; Mignon-Risse et al. 2020). These more sophisticated hybrid codes split the radiation field into two components, the stellar and the dust component, where the FLD method only solves for the latest part. In this treatment, the Dirichlet boundary condition at the outer edge only applies to the dust component. This relies on the assumption that the dust temperature is known at the interface with the interstellar medium. In the problem we consider, the temperature at the outer boundary is not known a priori and must be derived as part of the solution to the radiative transfer problem coupled with the radiative equilibrium equation. In a non-grey problem, we need BCs that can properly handle several regimes of optical thicknesses, for different frequencies.

We present new BCs for the FLD theory in circumstellar environments that we tested and implemented in the case of spherically symmetric envelopes. The condition is derived from the prescription of (i) the incident flux, derived from an extended stellar source and the self-heating of the envelope at the inner boundary and from (ii) the ratio of the mean specific intensity over the radiative flux at the free outer boundary. We show that they both may be written as mixed BCs relating the mean specific intensity and its gradient at the surfaces of the envelope. They consequently lead to a more realistic description of the radiation field (compared to simple Dirichlet or von Neumann boundary conditions) while still remaining sufficiently easy to implement. As a by-product of our investigations, we also derived an approximate expression for the emergent flux at the free outer surface.

The paper is organised as follows: in Sect. 2 we recall the bases of the FLD theory. In Sect. 3 we present the new boundary conditions and in Sect. 4 their numerical implementations. In Sect. 5 we test the accuracy of our results by comparing the temperature profile in the envelope and the spectral energy distribution (SED) of the outgoing flux with the results of two radiative transfer codes, namely (i) DUSTY (Ivezic & Elitzur 1997), which numerically solves the integral equation for the energy density, and (ii) a Monte Carlo (MC) radiative transfer code (Niccolini & Alcolea 2006). Additionally, we compare the derived boundary conditions with the original boundary conditions of Levermore & Pomraning (1981). Finally, in Sect. 6, we conclude and present some perspective for our future work.

2. The flux limited diffusion theory

In the following, we present the original work of L&P and introduce the relevant background for the derivation of the BCs in Sect. 3. The position is denoted by $\boldsymbol{r}$, the direction of propagation by $\hat{n}$, and the frequency by the subscript ν. The transport equation for the specific intensity $I_\nu(\boldsymbol{r},\hat{n},t)$ at the position $\boldsymbol{r}$ in the $\hat{n}$ direction with isotropic and coherent scattering is

$$\frac{1}{c}\partial_t I_\nu + \hat{n}.\boldsymbol{\nabla} I_\nu = -\kappa_\nu^{\rm ext} I_\nu + \kappa_\nu^{\rm abs} B_\nu + \kappa_\nu^{\rm sca} J_\nu. \tag{1}$$

$J_\nu = J_\nu(\boldsymbol{r},t)$ is the mean specific intensity, $B_\nu = B_\nu(T(\boldsymbol{r},t))$ is the Planck function and $\kappa_\nu^{\rm ext}$, $\kappa_\nu^{\rm abs}$ and $\kappa_\nu^{\rm sca}$ are the extinction, absorption and scattering coefficients, respectively. The zeroth and first moments of the specific intensity, namely J_ν and $\boldsymbol{H}_\nu$, are defined as

$$J_\nu = \frac{1}{4\pi}\int_{4\pi} I_\nu \,{\rm d}^2\hat{n}, \boldsymbol{H}_\nu = \frac{1}{4\pi}\int_{4\pi} I_\nu\,\hat{n}\,{\rm d}^2\hat{n}, \tag{2}$$

where the integration is performed over all directions. These quantities are linked by the zeroth moment of Eq. (1),

$$\frac{1}{c}\partial_t J_\nu + \boldsymbol{\nabla}.\boldsymbol{H}_\nu = \kappa_\nu^{\rm abs}(B_\nu - J_\nu). \tag{3}$$

The FLD approximation is a closure of the system of the moment equations by expressing $\boldsymbol{H}_\nu$ as a function of J_ν. This is done by expressing the specific intensity I_ν as a function of the mean specific intensity J_ν,

$$I_\nu = J_\nu\,\psi_\nu(\boldsymbol{r},\hat{n},t), \boldsymbol{H}_\nu = J_\nu\,\boldsymbol{h}_\nu(\boldsymbol{r},t), \frac{1}{4\pi}\int_{4\pi}\psi_\nu\,{\rm d}^2\hat{n} = 1, \tag{4}$$

where $\boldsymbol{h}_\nu$ is the normalised flux and is expressed as

$$\boldsymbol{h}_\nu(\boldsymbol{r},t) = \frac{1}{4\pi}\int_{4\pi}\hat{n}\,\psi_\nu(\boldsymbol{r},\hat{n},t)\,{\rm d}^2\hat{n}. \tag{5}$$

The ψ_ν function is called the normalised intensity and quantifies the anisotropy of the radiation field I_ν. In the optically thin and thick limits, this function reduces to a Dirac distribution and a constant, respectively. The FLD approximation consists of assuming that the anisotropy of the radiation field is a conserved quantity, yielding the expression for ψ_ν,

$$\psi_\nu(\boldsymbol{r},\hat{n},t) = \frac{1}{1+(\boldsymbol{h}_\nu - \hat{n}).\boldsymbol{R}_\nu}, \tag{6}$$

with

$$\boldsymbol{R}_\nu(\boldsymbol{r},t) = \frac{-\boldsymbol{\nabla}J_\nu}{\omega_\nu\,\kappa_\nu^{\rm ext}\,J_\nu}, \quad \omega_\nu = \frac{\kappa_\nu^{\rm abs}B_\nu + \kappa_\nu^{\rm sca}J_\nu}{\kappa_\nu^{\rm ext}J_\nu}. \tag{7}$$

The quantity denoted by R_ν plays a key role in the description of the local radiation field in the medium. It expresses the ratio of the (effective) mean free path over the characteristic length of the variation of the mean specific intensity. Consequently, the limits $R_\nu \gg 1$ and $R_\nu \ll 1$ correspond to the optical thin and thick regimes, respectively. The quantity ω_ν is called the effective albedo. It is equal to unity in the absence of true absorption ($\kappa_\nu^{\rm abs} = 0$). L&P showed that, using Eq. (6) in Eq. (5), $\boldsymbol{h}_\nu$ is proportional to $\boldsymbol{R}_\nu$,

$$\boldsymbol{h}_\nu = \lambda(R_\nu)\,\boldsymbol{R}_\nu, \quad \lambda(R_\nu) = \frac{1}{R_\nu}\left(\frac{1}{\tanh R_\nu} - \frac{1}{R_\nu}\right), \tag{8}$$

where R_ν is the norm of $\boldsymbol{R}_\nu$ and $\lambda(R_\nu)$ is the 'flux-limiting' parameter. Finally, using Eq. (8) in Eq. (4) allows Eq. (3) to be rewritten as a non-linear diffusion equation for the mean specific intensity

$$\frac{1}{c}\partial_t J_\nu - \boldsymbol{\nabla}.(D_\nu \boldsymbol{\nabla} J_\nu) = \kappa_\nu^{\rm abs}(B_\nu - J_\nu), \tag{9}$$

with the non-linear diffusion coefficient

$$D_\nu = \frac{\lambda(R_\nu)}{\omega_\nu \kappa_\nu^{\rm ext}}. \tag{10}$$

We note that in the FLD approach, the radiative net flux $\boldsymbol{H}_\nu$ is related to the gradient of the mean specific intensity J_ν by $\boldsymbol{H}_\nu = -D_\nu \boldsymbol{\nabla} J_\nu$. It shows some similarities with the Fick law, which applies in the stellar interior, but here the diffusion coefficient depends on a non-linear way on the mean specific intensity. In the optically thick regime, the FLD approximation reduces to a linear diffusion equation, whereas in the optically thin regime, it reduces to an advection equation, as expected.

3. Boundary conditions

In this section, we specify the time-independent BCs that were implemented for the FLD Eq. (9). They are defined at the specific boundaries of a circumstellar shell, namely an inner spherical cavity that is illuminated by an enclosed star, and an outer boundary with no incoming radiation.

The BCs for the radiative transfer equation Eq. (1) would be obtained by specifying the value of the incident specific intensity I_ν on the considered surface. In the framework of the FLD approximation, we face two problems: (i) The FLD equation applies to the mean specific intensity, whereas the physical constraint is on the ingoing specific intensity at the boundaries, and (ii) we also explained in Sect. 2 that the FLD approach implies a specific angular dependence of I_ν, given by the function ψ_ν (see Eq. (6)). This specific dependence would not be consistent with any arbitrary value of the incident radiation field at the surface. Consequently, the actual BCs for the radiative transfer equation are in general incompatible with the FLD solution.

This is expected because the FLD approximation is in principle not valid close to the boundaries of objects. Pomraning (1988) derived the BCs for the FLD equation from the decomposition of the radiative transfer problem into an interior problem described by the FLD equation and an additional boundary layer term. The match of the interior and boundary layer solutions yields the BCs for the FLD equation. A relation of the surface values of the mean specific intensity and its gradient is obtained, but with rather involved coefficients depending on integrals of the Chandrasekhar H function and on the surface value of R_ν. In the literature, Dirichlet BCs are often used with a prescribed value for the temperature at the outer boundary of the medium. As already pointed out, the surface temperature is not known a priori and must be derived from the solution of the radiative transfer problem.

Here, we propose to impose BCs for the zeroth and the first angular moments of the radiation field, in a form that is compatible with the FLD approach, in order to ensure a smooth match with the interior FLD solution. We obtained mixed Robin-type BCs that relate the surface values of the mean specific intensity and its gradient, but the coefficients are quite simple analytical functions of the surface value of R_ν.

3.1. Inner spherical cavity

3.1.1. Expression of the incident flux in the FLD formalism

One example of physical significance is to write a condition on the flux $F_\nu^{\rm in}$ entering a boundary surface at the position $\boldsymbol{r}_S$,

$$F_\nu^{\rm in}(\boldsymbol{r}_{\rm S}) = J_\nu(\boldsymbol{r}_{\rm S}) \int_{\hat{s}.\hat{n}\leq 0} \hat{s}.\hat{n}\, \psi_\nu(\boldsymbol{r}_{\rm S}, \hat{n})\, {\rm d}^2\hat{n}. \tag{11}$$

Here, $\hat{s}$ is the outward normal vector to the surface of the envelope ($\hat{s} = -\hat{r}$ at the inner edge). The right-hand side (RHS) of Eq. (11) is the expression of an incoming flux in the FLD formalism. Equation (11) is the general form of the inner BC without any assumption on the geometry of the problem. The integral can be performed analytically using Eq. (6) for ψ_ν if we assume that the vector $\boldsymbol{R}_\nu$ is normal to the surface ($\boldsymbol{R}_\nu = \pm R_\nu\, \hat{r}$), which is exact for spherically symmetric problems. The equation can then be rewritten as a non-linear mixed BC,

$$F_\nu^{\rm in}(\boldsymbol{r}_{\rm S}) = \pi\left(\alpha_\nu\, J_\nu(\boldsymbol{r}_{\rm S}) + \beta_\nu\, \hat{s}.\boldsymbol{\nabla} J_\nu|_{\boldsymbol{r}=\boldsymbol{r}_{\rm S}}\right) \tag{12}$$

with

$$\alpha_\nu = 2\frac{\ln(\cosh R_\nu)}{R_\nu \tanh R_\nu}\bigg|_{\boldsymbol{r}=\boldsymbol{r}_{\rm S}}, \quad \beta_\nu = 2D_\nu|_{\boldsymbol{r}=\boldsymbol{r}_{\rm S}}. \tag{13}$$

This BC may be regarded as an implicit relation of the surface values of J_ν and R_ν that yields an FLD solution compatible with the given incident flux. It is interesting to note that although Eq. (12) is different in its coefficients and construction from the original BC Eqs. (56) and (66) in L&P, they are analytically equivalent. In L&P, the coefficients were derived to give an exact transport result for the case of a source-free ($B_\nu = 0$) half-space media, with a constant $\kappa_\nu^{\rm ext}$, ω_ν and a particular incident intensity distribution $\Gamma(\boldsymbol{r}_{\rm S}, \mu)$ of the form

$$\Gamma(\boldsymbol{r}_{\rm S}, \mu) = \frac{1}{\coth(R_\nu(\boldsymbol{r}_{\rm S})) - \mu} = R_\nu(\boldsymbol{r}_{\rm S})\, \psi_\nu(\boldsymbol{r}_{\rm S}, \mu). \tag{14}$$

This specific form is proportional to the angular dependence in the FLD formalism. The correspondence between α_ν in Eq. (13) and Eq. (56) in L&P is

$$\gamma = \frac{\alpha_\nu - 2\lambda(R_\nu)\hat{s}.\boldsymbol{R}_\nu}{2 - 4\lambda(R_\nu)\hat{s}.\boldsymbol{R}_\nu}. \tag{15}$$

Hence, specifying the FLD flux at the boundaries of a spherically symmetric domain will actually give the same BC as is obtained by solving the exact transport result of a source-free ($B_\nu = 0$) half-space media, with a constant $\kappa_\nu^{\rm ext}$, ω_ν and a particular incident intensity distribution $\Gamma(\boldsymbol{r}_{\rm S}, \mu)$, given by Eq. (14). We note that this equivalence only applies for the spherical and planar symmetric systems and no longer holds when we specify Eq. (11) for other configurations, where the radiative flux is not orthogonal to the boundary surface.

3.1.2. Incident flux from an extended source and the envelope

We want to write the BC at an inner spherical cavity located at a distance $R_{\rm in}$ from the centre of a star of radius $R_\star$ ($\boldsymbol{r}_S = R_{\rm in}\, \hat{r}$) and surface temperature $T_\star$. For this, we need to specify the flux $F_\nu^{\rm in}$. We have two contributions,

$$F_\nu^{\rm in} = \int_{\hat{s}.\hat{n}\leq 0} \hat{s}.\hat{n}\left[B_\nu(T_\star) + I_\nu^{\rm e}(\boldsymbol{r}, -\hat{n})\right]\, {\rm d}^2\hat{n}. \tag{16}$$

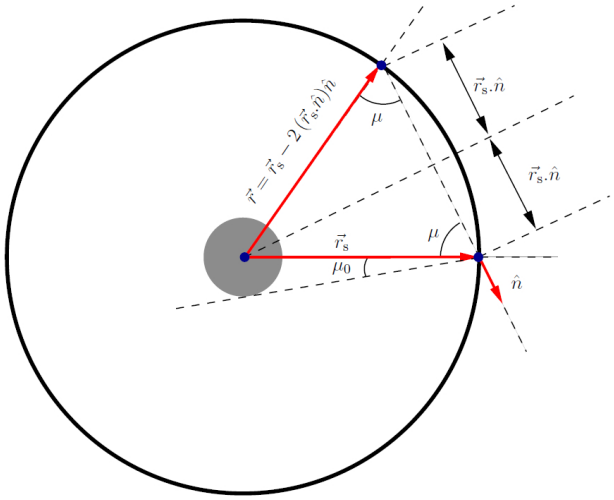

Fig. 1. Geometry of an inner spherical cavity (solid black line) illuminated by a central star (grey disc).

The first contribution, denoted by $B_\nu(T_\star)$ comes from the star and the other from the inner boundary itself and is expressed as $I^{\rm e}_\nu(\boldsymbol{r}, -\hat{n}) = J_\nu(\boldsymbol{r})\,\psi_\nu(\boldsymbol{r}, -\hat{n})$. As shown by Fig. 1, the vector $\boldsymbol{r} = \boldsymbol{r}_{\rm S} - 2(\boldsymbol{r}_{\rm S}.\hat{n})\,\hat{n}$ corresponds to the opposite point at the inner boundary, along $\hat{n}$. Because of this dependence, this BC is no longer local by nature and cannot be expressed in a closed form, except in spherical symmetry where $J_\nu(\boldsymbol{r}) = J_\nu(\boldsymbol{r}_{\rm S})$ and $\psi_\nu(\boldsymbol{r}, -\hat{n}) = \psi_\nu(\boldsymbol{r}_{\rm S}, -\hat{n})$. To perform the angular integration, we aligned the n_z axis with the unitary vector $\hat{r}$. For the star, the integration on $\mu = \cos(\theta)$ (θ being the angle between n_z and $\hat{n}$) spans from $\mu_0 = \sqrt{1 - (R_\star/R_{\rm in})^2}$ to 1, and for the inner cavity, it spans from 0 to μ_0,

$$F^{\rm in}_\nu = 2\pi\left(\int_{\mu_0}^{1} \mu\, B_\nu(T_\star)\, d\mu + J_\nu(\boldsymbol{r}_S)\int_{0}^{\mu_0} \mu\,\psi_\nu(\boldsymbol{r}_S, -\mu)\,\mathrm{d}\mu\right). \quad (17)$$

The incident flux $F^{\rm in}_\nu$ is then expressed as,

$$F^{\rm in}_\nu = \pi\left[\left(\frac{R_\star}{R_{\rm in}}\right)^2 B_\nu(T_\star) + \gamma_\nu\, J_\nu(\boldsymbol{r}_S)\right], \quad (18)$$

with,

$$\gamma_\nu = \left.\frac{2\left[\mu_0 \tanh R_\nu - \ln\left(1 + \mu_0 \tanh R_\nu\right)\right]}{R_\nu \tanh R_\nu}\right|_{\boldsymbol{r}=\boldsymbol{r}_S}. \quad (19)$$

The inner BC for the FLD equation in the case of an inner spherical cavity enclosing a star is

$$(\alpha_\nu - \gamma_\nu)\; J_\nu(R_{\rm in}) + \beta_\nu\; \hat{s}.\boldsymbol{\nabla} J_\nu|_{r=R_{in}} = \left(\frac{R_\star}{R_{\rm in}}\right)^2 B_\nu(T_\star), \quad (20)$$

with α_ν and β_ν, the quantities defined by Eq. (13).

We can analytically write the FLD solution with this inner boundary condition in the limit where the envelope is optically thin ($R_\nu \gg 1$) and compare it with the known analytical solution for the dilution of the mean specific intensity in free space,

$$J_\nu = \frac{B_\nu(T_\star)}{2}\left(1 - \sqrt{1 - \left(\frac{R_\star}{r}\right)^2}\right). \quad (21)$$

In the optically thin limit, the FLD Eq. (9) and the BC Eq. (20) reduce to

$$r^2 J_\nu = \text{const.} = R^2_{\rm in} J_\nu(R_{\rm in}),\; J_\nu(R_{\rm in}) = \frac{1}{4}\left(\frac{R_\star}{R_{\rm in}}\right)^2 B_\nu(T_\star), \quad (22)$$

respectively. The solution of the FLD equation, in this limit is then

$$J_\nu = \frac{1}{4}\left(\frac{R_\star}{r}\right)^2 B_\nu(T_\star), \quad (23)$$

in agreement with Eq. (21) when $(R_\star/r)^2 \ll 1$. The relative difference in temperature between Eq. (21) and the FLD solution Eq. (23) is $\approx$ 15% at the star surface, 1% at $r \approx 2.5\ R_\star$. For $r \gtrsim 10\ R_\star$ (values for our test cases presented in Sect. 5), this difference becomes negligible ($\lesssim$0.06%).

3.2. Outer boundary

For the inner cavity, we would like to impose that no incoming radiation enters the external shell of the envelope ($F^{\rm in}_\nu = 0$). However, in the FLD formalism, the angular dependence of the radiation is given by the specific form of the ψ_ν function (Eq. (6)). The incoming radiation vanishes only when R_ν becomes infinite, which also results in a sharp-peaked distribution for the emerging specific intensity. This is not physically realistic, and this inconsistency is expected because the FLD method is rigorously not valid close to the surface of the object. Another approach is then required to describe the behaviour of the radiation on the external edge. Inspired by L&P and Pomraning (1986), we seek a BC in the form of a closure relation between the mean specific intensity and the radiation flux at the surface, that is,

$$J_\nu(R_{\rm out}) - \zeta_\nu\; \hat{s}.\boldsymbol{H_\nu}(R_{\rm out}) = 0, \quad (24)$$

with ζ_ν, a coefficient we need to determine. At the outer edge and without incoming radiation, ζ_ν has to be understood as the ratio of the energy density over the emerging flux. This ratio can be expressed in spherical symmetry as

$$\zeta_\nu = \frac{\int_0^1 I_\nu\, \mathrm{d}\mu}{\int_0^1 \mu\, I_\nu\, \mathrm{d}\mu}. \quad (25)$$

It depends on the anisotropy of the emergent radiation field. In the optically thin limit, the radiation field is along the $\hat{s}$ direction (spherical symmetry), thus $I_\nu \propto \delta(\mu - 1)$ and hence $\zeta_\nu \to 1$. In the diffusion regime where the emergent field is isotropic, $\zeta_\nu \to 2$. In the original study of L&P, ζ_ν was chosen to be equal to 2, which means that it correctly describes the optically thick cases where $R_\nu \ll 1$. If the BC is to correctly describe different optical regimes, we need ζ_ν to be a function of R_ν. In the framework of the FLD approximation, $I_\nu = J_\nu\,\psi_\nu$ and the specific angular dependence of I_ν, given by ψ_ν, is used to compute the surface value of ζ_ν,

$$\zeta_\nu = \zeta(R_\nu) = \frac{2 + \alpha(R_\nu)\tanh(R_\nu)}{\alpha(R_\nu) + 2\lambda(R_\nu)R_\nu}. \quad (26)$$

In the two limits ($R_\nu \gg 1$ and $R_\nu \ll 1$), we recover $\zeta_\nu \to 1$ and $\zeta_\nu \to 2$. We note that the latter limit reduces to the boundary condition Eq. (56) in L&P. Now we need to specify the value of R_ν at the external boundary of the envelope. The behaviour of the radiation at this interface is only dictated by the interior solution

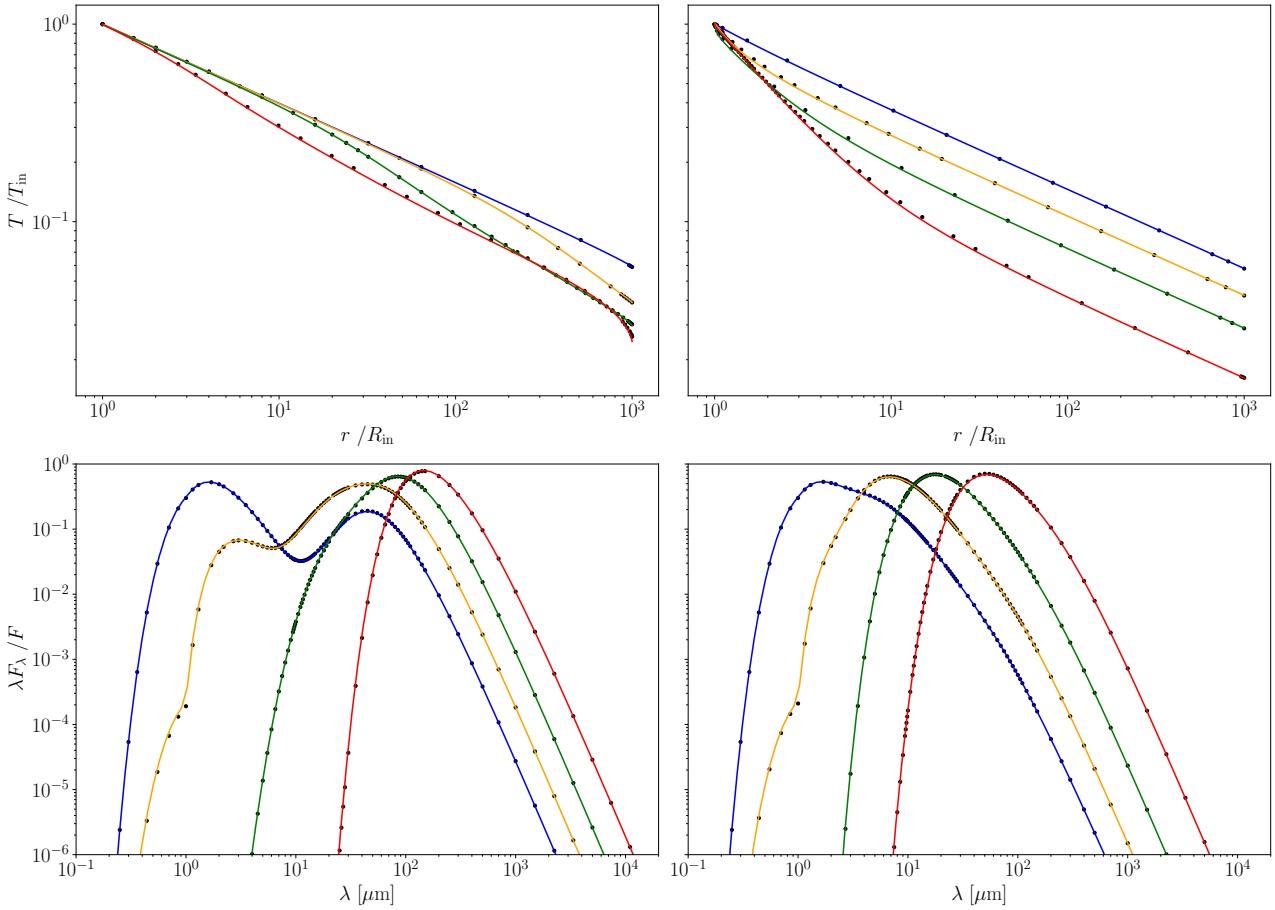

Fig. 2. Non-grey case: normalised temperature profiles (*upper panels*) and SEDs (*lower panels*) for four different opacities $\tau_{\nu_0} = 1, 10, 100,$ and 1000 (blue, orange, green and red, respectively) and two density power laws: $p = 0$ (*left panels*) and $p = 2$ (*right panels*). The solid lines represent the FLD curves, and the black dots indicate the benchmark profiles from Ivezic et al. (1997).

because there is no incoming radiation. Consequently, to ensure a smooth match of the BC and the interior FLD solution, we used a second-order extrapolated value for $R_\nu(R_{\rm out}) = R^{\rm e}_\nu$ (see Eq. (41)). Because we prescribe a value for R_ν at the external edge, $R^{\rm e}_\nu$ is also used to compute the non-linear diffusion coefficient $D_\nu(R_{\rm out}) = D_\nu(R^{\rm e}_\nu) = \lambda(R^{\rm e}_\nu)/\omega_\nu\kappa^{\rm ext}_\nu$ and the coefficients of the numerical scheme Eq. (34) on the external edge. The outer BC without incoming radiation that we implemented is then

$$J_\nu(R_{\rm out}) + \zeta(R^{\rm e}_\nu)\, D_\nu(R^{\rm e}_\nu)\, \hat{s}.\, \boldsymbol{\nabla} J_\nu|_{r=R_{\rm out}} = 0, \tag{27}$$

where we have expressed $\boldsymbol{H}_\nu(R_{\rm out}) = -D_\nu(R^{\rm e}_\nu)\ \boldsymbol{\nabla}\ J_\nu|_{r=R_{\rm out}}$. In Sect. 5.2 we compare this BC in an astrophysical application with respect to the original BCs of L&P.

3.3. Approximation for the emergent flux

We used an extrapolation of the non-linear diffusion coefficient $D_\nu(R^{\rm e}_\nu)$ to relate the flux at the external edge to the gradient of the mean specific intensity. As there is no incident flux, this provides us with an approximate expression for the emergent flux, given by

$$\boldsymbol{F}^{\rm out}_\nu = 4\pi\boldsymbol{H}_\nu(R_{\rm out}) = -4\pi\ D_\nu(R^{\rm e}_\nu)\ \ \boldsymbol{\nabla} J_\nu|_{r=R_{\rm out}}. \tag{28}$$

This approximation is tested in Sect. 5. It reproduces the results of different radiative transfer codes that solve the full transfer equation very well, as shown in Figs. 2 and 3.

3.4. Radiative equilibrium and warming of the stellar surface

Because of the geometric extension of the star (see Fig. 1), there is part of the radiation that emerges from the envelope that falls back onto the star,

$$\begin{aligned} F^{\rm fall}_\nu(R_{\rm in}) &= 2\pi J_\nu(R_{\rm in}) \int_{-1}^{-\mu_0} \mu\ \psi_\nu\,(R_{\rm in}, \mu)\ {\rm d}\mu \\ &= \frac{2\pi J_\nu(R_{\rm in})}{R_\nu \tanh R_\nu}\left[\ln\left(\frac{1+\tanh R_\nu}{1+\mu_0\tanh R_\nu}\right) - (1-\mu_0)\tanh R_\nu\right], \end{aligned} \tag{29}$$

with R_ν being evaluated at $r = R_{\rm in}$. We used the same conventions as in Sect. 3.1 to perform the angle integration. This part of the flux is hidden from the rest of the envelope, and the radiative equilibrium inside the cavity leads to a warming of the stellar surface (Niccolini et al. 2003). This effect can be quite dramatic, and reach up to 30% of the total stellar luminosity that is obscured for optically-thick grey shell, as in the test case presented in Sect. 5.2. This has to be taken into account to properly ensure the radiative equilibrium condition throughout the full space from the stellar surface to the outer boundary of the envelope. To fulfil the radiative equilibrium condition at the stellar surface we write

$$\sigma T^4_{\rm eff} = \sigma T^4_\star + \left(\frac{R_{\rm in}}{R_\star}\right)^2 \int_0^\infty F^{\rm fall}_\nu(R_{\rm in})\, d\nu. \tag{30}$$

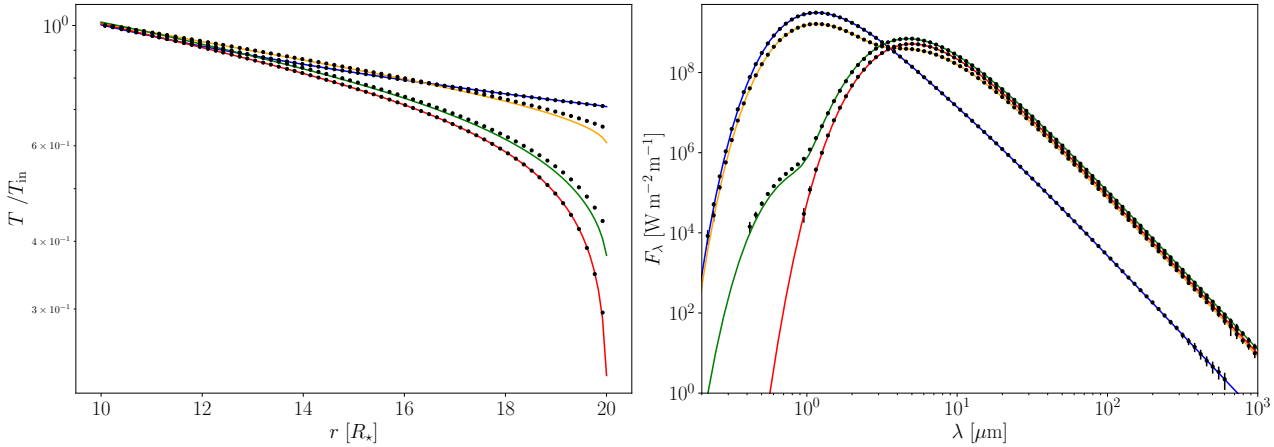

Fig. 3. Grey case: normalised temperature profiles (*left panel*) and emerging fluxes (*right panel*) for four different opacities $\tau = 0.01, 1, 10,$ and 100 (blue, orange, green and red, respectively) with a constant density profile ($p = 0$). The solid lines represent the FLD curves, and the black dots with the error bars σ indicate the MC profiles from Niccolini & Alcolea (2006).

We imposed a fixed value for $T_{\rm eff}$, and the temperature of the star $T_\star$ was updated accordingly.

4. Numerical implementation

The FLD Eq. (9) is a non-linear diffusion equation that has to be solved numerically for each point of space, time, and frequency. In the following, we limit ourselves to the 1D time-independent FLD equation,

$$\frac{1}{r^2}\partial_r\left(r^2 D_\nu\,\partial_r J_\nu\right) = \kappa_\nu^{\rm abs}\,(J_\nu - B_\nu)\,. \tag{31}$$

Here, r denotes the radial variable from the centre of the envelope. An additional constraint to Eq. (31) is given by the equation of the radiative equilibrium

$$\int_0^\infty \kappa_\nu^{\rm abs} B_\nu\,\mathrm{d}\nu = \int_0^\infty \kappa_\nu^{\rm abs} J_\nu\,\mathrm{d}\nu. \tag{32}$$

These equations are solved for a spherically symmetric envelope of inner radius $R_{\rm in}$ and outer radius $R_{\rm out}$, surrounding a star of radius $R_\star$.

4.1. Numerical scheme

4.1.1. Finite-difference approximation

Following a finite-difference procedure, we discretise and sample in a logarithmic way the frequency domain into n_ν points, denoted by the subscript k. Space is discretised into n_x cells and denoted by the subscript i. J_ν is computed at the cell centres and the vector $\boldsymbol{H}_\nu$ on the walls. The differential operator is approximated with a second-order finite differences operator. The equation is solved with respect to a new variable $x = f(r)$ on a regular grid of constant step $\Delta x = (x(R_{\rm out}) - x(R_{\rm in}))\,/\,(n_x - 2)$ to allow r to be non-uniformly sampled. We make use of one ghost cell for each grid border to ensure the BCs. We obtain the following system of equations:

$$A_{k,i+\frac{1}{2}} J_{k,i+1} - A_{k,i} J_{k,i} + A_{k,i-\frac{1}{2}} J_{k,i-1} = -b_{k,i} B_k(T_i). \tag{33}$$

The non-linear coefficients A are given by

$$A_{k,i\pm\frac{1}{2}} = r^2_{i\pm\frac{1}{2}}\,D_{k,i\pm\frac{1}{2}}\left.\frac{\mathrm{d}x}{\mathrm{d}r}\right|_{i\pm\frac{1}{2}},\quad A_{k,i} = A_{k,i+\frac{1}{2}} + b_{k,i} + A_{k,i-\frac{1}{2}},$$
$$b_{k,i} = \Delta x^2\left(\left.\frac{\mathrm{d}x}{\mathrm{d}r}\right|_i\right)^{-1} r_i^2\,\kappa_{k,i}^{\rm abs}. \tag{34}$$

The non-linear nature of the equation arises from the expression of the coefficients A and RHS in Eq. (33). They implicitly depend on J_ν, through the diffusion coefficient D_ν and the radiative equilibrium Eq. (32), respectively. The coefficients A require an estimation of J_ν and its gradient (see Eqs. (10) and (7)) at the cell walls, given by

$$J_{k,i+\frac{1}{2}} = \frac{1}{2}\left(J_{k,i+1} + J_{k,i}\right),\quad \nabla J_\nu|_{k,i+\frac{1}{2}} = \left.\frac{\mathrm{d}x}{\mathrm{d}r}\right|_{i+\frac{1}{2}}\frac{J_{k,i+1} - J_{k,i}}{\Delta x}\,\hat{r}. \tag{35}$$

4.1.2. Iterative scheme

Several strategies are possible in order to solve the FLD Eq. (33) coupled with Eq. (32). The simplest approach is to use an iterative method to fully solve Eq. (33) and to update the temperature through Eq. (32). Iterating between these two processes until convergence yields the solution of the problem. This procedure, commonly called the Λ-iteration in the literature (see Yorke & Sonnhalter 2002), becomes very slow and does not converge for large optical depths. In analogy with the usual accelerated Λ-iteration (ALI) methods, Yorke & Sonnhalter (2002) found an improved convergence behaviour by splitting the solution of equation Eq. (31) in Eq. (32).

We found a simple method, inspired by the Gauss-Seidel approach, to solve Eqs. (33) and (32) simultaneously instead of repetitively. If we denote by n the iteration of the method, we have

$$J_{k,i}^{n+1} = \frac{b_{k,i}B_k(T_i^n) + A^n_{k,i+\frac{1}{2}}J^n_{k,i+1} + A^n_{k,i-\frac{1}{2}}J^{n+1}_{k,i-1}}{A^n_{k,i}}, \tag{36}$$

and the temperature is updated after only one Gauss-Seidel spatial sweep at each frequency through Eq. (32), which we rewrite as

$$\sum_{k=0}^{n_\nu-1} W_k\,\kappa_{k,i}^{\rm abs} B_k(T_i^{n+1}) = \sum_{k=0}^{n_\nu-1} W_k\,\kappa_{k,i}^{\rm abs} J_{k,i}^{n+1}. \tag{37}$$

We replaced the frequency integration by a quadrature formula with the associated weights W_k. The left-hand side (LHS) of Eq. (37) was pre-computed and stored in a table, for a wide range of temperatures, allowing the RHS to be linearly interpolated in this table (in the logarithm of the integral for better accuracy). By doing so, we avoided using a Newton-Raphson procedure to determine the new temperature, which reduces the computational time.

Our procedure consisted of repeatedly updating J_ν and T with the help of Eqs. (36) and (37) until we reached convergence. The coefficients A Eq. (34) and the BCs Eq. (40) were immediately updated for each frequency k after one Gauss-Seidel spatial sweep. We note that this procedure is different from the usual Λ-iteration presented above because the temperature is updated simultaneously with J_ν, within the same iteration n.

4.2. Update of the stellar temperature

The radiative equilibrium inside the inner cavity requires updating the stellar temperature (see Sect. 3.4). Following Eq. (30), we updated the stellar temperature at the end of each iteration n of the numerical scheme,

$$T_\star^{n+1} = \left(T_{\rm eff}^4 - \frac{1}{\sigma}\left(\frac{R_{\rm in}}{R_\star}\right)^2 \sum_{k=0}^{n_\nu-1} W_k \, F_k^{{\rm fall},n+1} \right)^{\frac{1}{4}}. \tag{38}$$

Here again, we replaced the frequency integration by a quadrature formula with the associated weights W_k. $F_k^{{\rm fall},n+1}$ is given by Eq. (29) and computed with the freshly updated values of $J^{n+1}_{k,\frac{1}{2}}$ and $R^{n+1}_{k,\frac{1}{2}}$.

4.3. Boundary conditions

We used two ghosts cells (one at each boundary of the domain) in order to simplify the implementation of our BCs. In doing so, the inner BC was imposed at the wall between the first ($i = 0$) and second cell ($i = 1$), and at the outer BC between the last ($i = n_x - 1$) and penultimate cell ($i = n_x - 2$). As indicated by Eqs. (20) and (27), we need to specify J_ν and $\boldsymbol{\nabla} J_\nu$ at these interfaces. For this, we used Eq. (35) and write

$$\begin{aligned} J_\nu(R_{\rm in}|R_{\rm out}) &\approx \frac{J_{k,0|n_x-2} + J_{k,1|n_x-1}}{2}, \\ \hat{s}.\boldsymbol{\nabla} J_\nu|_{R_{\rm in}|R_{\rm out}} &\approx \left.\frac{dx}{dr}\right|_{\frac{1}{2}|n_x-\frac{3}{2}} \frac{J_{k,1|n_x-1} - J_{k,0|n_x-2}}{\Delta x}. \end{aligned} \tag{39}$$

Accordingly, the values of J_ν in the ghosts cells were updated immediately after one Gauss-Seidel sweep Eq. (36) to ensure the BCs,

$$\begin{aligned} J_{k,0} &= \frac{2\Delta x \left(\frac{R_\star}{R_{\rm in}}\right)^2 B_k(T_\star) - \left[\Delta x\,(\alpha_k - \gamma_k) - 2\frac{dx}{dr}|_{\frac{1}{2}}\beta_k\right] J_{k,1}}{\Delta x\,(\alpha_k - \gamma_k) + 2\frac{\mathrm{d}x}{\mathrm{d}r}|_{\frac{1}{2}}\beta_k}, \\ J_{k,n_x-1} &= \frac{\left[2\frac{\mathrm{d}x}{\mathrm{d}r}|_{n_x-\frac{3}{2}}\zeta(R_k^{\rm e})D_k(R_k^{\rm e}) - \Delta x\right] J_{k,n_x-2}}{2\frac{\mathrm{d}x}{\mathrm{d}r}|_{n_x-\frac{3}{2}}\zeta(R_k^{\rm e})D_k(R_k^{\rm e}) + \Delta x}, \end{aligned} \tag{40}$$

with α_k, β_k and γ_k being defined by Eqs. (13) and (19). For the extrapolated value $R_k^{\rm e}$ in $\zeta(R_k^{\rm e})$ Eq. (26) and $D_k(R_k^{\rm e})$, we used a second-order Lagrange extrapolation,

$$R_k^{\rm e} = 3\left(R_{k,n_x-\frac{5}{2}} - R_{k,n_x-\frac{7}{2}}\right) + R_{k,n_x-\frac{9}{2}}. \tag{41}$$

4.4. Initial conditions

Initial conditions for both J_ν and T must be provided in order to solve Eq. (33). It is clear that the overall convergence speed strongly depends on the initial setup of the solution, but there is also a trade-off with the stability, that is, the ability of the solution to converge, for a wide variety of cases. As an initial guess, we used the analytic solution of the FLD in the optically thin limit Eq. (23), and we write

$$J_{k,i}^0 = \frac{1}{4}\left(\frac{R_\star}{r_i}\right)^2 B_k(T_\star), \tag{42}$$

from which we deduce the corresponding temperature profile T^0 with the help of Eq. (37).

5. Numerical tests: spherically symmetric envelopes

5.1. Benchmarks from Ivezic et al. (1997)

We tested the accuracy of our FLD code with our Robin-type mixed boundary conditions in a general and realistic case, by comparing it with the 1D benchmark problems realised by Ivezic et al. (1997). We recall the conditions of the test and refer to the original paper for further information.

A point source surrounded by a spherically symmetric envelope of matter at radiative equilibrium irradiates as a black body at the temperature $T_\star = 2500$ K. This envelope extends from the inner radius $R_{\rm in}$ to the outer radius $R_{\rm out} = 1000\,R_{\rm in}$. The inner radius is set so that the temperature at the inner radius is always $T_{\rm in} = T(R_{\rm in}) = 800$ K. The density profile $n(r)$ is assumed to be a power law of the form $n(r) = n_0\,(R_{\rm in}/r)^p$. The radial optical depth τ_ν of the envelope is linked to the density profile by

$$\tau_\nu = \int_{R_{\rm in}}^{R_{\rm out}} \kappa_\nu^{\rm ext}\,\mathrm{d}r = \int_{R_{\rm in}}^{R_{\rm out}} C_\nu^{\rm ext}\,n(r)\,\mathrm{d}r, \tag{43}$$

where $C_\nu^{\rm ext}$ is the extinction cross-section coefficient. It is defined by

$$\begin{aligned} &C_\nu^{\rm abs} = C_{\nu_0}^{\rm abs}, C_\nu^{\rm sca} = C_{\nu_0}^{\rm sca} && \text{if } \nu \geq \nu_0, \\ &C_\nu^{\rm abs} = C_{\nu_0}^{\rm abs}\left(\tfrac{\nu}{\nu_0}\right), C_\nu^{\rm sca} = C_{\nu_0}^{\rm sca}\left(\tfrac{\nu}{\nu_0}\right)^4 && \text{if } \nu \leq \nu_0, \\ &C_\nu^{\rm ext} = C_\nu^{\rm sca} + C_\nu^{\rm abs}, \end{aligned} \tag{44}$$

with $C_{\nu_0}^{\rm abs} = (1-\eta)\,C_{\nu_0}^{\rm ext}$, $C_{\nu_0}^{\rm sca} = \eta\,C_{\nu_0}^{\rm ext}$, ν_0 the frequency corresponding to $\lambda = 1$ μm and η the albedo, set to 1/2 for these tests. The benchmark problems are thus completely defined by two parameters: (i) the exponent in the density power law $p = 0, 2$, and (ii) the radial optical depth of the envelope at ν_0, $\tau_{\nu_0} = 1, 10, 100$, and 1000. This created eight different cases to test the accuracy of our code. The coefficient n_0 in the density profile is derived with the help of τ_{ν_0} and p,

$$n_0 = \frac{(p-1)\,\tau_{\nu_0}}{C_{\nu_0}^{\rm ext} R_{\rm out}} \left(\frac{R_{\rm out}}{R_{\rm in}}\right)^p \left[\left(\frac{R_{\rm out}}{R_{\rm in}}\right)^{p-1} - 1\right]^{-1}. \tag{45}$$

The normalised temperature profile $T/T_{\rm in}$ and the normalised SED $\lambda F_\lambda / F$ ($F = \int_0^\infty F_\lambda\,\mathrm{d}\lambda$) of the envelope are shown in Fig. 2 for each case.

The Ivezic benchmarks were produced with version 2 of DUSTY[3] (Ivezic & Elitzur 1997). Because our code is of different nature, the spatial and frequency grids are different. We

[3] Available at http://faculty.washington.edu/ivezic/dusty_web/

then compared the results by linearly interpolating our profiles (in log – log scale) on the DUSTY grids. We used 128 points for space and frequency, with a logarithmic sampling. The corresponding relative differences are displayed in Table 1. We also point out that we restricted the comparison, for the normalised SEDs, to the frequency domain where $\lambda F_\lambda/F \geq 10^{-6}$ because of non-physical results of the DUSTY code below this threshold, for the smallest wavelengths.

The FLD results and the benchmarks agree well. The average relative differences in the temperature profiles mean($\epsilon(T)$) is of the order of 1%, with a maximum value of approximately 4%, achieved by the most optically thick envelopes ($\tau_{\nu_0} = 1000$). The average of the relatives differences in the normalised SEDs mean($\epsilon(\lambda F_\lambda/F)$) always stays below 3%, with the exception of the optically thick envelope with constant density profile, where this difference reaches 6%.

5.2. Grey spherical shell with the Monte Carlo code from Niccolini & Alcolea (2006)

We compared the FLD code with a 3D MC radiative transfer code (Niccolini & Alcolea 2006). We wished to test the new BCs in the less realistic but more extreme case of a spatially small spherically symmetric grey envelope. We expect the boundary effects to play a major role for this type of problems. The inner radius was set to $R_{\rm in} = 10\,R_\star$ and the outer radius $R_{\rm out} = 20\,R_\star$. We assumed a constant density profile ($p = 0$) in the envelope. Our test cases consisted of determining the normalised temperature profiles $T/T_{\rm in}$ and the emerging fluxes F_λ for several cases, ranging from optically thin ($\tau = 0.01$) up to the optically thick envelopes ($\tau = 100$). The corresponding profiles are shown in Fig. 3.

Because the codes are different, we interpolated our results linearly (in log – log scale) on the MC grids. The relative differences between the two codes, are displayed in Table 2. As an additional feature, the MC code also provides an estimation of the errors on the temperature $\sigma(T)$ and on the emerging flux $\sigma(F_\lambda)$, computed from the MC noise (Niccolini & Alcolea 2006). We used this information to compute a more relevant mean value for $\epsilon(T)$ and $\epsilon(F_\lambda)$,

$$\text{mean}(\epsilon(T)) = \frac{\sum_{i=0}^{N_x} W_i\,\epsilon(T_i)}{\sum_{i=0}^{N_x} W_i}, \text{mean}(\epsilon(F_\lambda)) = \frac{\sum_{k=0}^{N_\lambda} W_k\,\epsilon(F_k)}{\sum_{k=0}^{N_\lambda} W_k} \quad (46)$$

where N_x (N_λ) is the number of spatial (wavelength) points of the MC grid, $\epsilon(T_i)$ ($\epsilon(F_k)$) is the relative error (in %) on the temperature (emerging flux) between our results and the MC results, and W_i (W_k) is the inverse square of the MC relative errors, defined as

$$W_i = \left(\frac{\sigma(T_i)}{T_i}\right)^{-2}, W_k = \left(\frac{\sigma(F_k)}{F_k}\right)^{-2} \quad (47)$$

The two results agree well. The average of the relative differences of the temperature profile mean($\epsilon(T)$), remains of the order of 1% for all the cases we tested. The largest differences are reached for the intermediate cases ($\tau = 1, 10$) and are located on the external edge of the envelope. This is expected because the FLD approximation is known to perform well in the optically thin and thick regimes, but it is less well suited to describe these intermediate cases. Nevertheless, the temperature profile is still quite well reproduced and the emerging flux is not affected by the small errors on the temperature close to the outer edge. We point out that the BCs derived in this paper allow us to successfully reproduce the correct behaviour of the temperature profile for the optically thick envelope where it shows a quite steep decrease at the outer surface, as shown by Fig. 3. The emerging fluxes F_λ agree within 1% on average, except for the optically thick case ($\tau = 100$), where mean($\epsilon(F_\lambda)$) reaches about 5%.

Table 1. Results from the comparison with DUSTY.

τ_{ν_0}	$\epsilon(T)$		$\epsilon(\lambda F_\lambda/F)$	
	$p = 0$	$p = 2$	$p = 0$	$p = 2$
1	0/0/1	0/0/1	1/1/4	1/1/3
10	0/0/1	1/1/3	2/3/14	2/2/10
100	1/0/1	1/1/3	1/1/8	1/2/11
1 000	2/1/4	1/1/4	6/8/30	3/2/9

Notes. Relative differences ϵ (in %) for the temperature profiles $\epsilon(T)$ and for the SEDs $\epsilon(\lambda F_\lambda/F)$ shown in Fig. 2. The results are presented in the form mean(ϵ)/std(ϵ)/max(ϵ) and rounded to the closest percent.

Table 2. Results from the comparison with the MC code.

τ	$\epsilon(T)$	$\epsilon(F_\lambda)$
0.01	0/0/0	0/3/17
1	1/1/5	0/3/17
10	1/1/7	1/8/33
100	0/0/3	1/2/13

Notes. Relative differences ϵ (in %) for the temperature profile $\epsilon(T)$ and for emerging flux $\epsilon(F_\lambda)$ shown in Fig. 3. The differences are presented in the form mean(ϵ)/std(ϵ)/max(ϵ) and rounded to the closest percent. mean(ϵ) is given by Eq. (46).

We conclude this section with a comparison of the outer BC from this study Eq. (27) and the original BC Eq. (56) from L&P, given by,

$$J_\nu(R_{\rm out}) + 2D_\nu \hat{s}.\boldsymbol{\nabla} J_\nu|_{r=R_{\rm out}} = 0. \quad (48)$$

We previously mentioned in Sect. 3.1 that the inner BC Eq. (20) is analytically identical to that of L&P in spherical symmetry, so we restrict the comparison to the outer edge of the envelope. It is important to notice that the BC of L&P was not originally intended to describe this class of problems, but the comparison still remains instructive for studying the importance of the BCs for the accuracy of the solution. In Eq. (48), the factor 2 (Eq. (58) in L&P) was originally used to give the correct ratio of the energy density over the emerging radiative flux in plane-parallel geometry for an optically thin slab illuminated by an isotropic incident radiation field. However, for the special case of a spherical envelope surrounding a black-body star, this ratio becomes

$$\frac{\int_{\mu_0}^1 B_\nu(T_\star)\mathrm{d}\mu}{\int_{\mu_0}^1 \mu B_\nu(T_\star)\mathrm{d}\mu} = \frac{2\,(1-\mu_0)}{1-\mu_0^2} = \frac{2}{1+\mu_0} \quad (49)$$

with $\mu_0 = \sqrt{1-\left(\frac{R_\star}{R_{\rm out}}\right)^2}$, the cosine of the stellar angular size at $R_{\rm out}$. As $\mu_0 \to 0$ or equivalently $R_\star/R_{\rm out} \to 1$, this ratio increases to 2, as expressed by L&P, because we recover the case of a plane-parallel geometry with an isotropic incident radiation field. Far from the star ($\mu_0 \to 1$ or $R_\star/R_{\rm out} \to 0$), the ratio tends to 1, associated with an incoming sharp-peaked radiation. Hence,

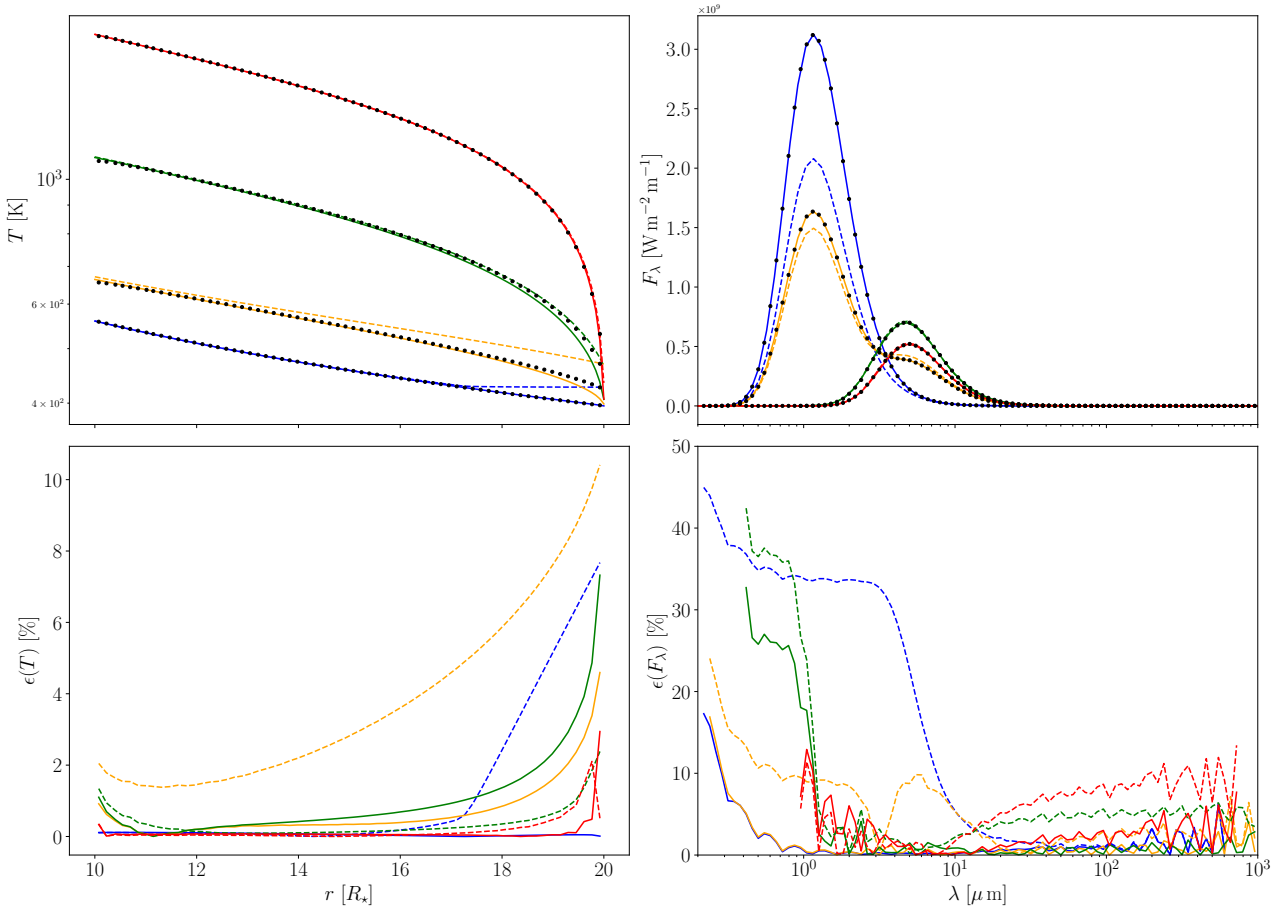

Fig. 4. Comparison of the outer boundary conditions presented here (solid lines) and from Levermore & Pomraning (1981) (dashed lines) for the test case presented in Sect. 5.2. The colour code is the same as in Fig. 3. The emerging fluxes are displayed in semi-log scale to highlight the differences between the BCs. The lower panels show the relative differences profiles with respect to the MC code from Niccolini & Alcolea (2006) in temperature (*left*) and in emerging flux (*right*).

the L&P BC that set the ratio to 2 will strongly deviate from the analytic limit 1, in the optically thin regime. In Fig. 4 we display the relative differences in the temperature profiles $\epsilon(T)$ and in the emerging fluxes $\epsilon(F_\lambda)$ for the same test case as presented at the beginning of this section. We note that this test case is not realistic, however, it allows to compare different optical regimes, in contrast to a more realistic problem in which the radiation is free in the external regions most of the time, such as for the test case presented in Sect. 5.1. We recall that the BC from L&P is a limiting case of the BC derived in this study, in the case $R \ll 1$, where the emerging radiation is almost isotropic (see Sect. 3.2), hence it is not surprising that the results converge to the same profile, for a optically thick grey envelope ($\tau = 100$). On the other-hand, in the optically thin case ($\tau = 0.01$) where we would expect the ζ coefficient Eq. (26) to be close to unity, the BC from L&P performs poorly as expected. For intermediates regimes ($\tau = 1, 10$), the entanglement of the error of the BC and FLD method itself makes any comparison very hard. We note that although the temperature profile is closer to the benchmark result for $\tau = 10$ with the BC of L&P, this is not the case for the associated emerging flux. We also note that the BC, although defined locally, can have a global effect on the whole solution, as shown by the temperature profile of the test case $\tau = 1$. To conclude, we also point out that we tried to implement the L&P BC in the non-grey cases (Sect. 5.1) but we were unable to reach a satisfying convergence of the computations.

6. Conclusion

The FLD approximation together with the new BCs, yields promising results in correctly describing the radiation transport inside spherically symmetric circumstellar envelopes. These conditions, derived in Sect. 3 from physically consistent constraints on the behaviour of the radiation field at the inner and outer surfaces, allow us to compute with a good accuracy the temperature profile and the SED for a wide range of configurations, from very small to very large optical thicknesses. As shown in Sect. 5, it reproduces the correct temperature profile within $\leq 2\%$, and the SED or emerging flux at less than $\leq 6\%$ on average, with respect to the solution of the full radiative transfer equation under radiative equilibrium.

The numerical solution of the 1D non-linear diffusion equation Eq. (31) coupled with the radiative equilibrium Eq. (32) was performed with a Gauss-Seidel method-based iterative scheme, in which the temperature is updated at each iteration step. Furthermore, we point out that the FLD approximation implemented with the proposed outer-boundary condition provides a simple approximation for the flux emitted by the envelope. This allows computing the SED or emerging flux without using any ray-tracing module, which is a significant gain in computational time.

The next step, which will be our main concern for our future work, is the generalisation of these boundary conditions to non-spherically symmetric media, in particular for circumstellar discs, where the BCs will take a more complex form. In this

regard, the extension to 2D will require numerical optimisations. Several directions of improvements are already being studied, such as the use of multi-frequency adaptive spatial grids, or acceleration procedures for efficiently solving the FLD equation under the radiative equilibrium condition. The last point is also crucial for solving extreme optically thick envelopes.

Acknowledgements. This study has been supported by the Lagrange laboratory of Astrophysics and funded under a 3-year PhD grant from Ecole Doctorale Sciences Fondamentales et Appliquées (EDSFA) of the Université Côte-d'Azur (UCA). The benchmark profiles were generated with the radiative transfer code DUSTY, available at `http://faculty.washington.edu/ivezic/dusty_web`. Part of the computations were carried out with the help of OPAL-Meso computing facilities. The authors are grateful to the OPAL infrastructure from Observatoire de la Côte d'Azur (CRIMSON) for providing resources and support.

References

Ivezic, Z., & Elitzur, M. 1997, MNRAS, 287, 799
Ivezic, Z., Groenewegen, M. A. T., Men'shchikov, A., & Szczerba, R. 1997, MNRAS, 291, 121
Kuiper, R., Klahr, H., Dullemond, C., Kley, W., & Henning, T. 2010, A&A, 511, A81
Levermore, C. D., & Pomraning, G. C. 1981, ApJ, 248, 321
Mignon-Risse, R., González, M., Commerçon, B., & Rosdahl, J. 2020, A&A, 635, A42
Niccolini, G., & Alcolea, J. 2006, A&A, 456, 1
Niccolini, G., Woitke, P., & Lopez, B. 2003, A&A, 399, 703
Pomraning, G. C. 1986, J. Quant. Spectr. Rad. Transf., 36, 325
Pomraning, G. C. 1988, J. Comput. Phys., 75, 73
Sonnhalter, C., Preibisch, T., & Yorke, H. W. 1995, A&A, 299, 545
Steinacker, J., Baes, M., & Gordon, K. D. 2013, ARA&A, 51, 63
Yorke, H. W., & Sonnhalter, C. 2002, ApJ, 569, 846

D.2 Discontinuous Galerkin finite element method for the continuum radiative transfer problem inside axis-symmetric circumstellar envelopes (submitted, under revision)

Astronomy & Astrophysics manuscript no. output
February 27, 2023

Discontinuous Galerkin finite element method for the continuum radiative transfer problem inside axis-symmetric circumstellar envelopes

J. Perdigon, M. Faurobert, and G. Niccolini

Université Côte d'Azur (UCA), Observatoire de la Côte d'Azur (OCA), CNRS, Laboratoire Lagrange, Lagrange, France
e-mail: jeremy.perdigon@oca.eu

Received <date>/Accepted <date>

ABSTRACT

Context. The study of the continuum radiative transfer problem inside circumstellar envelopes is both a theoretical and numerical challenge, especially in the frequency-dependent and multi-dimensional case. While approximate methods are easier to handle numerically, they often fail to accurately describe the radiation field in complex geometries. For these cases, it is necessary to directly solve numerically the radiative transfer equation.
Aims. We investigate the accuracy of the Discontinuous Galerkin finite element method (DG-FEM hereafter) applied to the frequency-dependent two dimensional radiative transfer equation, coupled with the radiative equilibrium equation, inside axis-symmetric circumstellar envelopes.
Methods. The DG-FEM is a variant of the finite element method. It employs discontinuous elements and flux integrals along their boundaries, guaranteeing local conservation. However, as opposed to the classical finite-element methods, the solution is discontinuous across element edges. We implemented the method and tested its accuracy by comparing our results with the benchmarks from the literature.
Results. For all the tested cases, the temperature profile agrees within one percent. Additionally, the emerging spectral energy distributions (SEDs) and images, obtained subsequently by ray-tracing techniques from the DG-FEM solution, agree on average within 5 % and 10 %, respectively.
Conclusions. We show that the DG-FEM can accurately describe the temperature profile, emerging SEDs and images inside axis-symmetric circumstellar envelopes. Together with Monte-Carlo and ray-tracing techniques, the DG-FEM provides an additional method for solving the radiative transfer equation, and could be used in cases that are more difficult to handle with the other methods.

Key words. Radiative transfer - Methods: numerical - Circumstellar matter

1. Introduction

The study of the continuum radiative transfer problem is crucial for the characterisation of circumstellar environments. Radiative processes play a major role in the determination of physical observable such as temperature, abundances, velocity fields, *etc*. The description of the radiation field is both a theoretical and numerical challenge, especially in the frequency-dependent and multi-dimensional case.

Several directions have been followed to tackle this problem. One approach involves approximate methods. It is usually done by assuming a particular form for the radiation field, most of the time based on symmetry arguments. The radiative transfer equation is then recast into a presumably simpler equation. This is the case for example of the Eddington approximation (Eddington 1920), where the radiation is assumed to be almost isotropic, which is accurate in the optically thick regime, and where the problem is described by a simple linear diffusion equation. More sophisticated approximations were later developed, e.g the Flux Limited diffusion (Levermore & Pomraning 1981), extending the validity domain to both optically thin and tick regimes, and where the radiation is described by a non-linear diffusion equation.

While approximate methods are easier to handle numerically, they often fail to accurately describe the radiation field in complex geometries (Kuiper & Klessen 2013). For these cases, it is necessary to directly numerically solve the radiative transfer equation (see Steinacker et al. 2013 for a thorough review of the different methods).

A first approach is to approximate the transport operator with finite-differences (e.g Steinacker et al. 2003), yielding a linear system of equations. It has the disadvantage of introducing numerical oscillations and negative values of the intensity, due to the strong spatial and angular variations of radiation field.

Other techniques, such as long/short characteristics (e.g Woitke et al. 2009), rely on the integral form of the radiative transfer equation. They are generally harder to implement than finite-differences methods, are numerically demanding, and can also exhibit negative values (Kunasz & Auer 1988). Both approaches allow however for explicit error control.

Finally, Monte Carlo methods (e.g Wolf 2003) are amongst the most popular because they are easy and fast to implement, can handle complex geometries and do not suffer from the flaws of the other methods. However, the associated noise inherent to their statistical nature makes it difficult to control the error of the solution, especially in optically thick regions where it is difficult for photons to escape the media.

Aside from these techniques, finite-element methods have already been used to solve the radiative transfer equation. A

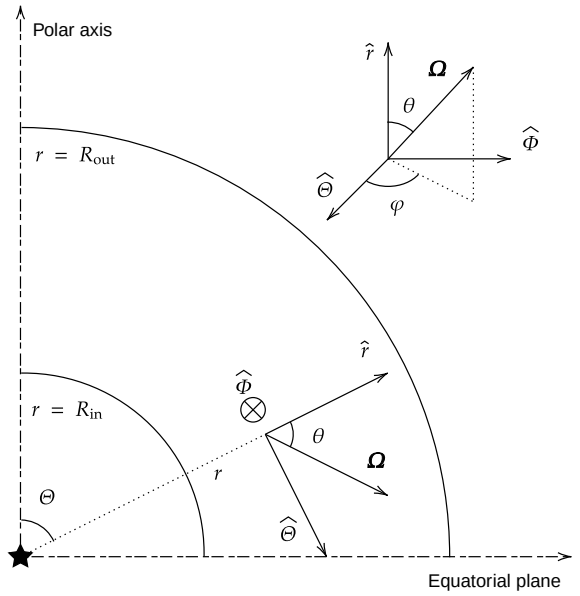

Fig. 1. Illustration picturing the coordinate system. $(\hat{r}, \hat{\Theta}, \hat{\Phi})$ is the standard spherical basis. The radiation field in the envelope, at a given position $\boldsymbol{r}$, in a given direction $\boldsymbol{\Omega}$ is a function of two spatial (r, Θ) and two angular $(\mu = \cos\theta, \varphi)$ coordinates.

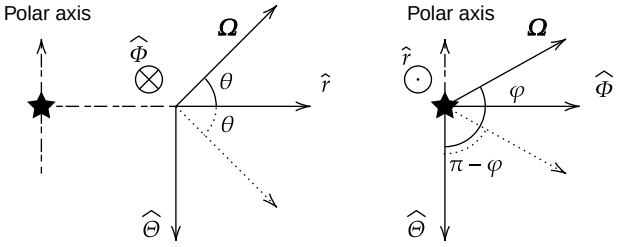

Fig. 2. Representation of the direction vector $\boldsymbol{\Omega}$ at the equator. The dot-arrows represent the symmetric of $\boldsymbol{\Omega}$ with respect to the equatorial plane $(\hat{r}, \hat{\Phi})$. The left and right two-dimensional views allow to see the corresponding direction angles.

variant of it, the discontinuous Galerkin finite element method (Reed & Hill 1973, DG-FEM hereafter), make use of discontinuous elements and flux integrals along their boundaries, guaranteeing local conservation. However, as opposed to the classical finite-element methods, the reconstructed solution is discontinuous across element edges. One of the main strength of the method is its ability to produce a high-order numerical scheme, meaning a coarse computational grid can be used to acheive a small error. This feature is particularly interesting in the context of radiative transfer, where we are often limited by computational ressources. Furthermore, the solution present little to no oscillations, even in the cases where the solution displays a non-smooth behaviour (Nair et al. 2011), which is again often the case in radiative transfer.

The DG-FEM was successfully applied to the one-dimensional spherical transport problem, in the context of neutron transport (Machorro 2007) or more recently in grey stellar atmospheres (Kitzmann et al. 2016). Extension to 2-D radiative transfer, in cylindrical coordinates, exist in another context (see e.g Cui & Li 2005).

In this study, we present the DG-FEM applied to the frequency-dependent dust continuum radiative transfer problem, with isotropic scattering, coupled with the radiative equilibrium equation, in axis-symmetric circumstellar environments. We show that this method can successfully determine the correct temperature profile, and allows to compute images and spectral energy distributions (SEDs) by ray-tracing techniques. The paper is organised as follows: in Sect. 2 we present the radiative transfer problem for axis-symmetric configurations. In Sect. 3 we explain the DG-FEM, and some implementation features in Sect. 4. In Sect. 5, we compare this method, for spherically and axis-symmetric test cases, with other codes from the literature. Finally, in Sect. 6, we conclude and present some perspectives.

2. Description of the problem

We want to describe the radiation field inside an axis-symmetric circumstellar envelope. The situation is illustrated in Fig. 1. A central star of radius $R_\star$ lies inside an inner cavity, free of matter, of radius $R_{\rm in}$. The envelope itself spans from the radius $R_{\rm in}$ up to an outer radius $R_{\rm out}$. We assume that no matter is present after this radius. We consider the material to be exclusively made of dust. In addition to the axial symmetry around the pole ($\Theta = 0$), we also assume a planar symmetry with respect to the equatorial plane, at $\Theta = \pi/2$. We choose to describe the problem with the spherical coordinate system, both for the spatial and angular variables, hence, given the symmetries, the domain of definition is $D \subset \mathbb{R}^4$ with $D \ni \boldsymbol{x} = [r, \Theta, \mu = \cos\theta, \varphi] \in [R_{\rm in}, R_{\rm out}] \times]0, \pi/2] \times [-1, 1] \times [0, \pi]$. The associated radiation field is described by the time-independent radiation transfer equation (for a thorough derivation see e.g Pomraning 1973, II-5),

$$\begin{aligned} &\boldsymbol{\Omega}.\nabla I_\nu + \kappa_\nu^{\rm ext} I_\nu = \eta_\nu, \\ \text{with}\quad &\boldsymbol{\Omega}.\nabla I_\nu = \mu\,\partial_r I_\nu + \frac{\sqrt{1-\mu^2}\cos\varphi}{r}\partial_\Theta I_\nu + \frac{1-\mu^2}{r}\partial_\mu I_\nu \\ &\qquad - \frac{\cot\Theta\sqrt{1-\mu^2}\sin\varphi}{r}\partial_\varphi I_\nu. \end{aligned} \tag{1}$$

The subscript ν denotes the frequency dependence, I_ν is the specific intensity and $\boldsymbol{\Omega}.\nabla$ is the directional derivative in the direction $\boldsymbol{\Omega}$, expressed in the spherical coordinate system. $\kappa_\nu^{\rm ext}$ is the extinction coefficient and η_ν is the emissivity containing the thermal emission and scattering. We consider here the matter to be at local thermal equilibrium and the scattering to be isotropic, for the purpose of the numerical tests (although it can be generalised to anisotropic scattering with no difficulty). Hence, the emissivity is $\eta_\nu = \kappa_\nu^{\rm abs} B_\nu(T) + \kappa_\nu^{\rm sca} J_\nu$, with $\kappa_\nu^{\rm abs}$, $\kappa_\nu^{\rm sca}$ the absorption and scattering coefficients, respectively. B_ν is the Planck function associated with the temperature T of the dust and J_ν the mean specific intensity, which is the zeroth-order angular moment of the specific intensity I_ν,

$$J_\nu = \frac{1}{4\pi}\int_{4\pi} I_\nu \,\mathrm{d}\boldsymbol{\Omega} = \frac{1}{2\pi}\int_0^\pi \mathrm{d}\varphi \int_{-1}^{1} I_\nu \,\mathrm{d}\mu. \tag{2}$$

The radiation field and the temperature are coupled via the equation of radiative equilibrium,

$$\int_0^\infty \kappa_\nu^{\rm abs} B_\nu(T)\ \mathrm{d}\nu = \int_0^\infty \kappa_\nu^{\rm abs} J_\nu \,\mathrm{d}\nu. \tag{3}$$

The circumstellar matter is illuminated by a central star and it is customary to decompose the radiation field into two contributions (see e.g Steinacker et al. 2003) $I_\nu = I_\nu^\star + I_\nu^{\rm env}$, with $I_\nu^\star$ the direct unprocessed stellar radiation field attenuated by the circumstellar extinction and $I_\nu^{\rm env}$, the radiation emitted by the envelope (either via thermal emission or scattering). Eq. (1) can then be recast into the following system of equations,

$$\begin{cases} \boldsymbol{\Omega}.\nabla I_\nu^\star + \kappa_\nu^{\rm ext} I_\nu^\star = 0, \\ \boldsymbol{\Omega}.\nabla I_\nu^{\rm env} + \kappa_\nu^{\rm ext} I_\nu^{\rm env} = \kappa_\nu^{\rm abs} B_\nu + \kappa_\nu^{\rm sca} J_\nu, \end{cases} \tag{4}$$

with $J_\nu = J_\nu^\star + J_\nu^{\rm env}$. We note that in Steinacker et al. (2003), the thermal emission term is put into the right-hand side (RHS hereafter) of the first Eq. (4), but having it in the second equation is advantageous if the optical coefficients are independent of temperature. In such cases, the equations decouple and $I_\nu^\star$ can be solved and computed once and for all. The first Eq. (4) can be integrated along a given ray, yielding the formal solution for the stellar contribution,

$$I_\nu^\star = \begin{cases} \Gamma_\nu^\star\,(R_\star,\mu)\,\exp\left\{-\int_0^{s(R_{\rm in})} \kappa_\nu^{\rm ext}(s')\,{\rm d}s'\right\} & \text{if } \mu_\star \le \mu \le 1, \\ 0 & \text{otherwise.} \end{cases} \tag{5}$$

$\Gamma_\nu^\star\,(R_\star,\mu)$ is the incident stellar radiation field. Again, for the purpose of the numerical tests, we will assume the star to radiate as a black body at the temperature $T_\star$. $\mu_\star = (1-(R_\star/r)^2)^{1/2}$ is the cosine of the angle under which the star is seen at radius r and $s(R_{\rm in})$ is the distance between a given point $\boldsymbol{r}$ in the envelope and the inner radius, along a given ray $\boldsymbol{\Omega}$. The argument in the exponential is the opposite of the optical depth integrated along the ray. In the point source approximation, the stellar mean intensity can be expressed analytically as,

$$J_\nu^\star\,(r,\Theta) \approx \frac{(1-\mu_\star)}{2}\,B_\nu\,(T_\star)\,\exp\left\{-\int_{R_{\rm in}}^{r} \kappa_\nu^{\rm ext}(r',\Theta)\,{\rm d}r'\right\}. \tag{6}$$

In general, the integral in Eq. (6) can be carried out numerically, providing the stellar source term for Eq. (4).

To complete the description of the problem, we need to specify the boundary conditions for $I_\nu^{\rm env}$. We achieve this by specifying the incident distribution of intensity $\Gamma_\nu^{\rm env}\,(\boldsymbol{r}_s,\boldsymbol{\Omega})$ upon the surface of the domain located at $\boldsymbol{r}_s$,

$$I_\nu^{\rm env}\,(\boldsymbol{r}_s,\boldsymbol{\Omega}) = \Gamma_\nu^{\rm env}\,(\boldsymbol{r}_s,\boldsymbol{\Omega}) \quad \forall\ \hat{s}.\boldsymbol{\Omega} < 0, \tag{7}$$

where $\hat{s}$ the unit vector normal to the surface of D, pointing outside of the domain. At the inner radius $r = R_{\rm in}$ ($\hat{s} = -\hat{r}$), the incident radiation, in a given direction (μ,φ), comes directly from the opposite point of the cavity,

$$I_\nu^{\rm env}\,(R_{\rm in},\Theta,\mu,\varphi) = I_\nu^{\rm env}\,(R_{\rm in},\Theta',\mu',\varphi') \quad \forall\ 0 < \mu < \mu_\star, \tag{8}$$

with $(R_{\rm in},\Theta',\mu',\varphi')$ the local coordinates of the opposite point. Their derivation is given in appendix A. On the outer edge $r = R_{\rm out}$ ($\hat{s} = \hat{r}$), we assume that there is no incident radiation upon the surface,

$$I_\nu^{\rm env}\,(R_{\rm out},\Theta,\mu,\varphi) = 0 \quad \forall\ \mu < 0. \tag{9}$$

At the equator $\Theta = \pi/2$ ($\hat{s} = \hat{\Theta}$), the planar symmetry requires the radiation field to verify, as pictured by Fig. 2,

$$I_\nu^{\rm env}\,(r,\pi/2,\mu,\varphi) = I_\nu^{\rm env}\,(r,\pi/2,\mu,\pi-\varphi) \quad \forall\ \varphi > \pi/2. \tag{10}$$

3. The radiative transfer equation with the discontinuous Galerkin finite element method

We present the DG-FEM applied to the general radiative transfer Eq. (1). We use some elements of notation from Kitzmann et al. (2016) and Hesthaven & Warburton (2007). For simplicity, we omit the frequency subscript. The conservative form of Eq. (1) is

$$\nabla_{\boldsymbol{x}}.\boldsymbol{F} + \kappa^{\rm ext}\tilde{I} = \tilde{\eta}\,, \tag{11}$$

with $\tilde{\eta} = r^2\,\sin\Theta\,\eta$. We introduce the variable $\tilde{I} = r^2\,\sin\Theta\,I$ which is the quantity that is conserved in Eq. (11). Using this quantity is important because it improves the stability of the numerical scheme, especially near the polar axis ($\Theta = 0$) where the equation is not defined when using the spherical coordinate system. $\nabla_{\boldsymbol{x}}.\boldsymbol{F}$ is the Cartesian divergence operator with respect to $\boldsymbol{x} = [r,\Theta,\mu,\varphi]$, applied to the flux vector $\boldsymbol{F}$ of $\tilde{I}$,

$$\boldsymbol{F} = \boldsymbol{a}\tilde{I} = \begin{bmatrix} a_r \\ a_\Theta \\ a_\mu \\ a_\varphi \end{bmatrix} \tilde{I} = \begin{bmatrix} \mu \\ \sqrt{1-\mu^2}\cos\varphi/r \\ (1-\mu^2)/r \\ -\cot\Theta\,\sqrt{1-\mu^2}\sin\varphi/r \end{bmatrix} \tilde{I}\,. \tag{12}$$

We decompose the domain D into $N = N_r \times N_\Theta \times N_\mu \times N_\varphi$ non-overlapping rectangular elements $D^{i,j,k,l}$, with N_r, N_Θ, N_μ, N_φ the number of elements along the r, Θ, μ, φ coordinate, respectively. Each element is denoted with the help of four indexes i, j, k, l, ranging from 0 to N_r-1, $N_\Theta-1$, $N_\mu-1$, $N_\varphi-1$. Within each element $D^{i,j,k,l}$, we use the nodal representation and we approximate the local solution by a four-dimensional polynomial expansion

$$\tilde{I}_h^{i,j,k,l}\,(\boldsymbol{x}) = \begin{cases} \sum_{a=0}^{n_a-1}\sum_{b=0}^{n_b-1}\sum_{c=0}^{n_c-1}\sum_{d=0}^{n_d-1} \tilde{I}_{a,b,c,d}^{i,j,k,l}\,h_{a,b,c,d}\,(\boldsymbol{x}) & \text{if } \boldsymbol{x} \in D^{i,j,k,l}, \\ 0 & \text{otherwise.} \end{cases} \tag{13}$$

with n_a, n_b, n_c, n_d, the number of nodes in each element $D^{i,j,k,l}$, along the r, Θ, μ, φ coordinate, respectively. $h_{a,b,c,d}$ is the four-dimensional Lagrange polynomial defined as,

$$\begin{aligned} h_{a,b,c,d}\,(\boldsymbol{x}) &= h_a\,(r)\,h_b\,(\Theta)\,h_c\,(\mu)\,h_d\,(\varphi) \\ &= \prod_{\substack{\alpha=0\\ \alpha\neq a}}^{n_a-1} \frac{r-r_\alpha}{r_a-r_\alpha} \prod_{\substack{\beta=0\\ \beta\neq b}}^{n_b-1} \frac{\Theta-\Theta_\beta}{\Theta_b-\Theta_\beta} \prod_{\substack{\gamma=0\\ \gamma\neq c}}^{n_c-1} \frac{\mu-\mu_\gamma}{\mu_c-\mu_\gamma} \prod_{\substack{\delta=0\\ \delta\neq d}}^{n_d-1} \frac{\varphi-\varphi_\delta}{\varphi_d-\varphi_\delta}. \end{aligned} \tag{14}$$

By definition, the coefficients $\tilde{I}_{a,b,c,d}^{i,j,k,l} = \tilde{I}_h^{i,j,k,l}\,(\boldsymbol{x}_{a,b,c,d})$ correspond to the value of $\tilde{I}_h^{i,j,k,l}$ at the nodes of coordinates $\boldsymbol{x}_{a,b,c,d} = [r_a,\Theta_b,\mu_c,\varphi_d]$.

An example of an element $D^{i,j,k,l}$ with the associated nodes is shown in Fig. B.1. The global approximation of the solution I_h across the domain D is formed by the sum of the N piece-wise continuous solutions of each element,

$$\tilde{I}\,(\boldsymbol{x}) \approx \tilde{I}_h\,(\boldsymbol{x}) = \sum_{i=0}^{N_r-1}\sum_{j=0}^{N_\Theta-1}\sum_{k=0}^{N_\mu-1}\sum_{l=0}^{N_\varphi-1} \tilde{I}_h^{i,j,k,l}\,(\boldsymbol{x})\,. \tag{15}$$

We note that no continuity is imposed at the surface between each element.

Let us introduce now $\mathcal{R}_h$, the residual of Eq. (11),

$$\mathcal{R}_h\,(\boldsymbol{x}) = \nabla_{\boldsymbol{x}}.\boldsymbol{F}_h + \kappa^{\rm ext}\tilde{I}_h - \tilde{\eta}, \tag{16}$$

with $\boldsymbol{F}_h = \boldsymbol{a}\tilde{I}_h$. We form the classical Galerkin formulation (see e.g Eq. 2.3 of Hesthaven & Warburton 2007) by requiring the residual to be orthogonal, within each element, to the same set of functions used for the solution representation,

$$\int_{D^{i,j,k,l}} \mathcal{R}_h(\boldsymbol{x})\, h_{a',b',c',d'}(\boldsymbol{x})\ \mathrm{d}^4\boldsymbol{x} = 0 \quad \forall\, D^{i,j,k,l},\ h_{a',b',c',d'}. \tag{17}$$

The divergence term that appears in Eq. (17) can be recast with the help of the divergence theorem (Green-Ostrogradsky), yielding the following so-called weak formulation of the radiative transfer equation Eq. (11),

$$\oint_{\partial D^{i,j,k,l}} \hat{s}.\boldsymbol{F}^*\, h_{a',b',c',d'}\ \mathrm{d}^3\boldsymbol{x} - \int_{D^{i,j,k,l}} \boldsymbol{F}_h.\nabla h_{a',b',c',d'}\ \mathrm{d}^4\boldsymbol{x}$$
$$+ \int_{D^{i,j,k,l}} \left(\kappa^{\mathrm{ext}}\tilde{I}_h - \tilde{\eta}\right) h_{a',b',c',d'}\ \mathrm{d}^4\boldsymbol{x} = 0 \quad \forall\, D^{i,j,k,l},\ h_{a',b',c',d'}. \tag{18}$$

The first term in Eq. (18) is a surface integral on the boundaries of $D^{i,j,k,l}$. $\hat{s}$ is the outward normal vector to the surface element and $\boldsymbol{F}^*$ is an estimate of the flux at the cell interface, called numerical flux. It arises because the solution is not uniquely defined at the edge due to the discontinuous form of the solution. We recall that $D^{i,j,k,l}$ is a four-dimensional rectangular element, hence each element has 2×4 boundary surfaces. The second and third terms in Eq. (18) are volume integrals and are purely local terms that depend on the solution inside the element considered.

For $\boldsymbol{F}^*$, several choices are possible, depending on the nature of the problem (Cockburn 2003). In our case and as it is commonly employed for transport problems, we use the Lax-Friedrichs numerical flux, defined as (e.g on the radial right element edge where $\hat{s} = \hat{r}$),

$$\hat{r}.\boldsymbol{F}^* = \frac{1}{2}\left[F_r(\tilde{I}^-) + F_r(\tilde{I}^+) - |a_r|\left(\tilde{I}^+ - \tilde{I}^-\right)\right], \tag{19}$$

with $\tilde{I}^-$ and $\tilde{I}^+$ denotes the left and right values of $\tilde{I}$ at the element edge, a_r and F_r as defined in Eq. (12). The same form of expression holds for the other surfaces of the element.

Eq. (18) can be assembled into a system of $N' = N \times n$ equations with $n = n_a \times n_b \times n_c \times n_d$, relating the coefficients $\tilde{I}^{i,j,k,l}_{a,b,c,d}$. The integrals are numerically estimated with the help of quadrature formulae. The choice of the quadrature, with the associated roots (nodes) is not unique and is usually problem-dependent (for an extensive review see e.g Kopriva & Gassner 2010). In general, we can put the system of Eq. (18) in the form

$$\mathcal{A}\tilde{\boldsymbol{I}}_h = \mathcal{B}, \tag{20}$$

with $\tilde{\boldsymbol{I}}_h$ the vector of size N' containing the solution points of the full domain D, $\mathcal{A}$ a sparse matrix of size $N' \times N'$ coupling the elements of $\tilde{\boldsymbol{I}}_h$ and $\mathcal{B}$ a vector of size N' containing the emissivity term $\tilde{\eta}$.

4. Solution strategy and numerical considerations

The solution of the complete problem presented in Sect. 2 involves the determination of the full radiation field I_ν Eq. (1) coupled with the equation of radiative equilibrium Eq. (3). For the test cases we consider in Sect. 5, the star is treated in the point source approximation, hence we directly use Eqs. (5) and (6) to solve for $I^\star_\nu$ and $J^\star_\nu$. The radiation field of the envelope I^{env}_ν Eq. (4) is solved with the DG-FEM presented in Sect. 3. For simplicity, we omit the envelope superscript but implicitly refer to this contribution below.

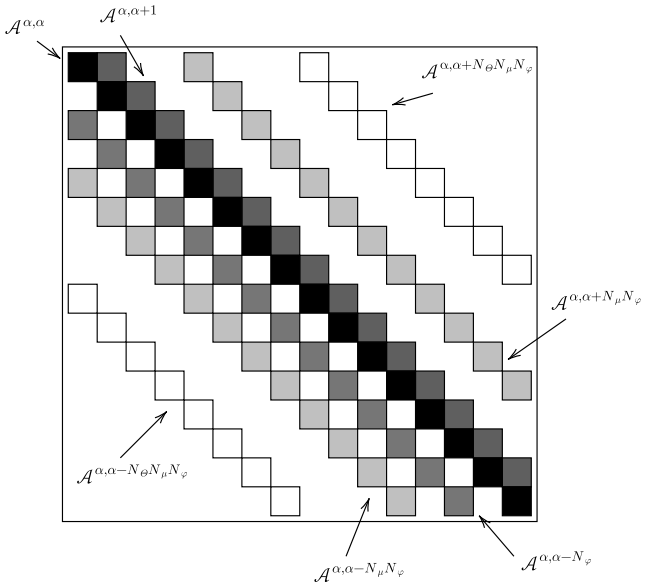

Fig. 3. Example of the sparse structure of $\mathcal{A}$ with $N_r = N_\Theta = N_\mu = N_\varphi = 2$. The squares represent the blocks of size $n \times n$ containing non-zero values. The matrix has bands corresponding to the coupling blocks $\mathcal{A}^{\alpha,\alpha}$, $\mathcal{A}^{\alpha,\alpha+1}$, $\mathcal{A}^{\alpha,\alpha-N_\varphi}$, $\mathcal{A}^{\alpha,\alpha\pm N_\mu N_\varphi}$, $\mathcal{A}^{\alpha,\alpha\pm N_\Theta N_\mu N_\varphi}$ blocks.

The high-dimensional nature of the radiative-transfer problem often results in a very large number of points N' and the resolution of the system Eq. (20) becomes numerically tedious. However, $\mathcal{A}$ is sparse, because each solution point $\tilde{I}^{i,j,k,l}_{a,b,c,d}$ within a given element $D^{i,j,kl}$ only depends on the other points within the same element and the neighbouring cells $D^{i\pm1,j\pm1,k-1,l+1}$. This property allows us to rewrite Eq. (20) as

$$\begin{aligned}\mathcal{A}^{i,j,k,l}\tilde{\boldsymbol{I}}_h^{i,j,k,l} + \mathcal{A}^{i+1,j,k,l}\tilde{\boldsymbol{I}}_h^{i+1,j,k,l} + \mathcal{A}^{i-1,j,k,l}\tilde{\boldsymbol{I}}_h^{i-1,j,k,l} \\ + \mathcal{A}^{i,j+1,k,l}\tilde{\boldsymbol{I}}_h^{i,j+1,k,l} + \mathcal{A}^{i,j-1,k,l}\tilde{\boldsymbol{I}}_h^{i,j-1,k,l} + \mathcal{A}^{i,j,k-1,l}\tilde{\boldsymbol{I}}_h^{i,j,k-1,l} \\ + \mathcal{A}^{i,j,k,l+1}\tilde{\boldsymbol{I}}_h^{i,j,k,l+1} = \mathcal{B}^{i,j,k,l}, \quad \forall\, i,j,k,l.\end{aligned} \tag{21}$$

$\mathcal{A}^{i,j,k,l}$ are the diagonal blocks of $\mathcal{A}$, of size $n \times n$ while $\mathcal{A}^{i\pm1,j\pm1,k-1,l+1}$ are the only non-diagonal blocks (of size $n \times n$ still) which contain non-zeros elements. We note that the elements $D^{i,j,k+1,l}$ and $D^{i,j,k,l-1}$ do not contribute because of the expression of the Lax-Friedrichs numerical flux Eq. (19) ($a_\mu \geq 0, a_\varphi \leq 0, \forall x \in D$). $\tilde{\boldsymbol{I}}_h^{i,j,k,l}$ and $\mathcal{B}^{i,j,k,l}$ are the sub-vector of $\tilde{\boldsymbol{I}}_h$, and $\mathcal{B}$ respectively, of length n, containing the local terms in $D^{i,j,k,l}$.

To put $\mathcal{A}$ in a matrix form, we make use of a global index $\alpha = i N_\Theta N_\mu N_\varphi + j N_\mu N_\varphi + k N_\varphi + l$. An example of the structure of the matrix $\mathcal{A}$ with the associated blocks is displayed in Fig. 3. The formulation Eq. (21) avoids the storage and computation of the full matrix $\mathcal{A}$, which reduces the computational effort.

In general, the simplest approach to obtain a solution from the complete problem is to fully solve Eq. (21) and to update the temperature with Eq. (3). Iterating between these two processes until convergence yields the solution of the problem. This procedure, commonly called the Λ-iteration in the literature becomes very slow and does not converge for large optical depths (Mihalas & Mihalas 1984, VI-83). Our solution strategy is directly inspired from Perdigon et al. (2021). The key point of the method is to solve simultaneously instead of repetitively Eq. (21)

and Eq. (3). This procedure can be assimilated to an acceleration procedure, for optically-thin to moderately-thick envelopes. We however note that, as in the usual Λ-iteration, it converges very slowly for optically thick envelopes.

Our solution strategy proceed as follow: if we denote by the superscript index n the iteration of the method, we first (i) compute the stellar mean radiation field $J_\nu^\star$ with Eq. (6) and set $[I_\nu^{\rm env}]^{n=0} = 0$, as an initial condition. This allows us to compute the initial temperature profile T^0, with the help of Eq. (3), where $J_\nu^0 = J_\nu^\star$. (ii) Then, for each frequency, we compute $[I_\nu^{\rm env}]^{n+1}$ with the help of Eq. (21), that we rewrite, performing a block Gauss-Seidel sweep (see e.g Karniadakis & Kirby II 2003, VII-2).

$$\begin{aligned}\mathcal{A}^{i,j,k,l}\left[\tilde{\boldsymbol{I}}_h^{i,j,k,l}\right]^{n+1} = \left[\mathcal{B}^{i,j,k,l}\right]^n - \mathcal{A}^{i+1,j,k,l}\left[\tilde{\boldsymbol{I}}_h^{i+1,j,k,l}\right]^n \\ -\mathcal{A}^{i-1,j,k,l}\left[\tilde{\boldsymbol{I}}_h^{i-1,j,k,l}\right]^{n+1} - \mathcal{A}^{i,j+1,k,l}\left[\tilde{\boldsymbol{I}}_h^{i,j+1,k,l}\right]^n \\ -\mathcal{A}^{i,j-1,k,l}\left[\tilde{\boldsymbol{I}}_h^{i,j-1,k,l}\right]^{n+1} - \mathcal{A}^{i,j,k-1,l}\left[\tilde{\boldsymbol{I}}_h^{i,j,k-1,l}\right]^{n+1} \\ -\mathcal{A}^{i,j,k,l+1}\left[\tilde{\boldsymbol{I}}_h^{i,j,k,l+1}\right]^n .\end{aligned} \tag{22}$$

We give in appendix B the expressions of $\mathcal{A}^{i,j,k,l}$ and the RHS in Eq. (22). We note that Eq. (22) represents N linear systems to solve. The components of $[\tilde{\boldsymbol{I}}_h^{i,j,k,l}]^{n+1}$ are found by direct inversion of $\mathcal{A}^{i,j,k,l}$, using the Gauss elimination algorithm (see e.g Karniadakis & Kirby II 2003, IX-1). (iii) We compute $J_\nu^{\rm env}$ and consequently update the temperature via Eq. (3). The new temperature allows us to update the RHS of Eq. (22) and to repeat step (ii) and (iii), until convergence. We point out that the method is different from the common Λ-iteration as temperature is updated together with I_ν during the iterative scheme Eq. (22).

Finally, concerning the implementation of the boundary conditions, we directly followed the prescription from Kitzmann et al. (2016, Appendix A.6).

5. Numerical tests

The lack of analytic solutions for the radiative transfer problem, especially in the multi-dimensional and frequency-dependent case, restricts our possibilities for testing the validity of the method. In general, we have to compare the numerical solutions with other results from the literature. For this purpose, benchmark problems have been proposed. The first test case we consider in Sect. 5.1 is the frequency-dependent radiative transfer problem inside a spherically-symmetric envelope, from Ivezic et al. (1997). Then, in Sect. 5.2, we treat the frequency-dependent radiative transfer inside an axis-symmetric envelope (disc), from Pascucci et al. (2004). We note that both tests are compatible with the boundary conditions presented in Sect. 2. A summary of the main results is presented in Table 1.

5.1. 1D spherically symmetric envelope

A point source, surrounded by a spherically symmetric envelope of dust at radiative equilibrium, radiates as a black body at the temperature $T_\star = 2\,500$ K. This envelope extends from the inner radius $R_{\rm in}$ to the outer radius $R_{\rm out} = 1\,000\,R_{\rm in}$. The inner radius is set so that the temperature at the inner radius is always $T_{\rm in} = T(R_{\rm in}) = 800$ K. The number density profile $n(r)$ is assumed to be a power law of the form $n(r) = n_0\,(R_{\rm in}/r)^2$. n_0 is determined to set the value of τ_{ν_0} , the radial optical depth integrated though the envelope, at $\nu_0 = c/\lambda_0$ with $\lambda_0 = 1\ \mu$m,

$$\tau_{\nu_0} = \int_{R_{\rm in}}^{R_{\rm out}} \kappa_{\nu_0}^{\rm ext}\,{\rm d}r = C_{\nu_0}^{\rm ext}\int_{R_{\rm in}}^{R_{\rm out}} n\,{\rm d}r = C_{\nu_0}^{\rm ext}\,n_0\,R_{\rm in}\left(1-\frac{R_{\rm in}}{R_{\rm out}}\right) \tag{23}$$

$C_{\nu_0}^{\rm ext}$ is the extinction cross-section coefficient at ν_0. In this test we consider $\tau_{\nu_0} = 1,\ 10^2$, corresponding to moderately thin and tick envelopes, respectively. The opacity laws are directly taken from Ivezic et al. (1997). The absorption and scattering cross-section coefficients $C_\nu^{\rm abs}$ and $C_\nu^{\rm sca}$ feature a bilinear behavior in log-log scaling, with a constant profile for $\nu \geq \nu_0$ and a power-law dependence $\propto (\nu/\nu_0)^\alpha$ for $\nu \leq \nu_0$ with $\alpha = 1, 4$ for absorption and scattering respectively. This dependence aims at mimicking the behaviour of spherical astronomical Silicate grains. The benchmarks from Ivezic et al. (1997) were produced with version 2 of DUSTY[1]. Although the envelope is spherically symmetric, we use a grid of $N = N_r\times N_\Theta\times N_\mu\times N_\varphi = 16^4$ elements with each elements containing $n_a\times n_b\times n_c\times n_d = 3\times2\times3\times3$ nodes, as pictured by Fig. B.1. For the radial coordinates, the cell edges are logarithmically spaced, to account for the important dynamic of the solution with respect to the radius. The frequency grid consists of 60 logaritmically spaced points, ranging from $\lambda = 10^{-2}\ \mu$m to $\lambda = 3.6\times10^4\ \mu$m.

The temperature profile T and the normalised spectral energy distribution (SED) $\lambda F_\lambda/F\ \left(F = \int_0^\infty F_\lambda\,{\rm d}\lambda\right)$ of the envelope are shown in Fig.4. For the DG-FEM code, the temperature corresponds to the mean radial profile across all angular points Θ. Additionally, the normalised SEDs were computed with the help of a ray-tracing module we present in appendix C. The spatial and frequency grids differ between both codes and we perform a linear interpolation (in log-log scaling) of the DUSTY profiles at our grid points in order to do the comparison. We observe a good agreement between the two codes. On average, the absolute relative differences stay below 1 % for the temperature and 2 % for the SEDs.

5.2. 2D axis-symmetric envelope

A point source surrounded by an axis-symmetric envelope of dust, describing a disc, at radiative equilibrium, radiates as a black body at the temperature $T_\star = 5\,800$ K. This disc extends from the inner radius $R_{\rm in} = 1$ AU to the outer radius $R_{\rm out} = 1\,000$ AU. The density profile $n(r,\Theta)$ is assumed to be on the form,

$$n(r,\Theta) = n_0\frac{r_d}{r\sin\Theta}\exp\left\{-\frac{\pi}{4}\left(\frac{r\cos\Theta}{h}\right)^2\right\} \tag{24}$$

with $h = z_d\,(r\sin\Theta/r_d)^{\frac{9}{8}}$, $r_d = R_{\rm out}/2$ and $z_d = R_{\rm out}/8$. This density law is characteristic of a Keplerian disc hydrostatically supported in the vertical direction, assuming a constant temperature along this direction (Chiang & Goldreich 1997). Again, n_0 is determined to set τ_{ν_0}, the radial optical depth, integrated though the disc mid-plane ($\Theta = \pi/2$), at frequency $\nu_0 = c/\lambda_0$ with $\lambda_0 = 0.55\ \mu$m,

$$n_0 = \frac{\tau_{\nu_0}}{C_{\nu_0}^{\rm ext}\,r_d\,\ln\left(\frac{R_{\rm out}}{R_{\rm in}}\right)}. \tag{25}$$

The opacities are taken from Draine & Lee (1984). A table of pre-computed values is available in Pascucci et al. (2004).

[1] available at http://faculty.washington.edu/ivezic/dusty_web/

Table 1. Summary of the main results

	Ivezic et al. (1997)	Sect. 5.1	Pascucci et al. (2004)	Sect. 5.2
Optical depth τ_{ν_0}	1	10^2	10^{-1}	10^2
$\epsilon(T)$ (%)	0/0/0	0/0/1	0/0/0	1/0/2
ϵ (SED)$_{i=12.5\mathrm{deg}}$ (%)	-/-/-	-/-/-	2/2/6	2/3/10
ϵ (SED)$_{i=77.5\mathrm{deg}}$ (%)	2/2/8	1/2/2	2/2/5	3/4/24

Notes. Relative differences for the temperature profiles $\epsilon(T)$ and for the SEDs ϵ (SED) of the two test problems. The results are presented in the form mean($|\epsilon|$) / std($|\epsilon|$) / max($|\epsilon|$) and rounded to the closest percent.

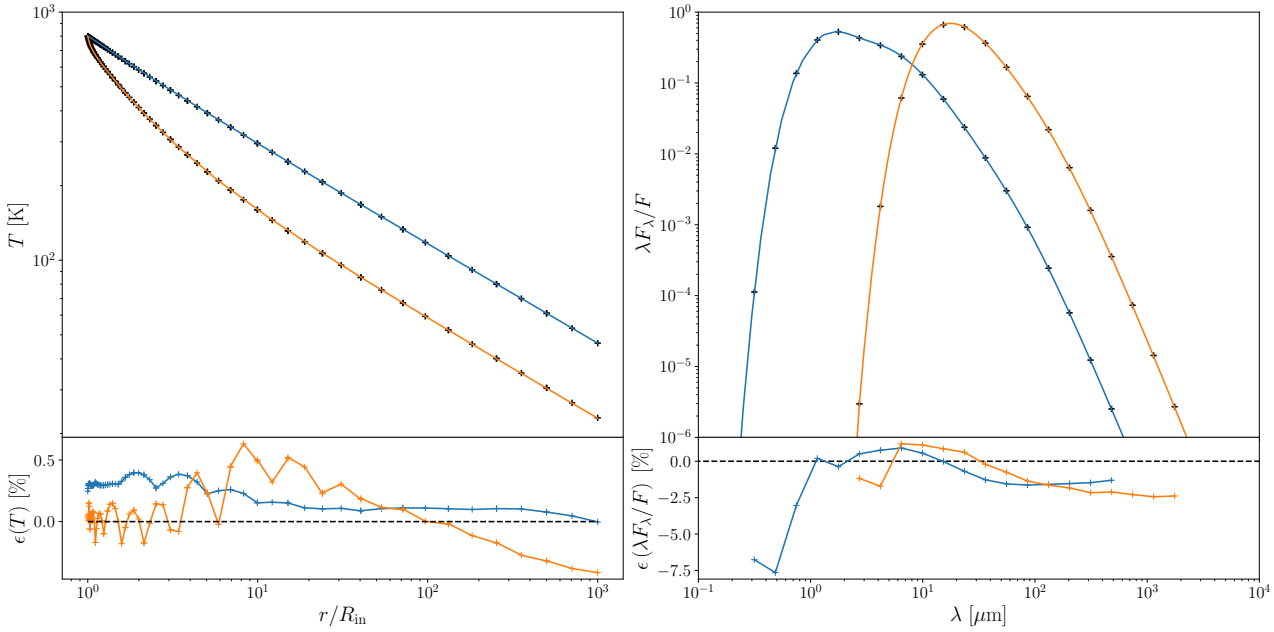

Fig. 4. Temperature profiles (left panels) and normalised SEDs (right) for the spherically symmetric envelope, with $\tau_{\nu_0} = 1$ (blue curve) and $\tau_{\nu_0} = 10^2$ (orange curve). The cross marks represent the solution from this study and the solid curves are computed with DUSTY (Ivezic et al. 1997). The lower panels display the relative differences between the two codes.

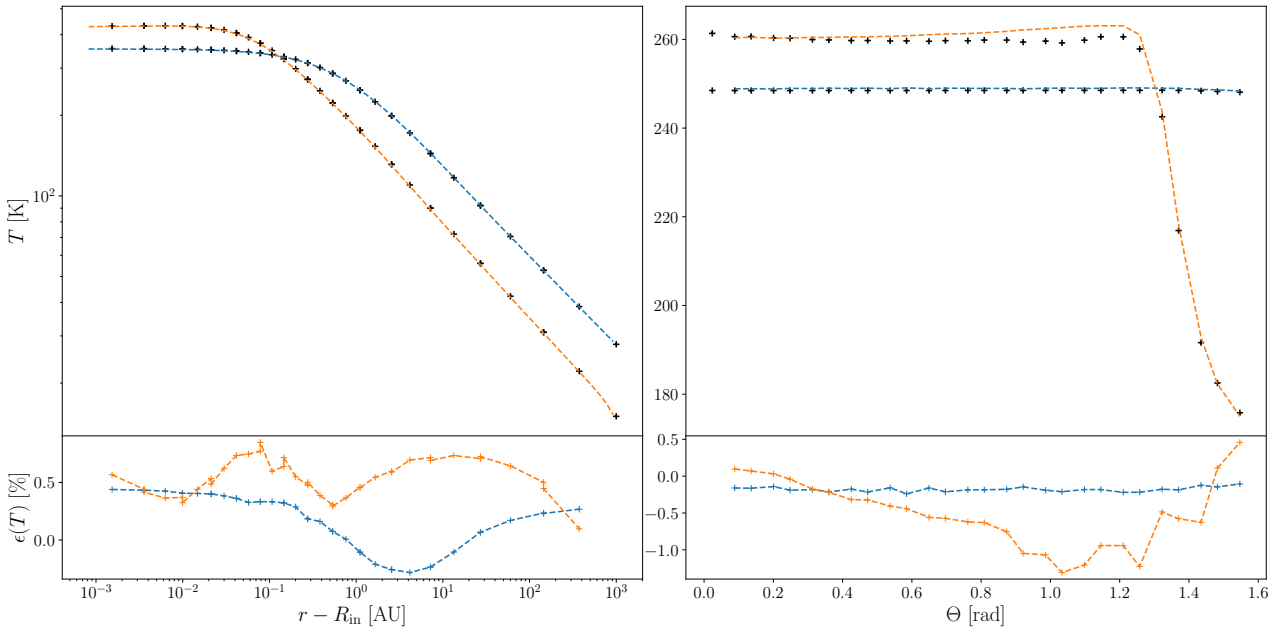

Fig. 5. Temperature profiles for the axis-symmetric envelope with $\tau_{\nu_0} = 10^{-1}$ (blue curve) and $\tau_{\nu_0} = 10^2$ (orange curve), in the in the disc-mid-plane (left panel) and at r=2 AU (right panel). The cross marks represent the solution from this study and the solid curves are computed with RADMC-3D. The lower panels display the relative differences between the two codes.

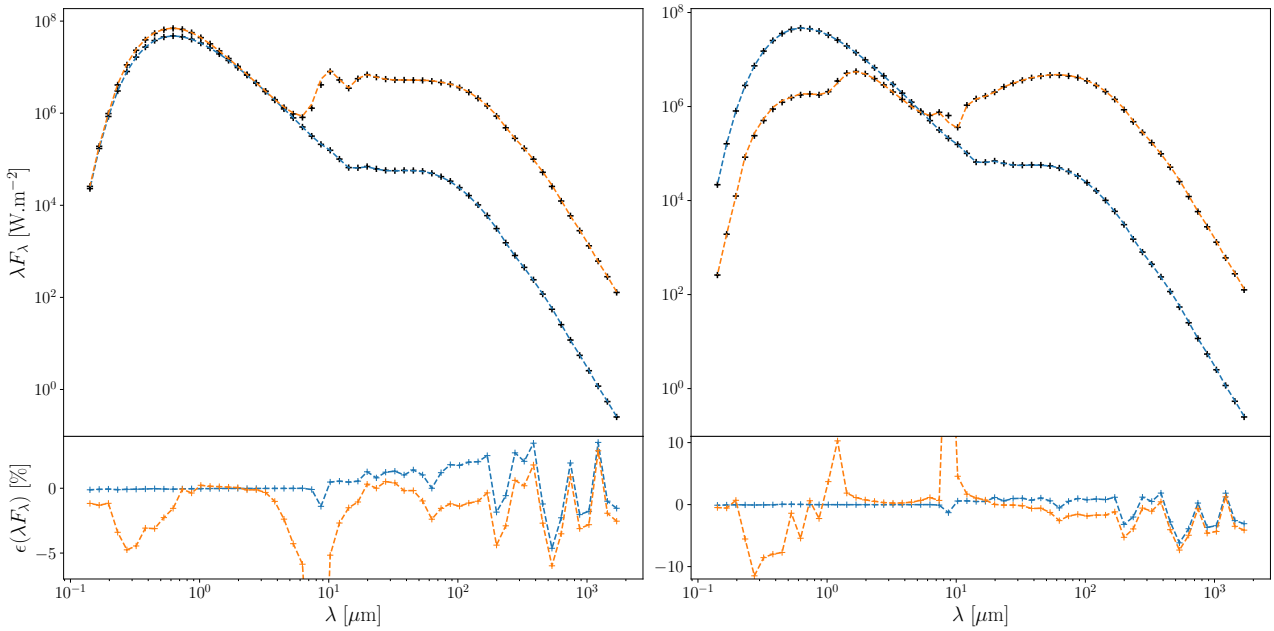

Fig. 6. SEDs profiles for the axis-symmetric envelope with $\tau_{\nu_0} = 10^{-1}$ (blue curve) and $\tau_{\nu_0} = 10^{2}$ (orange curve). The left and right panels correspond to $i = 12.5, 77.5$ deg, respectively. The cross marks represent the solution from this study and the solid curves are computed with RADMC-3D. The lower panels display the relative differences between the two codes.

We consider the optically thin and thick cases $\tau_{\nu_0} = 10^{-1}, 10^{2}$, respectively. We compare our results with the outputs from RADMC-3D[2] (Dullemond et al. 2012) , a Monte-Carlo radiative transfer code. For our code, we use the same spatial and frequency grids than the previous test. For RADMC-3D, we use 128 points in both radial and angular direction, with a logarithmic sample in the radial direction.

The temperature T of the disc is displayed in Fig.5. The DG-FEM code successfully reproduces the temperature profile. The temperature regions with steep gradients are always well reproduced, even with a fairly reasonable number of nodes. This result is a direct consequence of having a high-order numerical scheme. The radiation field can exhibit discontinuities, because of boundary conditions or very strong density gradients. Our numerical tests revealed no oscillations and very few negative values for the specific intensity that did not pollute the computation of the mean radiation field. On average, the absolute relative differences stay below one percent for both test cases. The temperature in the disc mid-plane is very-well reproduced, highlighting that the method is able to correctly capture the shadow of the disc (the cool disc mid-plane outer regions shadowed by the dense disc mid-plane inner regions).

In Fig. 6, we display the corresponding emerging SEDs, for two inclinations with respect to the polar axis $i = 12.5, 77.5$ deg. Again our SEDs, computed from ray-tracing of the emissivity η_ν derived with the DG-FEM code. Their are made of the stellar and envelope contributions. The stellar component peaks at around $\lambda \approx 0.6$ μm is computed "exactly" (with the help of Eq. C.2) and the discrepancies are always < 1 % where this part dominates. Concerning the contribution from the envelope, both the scattering (< 1 μm) and emission (> 10 μm) parts agree well. On average, the absolute relative differences stays below 5 %. We note a peak in the discrepancies for the optically-thick case, between 8.7 and 10.2 μm (according to the resolution of our frequency grid). The same behaviour was previously observed in Pascucci et al. (2004), between a grid-based and a Monte-Carlo code. The authors suggested that, at these wavelengths, the flux mainly comes from the inner disc regions (between 1 and 2 AU) and the numerical simulations are particularly sensitive to the resolution of the inner parts. However we tried to increase the resolution in these regions which did not result in any improvement.

In Fig. 7, we show a set of images from the DG-FEM code of the 10 AU disc inner regions, at $\lambda = 2.3, 4.5, 12.1$ μm and for several inclinations $i = 12.5, 77.5, 90$ deg. These wavelengths are characteristic of the operating spectral bands of instruments such as GRAVITY (Gravity Collaboration et al. 2017) and MATISSE (Lopez et al. 2022). On average, the agreement between the images from the DG-FEM code and the images from RADMC-3D is around 10 % for all frequencies and inclinations. We show in Fig. 8 the comparison of an image slice at $x = 0$ AU, for two inclinations $i = 12.5, 77.5$ deg and for $\lambda = 2.3, 4.5, 12.1$ μm. In general, the disc emitting inner regions (peaks in Fig. 7) are reproduced very well ($\epsilon(I_\nu^{\rm env}) \leq 3$ %). The biggest discrepancies occur in the wings of the peaks, where the gradient is the steepest (in logarithmic scaling).

6. Conclusions

In this study, we applied the DG-FEM to the frequency-dependent two dimensional radiative transfer equation coupled with the radiative equilibrium equation, inside axis-symmetric circumstellar envelopes. We showed that it can accurately compute the temperature field and allow the correct determination of images and SEDs profiles via ray-tracing techniques. A desirable feature of the method is the ability to control the order of the numerical scheme via the number of nodes within each element, meaning that a high-order numerical scheme can simply be achieved by increasing the number of nodes n inside each elements.

[2] available at https://www.ita.uni-heidelberg.de/ dullemond/software/radmc-3d/

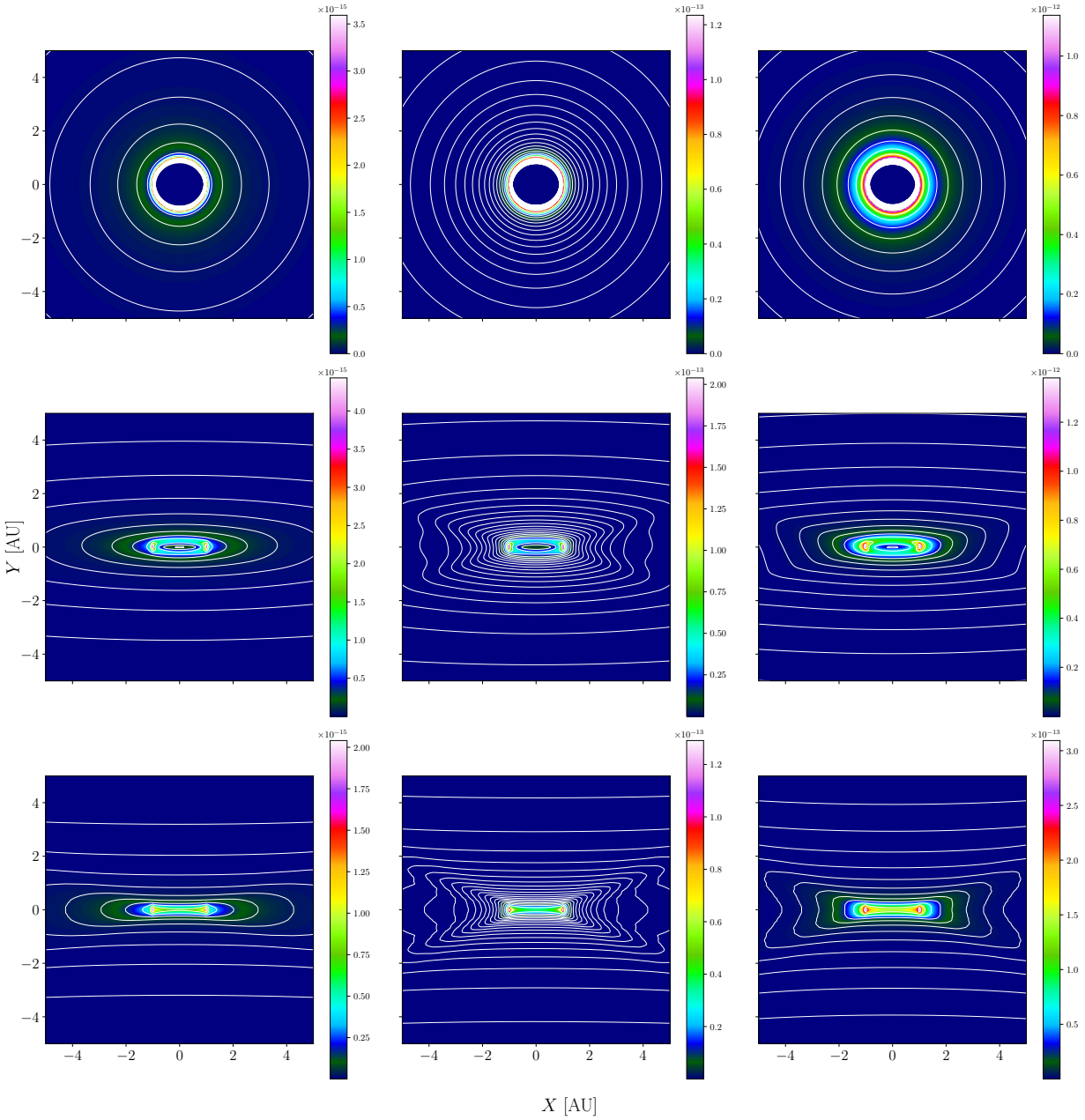

Fig. 7. Images at $\lambda = 2.3, 4.5, 12.1$ μm (left, middle, right panels, respectively) of the 10 AU inner regions of the axis-symmetric envelope (Sect. 5.2) and computed from the DG-FEM solution with the ray-tracing module (appendix C). The top middle and bottom panels correspond to the inclinations $i = 12.5, 77.5, 90$ deg, respectively. The color-code shows the specific intensity value (in W.m^{-2}.Hz^{-1}.sr^{-1}) of the envelope $I_\nu^{\rm env}$, inside each pixel. The white solid lines displays the iso-contours of $I_\nu^{\rm env}$.

The DG-FEM formulation Eq. (18) is particularly adapted to parallelisation and adaptive mesh refinement (AMR) grids (e.g Frisken & Perry 2002). In this regard, the direct access to the residual Eq. (16) might provide a robust estimate of the error that could be used as a criterion for the grid refinement (see e.g Richling et al. 2001). We also note that a further three-dimensional generalisation is also possible and straight-forward.

Together with Monte-Carlo and ray-tracing techniques, the DG-FEM provides an additional method for solving the radiative transfer problem, and could be used in the cases where the other methods are expected to be less efficient.

Acknowledgements. This study has been supported by the Lagrange laboratory of Astrophysics and funded under a 3-year PhD grant from Ecole Doctorale Sciences Fondamentales et Appliquées (EDSFA) of the Université Côte-d'Azur (UCA). The 1-D benchmark profiles were generated with the radiative transfer code DUSTY, available at http://faculty.washington.edu/ivezic/dusty_web. The 2-D benchmark were computed with RADMC-3D: https://www.ita.uni-heidelberg.de/ dullemond/software/radmc-3d/ Part of the computations were carried out with the help of OPAL-Meso computing facilities. The authors are grateful to the OPAL infrastructure from Observatoire de la Côte d'Azur (CRIMSON) for providing resources and support.

References

Chiang, E. I. & Goldreich, P. 1997, ApJ, 490, 368
Cockburn, B. 2003, Zeitschrift Angewandte Mathematik und Mechanik, 83, 731
Cui, X. & Li, B. Q. 2005, Journal of Quantitative Spectroscopy and Radiative Transfer, 96, 383
Draine, B. T. & Lee, H. M. 1984, ApJ, 285, 89

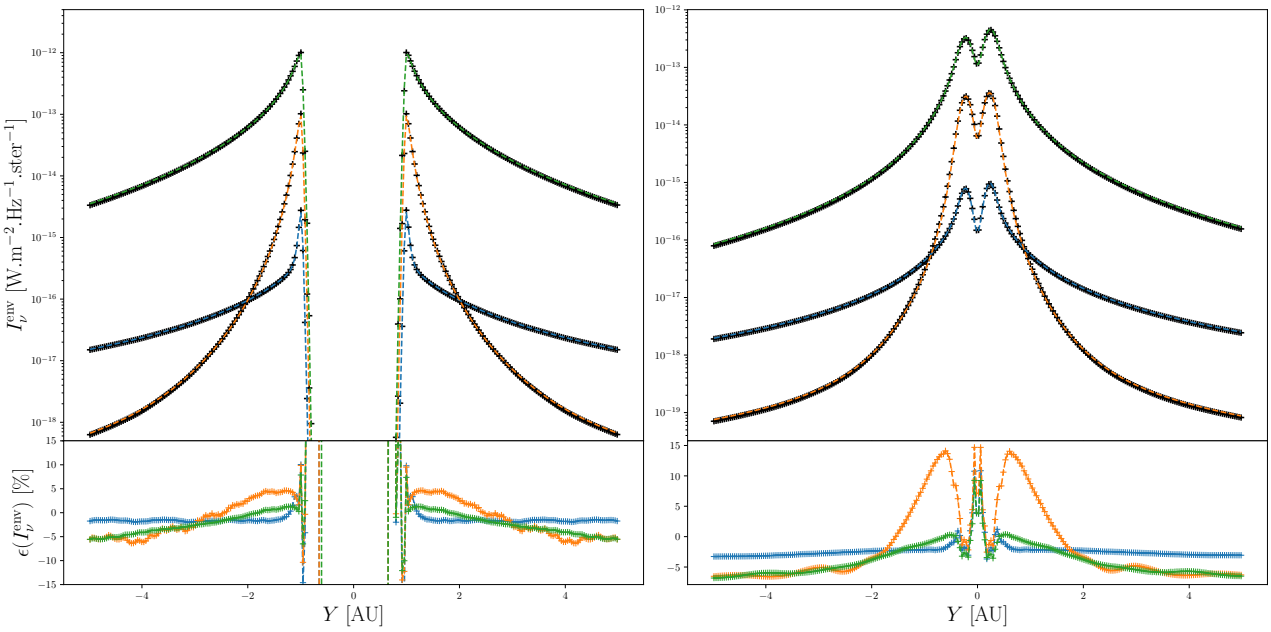

Fig. 8. Image slices at $x = 0$ AU, for two inclinations $i = 12.5, 77.5$ deg (left and right panels, respectively). The blue, orange, green curves are the RADMC-3D intensities at $\lambda = 2.3, 4.5, 12.1$ μm, respectively. The cross marks represent the solution from this study. The lower panels display the relative differences between the two codes.

Dullemond, C. P., Juhasz, A., Pohl, A., et al. 2012, RADMC-3D: A multi-purpose radiative transfer tool, Astrophysics Source Code Library, record ascl:1202.015
Eddington, A. S. 1920, The Scientific Monthly, 11, 297
Frisken, S. & Perry, R. 2002, Journal of Graphics Tools, 7
Gravity Collaboration, Abuter, R., Accardo, M., et al. 2017, A&A, 602, A94
Hesthaven, J. S. & Warburton, T. 2007, Nodal Discontinuous Galerkin Methods: Algorithms, Analysis, and Applications (Springer Science & Business Media)
Ivezic, Z., Groenewegen, M. A. T., Men'shchikov, A., & Szczerba, R. 1997, MNRAS, 291, 121
Karniadakis, G. E. & Kirby II, R. M. 2003, Parallel Scientific Computing in C and MPI: A Seamless Approach to Parallel Algorithms and their Implementation (Cambridge University Press)
Kitzmann, D., Bolte, J., & Patzer, A. B. C. 2016, A&A, 595, A90
Kopriva, D. A. & Gassner, G. 2010, Journal of Scientific Computing, 44, 136
Kuiper, R. & Klessen, R. S. 2013, A&A, 555, A7
Kunasz, P. & Auer, L. H. 1988, J. Quant. Spectr. Rad. Transf., 39, 67
Levermore, C. D. & Pomraning, G. C. 1981, ApJ, 248, 321
Lopez, B., Lagarde, S., Petrov, R. G., et al. 2022, A&A, 659, A192
Machorro, E. 2007, Journal of Computational Physics, 223, 67
Mihalas, D. & Mihalas, B. W. 1984, Foundations of radiation hydrodynamics
Nair, R. D., Levy, M. N., & Lauritzen, P. H. 2011, Emerging Numerical Methods for Atmospheric Modeling (Berlin, Heidelberg: Springer Berlin Heidelberg), 251–311
Olson, G. L., Auer, L. H., & Buchler, J. R. 1986, J. Quant. Spectr. Rad. Transf., 35, 431
Pascucci, I., Wolf, S., Steinacker, J., et al. 2004, A&A, 417, 793
Perdigon, J., Niccolini, G., & Faurobert, M. 2021, A&A, 653, A139
Pinte, C., Harries, T. J., Min, M., et al. 2009, A&A, 498, 967
Pomraning, G. C. 1973, The equations of radiation hydrodynamics
Reed, W. H. & Hill, T. R. 1973, Triangular mesh methods for the neutron transport equation, Tech. rep., Los Alamos Scientific Lab., N. Mex.(USA)
Richling, S., Meinköhn, E., Kryzhevoi, N., & Kanschat, G. 2001, A&A, 380, 776
Steinacker, J., Baes, M., & Gordon, K. D. 2013, ARA&A, 51, 63
Steinacker, J., Henning, T., Bacmann, A., & Semenov, D. 2003, A&A, 401, 405
Woitke, P., Kamp, I., & Thi, W. F. 2009, A&A, 501, 383
Wolf, S. 2003, Computer Physics Communications, 150, 99

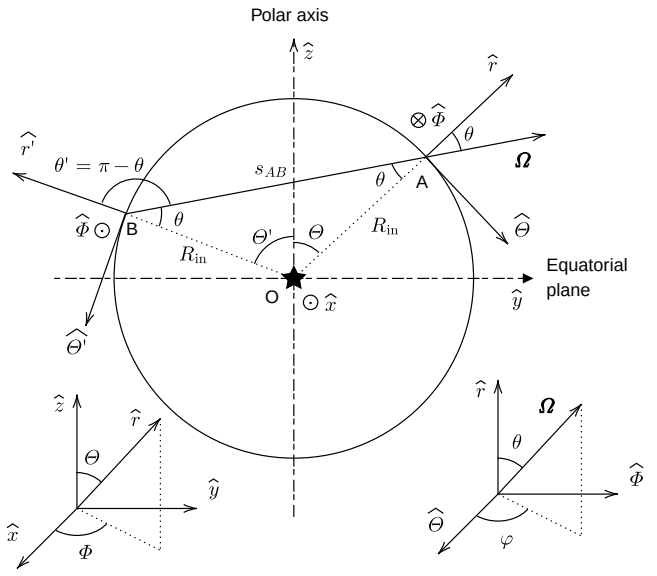

Fig. A.1. Geometry of a ray on the inner cavity. The point B corresponds to the opposite point A, along the direction $\boldsymbol{\Omega}$.

Appendix A: Boundary conditions on a spherical enclosed cavity

The boundary condition in Eq. (7) requires to know, for a given point A on the cavity of radius $R_{\rm in}$ and a given incoming direction $\boldsymbol{\Omega}$ ($\boldsymbol{\Omega}.\hat{r} > 0$), the coordinates on the opposite point B ($R_{\rm in}, \Theta', \mu' = \cos\theta', \varphi'$). The situation is illustrated in Fig. A.1. We define the Cartesian coordinate system $(\hat{x}, \hat{y}, \hat{z})$ with $\hat{z}$ aligned along the polar axis and the plane $(\hat{x}, \hat{y})$ coinciding with the equatorial plane. Since the problem is axis-symmetric around the polar axis $\hat{z}$, the coordinates do not depend on the azimutal angle Φ and we can arbitrarily choose A and B to be in the same plane at $\Phi = \pi/2$. This convention simplifies the computations.

First, we see that $\theta' = \pi - \theta$, because the OAB triangle is isosceles, so

$$\mu' = -\mu. \tag{A.1}$$

The position $\boldsymbol{r}_B$ of the point B, is linked to the position $\boldsymbol{r}_A$ of the point A through the relation

$$\boldsymbol{r}_B = \boldsymbol{r}_A - s_{AB}\boldsymbol{\Omega} \tag{A.2}$$

with s_{AB}, the distance between the point A and B. The direction vector $\boldsymbol{\Omega}$ is

$$\boldsymbol{\Omega} = \begin{bmatrix} \mu \\ \sqrt{1-\mu^2}\cos\varphi \\ \sqrt{1-\mu^2}\sin\varphi \end{bmatrix}_{(\hat{r},\hat{\Theta},\hat{\Phi})} = \begin{bmatrix} -\sqrt{1-\mu^2}\sin\varphi \\ \sin\Theta\mu + \cos\Theta\sqrt{1-\mu^2}\cos\varphi \\ \cos\Theta\mu - \sin\Theta\sqrt{1-\mu^2}\cos\varphi \end{bmatrix}_{(\hat{x},\hat{y},\hat{z})} \tag{A.3}$$

and Eq. (A.2) is rewritten

$$R_{\rm in}\begin{bmatrix} 0 \\ \sin\Theta' \\ \cos\Theta' \end{bmatrix}_{(\hat{x},\hat{y},\hat{z})} = R_{\rm in}\begin{bmatrix} 0 \\ \sin\Theta \\ \cos\Theta \end{bmatrix}_{(\hat{x},\hat{y},\hat{z})} - s_{AB}\begin{bmatrix} -\sqrt{1-\mu^2}\sin\varphi \\ \sin\Theta\mu + \cos\Theta\sqrt{1-\mu^2}\cos\varphi \\ \cos\Theta\mu - \sin\Theta\sqrt{1-\mu^2}\cos\varphi \end{bmatrix}_{(\hat{x},\hat{y},\hat{z})} \tag{A.4}$$

The length $s_{AB} = 2\mu R_{\rm in}$ is simply deduced from the length of the base of the isosceles triangle OAB, with $OA = OB = R_{\rm in}$. A relation between Θ' and the coordinates of the point A is then obtained, rewriting the z-component of Eq. (A.4)

$$\cos\Theta' = \left(1 - 2\mu^2\right)\cos\Theta + 2\mu\sqrt{1-\mu^2}\cos\varphi\sin\Theta, \tag{A.5}$$

and consequently $\Theta' = \arccos|\cos\Theta'|$. The absolute value occurs if we consider the planar symmetry with respect to the equatorial plane. The angle φ' at the point B verifies

$$\tan\varphi' = \frac{\boldsymbol{\Omega}.\hat{\Phi}'}{\boldsymbol{\Omega}.\hat{\Theta}'}. \tag{A.6}$$

with

$$\begin{aligned} \hat{\Phi}' &= \begin{bmatrix} -1 \\ 0 \\ 0 \end{bmatrix}_{(\hat{x},\hat{y},\hat{z})} \\ \hat{\Theta}' &= \begin{bmatrix} 0 \\ \cos\Theta' \\ -\sin\Theta' \end{bmatrix}_{(\hat{x},\hat{y},\hat{z})} \\ &= \begin{bmatrix} 0 \\ \cos\Theta - 2\mu\left(\sin\Theta\mu + \cos\Theta\sqrt{1-\mu^2}\cos\varphi\right) \\ -\sin\Theta + 2\mu\left(\cos\Theta\mu - \sin\Theta\sqrt{1-\mu^2}\cos\varphi\right) \end{bmatrix}_{(\hat{x},\hat{y},\hat{z})} \end{aligned} \tag{A.7}$$

and $\boldsymbol{\Omega}$ given by Eq. (A.3). Then Eq. (A.6) simplifies to

$$\tan\varphi' = \frac{\sin\varphi\sin\Theta}{(1-2\mu^2)\cos\varphi\sin\Theta - 2\mu\sqrt{1-\mu^2}\cos\Theta}. \tag{A.8}$$

Consequently $\varphi' = \arctan|y|/x$ with y and x being the numerator and denominator in Eq. (A.8), respectively. This time, the absolute value is present because of the symmetry around the polar axis ($\varphi' \in [0, \pi]$). Note that the previous formula breaks for the couples $(\mu, \varphi) = (\sin(\Theta/2), 0)$ and $(\mu, \varphi) = (\cos(\Theta/2), \pi)$, as expected, because it corresponds to the opposite point B on the poles, where $\hat{\Theta}'$ and $\hat{\Phi}'$ are not defined. These particular cases are not important since the radiation field is independent of φ' at these points.

Appendix B: DG-FEM calculations

The computation of the terms in Eq. (18), requires the choice of a particular quadrature in the cell $D^{i,j,k,l}$ for each coordinate $(r, \Theta, \mu, \varphi)$. For the r, μ, φ coordinates, we make use of the Gauss-Lobatto quadrature which has the advantage of having roots at the end points of the cell. This avoids the use of an interpolation formula when computing the numerical flux $\boldsymbol{F}_h^*$ at the element edges. The Gauss-Lobatto quadrature can exactly integrate polynomials up to degree $2n-3$ with n the number of nodes. For the Θ coordinate, we cannot use the Gauss-Lobatto quadrature, at least in the cells that are touching $\Theta = 0$, because the radiative transfer equation is not defined at the pole in spherical coordinates. For this reason and to keep an homogeneous method along the Θ coordinate, we use a Gauss-Legendre quadrature for this coordinate. The Gauss-Legendre quadrature is more precise and can exactly integrate polynomials up to degree $2n-1$, but at the expense of the need of an interpolation method to compute the flux at the cell edges. An example of an element $D^{i,j,k,l}$ with the chosen nodes is displayed in Fig. B.1.

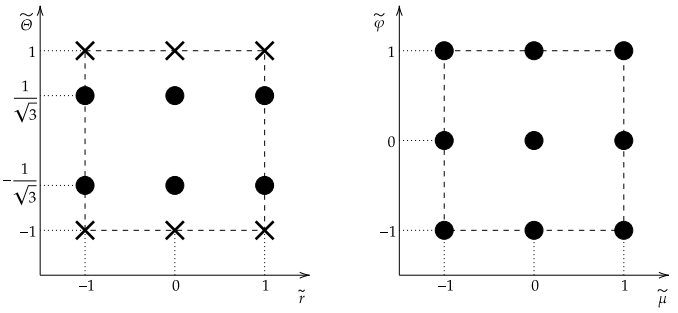

Fig. B.1. Example of an element $D^{i,j,k,l}$ (dashed lines) using $n_a = n_c = n_d = 3$ and $n_b = 2$ points. The left and right panels correspond to two-dimensional slices in the (r, Θ) and (μ, φ) planes, respectively (we display here the local coordinate system given by Eq. (B.2)). The black dots correspond to the nodes where the solution is computed while the crosses correspond to the interpolated value of I used to compute the numerical flux F_h^* at the interface, along the Θ-coordinate.

In the following, all the superscript indexes refer to the element identification while the subscripts denote each node in the considered element. We start with the volume term in Eq. (18),

$$\begin{aligned}
&\int_{D^{i,j,k,l}} \left(\kappa^{\rm ext}\tilde{I}_h - \tilde{\eta}\right) h_{a',b',c',d'}\,\mathrm{d}^4\boldsymbol{x} \\
&= \frac{\Delta x^{i,j,k,l}}{16}\int_{-1}^{1}\left(\kappa^{\rm ext}\tilde{I}_h^{i,j,k,l} - \tilde{\eta}^{i,j}\right) h_{a',b',c',d'}\,\mathrm{d}^4\tilde{\boldsymbol{x}} \\
&= \frac{\Delta x^{i,j,k,l}}{16}\sum_{a,b,c,d} W_{a,b,c,d}\left(\kappa_{a,b}^{{\rm ext}\,i,j}\tilde{I}_{a,b,c,d}^{i,j,k,l} - \tilde{\eta}_{a,b}^{i,j}\right) h_{a',b',c',d'}\left(\tilde{\boldsymbol{x}}_{a,b,c,d}\right).
\end{aligned} \tag{B.1}$$

$\Delta x^{i,j,k,l} = \Delta r^i \Delta\Theta^j \Delta\mu^k \Delta\varphi^l$ is the four-dimensional volume of the element $D^{i,j,k,l}$. For integration, we used the local coordinate system $[\tilde{r}, \tilde{\Theta}, \tilde{\mu}, \tilde{\varphi}]$, defined as (for instance, for the r coordinate),

$$\tilde{r} = \frac{2}{\Delta r^i}\left(r - r^{i+1/2}\right). \tag{B.2}$$

Δr^i is the element width along the r-coordinate, and $r^{i+1/2}$ the centre of the element. The same expression holds for the other coordinates. $W_{a,b,c,d} = W_r(\tilde{r}_a)\, W_\Theta(\tilde{\Theta}_b)\, W_\mu(\tilde{\mu}_c)\, W_\varphi(\tilde{\varphi}_d)$ are the weights associated with the different quadrature in each direction. Finally, $h_{a',b',c',d'}\left(\tilde{\boldsymbol{x}}_{a,b,c,d}\right)$ is the four-dimensional Lagrange polynomials, defined in Eq. (14), evaluated at the node $\tilde{\boldsymbol{x}}_{a,b,c,d} = \left[\tilde{r}_a, \tilde{\Theta}_b, \tilde{\mu}_c, \tilde{\varphi}_d\right]$. By definition of the Lagrange polynomials, we have,

$$h_{a',b',c',d'}\left(\tilde{r}_a, \tilde{\Theta}_b, \tilde{\mu}_c, \tilde{\varphi}_d\right) = \delta_{a',a}\,\delta_{b',b}\,\delta_{c',c}\,\delta_{d',d}, \tag{B.3}$$

with $\delta_{a',a}$ the usual delta Kronecker. The other volume term in Eq. (18) is expressed as,

$$\begin{aligned}
&\int_{D^{i,j,k,l}} \boldsymbol{F}_h.\nabla_{\boldsymbol{x}} h_{a',b',c',d'}\,\mathrm{d}^4\boldsymbol{x} \\
&= \int_{D^{i,j,k,l}} a_r\tilde{\boldsymbol{I}}_h\,\partial_r h_{a',b',c',d'}\,\mathrm{d}^4\boldsymbol{x} + \int_{D^{i,j,k,l}} a_\Theta\tilde{\boldsymbol{I}}_h\,\partial_\Theta h_{a',b',c',d'}\,\mathrm{d}^4\boldsymbol{x} \\
&+ \int_{D^{i,j,k,l}} a_\mu\tilde{\boldsymbol{I}}_h\,\partial_\mu h_{a',b',c',d'}\,\mathrm{d}^4\boldsymbol{x} + \int_{D^{i,j,k,l}} a_\varphi\tilde{\boldsymbol{I}}_h\,\partial_\varphi h_{a',b',c',d'}\,\mathrm{d}^4\boldsymbol{x} \\
&= \frac{\Delta x^{i,j,k,l}}{8}\sum_{a,b,c,d} W_{a,b,c,d}\tilde{I}_{a,b,c,d}^{i,j,k,l}\left(\frac{a_{\tilde{r}\,a,b,c,d}^{i,j,k,l}\partial_{\tilde{r}}h_{a',b',c',d'}|_{\tilde{\boldsymbol{x}}_{a,b,c,d}}}{\Delta r^i}\right. \\
&+ \frac{a_{\tilde{\Theta}\,a,b,c,d}^{i,j,k,l}\partial_{\tilde{\Theta}}h_{a',b',c',d'}|_{\tilde{\boldsymbol{x}}_{a,b,c,d}}}{\Delta\Theta^j} + \frac{a_{\tilde{\mu}\,a,b,c,d}^{i,j,k,l}\partial_{\tilde{\mu}}h_{a',b',c',d'}|_{\tilde{\boldsymbol{x}}_{a,b,c,d}}}{\Delta\mu^k} \\
&\left. + \frac{a_{\tilde{\varphi}\,a,b,c,d}^{i,j,k,l}\partial_{\tilde{\varphi}}h_{a',b',c',d'}|_{\tilde{\boldsymbol{x}}_{a,b,c,d}}}{\Delta\varphi^l}\right).
\end{aligned} \tag{B.4}$$

In Eq. (B.4), we made use of the definition of the flux Eq. (12). $\partial_{\tilde{r}}h_{a',b',c',d'}|_{\boldsymbol{x}_{a,b,c,d}}$ is the partial derivative of the Lagrange polynomial, with respect to the r-coordinate, evaluated at the node $\tilde{\boldsymbol{x}}_{a,b,c,d}$ (with similar definitions for the other coordinates).

The last term to evaluate is the surface integral (first term in Eq. 18). The four-dimensional element is delimited by $2\times4 = 8$ surfaces. We give here the derivation for the surfaces integral normal to the r-coordinate and the other terms will follow by substitution of the indices. We have $\hat{s} = \pm\hat{r}$ for the radial right and left surfaces ($\tilde{r} = \pm1$), respectively,

$$\begin{aligned}
&\oint_{\partial D^{i,j,k,l}} \left[F_r^* h_{a',b',c',d'}\right]_{\tilde{r}=-1}^{\tilde{r}=1}\,\mathrm{d}\Theta\,\mathrm{d}\mu\,\mathrm{d}\varphi \\
&= \frac{\Delta x^{i,j,k,l}}{8\,\Delta r^i} W_{b',c',d'}\left[F_{\tilde{r}}^*\left(\tilde{r}, \tilde{\Theta}_{b'}, \tilde{\mu}_{c'}, \tilde{\varphi}_{d'}\right) h_{a'}\left(\tilde{r}\right)\right]_{\tilde{r}=-1}^{\tilde{r}=1}.
\end{aligned} \tag{B.5}$$

At the cell boundaries, we use the upwind numerical flux, e.g at the right edge,

$$\begin{aligned}
&F_{\tilde{r}}^*\left(\tilde{r}=1, \tilde{\Theta}_{b'}, \tilde{\mu}_{c'}, \tilde{\varphi}_{d'}\right) = \\
&\max\left\{a_{\tilde{r}}^{i,j,k,l}\left(1, \tilde{\Theta}_{b'}, \tilde{\mu}_{c'}, \tilde{\varphi}_{d'}\right), 0\right\}\tilde{\boldsymbol{I}}_h^{i,j,k,l}\left(1, \tilde{\Theta}_{b'}, \tilde{\mu}_{c'}, \tilde{\varphi}_{d'}\right) \\
&+ \min\left\{a_{\tilde{r}}^{i,j,k,l}\left(1, \tilde{\Theta}_{b'}, \tilde{\mu}_{c'}, \tilde{\varphi}_{d'}\right), 0\right\}\tilde{\boldsymbol{I}}_h^{i+1,j,k,l}\left(-1, \tilde{\Theta}_{b'}, \tilde{\mu}_{c'}, \tilde{\varphi}_{d'}\right).
\end{aligned} \tag{B.6}$$

The use of the Gauss-Lobatto quadrature further simplify the computation because the quadrature nodes include the end-points $\tilde{r} = \pm1$. The numerical flux can then be expressed as

$$\begin{aligned}
&\left[F_{\tilde{r}}^*\left(\tilde{r}, \tilde{\Theta}_{b'}, \tilde{\mu}_{c'}, \tilde{\varphi}_{d'}\right) h_{a'}\left(\tilde{r}\right)\right]_{\tilde{r}=-1}^{\tilde{r}=1} = \\
&\delta_{a',n_a-1}\max\left\{a_{\tilde{r}\,n_a-1,b',c',d'}^{i,j,k,l}, 0\right\}\tilde{I}_{n_a-1,b',c',d'}^{i,j,k,l} \\
&+\delta_{a',n_a-1}\min\left\{a_{\tilde{r}\,n_a-1,b',c',d'}^{i,j,k,l}, 0\right\}\tilde{I}_{0,b',c',d'}^{i+1,j,k,l} \\
&-\delta_{a',0}\max\left\{a_{\tilde{r}\,0,b',c',d'}^{i,j,k,l}, 0\right\}\tilde{I}_{n_a-1,b',c',d'}^{i-1,j,k,l} \\
&-\delta_{a',0}\min\left\{a_{\tilde{r}\,0,b',c',d'}^{i,j,k,l}, 0\right\}\tilde{I}_{0,b',c',d'}^{i,j,k,l}.
\end{aligned} \tag{B.7}$$

The same form holds for the surface integrals normal to the μ and φ coordinates. We however note that we have $a_\mu \geq 0$, $a_\varphi \leq 0\,\forall\,\boldsymbol{x} \in D$, so there are no terms proportional to $\tilde{I}^{i,j,k+1,l}$ and

$\tilde{I}^{i,j,k,l-1}$. For the flux computation normal to the Θ coordinate, we do not directly have the value of the solution at the element interface (see Fig. B.1), we need to interpolate the solution with the help of Eq. (13),

$$\begin{aligned} F^{*}_{\tilde{\Theta}}\left(\tilde{r}_{a'}, \tilde{\Theta}=1, \tilde{\mu}_{c'}, \tilde{\varphi}_{d'}\right) = \\ \max\left\{a^{i,j,k,l}_{\tilde{\Theta}}\left(\tilde{r}_{a'}, 1, \tilde{\mu}_{c'}, \tilde{\varphi}_{d'}\right), 0\right\} \sum_{b} \tilde{I}^{i,j,k,l}_{a',b,c',d'} h_b\left(1\right) \\ + \min\left\{a^{i,j,k,l}_{\tilde{\Theta}}\left(\tilde{r}_{a'}, 1, \tilde{\mu}_{c'}, \tilde{\varphi}_{d'}\right), 0\right\} \sum_{b} \tilde{I}^{i,j+1,k,l}_{a',b,c',d'} h_b\left(-1\right). \end{aligned} \tag{B.8}$$

All the terms in this section can be put in the form of the system of equations, given by Eq. (22),

$$\mathcal{A}^{i,j,k,l}\, \tilde{\boldsymbol{I}}^{i,j,k,l}_{h} = \boldsymbol{b}^{i,j,k,l} \tag{B.9}$$

In Eq. (B.9), we replaced the RHS by $\boldsymbol{b}^{i,j,k,l}$ because we do not need to formally write the non-diagonal matrices $\mathcal{A}^{i\pm1,j\pm1,k-1,l+1}$. To assemble $\mathcal{A}^{i,j,k,l}$, we make use of the global index $\alpha = a\, n_b n_c n_d + b\, n_c n_d + c\, n_d + d$. The elements of $\mathcal{A}^{i,j,k,l}$ and $\boldsymbol{b}^{i,j,k,l}$ are then,

$$\begin{aligned} \mathcal{A}^{i,j,k,l}_{\alpha'\alpha} &= W_{a,b,c,d}\, \kappa^{\mathrm{ext}\,i,j}_{a,b} \delta_{a',a}\, \delta_{b',b}\, \delta_{c',c}\, \delta_{d',d} \\ &+ \frac{2}{\Delta r^{i}} \delta_{b',b}\delta_{c',c}\delta_{d',d} W_{b,c,d} \left(\max\left\{a^{i,j,k,l}_{\tilde{r}\,a,b,c,d}, 0\right\}\delta_{a',n_a-1}\delta_{a,n_a-1} \right. \\ &\left. - \min\left\{a^{i,j,k,l}_{\tilde{r}\,a,b,c,d}, 0\right\}\delta_{a',0}\delta_{a,0} - W_a\, a^{i,j,k,l}_{\tilde{r}\,a,b,c,d}\, \partial_{\tilde{r}} h_{a'}|_{\tilde{r}_a}\right) \\ &+ \frac{2}{\Delta\Theta^{j}} \delta_{a',a}\delta_{c',c}\delta_{d',d} W_{a,c,d} \left(\max\left\{a^{i,j,k,l}_{\tilde{\Theta}\,a,c,d}|_{\tilde{\Theta}=1}, 0\right\} h_{b'}|_{\tilde{\Theta}=1} h_b|_{\tilde{\Theta}=1} \right. \\ &\left. - \min\left\{a^{i,j,k,l}_{\tilde{\Theta}\,a,c,d}|_{\tilde{\Theta}=-1}, 0\right\} h_{b'}|_{\tilde{\Theta}=-1} h_b|_{\tilde{\Theta}=-1} - W_b\, a^{i,j,k,l}_{\tilde{\Theta}\,a,b,c,d}\, \partial_{\tilde{\Theta}} h_{b'}|_{\tilde{\Theta}_b}\right) \\ &+ \frac{2}{\Delta\mu^{k}} \delta_{a',a}\delta_{b',b}\delta_{d',d} W_{a,b,d} a^{i,j,k,l}_{\tilde{\mu}\,a,b,c,d} \left(\delta_{c',n_c-1}\delta_{c,n_c-1} - W_c \partial_{\tilde{\mu}} h_{c'}|_{\tilde{\mu}_c}\right) \\ &- \frac{2}{\Delta\varphi^{l}} \delta_{a',a}\delta_{b',b}\delta_{c',c} W_{a,b,c} a^{i,j,k,l}_{\tilde{\varphi}\,a,b,c,d} \left(\delta_{d',0}\delta_{d,0} + W_d \partial_{\tilde{\varphi}} h_{d'}|_{\tilde{\varphi}_d}\right). \end{aligned} \tag{B.10}$$

$$\begin{aligned} b^{i,j,k,l}_{\alpha'} &= W_{a',b',c',d'}\, \tilde{\eta}^{i,j}_{a',b'} \\ &+ \frac{2}{\Delta r^{i}} W_{b',c',d'} \left(\max\left\{a^{i-1,j,k,l}_{\tilde{r}\,n_a-1,b',c',d'}, 0\right\}\tilde{I}^{i-1,j,k,l}_{n_a-1,b',c',d'}\delta_{a',0} \right. \\ &\left. - \min\left\{a^{i+1,j,k,l}_{\tilde{r}\,0,b',c',d'}, 0\right\}\tilde{I}^{i+1,j,k,l}_{0,b',c',d'}\delta_{a',n_a-1}\right) \\ &+ \frac{2}{\Delta\Theta^{j}} W_{a',c',d'} \left(\max\left\{a^{i,j-1,k,l}_{\tilde{\Theta}\,a',c',d'}|_{\tilde{\Theta}=1}, 0\right\} h_{b'}|_{\tilde{\Theta}=-1} \sum_{b} \tilde{I}^{i,j-1,k,l}_{a',b,c',d'} h_b|_{\tilde{\Theta}=1} \right. \\ &\left. - \min\left\{a^{i,j+1,k,l}_{\tilde{\Theta}\,a',c',d'}|_{\tilde{\Theta}=-1}, 0\right\} h_{b'}|_{\tilde{\Theta}=1} \sum_{b} \tilde{I}^{i,j+1,k,l}_{a',b,c',d'} h_b|_{\tilde{\Theta}=-1}\right) \\ &+ \frac{2}{\Delta\mu^{k}} W_{a',b',d'} a^{i,j,k-1,l}_{\tilde{\mu}\,a',b',n_c-1,d'} \tilde{I}^{i,j,k-1,l}_{a',b',n_c-1,d'}\delta_{c',0} \\ &- \frac{2}{\Delta\varphi^{l}} W_{a',b',c'} a^{i,j,k,l+1}_{\tilde{\varphi}\,a',b',c',0} \tilde{I}^{i,j,k,l+1}_{a',b',c',0}\delta_{d',n_d-1}. \end{aligned} \tag{B.11}$$

Appendix C: Ray-tracing module

The SEDs and intensity maps from the DG-FEM code, displayed in Sect 5, are computed with the help of the ray tracing routine we present here.

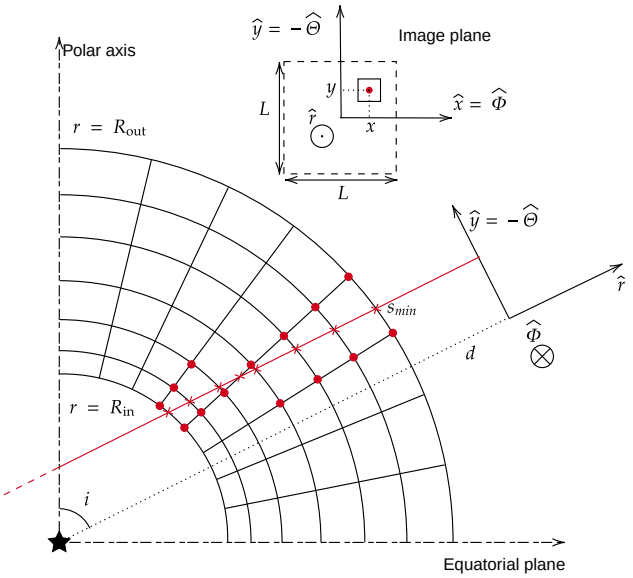

Fig. C.1. Example of a ray (red line) normal to the image plane, crossing the spherical grid. In this example, we display a square image of size $L \times L$. The red crosses represent the intersections between the ray and the grid. The values of $\kappa^{\mathrm{ext}}_{\nu}$ and S_{ν} at these intersections are linearly interpolated from the grid-adjacent values (red dots).

For the SED, we need to estimate the total flux f^{obs}_{ν} that an observer receive from the object, situated at a distance $d \gg R_{\mathrm{out}}$ and doing an angle i with the polar axis (see Fig. C.1). Because we decouple the stellar from the envelope radiation (see Eq. 4), the total flux is made of the stellar and envelope total flux,

$$f^{\mathrm{obs}}_{\nu}(i,d) = f^{\mathrm{obs},\star}_{\nu} + f^{\mathrm{obs,env}}_{\nu}. \tag{C.1}$$

If we assume the star to be an unresolved black-body point source, the stellar flux at distance d is the flux of the star at the stellar surface attenuated by the circumstellar matter present in the direction of the line of sight (black dotted line in Fig. C.1), and with the dilution factor $(R_{\star}/d)^2$,

$$\begin{aligned} f^{\mathrm{obs},\star}_{\nu}(i,d) &= \pi \left(\frac{R_{\star}}{d}\right)^{2} B_{\nu}(T_{\star}) \exp\left\{-\tau(i)\right\} \\ \text{with} \quad \tau(i) &= \int_{R_{\mathrm{in}}}^{R_{\mathrm{out}}} \kappa^{\mathrm{ext}}_{\nu}(r,i)\, \mathrm{d}r \end{aligned} \tag{C.2}$$

To compute the envelope flux and intensity maps, we define an image plane $(\hat{x}, \hat{y})$, at a distance $d \gg R_{\mathrm{out}}$ from the star and tilted with an angle i with respect to the polar axis. The x and y axes are oriented with the help of the spherical coordinates system $(\hat{r}, \hat{\Theta}, \hat{\Phi})$. In this plane, we can construct images of any geometry but we only consider the special cases of a square image of width L and a circular image of radius R. Since $d \gg R_{\mathrm{out}}$, the flux inside the image can formally be written

$$\begin{aligned} f^{\mathrm{obs,env}}_{\nu}(i) &= \int_{-\frac{L}{2}}^{\frac{L}{2}} \int_{-\frac{L}{2}}^{\frac{L}{2}} I^{\mathrm{env}}_{\nu}(x,y,\hat{r})\, \frac{\mathrm{d}x\, \mathrm{d}y}{d^2}, \\ \text{or} \quad f^{\mathrm{obs,env}}_{\nu}(i) &= \int_{0}^{2\pi} \int_{0}^{R} I^{\mathrm{env}}_{\nu}(r,\omega,\hat{r})\, \frac{r\, \mathrm{d}\omega\, \mathrm{d}r}{d^2}. \end{aligned} \tag{C.3}$$

In practice, images are made of a collection of pixels in which we evaluate the emerging specific intensity at the pixel centre. A square (circular) image, is divided into $N \times N$ ($N_r \times N_\omega$) pixels and the flux in the image can then be rewritten

$$f_\nu^{\rm obs,env}(i) \approx \sum_{i=0}^{N-1}\sum_{j=0}^{N-1} I_\nu^{\rm env}(x_i, y_j, \hat{r})\ \frac{\Delta x_i\, \Delta y_i}{d^2},$$
$$\text{or} \quad f_\nu^{\rm obs,env}(i) \approx \sum_{i=0}^{N_r}\sum_{j=0}^{N_\omega} I_\nu^{\rm env}(r_i, \omega_j, \hat{r})\ \frac{r_i\, \Delta\omega_j\, \Delta r_i}{d^2}, \tag{C.4}$$

with $\Delta x_i \Delta y_i$ ($r_i\, \Delta\omega_j\, \Delta r_i$) the pixel size of the square (circular) image. We note that the circular image is particularly well-suited for the computation of $f_\nu^{\rm obs,env}(i)$ since we can easily increase the number of pixels in the centre of the image in order to resolve the disc inner parts.

In practice, we already know $I_\nu^{\rm env}(x_i, y_j, \hat{r})$ from the DG-FEM solution at the outer edge of the envelope. It is however not advised to use it because of its poor accuracy, due to the poor resolution of the grid ($\Delta\Theta$ is large at $r = R_{\rm out}$). This effect is even more important if we are interested in zooming on the inner parts of the disc and hence probing a very-small part of the outer shell of the envelope. Consequently a post-processing ray tracing step usually needed in order to accurately capture all the features of the disc. We note that this procedure is quite generally used in the literature, for all type of codes, and is not a limitation of the DG-FEM method itself (see e.g Pinte et al. 2009, Sect 2.2.3)

The emerging specific intensity crossing each pixel centre $\boldsymbol{r}_0 = x_i\, \hat{x} + y_j\, \hat{y} + d\, \hat{r}$ ($\boldsymbol{r}_0 = r_i \sin\omega_j\, \hat{x} + r_i \cos\omega_j\, \hat{y} + d\, \hat{r}$ for a circular image), along the ray normal to the image plane (red line in Fig. C.1) is computed by integration of the emissivity along the ray,

$$I_\nu^{\rm env}(\boldsymbol{r}_0, \hat{r}) = \int_{s_{min}}^{s_{max}} \eta_\nu \exp\{-\tau_\nu(s)\}\, {\rm d}s,$$
$$\text{with} \quad \tau_\nu(s) = \int_{s_{min}}^{s} \kappa_\nu^{\rm ext}\, {\rm d}s'. \tag{C.5}$$

s is the distance from the pixel centre $\boldsymbol{r}_0$ in the image plane to a given point on the ray. η_ν and $\kappa_\nu^{\rm ext}$ are the emissivity and the extinction coefficient, respectively, as defined in Eq. (1), s_{min} and s_{max} correspond to the two intersections of the ray with the sphere of radius $R_{\rm out}$. In practice, η_ν and $\kappa_\nu^{\rm ext}$ are defined on a discrete grid and the previous integral can be rewritten as

$$I_\nu^{\rm env}(\boldsymbol{r}_0, \hat{r}) = \sum_{i=0}^{n-2} \int_{s_i}^{s_{i+1}} \eta_\nu\ \exp\{-\tau_\nu(s)\}\, {\rm d}s \tag{C.6}$$

The $\{s_i\}$ are the n intersections of the ray with the grid (red crosses in Fig. C.1), with $s_0 = s_{min}$ and $s_{n-1} = s_{max}$. The coordinates of all intersections can be easily computed, in the Cartesian coordinate system. We can express ΔI_ν^i, the contribution to the total intensity $I_\nu^{\rm env}(x, y, \hat{r})$ of each portion between two consecutive intersections as,

$$I_\nu^{\rm env}(\boldsymbol{r}_0, \hat{r}) = \sum_{i=0}^{n-2} \exp\left\{-\tau_\nu^i\right\} \Delta I_\nu^i,$$
$$\text{with} \quad \Delta I_\nu^i = \int_{s_i}^{s_{i+1}} \eta_\nu\ \exp\left\{-\int_{s_i}^{s} \kappa_\nu^{\rm ext}\, {\rm d}s'\right\} {\rm d}s$$
$$\text{and} \quad \tau_\nu^i = \int_{s_{min}}^{s_i} \kappa_\nu^{\rm ext}\, {\rm d}s'. \tag{C.7}$$

Following Olson et al. 1986, we assume that η_ν and $\kappa_\nu^{\rm ext}$ are linear functions between two consecutive intersections. Each contribution ΔI_ν^i is given by

$$\Delta I_\nu^i \approx \left(1 - \exp\left\{-\Delta\tau_\nu^i\right\} - \beta\right) S_\nu(s_i) + \beta\, S_\nu(s_{i+1}),$$
$$\text{with} \quad \beta = \frac{\Delta\tau_\nu^i - 1 + \exp\left\{-\Delta\tau_\nu^i\right\}}{\Delta\tau_\nu^i}$$
$$\text{and} \quad \Delta\tau_\nu^i = \frac{\kappa_\nu^{\rm ext}(s_i) + \kappa_\nu^{\rm ext}(s_{i+1})}{2}\, (s_{i+1} - s_i), \tag{C.8}$$

with $S_\nu = \eta_\nu / \kappa_\nu^{\rm ext}$. The values of S_ν and $\kappa_\nu^{\rm ext}$ at the intersections s_i and s_{i+1} are estimated by linear interpolation from the grid-adjacent values (red dots in Fig. C.1). τ_ν^i can be computed recursively,

$$\tau_\nu^{i+1} = \tau_\nu^i + \int_{s_i}^{s_{i+1}} \kappa_\nu^{\rm ext}\, {\rm d}s' = \tau_\nu^i + \Delta\tau_\nu^i, \tag{C.9}$$

with $\tau_\nu^0 = 0$ and $\Delta\tau_\nu^i$ defined in Eq. (C.8).